

**MODELING AND PROCESS PLANNING FOR EXPOSURE CONTROLLED PROJECTION  
LITHOGRAPHY**

A Thesis  
Presented to  
The Academic Faculty

By

**Amit S. Jariwala**

In Partial Fulfillment  
Of the Requirements for the Degree of  
Doctor of Philosophy in Mechanical Engineering

Georgia Institute of Technology

May, 2013

Copyright © 2013 by Amit S. Jariwala

**MODELING AND PROCESS PLANNING FOR EXPOSURE CONTROLLED PROJECTION  
LITHOGRAPHY**

Approved by

Dr. David W. Rosen, Chair  
Professor, Mechanical Engineering  
Georgia Institute of Technology

Dr. Suman Das  
Professor, Mechanical Engineering  
Georgia Institute of Technology

Dr. Victor Breedveld  
Associate Professor,  
Chemical and  
Biomolecular Engineering  
Georgia Institute of Technology

Dr. Shreyes N. Melkote, Co-Chair  
Professor, Mechanical Engineering  
Georgia Institute of Technology

Dr. Christiaan Paredis  
Professor, Mechanical Engineering  
Georgia Institute of Technology

Dr. Clifford L. Henderson  
Professor,  
Chemical and  
Biomolecular Engineering  
Georgia Institute of Technology

Date approved: April 1, 2013

*Dedicated to my parents*

*To whom I owe an enormous debt of gratitude*

## ACKNOWLEDGEMENTS

I would like to express my sincere thanks to my Ph.D. advisor Dr. David W. Rosen for providing me with such an intriguing project to work on, and for guiding me through it. I thank him for his understanding, support, patience, inspiration and confidence in my abilities. His experiences and insights provoked me to elevate my level of understanding far higher than I had thought possible. I would also like to thank Dr. Melkote, for agreeing to be a co-advisor and being a part of my committee.

I thank my committee members, Dr. Suman Das, Dr. Chris Paredis, Dr. Victor Breedveld and Dr. Cliff Henderson for providing their insightful comments and suggestions during the course of my PhD research. I would also like to thank Dr. Martha Grover for providing valuable guidance on photochemical modeling.

I was fortunate to have had the opportunity to work with past contributors to the research: Dr. Fei Ding, Dr. Santosh Rahane, Ms. Xiayun Zhao, and Ms. Aparna Boddapatti. I would also like to thank consultants and post-docs from Georgia Tech and AlpZhi, Inc. for the sharing their valuable suggestions – Dr. Stephen Ralph, Dr. Robert Amaro, Dr. Robert Cormack & Mr. Doug Palmer. Thanks also to the undergraduate student researchers who contributed to this project – Prisca Cleveland (ECE), Andrew Perez (ECE), Rachel Van Stelle, Harold Nikoue (AE), Troy Messina (ECE), Michael Werve (ECE), Renea Neal (PTFE/MSE), Amanda Loftin (PTFE/MSE), DongHoon Yeum (MSE), Yunfeng Chen (ECE), Aditi Chandak (ME), Joel Mathew (ME), Benjamin Sullivan (MSE), William Borzon (ME) & Abhishek Kwatra (ME).

I would specially like to thank Dr. Robert (Bob) Schwerzel (Chief Research Scientist, AlpZhi, Inc.) for sharing his insights into photochemistry and for the thought provoking

discussions; I used to have with him during the course of this research. I also thank all my friends from the lab: Jane Kang, Wenchao Zhao, Namin Jeong, Harrison Jones, Chad Hume, Sangin Park, Dazhong Wu, Jiten Patel, Jason Nguyen, Patrick Chang and everyone for their support. Finally, I wish to express my endless gratitude to my parents and my brother for encouraging me to push myself to the best of my abilities.

## TABLE OF CONTENTS

<b>Acknowledgements .....</b>	<b>iv</b>
<b>List of Tables .....</b>	<b>x</b>
<b>List of Figures.....</b>	<b>xi</b>
<b>List of Symbols and Abbreviations.....</b>	<b>xx</b>
<b>Summary.....</b>	<b>xxi</b>
<b>1 Introduction &amp; Motivation .....</b>	<b>1</b>
1.1 Introduction .....	1
1.1.1 Stereolithography .....	2
1.1.2 Micro stereolithography.....	4
1.1.3 Motivation for developing an ECPL process.....	10
1.2 ECPL process overview .....	12
1.3 Identifying research gaps .....	13
1.3.1 Process monitoring.....	14
1.3.2 Photochemistry .....	14
1.3.3 Process planning .....	15
1.4 Research objective.....	15
1.5 Organization of this dissertation .....	15
<b>2 Literature Review and Formulation of Research Questions.....</b>	<b>18</b>
2.1 Photopolymerization .....	18
2.1.1 Empirical modeling approach.....	19
2.1.2 Chemical reaction modeling approach.....	24
2.2 Process planning.....	31
2.3 Research questions and hypotheses.....	39
2.3.1 Process monitoring.....	39
2.3.2 System modeling.....	40
2.3.3 Material modeling.....	42
2.3.4 Process planning .....	43
2.4 Chapter Summary.....	44

<b>3</b>	<b>Design and Assembly of the ECPL Fabrication System .....</b>	<b>45</b>
3.1	Existing system design .....	45
3.2	Design of the ECPL fabrication system .....	50
3.2.1	Module – 1: Selection of the UV light source and design of the beam conditioning system.....	50
3.2.2	Module – 2: Design of projection system with the DMD™.....	56
3.2.3	Module – 3: Design of the resin chamber.....	59
3.3	Experimental procedure .....	62
3.3.1	Photopolymer material.....	64
3.3.2	Exposure control.....	65
3.4	Experimental results.....	66
3.5	Chapter summary .....	67
<b>4</b>	<b>ECPL Process Monitoring System.....</b>	<b>69</b>
4.1	Motivation for development of a real-time cure monitor.....	69
4.2	Existing monitoring techniques.....	72
4.3	Theory & Principle of an Interferometric Monitoring System .....	74
4.4	One dimensional monitoring system design .....	79
4.4.1	Experimental Procedure.....	80
4.4.2	Typical Interferogram .....	80
4.4.3	Experimental Results .....	81
4.5	Development of Post-Processing Method.....	83
4.6	In-situ part height metrology.....	87
4.7	Two dimensional monitoring system design.....	89
4.8	Experimental validation for cure monitoring system.....	93
4.8.1	Current limitations of the monitoring system .....	97
4.9	Chapter summary .....	98
<b>5</b>	<b>ECPL Process Model.....</b>	<b>100</b>
5.1	Introduction .....	100
5.2	ECPL process model .....	104
5.3	Phase – I: Apply energy .....	106
5.3.1	Irradiance model .....	106
5.3.2	Calculation of single ray power .....	109
5.3.3	Experimental validation .....	109

5.4	Phase – II: Process.....	112
5.4.1	Investigation on effects of optical self-focusing.....	117
5.4.2	Investigation on presence of oxygen inhibition.....	123
5.4.3	Investigation on presence of dark reaction.....	125
5.4.4	Investigation on effects of shrinkage.....	127
5.5	Phase – III: Post-Process.....	129
5.6	Chapter Summary.....	135
<b>6</b>	<b>Formulation of a Photopolymerization Model.....</b>	<b>137</b>
6.1	One-dimensional modeling & simulation results.....	138
6.1.1	Results from the fitted rate constants.....	142
6.1.2	Need to modify the rate constants.....	145
6.1.3	Estimating kinetic rate constants.....	146
6.2	Two-dimensional modeling & simulation results.....	152
6.2.1	Numerical finite element model.....	153
6.2.2	Simulation results & comparison with experiments.....	155
6.3	Preliminary observations from axi-symmetric simulations.....	160
6.4	Design of experiments for development of an empirical model.....	164
6.4.1	Case study.....	167
6.5	Validation of empirical material model.....	171
6.5.1	Varying intensity at constant time.....	175
6.5.2	Varying time at constant intensity.....	177
6.6	Chapter summary.....	180
<b>7</b>	<b>Process Plan Formulation.....</b>	<b>182</b>
7.1	Product Specifications.....	187
7.2	Material Module.....	188
7.3	System Module.....	193
7.4	Optimization Module.....	195
7.5	Validation of Hypothesis for Research Question 4.....	198
7.5.1	Conical Lens Example.....	201
7.5.2	Aspheric Lens Example.....	205
7.6	Error Analysis.....	209
7.7	Effect of DMD operation on curing.....	213
7.8	Chapter Summary.....	213



<b>8</b>	<b>Revised Process Planning Method .....</b>	<b>215</b>
8.1	Need for Revised Process Planning Method .....	215
8.2	Holistic process planning approach.....	217
8.2.1	Estimating first set of process inputs .....	221
8.2.2	Estimating subsequent set of process inputs.....	224
8.3	Validation of Revised Hypothesis for Research Question 4.....	227
8.3.1	Spherical Lens Example .....	227
8.3.2	Conical Lens Example .....	230
8.3.3	Aspheric Lens Example .....	233
8.4	Error Analysis & limitations .....	237
8.5	Chapter Summary.....	239
<b>9</b>	<b>Closure and Contributions .....</b>	<b>240</b>
9.1	Summary of the Dissertation.....	240
9.1.1	ECPL system design .....	241
9.1.2	Process and material model .....	242
9.1.3	Process planning method .....	243
9.2	Revisiting Research Questions.....	243
9.2.1	Research Question 1 .....	244
9.2.2	Research Question 2 .....	245
9.2.3	Research Question 3 .....	246
9.2.4	Research Question 4 .....	247
9.3	Knowledge Contributions .....	249
9.4	Developmental/Engineering Contributions.....	252
9.5	Recommendations for future work.....	253
<b>A.</b>	<b>Appendix A.....</b>	<b>254</b>
<b>B.</b>	<b>Appendix B.....</b>	<b>256</b>
<b>C.</b>	<b>Appendix C.....</b>	<b>258</b>
	<b>Works Cited.....</b>	<b>294</b>

## LIST OF TABLES

Table 1 Advantages and limitations of existing photopolymerization modeling approaches (concerning the ECPL process) .....	30
Table 2 Specifications of the components used in the ECPL system .....	62
Table 3 Technical Specifications for the UV CCD Camera used in this research .....	63
Table 4 Design of Experiments table to determine the cure recipe to avoid dark reaction .....	127
Table 5 Table showing the images from the experiments conducted to study the influence of post-processing on cured part shape (for a sample with 30s exposure) .....	132
Table 6 Physical parameters used in this study .....	142
Table 7 Experimental data on gel times from Dr. Slopek [45] .....	147
Table 8 Calculation for concentration of double-bond and photoinitiator .....	153
Table 9 Input variables and response factors for Design of Experiments .....	166
Table 10 Values of $E_c$ & $D_p$ obtained by curve fitting for total exposed radius of 300 $\mu\text{m}$ .....	168
Table 11 Summary of average errors observed from experiments .....	209
Table 12 Parameters used to create the revised material model ('Pixel to Cure' Database) .....	221
Table 13 Summary of average errors observed from experiments (revised process plan) .....	238

## LIST OF FIGURES

Figure 1 Schematic of a stereolithography machine [1] .....	3
Figure 2 Principle of Scanning Micro-Stereolithography [3] .....	5
Figure 3 Schematic of mask projection micro-stereolithography [8] .....	5
Figure 4 Illustration of stair-stepping effect caused in conventional layer based stereolithography systems [9] .....	6
Figure 5 Photograph of EnvisionTec’s Perfactory Machine [11] .....	7
Figure 6 Schematic of the system used by Erdmann et al. for micro-lens fabrication .....	8
Figure 7 Optimization cycle for improving fabricated topology [12] .....	9
Figure 8 Block diagram of the ECPL Process .....	13
Figure 9 Complex stereolithography process and modeling approaches [38] .....	19
Figure 10 Modeling layer curing as a transient phenomenon [43] .....	22
Figure 11 Working curve for PEGDA Hydrogel .....	23
Figure 12 Conversion data by FTIR experiments, along with the model-predicted conversions [44] .....	29
Figure 13 Schematic of the MPSLA system used by Limaye [43] .....	31
Figure 14 Schematic of the layer cure model from Limaye [43] .....	32
Figure 15 Schematic of the Inverse layer cure model from Limaye [55] .....	33
Figure 16 Schematic of the TfMPSLA system [56] .....	34
Figure 17 Flow-chart of the process plan from Jariwala et al. [33] .....	35
Figure 18 CAD model of the desired part shape [14] .....	36
Figure 19 Bitmaps generated by process plan used by Zhao X. [14] .....	37
Figure 20 Experimental observation of the final cured part using the process plan from Zhao X. [14] .....	38
Figure 21 Irradiance line profile obtained from UV CCD [14] .....	46
Figure 22 Modified TfMP $\mu$ SLA experimental system .....	46
Figure 23 Schematic showing the location of the UV CCD [14] .....	47
Figure 24 Irradiance profile plot obtained by static and rotating diffuser [14] .....	48
Figure 25 Photograph of the modified experimental setup .....	49

Figure 26 Photograph showing the intensity profile resulting from the UV light source from the light guide.....	51
Figure 27 Schematic of the optics within a DLP projector by Texas Instruments [58]....	53
Figure 28 Photographs of Integrator Rods [59] .....	53
Figure 29 Photograph showing the divergence of the light resulting from the light guide .....	54
Figure 30 Photograph showing the front view of the beam conditioning system; with the mirror to fold the light on the DMD Chip.....	55
Figure 31 Photograph showing the experimental setup used to assemble the beam conditioning system .....	56
Figure 32 Photograph showing the mirror, DMD Chip and the projection system .....	58
Figure 33 Photograph of the second-generation resin chamber.....	60
Figure 34 Schematic of the Resin Chamber .....	61
Figure 35 Figure showing the steps in constructing the resin chamber .....	61
Figure 36 Camera image of the irradiation (on left) and average irradiation plot (on right) .....	63
Figure 37 Optical transmittance of cured photopolymer (red) and that of blank glass slide (blue), used for comparison .....	64
Figure 38 Plot showing the cured part height as a function of exposure time.....	67
Figure 39 Potential causes of variations during fabrication in the ECPL process.....	70
Figure 40 Schematic of the experimental setup used by Slopek [45].....	73
Figure 41 Schematic of the monitoring system based on interferometry .....	75
Figure 42 Photograph showing part of the ECPL system, with the components of the interferometric monitoring sytem .....	79
Figure 43 Results from the one-dimensional interferometric monitoring system for curing a 250 thick sample. Horizontal axis corresponds to timer ad the Y-axis shows the output voltage detected from the photo detector.....	81
Figure 44 Plot of the intensity signals from the interferometric system obtained by curing three consecutive experiments with same experimental conditions .....	82

Figure 45 Schematic of the steps involved in washing process (Dark green region shows cured part, blue arrows indicate the random direction of the compressed nitrogen gas on the cured sample) .....	84
Figure 46 Images of cured sample from 3D laser confocal microscopy. Using old method (above) and refined method (below).....	85
Figure 47 Plot showing superimposed profiles from six discrete experiments .....	86
Figure 48 Results from the monitoring system based on interferometry (each color represents a specific exposure dose).....	87
Figure 49 Results showing the height correlation with total phase angle.....	88
Figure 50 Photograph showing the ECPL system with the two-dimensional monitoring system .....	90
Figure 51 Bitmap projected on the DMD .....	91
Figure 52 Snapshot of the user interface developed for 2D monitoring system, showing the results after curing the bitmap with stepped intensity profile.....	92
Figure 53 Results from the confocal microscope for the sample cured with stepped intensity profile .....	93
Figure 54 Cure monitoring of centered bitmap photopolymerization. (A) Bitmap and DMD frame; (B) Two-dimensional cure monitor image showing cured shape in center and location of center pixel monitored for time evolution of polymerization (arrow); (C) Time evolution of small--aperture interference pattern at center pixel during center photopolymerization; (D) Photograph of polymerized shape after washing and flood-cure .....	94
Figure 55 Cure monitoring of off-center bitmap photopolymerization. (A) Bitmap and DMD frame; (B) Two-dimensional ICM image showing cured shape at lower left and location of center pixel monitored for time evolution of polymerization (arrow); (C) Time evolution of small-aperture interference pattern at center pixel during off-center photopolymerization; (D) Photograph of polymerized shape after washing and flood-cure .....	96
Figure 56 Working Curves for PEGDA hydrogel using varying shapes of bitmaps.....	101

Figure 57 Experimental results showing the cured part profiles for different exposure times.....	102
Figure 58 Cured part profiles obtained by varying exposed line widths .....	103
Figure 59 Block diagram of the ECPL Process Model.....	104
Figure 60 Schematic of ray tracing algorithm [42].....	107
Figure 61 Irradiance produced at the resin substrate by switching a single micromirror. a) Central Micromirror switched on; b) Edge Micromirror switched on.....	109
Figure 62 Exposure profile by varying projected line widths on DMD chip .....	110
Figure 63 Comparison of simulation results from Irradiance model (solid lines) with data from Camera (dashed lines). Red corresponds to 10pixels; green to 60pixels and blue to 90pixels.....	111
Figure 64 Results of investigation on the factors affecting the cured part due to Apply Energy Phase.....	112
Figure 65 Experimentally obtained data shown in green dots fitted on a working curve (in red) .....	114
Figure 66 Plot showing the inadequacy of the existing empirical model to explain the cured part profile. The solid lines show the experimentally observed cured part shapes and the dotted lines depict the predictions using empirical model based on Beer-Lambert's law from Eq. 5-3.....	115
Figure 67 Schematic of the optical projection system modeled in LightTools .....	118
Figure 68 Change in refractive index as a function of cured part height.....	120
Figure 69 Comparison of light path when curing through a cured part. Left: in presence of resin. Right: in absence of resin.....	122
Figure 70 Intensity plots obtained from LightTools ray-tracing simulation from the spherical receiver (red and blue curves overlap) .....	123
Figure 71 Results showing the effect of spacer thickness .....	124
Figure 72 Block diagram of the photopolymerization process for ECPL; highlighting the source of dark reaction.....	126
Figure 73 Results of investigation on the factors affecting the cured part due to Processing Phase.....	127

Figure 74 Schematic describing location of the sample in the fluorescence confocal microscope .....	130
Figure 75 Plot of measured heights for samples exposed for 30s and 10s .....	134
Figure 76 Results of investigation on the factors affecting the cured part due to Post Processing Phase.....	135
Figure 77 Conversion data by FTIR, along with the model-predicted conversions a) deoxygenated conditions and b) oxygenated conditions. x's represents data points used in the fit, and the o's represents data points not used to fit the rate constants [44] .....	143
Figure 78 Simulation results from 1D COMSOL® simulation (Red curve shows fractional monomer conversion; blue curve shows normalized concentration of oxygen; time is in seconds).....	144
Figure 79 Simulation plots showing double-bond conversion for deoxygenated samples. Green dots show experimental data. Left figure shows the simulation results prior to changing the rate constants. Right figure shows the results after using the new rate constants $K_p, K_t = 1.66, 1.31 \text{ m}^3\text{mol}^{-1}\text{s}^{-1}$ .....	148
Figure 80 Simulation plot showing the normalized oxygen concentration (blue) and fractional double-bond conversion (red). The experimental data points are shown as green dots.....	151
Figure 81 Simulation results from COMSOL® 1D model (using revised rate constants) $K_p, K_t \& K_t, O_2 = 1.66, 1.31, 125 \text{ m}^3\text{mol}^{-1}\text{s}^{-1}$ .....	152
Figure 82 Schematic of the resin chamber used for simulation purposes.....	154
Figure 83 a.) Schematic of the FE mesh geometry simulated using COMSOL®; b.) Enlarged view of the FE mesh .....	155
Figure 84 Experimentally obtained working curve (in red) fitted with experimental data shown in green dots .....	156
Figure 85 Working curve (in red) obtained from COMSOL® simulations with experimental data shown in green dots.....	157
Figure 86 Working curve (red) obtained from COMSOL® simulations using simpler Ec-Dp model to fit experimental data (green dots) .....	158

Figure 87 Comparison of experimental profiles (solid lines) with simulated profiles (dashed lines) Red: 5s exposure; Green: 10s exposure; Blue: 30s exposure. X & Y axes are in micrometers.....	159
Figure 88 Simulated cured part profiles obtained from COMSOL® simulations for radius of 300 microns for varying exposure doses .....	161
Figure 89 Simulated cured part profiles obtained from COMSOL® simulations for radius of 50 microns for varying exposure doses .....	162
Figure 90 Predicted part profiles for a total exposure of 30s by varying exposed widths .....	163
Figure 91 Working curves obtained for total exposed radius of 300 $\mu\text{m}$ . Different colors correspond to the working curves obtained at different distances from the center. ....	167
Figure 92 Working curve obtained for edge of the exposed region for a total exposed region of 300 $\mu\text{m}$ .....	168
Figure 93 Variation of $E_c$ as a function of distance from center for a total exposed region of 300 $\mu\text{m}$ .....	169
Figure 94 Variation of $D_p$ as a function of distance from center for a total exposed region of 300 $\mu\text{m}$ .....	169
Figure 95 Plot showing the variation of $E_c$ and $D_p$ as a function of radius for different exposed regions (red corresponds to 300 $\mu\text{m}$ and blue corresponds to 10 $\mu\text{m}$ of total exposed radius) .....	170
Figure 96 Half-sectional view of the desired part geometry.....	172
Figure 97 Figure showing the radial variation of $E_c$ and $D_p$ for desired cured part of 100 $\mu\text{m}$ radius .....	173
Figure 98 Calculated exposure profile for curing the spherical structure shown in Figure 96.....	174
Figure 99 Automatically generated finite element mesh used to simulate the exposure conditions.....	176
Figure 100 Simulation result showing the simulated cured part geometry (red) with the desired part geometry (dashed black) .....	177



Figure 101 Simulation results showing the simulated cured part geometry from sequentially clustered exposures and the desired part geometry (dashed black). The red curve closest to the black dashed curve is the final simulated cured part shape .....	180
Figure 102 Process Planning - the design/manufacturing interface [84] .....	182
Figure 103 Figure showing the desired geometrical profile and the micromirrors .....	185
Figure 104 Flow-chart showing the partial formulation of the process-planning algorithm (derived from hypothesis to research question 4.1) .....	186
Figure 105 Aspheric lens geometry, adapted from [85] .....	188
Figure 106 Profile of desired spherical lens geometry .....	190
Figure 107 Desired radial exposure profile .....	191
Figure 108 Figure showing the gradient profile of the desired exposure at the substrate level in terms of substrate pixels.....	192
Figure 109 Figure showing the cross-sectional profile of the desired exposure at the substrate level in terms of substrate pixels .....	192
Figure 110 Flow-chart of the Process Plan for the ECPL system.....	195
Figure 111 Estimated time for micromirrors on the DMD chip .....	198
Figure 112 Calculated bitmaps and corresponding exposure times.....	199
Figure 113 Snapshot of the image of the cured sample from LEXT 3D confocal microscope .....	200
Figure 114 Comparison of the half-sectional profiles of the cured part sample and the desired part geometry.....	200
Figure 115 Half-sectional profile of desired cylindrical lens geometry .....	201
Figure 116 Desired radial exposure profile to cure conical lens .....	202
Figure 117 Snapshot of the calculated exposure profile in terms of substrate pixels.....	202
Figure 118 Calculated bitmaps and corresponding exposure times.....	203
Figure 119 Snapshot of the image of the cured sample from LEXT 3D confocal microscope .....	204
Figure 120 Comparison of the half-sectional profiles of the cured part sample and the desired part geometry.....	204
Figure 121 Half-sectional profile of desired aspherical lens geometry .....	205

Figure 122 Desired radial exposure profile to cure aspheric lens.....	206
Figure 123 Snapshot of the calculated exposure profile in terms of substrate pixels.....	206
Figure 124 Calculated bitmaps and corresponding exposure times.....	207
Figure 125 Snapshot of the image of the cured sample from LEXT 3D confocal microscope .....	207
Figure 126 Comparison of the half-sectional profiles of the cured part sample and the desired part geometry.....	208
Figure 127 Invalid implicit assumptions in the process-planning algorithm.....	212
Figure 128 Illustration of the parameters of the process inputs for the revised process planning method.....	219
Figure 129 Process Plan - STEP #1 .....	222
Figure 130 Variables used in the optimization problem.....	224
Figure 131 Process Plan - STEP #2 (Simulated cured height field, $Z_i$ is obtained using COMSOL simulation).....	225
Figure 132 Profile of desired spherical lens geometry .....	228
Figure 133 Calculated bitmaps and corresponding exposure times for spherical lens example.....	228
Figure 134 Simulated cured part height from individual bitmaps resulting from the process plan.....	229
Figure 135 Comparison of the half-sectional profiles of the cured part sample and the desired part geometry (Desired part profile is in red and experimentally cured profile is shown in blue).....	230
Figure 136 Half-sectional profile of desired cylindrical lens geometry .....	231
Figure 137 Calculated bitmaps and corresponding exposure times for conical lens example.....	232
Figure 138 Simulated cured part height from individual bitmaps resulting from the process plan for conical lens example .....	232
Figure 139 Comparison of the half-sectional profiles of the cured part sample and the desired part geometry.....	233
Figure 140 Half-sectional profile of desired aspherical lens geometry .....	234

Figure 141 Calculated bitmaps and corresponding exposure times.....	235
Figure 142 Simulated cured part height from individual bitmaps resulting from the process plan for aspheric lens example.....	236
Figure 143 Comparison of the half-sectional profiles of the cured part sample and the desired part geometry.....	237

## LIST OF SYMBOLS AND ABBREVIATIONS

ECPL	Exposure Controlled Projection Lithography
CAD	Computer Aided Design
UV	Ultraviolet
SLA	Stereolithography Apparatus
SL	Stereolithography
DMD	Digital Micromirror Device

## SUMMARY

A novel approach to Microfabrication based on stereolithography is presented in this thesis. This fabrication process is referred to as, ‘Exposure Controlled Projection Lithography’ (ECPL). In the ECPL process, incident radiation, patterned by a dynamic mask, passes through a transparent substrate to cure photopolymer resin. By controlling the amount of exposure, the height field of the cured film can be controlled.

As part of this dissertation, an ECPL system was designed and assembled. Factors affecting the accuracy of the ECPL process in fabricating micron shaped features are identified and studied. A real-time in-situ photopolymerization monitoring system was designed and assembled within the ECPL system to help identify the sources of variations present in the system. This system can be potentially developed further to aid in real-time sensing and ultimately provide feedback control to the process.

Parts are fabricated from the ECPL process because of polymerization (or cross-linking) of monomer resin using light energy. Photopolymerization is a complex process involving a coupling between several phenomena. This thesis research is focused on utilizing an understanding of the known polymerization reaction kinetics with incorporating the effects of oxygen inhibition and diffusion. Based on this knowledge and the experimental results, an empirical model of the material response is developed.

The material model developed in this thesis is used to formulate a process-planning method to estimate the manufacturing process inputs required to cure a part of desired shape and dimensions. The process planning method is validated through simulations and experiments.

## **CHAPTER ONE**

### **INTRODUCTION & MOTIVATION**

The Exposure Controlled Projection Lithography (ECPL) process was developed based on the stereolithography based rapid prototyping process. The primary motivation for the development of ECPL was to develop a rapid prototyping process for fabrication of precise microstructures for micro-optics application. The following sections present an introduction to the stereolithography process and the background towards the development of ECPL process. A detailed explanation on the motivation for the development of the ECPL is also presented. The knowledge gap involved in utilizing the ECPL as a reliable manufacturing process is presented. This provides a foundation for investigation of the research issues associated with the ECPL process.

#### **1.1 Introduction**

Manufacturing processes have evolved over the years and countless researchers have contributed towards the development of this field. Several of these fabrication processes have been commercialized and put into practice by the industry. However, newer product design innovations continue to challenge the limits of the existing fabrication processes. This places a strong demand on developing existing processes and innovating advanced fabrication methods. This thesis research is primarily focused towards the development of a novel micro-fabrication method based on stereolithography for fabrication of sub-millimeter shaped parts, including micro-optic elements. The ECPL

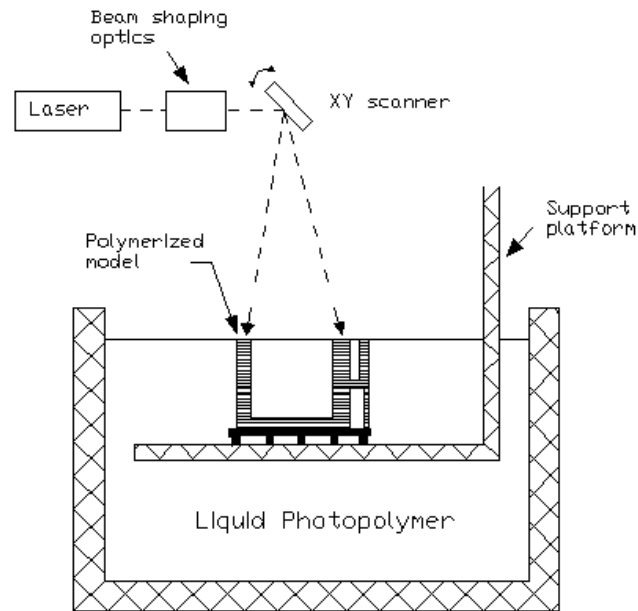
process evolved from the stereolithography processes and the following section provides an overview on the stereolithography process.

### **1.1.1 Stereolithography**

Stereolithography was the first rapid prototyping process [1] and it is an additive manufacturing process used to build physical parts from photopolymer resin. Stereolithography process was invented by Charles (Chuck) Hull as a method and apparatus for generating three-dimensional objects by ‘adding’ layers of material cured by ultraviolet light. The liquid raw material used in this process is a photopolymer resin, which cures or solidifies when it receives ultraviolet (UV) light.

The overall process starts by preparing a three-dimensional CAD file of the part to be fabricated. The file is then processed by software to slice the part into a series of horizontal layers and this information is sent over to the stereolithography apparatus (SLA). The SLA machine comprises of a resin bath, a support platform, ultraviolet (UV) laser light source, beam shaping optics and a scanning head. The resin bath contains the liquid photopolymer resin. The support platform is connected with a stage, which can translate along the Z-axis. The scanning head comprises of a mirror galvanometer that directs the UV light in two dimensions on the resin surface. Each cross sectional layer is scanned by UV light on the resin layer. The platform then descends by a single layer thickness and a new layer of resin is added on top of the cured layer. The next layer is then cured and the process repeats until the entire part is fabricated. The completely fabricated final part is removed from the resin bath, cleaned in a solvent and then post-cured by providing flood exposure in a UV oven.

The schematic of the stereolithography process is shown in Figure 1.



**Figure 1 Schematic of a stereolithography machine [1]**

The liquid raw material used in this process is a photopolymer resin, which is curable in ultraviolet light. When the liquid photopolymer resin receives ultraviolet (UV) light, it cures or solidifies in the region that receives light.

Stereolithography process was commercialized by 3D Systems, Inc. The original intent behind developing this technology was to provide a means to the designer to quickly prototype their designs. Designers would use the prototypes to make changes to the designs, if necessary before sending the part for mass manufacturing. Over the past 25 years, the technology has developed significantly yielding in improvements in materials, dimensional accuracy, surface finish and the maximum possible build volume. Several variants of the stereolithography process have also been developed to suit different applications by modifying one or many aspects of the machine. One such variant of the



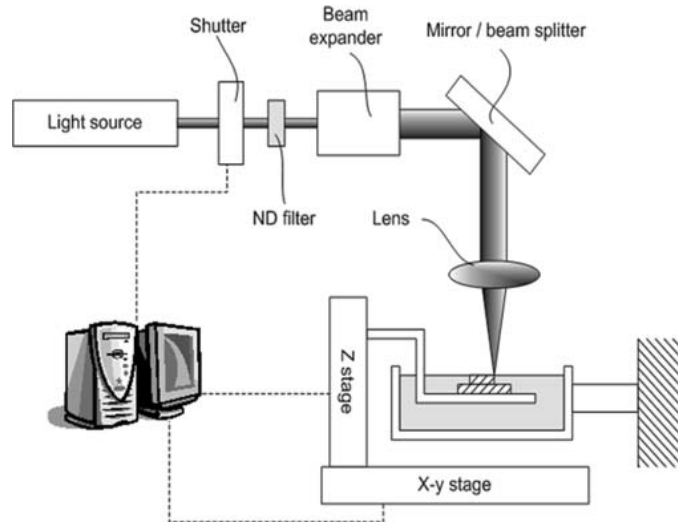
technology is the micro-stereolithography process and is presented in the following section.

### **1.1.2 Micro stereolithography**

Micro stereolithography is the application of the principle of stereolithography for fabricating micro parts with a finer resolution than conventional stereolithography. This process was introduced by Ikuta et al. [2]. The development of these processes has fueled the creation of advanced technologies in the field of tissue engineering, micro electromechanical systems (MEMS), photonics, etc. Micro-stereolithography process has been studied and developed by several researchers across the world. Based on the methods employed to direct light energy into the photopolymer resin, this process can be classified into two major categories as follows:

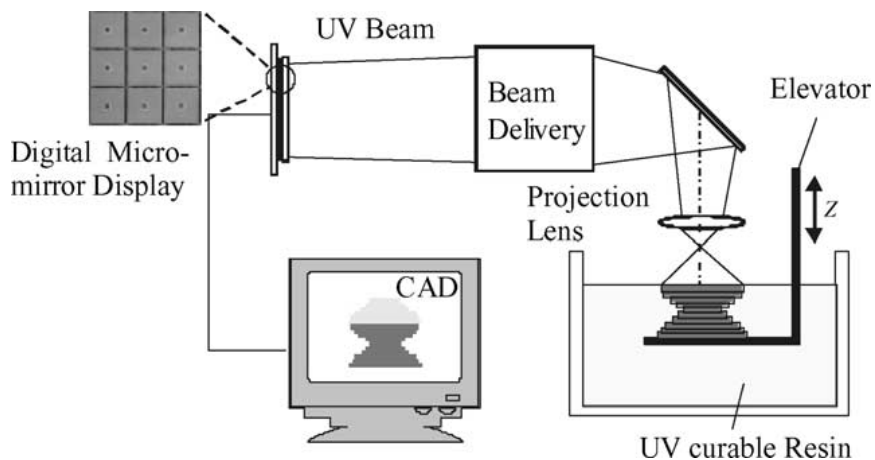
- Scanning Micro-Stereolithography
- Mask Projection Micro-stereolithography

. The principle of Scanning Micro-Stereolithography system is shown in Figure 2 and it differs from conventional stereolithography in that the beam stays at a fixed location and the stage moves along X, Y and Z-axes. The advantage of this approach is that the beam always stays in focus, eliminating errors induced by defocusing of the beam during scanning but the optical system. This process has been studied by Lee et al. [3], Maruo & Kawata [4].



**Figure 2 Principle of Scanning Micro-Stereolithography [3]**

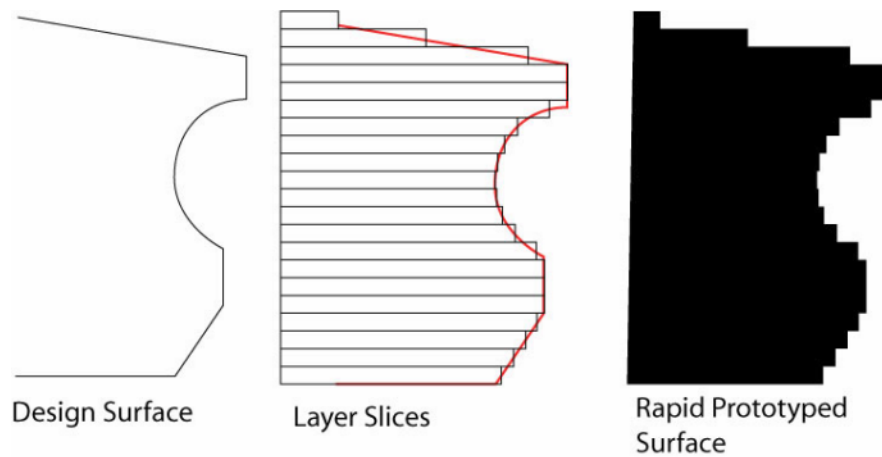
The principle of mask projection micro-stereolithography systems is shown in Figure 3. Unlike the scanning micro-stereolithography process, in this process, light energy is projected on the resin using a Liquid Crystal Display (LCD) or Digital Micromirror Device (DMD) based pattern generation system and the stage moves only along the z-axis. This technology has been demonstrated in various papers, like Bertsch et al. [5], Chatwin [6], Monneret et al. [7], Sun et al. [8] and Limaye and Rosen [5].



**Figure 3 Schematic of mask projection micro-stereolithography [8]**

In the mask projection based systems, the stage remains fixed while curing the entire layer, which reduces the possibility of errors resulting from the translation of the stage along X-Y axis. Moreover, curing of the entire layer using a mask leads to shorter fabrication time when compared to scanning micro-stereolithography processes.

In all of the above processes, the entire part is fabricated as a fusion of several discrete layers. This process causes stair-stepping on the boundary of smooth surfaces, which is illustrated Figure 4.



**Figure 4 Illustration of stair-stepping effect caused in conventional layer based stereolithography systems [9]**

Sager & Rosen [10] presented a gray-scale laser scanning method for obtaining smooth down-facing surfaces. Pan et al. [9] further extended this approach to improve the surface finish of the cured parts for mask projection based stereolithography systems. The researchers presented an approach to project gray scale images from the DMD mask, instead of conventional binary images in order to cure a single layer.

Due to their advantages in providing a finer resolution, mask projection based systems have been commercialized for applications beyond the fabrication of microstructures. The Perfactory® range of machines from EnvisionTec, Germany, also uses one or more DMD chips to pattern the light to cure each layer. Figure 5 shows the photograph of one of the several EnvisionTec's Perfactory Machines.



**Figure 5 Photograph of EnvisionTec's Perfactory Machine [11]**

The fundamental difference between the Perfactory range of machines and the stereolithography machine is that it eliminates the process of planarizing the resin surface by fabricating the model upside-down. Light is projected through a transparent substrate into a shallow vat of resin. After the first layer is cured, the build platform rises and the next layer is cured between the glass substrate and the previously cured part.

Curing through substrates has been explored by other researchers as well. Erdmann et al. [12] have used mask projection stereolithography through transparent substrates for

the fabrication of simple micro-lens arrays. The dynamic mask, which is the DMD chip in this case, is imaged into a photoresist layer using a lithography objective. The image is magnified to the ratio 10:1. They used a single micromirror from the DMD chip to form the individual microlens element in the micro-lens array. This way they were able to fabricate close to 800,000 individual elements in a single exposure.

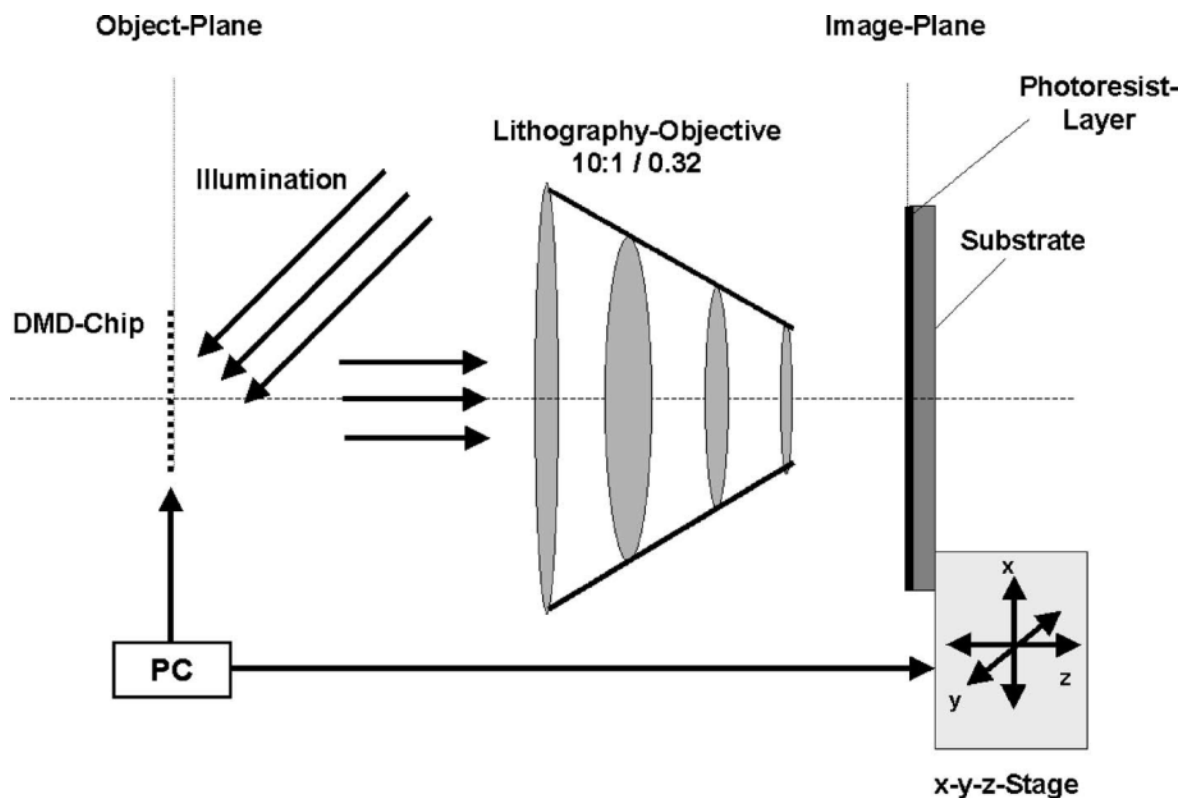
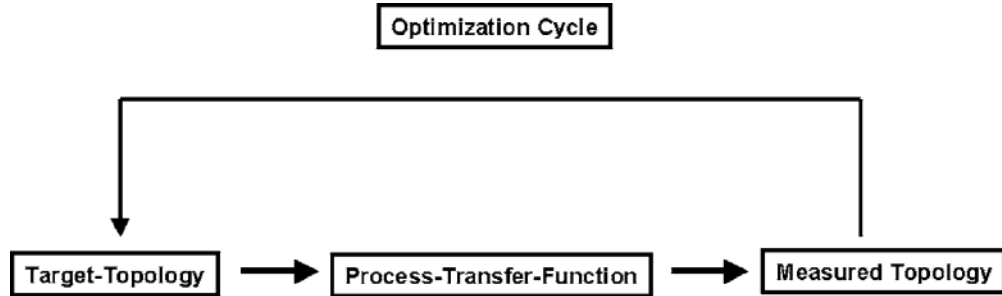


Figure 6 Schematic of the system used by Erdmann et al. for micro-lens fabrication

Figure 6 shows the schematic of the setup used by Erdmann et al.[12] to fabricate microlenses. The substrate was mounted on an X-Y-Z stage to enable fabrication of large array of microlenses up to 50 x 50mm. The authors proposed formulating a transfer function based on the differences between actual measurements and the target topology.

They suggested using this transfer function in an optimization cycle, as shown in Figure 7, to improve the fabricated topology.



**Figure 7 Optimization cycle for improving fabricated topology [12]**

The authors experimentally showed the viability of this process to fabricate microlens arrays with each element resulting from a single pixel on the DMD. The size of each element on the DMD was controlled by the lithography projection objective and the exposure time. The researchers did not explore the utility of the process to fabricate large optical elements by simultaneously using multiple pixels on the DMD to form a single lens element. Despite these limitations, their research provided a starting step towards the use of DMD for fabricating flexible micro-optic elements.

One of the significant differences between the typical conventional stereolithography and micro stereolithography is the dimensional scales of the finally produced parts. For larger stereolithography machines, the typical product dimension ranges from few millimeters to half a meter [13]. Although, machine manufacturers do not publish or claim a minimum feature size, such machines are typically not used to fabricate standalone features of less than a millimeter. The best accuracy achievable from these machines is rated as 0.025mm per inch, which is around 0.1%. The accuracy rating

is dependent on build parameters, part geometry, post-processing, etc. Hence, although the accuracy is specified to be very high, it is not scalable for fabricating sub-millimeter structures. In other words, it is not reasonable to expect commercial SLA machines to fabricate structures in the dimension range of 1mm and expect an accuracy of 1micron (which is 0.1%). The accuracy of the commercial SLA technology is dependent on several factors, including the uncertainty associated with build parameters, post-processing, etc. It is also to be noted that several of these scalability issues arise from different phenomena working at smaller size scales compared to large scaled structures. For instance, shrinkage effects would be more predominant for fabricating large structures compared to sub-millimeter structures, since shrinkage is typically linearly dependent on the overall part size. On other hand, effects of washing may become more prominent for fabricating smaller structures, if the entire part is not cross-linked completely. As commercial SLA was modified into micro-SLA, the effects of dimensional scaling were largely ignored. Researchers would typically use empirical methods like the one shown in Figure 7 to fabricate accurate parts from micro SLA. This thesis research seeks to provide a great scientific understanding of the phenomena governing the curing process at a sub-millimeter scale.

### **1.1.3 Motivation for developing an ECPL process**

The motivation for this thesis research stems from the growing developments in the field of micro-stereolithography. Dynamic mask (DMD) based projection lithography techniques provide design flexibility for fabricating microstructures. When compared to hard mask based fabrication methods, mask projection stereolithography methods are

inexpensive, since no hard tooling is required to fabricate a different design. Using mask projection lithography for curing through a substrate was investigated in detail in our past labmate's Master's thesis [14]. This thesis research is directed towards developing a manufacturing process, which can be used to fabricate microstructures like micro-optics, micro-channels, etc.

Several micro-fabrication techniques have been explored for creating micro channels. These structures have numerous applications in inkjet printers, lab-on-a-chip, chemical analysis systems, biological sensing, drug delivery, optical switching and molecular separation. Several techniques explored to make microchannels include embossing [15], injection molding [16], [17], [18], plasma etching ablation [19], soft lithography [20] and laser-based [21]. However, these fabrication techniques are limited in their ability to fabricate microchannels with complex geometry, especially with smooth walls. The ECPL process can be used for such an application, due to the low-cost flexible manufacturing.

Like micro-channels, several microfabrication processes have also been investigated for fabricating micro-optics. Micro-optics are used for several applications including laser beam homogenization [22]. Conventionally, microlenses are fabricated by modified LIGA [23], hot-embossing [24], ion exchange [25], photoresist flow [26], ion etching [27], direct writing [28], deep lithography with protons [29], laser ablation [30], microjet printing [31], etc. Those techniques either have less ability in the shape control or are expensive and time-consuming. Moreover, most of these techniques are limited to fabricating constant focal length, near-spherical lenses on flat substrates only.



Nonspherical lenses of varying focal lengths on non-planar substrates may be required for advanced imaging applications. It is also interesting to note that the industry has a strong demand for quick fabrication of micro-optics prototypes. Reinhard Voelkel, CEO of SUSS Microoptics, one of the world's largest supplier of micro-optics solutions notes that, "Micro-optics is manufactured on customer's request. Micro-optics is often a difficult-to-implement and exotic solution. A small supplier base, high prototyping costs, unwanted diffraction or interference effects, and difficulties to measure and classify the quality are the major drawbacks." [32]. This thesis research was thus conducted to enable the development of a highly flexible manufacturing process for fabricating customized microstructures, which could be used as a low-cost rapid prototyping for micro-optics as well as for micro-channels.

## **1.2 ECPL process overview**

The ECPL process is similar to the mask projection stereolithography system, except that the curing of the photopolymer resin occurs by passing light energy through a transparent substrate. The block diagram of the ECPL process is illustrated in Figure 8. A UV light source is used (with a 365nm filter) and the light is passed onto the beam conditioning system. The objective of this beam conditioning system is to homogenize the light output from the light source and project it onto the DMD chip, which is used as a dynamic mask to project grayscale images. The projection system reduces the size of the image projected on the DMD and focuses it into the resin chamber. The resin chamber consists of a standard glass microscope slide which acts as a base/substrate, an identical glass slide which serves as a top, and spacers of various thicknesses depending

on the dimensions of the object to be formed; the liquid photopolymer is placed inside this chamber.

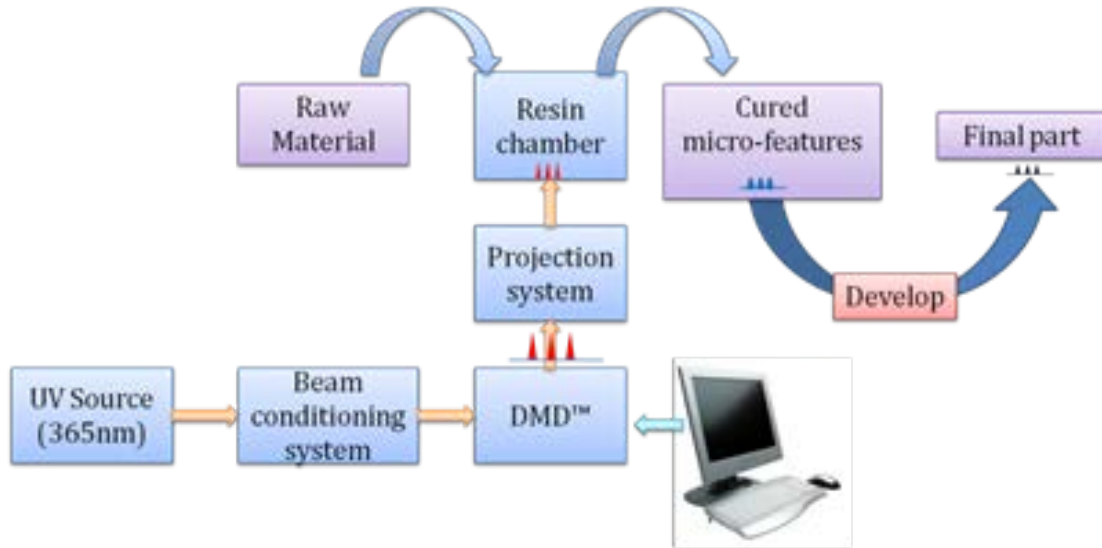


Figure 8 Block diagram of the ECPL Process

Grayscale images are formed on the DMD using the computer and projected from the DMD into the resin chamber, through the projection system. Red triangles show the intensity profile of the irradiation. The regions of the liquid photopolymer resin, which receive irradiation get cross-linked and are converted into a cross-linked polymer. The vertical profile bears a direct relationship with the intensity profile of the incident light. The uncured monomer is then washed off the cured part in the “developing” process, and the final cured part is obtained on the glass slide.

### 1.3 Identifying research gaps

Past research in the area of mask projection lithography for curing through a transparent substrate [14, 33, 34] was conducted. However, there are several knowledge

gaps, which restrict the use of this process as a reliable commercial fabrication method. There is a substantial lack of knowledge with regard to controlling the process in order to achieve the desired accuracy and precision over the final cured parts. Not enough research efforts have been spent to understand the various factors affecting the geometry and surface finish of the final product resulting from such a process. These research issues are discussed in this subsection.

### **1.3.1 Process monitoring**

In order to develop a photopolymerization model, it is necessary to develop a method, which can provide insights into the curing process without altering the fabrication process. Further, maturing the ECPL process into a commercial manufacturing process will require the development of a real-time monitoring system, which can monitor the material response and potentially provide a closed loop feedback control. A novel in-situ real-time photopolymerization monitor was designed and developed as part of this thesis research.

### **1.3.2 Photochemistry**

Traditionally, photopolymerization research was focused towards understanding the reaction as a bulk phenomenon. The ECPL process induces photopolymerization for curing sub-millimeter parts. Hence, spatial effects of the polymerization process have to be studied in depth to help understand the governing phenomena. Existing research in the field of photopolymerization is inadequate to explain the complex material response. The author, in collaboration with other researchers, had assumed a simple empirical model of photopolymerization [14, 33, 34]. However, during the course of continued research, this empirical model was found inadequate to explain the material response on a micron scale.

A material response model is necessary which is based on the detailed understanding of the photochemistry process on a micron scale. This model is developed in this thesis.

### **1.3.3 Process planning**

Utilizing the developed material model and the existing process planning method [34], a new process planning algorithm was formulated and implemented in this research.

## **1.4 Research objective**

The overall research objective is abstracted as follows:

*To formulate a process planning method to build sub-millimeter lens shaped structures  
from the ECPL process*

To achieve this objective, research was conducted to first identify the major sources of variations in the process. These sources were systematically analyzed and the process was improved to reduce variations. Having identified the different sources of process variations, in-depth research was conducted to understand the impact of various factors that govern the formation of the shape of the parts cured from the ECPL Process.

## **1.5 Organization of this dissertation**

A brief introduction to the stereolithography process is presented in Chapter 1. This chapter also presents the motivation for the ECPL process with the process overview presented in Section 1.2. The research gaps in realizing a commercial ECPL process are identified in Section 1.3, followed by the research objective in Section 1.4.

Chapter 2 presents the knowledge required to achieve the research objective. Following the literature review, a detailed explanation of the research gaps is presented followed by research questions and hypothesis.

Chapter 3 presents the design of the ECPL system as realized during the course of this research. The experimental procedure typically used to fabricate parts from the ECPL process is discussed. Results from preliminary experiments are presented which indicate a high degree of variability in the manufacturing process.

Chapter 4 focuses on differentiating between the factors governing the shape of the cured part and the fabrication errors. It was found necessary to develop an in-situ real-time photopolymerization monitoring system. A novel monitoring system was designed and installed as an augmentation to the ECPL system. The first research question is presented and its hypothesis is validated in this chapter. This monitoring system was then used to develop a repeatable post-processing method. The experimental results from the monitoring system and the post-processing method are presented.

In Chapter 5, the ECPL process model is presented. Several experimental and simulation studies are conducted to explore the phenomena governing the final cured part shape resulting from the ECPL process. The second research question and its hypothesis are presented in this chapter.

In Chapter 6, the photopolymerization model based on oxygen inhibition and diffusion is developed. Photochemistry simulations were conducted in a commercial finite element simulation package. The results from these simulation and experiments

were combined together to formulate an empirical material model. A database of empirical material properties was developed for the material chemistry investigated in this research.

In Chapter 7, an existing process-planning algorithm was modified to incorporate the empirical material database developed in Chapter 6. It was identified that the refined process plan was inadequate to fabricate accurate structures and hence an improved version of the process plan was presented in Chapter 8. Test samples were fabricated from a photopolymer resin to validate the process plan.

In Chapter 9, the research questions are revisited and the contributions resulting from this work are summarized. The limitations of this work and directions for future work are also discussed.

## CHAPTER TWO

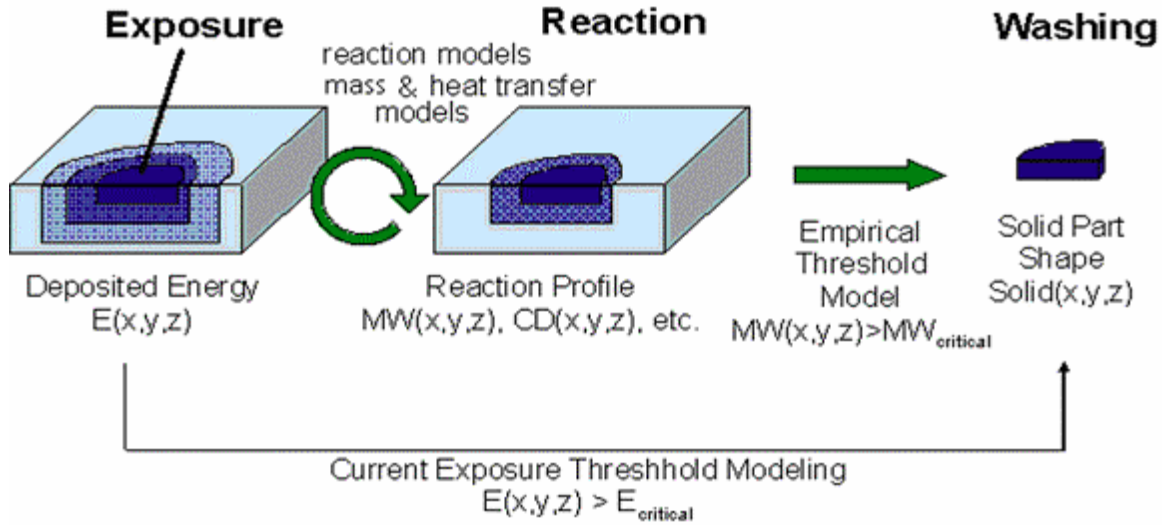
### LITERATURE REVIEW AND FORMULATION OF RESEARCH QUESTIONS

This chapter presents the background knowledge relevant to the ECPL process. The overall objective of this research was to formulate a process planning method, which would help in the reliable estimation of the process inputs to generate the cured part of a desired shape and dimensions. In order to estimate the process inputs, it is necessary to utilize adequately reliable material models, which can explain the phenomena governing the manufacturing process. The following sections present the existing photopolymerization models, the process planning methods used in literature and the research question and hypothesis.

#### 2.1 Photopolymerization

Parts are fabricated in the ECPL system through the photopolymerization process. Photopolymerization is defined as the reaction of monomers or macromers to produce solid polymeric structures by light-induced initiation and polymerization [35]. Of interest for this research is a photopolymerization model that can relate the incident exposure to the shape of the cured part. Researchers have utilized several approaches ranging from empirical models to simplified kinetics for estimating the height of the cured part [1, 36-40]. Figure 9 [38] shows the complexity of the stereolithography process and the modeling approaches. One approach is to utilize a mechanistic modeling approach, wherein reaction models based on chemical kinetics and heat and mass transfer are developed, followed by using an empirical threshold to estimate the shape of the cured

part. Another approach is to utilize a non-mechanistic model to connect the input exposure with the shape of the final cured part.



**Figure 9 Complex stereolithography process and modeling approaches [38]**

The following sub-sections explain the models developed with the two different approaches and present the pros and cons of their application in the ECPL process.

### 2.1.1 Empirical modeling approach

The exposure threshold model is derived from the Beer Lambert's law of absorption. This model is simple to use and is commonly used in the industry for conventional stereolithography (SL) processes.

According to Beer Lambert's law of absorption, the exposure ( $\text{mJ}/\text{cm}^2$ ) decreases exponentially with depth [1],  $z$ .



$$E(z) = E_{max} e^{\frac{-z}{D_p}} \quad (2-1)$$

where  $D_p$  is the resin “penetration depth” (a resin parameter) at the given wavelength and  $E_{max}$  is the exposure at the surface of the resin ( $z = 0$ ).

In practice, polymerization does not proceed beyond a limited depth where the exposure falls below a threshold value. This is primarily due to absorption and oxygen inhibition, which imposes a minimal threshold to start polymerization. The exposure threshold for the formation of gel is known as the “Critical Exposure” ( $E_c$ ) [1]. Current models of the SL process assume that the extent of resin cure is a function of only the amount of exposure to UV radiation [1]. They utilize an exposure threshold model that assumes a dose  $E(x, y, z)$  that is greater than a minimum “critical exposure,”  $E_c$  causes the resin to solidify at point  $(x, y, z)$ .

Nagamori, S. A. [41] performed SL curing tests to investigate how the laser power, laser beam diameter, and laser scanning speed affect the cured depth and width. He correlated the cured depth with energy density (exposure) and found a linear relation on the semi-log graph. All these studies were trying to connect the laser exposure to the part dimensions, as in the exposure threshold model introduced above.

The model in Eq. (2-1) is based on an assumption that the attenuation of radiation through a cured layer is the same as that through uncured resin. It does not consider the effects of radiation through a cured part, which is in solid phase. Limaye & Rosen [42] have observed experimentally that the attenuation through a cured layer is significantly

less than that through the liquid resin. Thus, the depth of penetration for a cured layer  $D_{pS}$  is expected to be different from that for the liquid resin  $D_{pL}$ .

Figure 10 shows the schematic of how the curing process proceeds as a transient phenomenon. Assume that, after an exposure for a time  $t$ , the thickness of the film cured is equal to  $z$ . The energy at the bottom surface of this film will be equal to the critical energy,  $E_c$ . At an incremental time,  $dt$ , the next dose of energy equal to  $H * dt$  will be incident on the top of the cured film, where  $H$  is the irradiation incident on the resin surface. This energy will be attenuated following the Beer Lambert's law of attenuation as it would pass through the cured layer of thickness  $z$  and the energy reaching its bottom surface would be  $H * dt * \exp(-z/D_{pS})$ . Here, it will add up with  $E_c$ , the energy already at the bottom of the film and cause an incremental curing equal to  $dz$ . This incremental curing will be given by

$$dz = D_{pL} \ln \left[ 1 + \frac{dE * e^{\frac{-z}{D_{pS}}}}{E_c} \right] \quad (2-2)$$

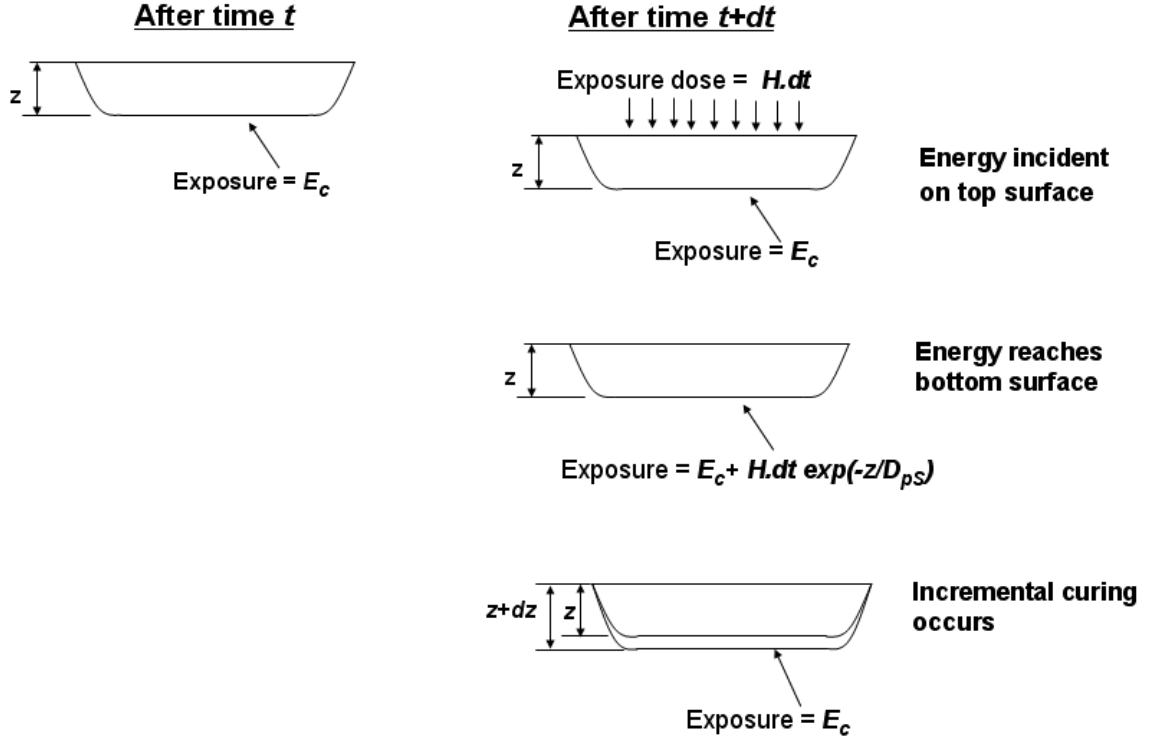


Figure 10 Modeling layer curing as a transient phenomenon [43]

An analytical solution of Eq. 2-2 was found by applying Taylor series expansion by Zhao X. [14]. By omitting the higher order terms, Eq. (2.2) can be further simplified as

$$dz \approx D_{pL} \frac{dE * e^{\frac{-z}{D_{pS}}}}{E_c} \quad (2-3)$$

The layer curing model is obtained after solving the ordinary differential equation above,

$$z \approx D_{pS} \ln \left[ \frac{D_{pL} E}{D_{pS} E_c} + 1 - \frac{D_{pL}}{D_{pS}} \right] \quad (2-4)$$

The following experiments were performed to determine the values of  $E_c$ ,  $D_{pS}$  and  $D_{pL}$  for PEGDA hydrogel with the ECPL system. A thin film is cured on a flat glass

substrate by exposing it to radiation for different time durations. By varying the time of exposure, the radiant energy received by the film is varied. The thickness of the cured film is plotted against the exposure received by the film as shown in Figure 11. By fitting the experimental data using Equation (2.4), the values of  $E_c$ ,  $D_{pS}$  and  $D_{pL}$  are found to be  $0.36\text{mJ/cm}^2$ ,  $1.78\text{mm}$  and  $0.47\text{mm}$ , respectively.

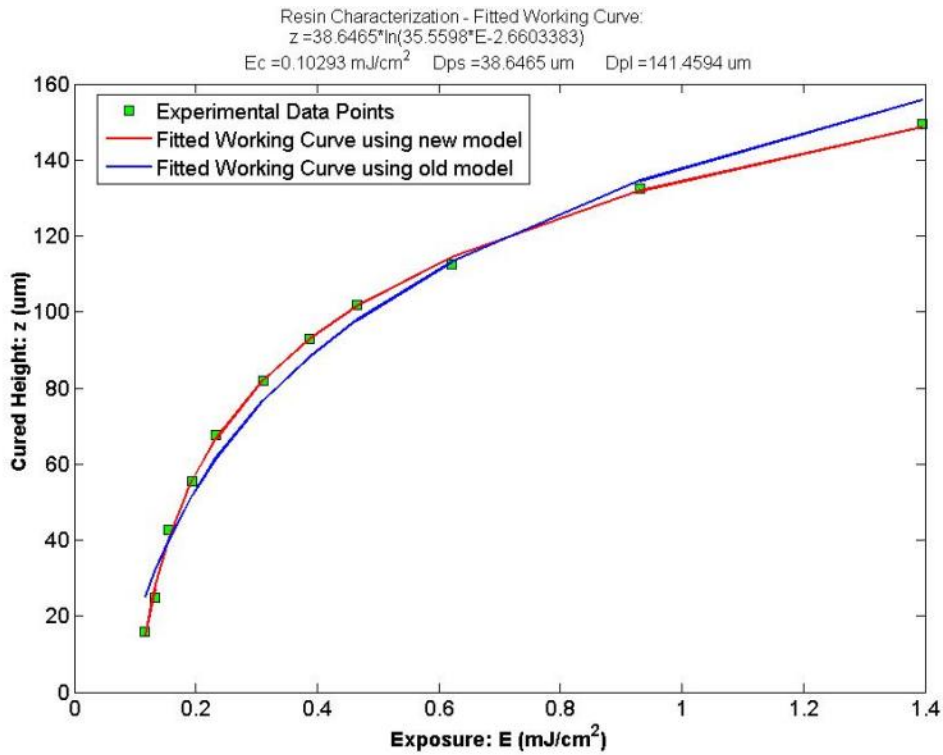


Figure 11 Working curve for PEGDA Hydrogel

This exposure threshold model is an oversimplification of the stereolithography process. It directly connects the exposure to the resin and the final solid part shape. It ignores many important intermediate steps. Although it can predict the height of the cured part with substantial accuracy, its ability to predict the cured part shape is challenged especially when part resolution is in demand. Therefore, it is necessary to

probe further into the resin kinetics to understand the factors that influence the size, shape and properties of parts fabricated by stereolithography.

### **2.1.2 Chemical reaction modeling approach**

The primary thrust in developing mechanistic models based on chemical reactions during photopolymerization was directed towards estimating the time (or energy) required to initiate cross-linking of the monomer to the extent that a gel is formed. The models would determine the dynamic concentration of the individual species within the photopolymer resin as a function of exposure time. Several researchers [38, 39, 44] have attempted to model the photochemistry process by incorporating models for chemical reaction kinetics, heat and mass transfer. Yanyan Tang [38] developed a stereolithography curing model (referred to as the ‘degree of cure’ model). Coupled partial differential equations, representing the chemical kinetics and heat and mass transfer, were solved to estimate the height and width of the cured part for the typical scanning based stereolithography process. The degree of cure model provided greater prediction capability than the empirical model. However, the model was developed for scanning stereolithography process, which significantly differs from the process conditions used in the ECPL process. This renders it ineffective to be used directly for this research.

Slopek [45] found that when the experimental conditions are such that the intensity is lowered and the photopolymer has dissolved oxygen, the dissolved oxygen in the photopolymer resin severely inhibits the curing process. He used particle-tracking microrheology to estimate the effect of oxygen inhibition on the time required to start the

photopolymerization process. The inhibitory effects of oxygen on the part dimensions were not modeled earlier and so Bodappati [39] modeled the photopolymerization process by assuming the chemical kinetics and mass transfer for oxygen only. The following text briefly explains the chemical kinetics model while incorporating oxygen inhibition and diffusion.

Most Stereolithography (SL) resins contain acrylate monomers. For an acrylate resin system, the usual catalyst is a free radical. In Stereolithography, the radical is generated photo chemically. The source of the photo chemically generated radical is a photo initiator, which reacts with an actinic photon. This produces radicals that catalyze the polymerization process. As the photons penetrate the resin, they are progressively absorbed by initiators [42]. The dynamic concentrations of all these species are based on the reaction mechanism, which can be described through appropriate models. In the case of monofunctional acrylates, the change in concentration of all the species in a well-mixed bulk reaction volume can be defined by a set of ordinary differential equations [46]. Boddapati et al. [44] further simplified the kinetic model and modeled the reaction process for double bond conversion. The researchers modeled the concentrations of photoinitiator [In], radicals [ $R \cdot$ ], unreacted double bonds [DB], and oxygen [ $O_2$ ]. The kinetic reactions considered by them were as follows[44]. When the photopolymer resin receives light energy, the photoinitiator absorbs it and decomposes into two radicals with first order rate constant of,  $K_d$



The radicals can then react with the double bonds to form longer chains, or form a dead radical or be quenched with dissolved oxygen as depicted by the following three equations.



$R_{dead}$  is species produced that destroys one or more radicals. The rate constants used are  $K_p$  for propagation of a radical through an acrylate double bond,  $K_t$  for termination between two radicals, and  $K_{t,O_2}$  for termination of a radical with an oxygen molecule.

Oxygen present in the photopolymer resin can act as a radical scavenger, inhibiting the propagation reaction (shown in Eq. 2.6) and the termination reaction (shown in Eq. 2.8). Loss of radicals due to oxygen inhibition is a problem that is pervasive in polymerization involving radicals [47-50]. Oxygen competes strongly for the radicals to form a stable radical, which is unlikely to act as a free radical. Until most of the oxygen in the reaction volume has been used up, there is very little consumption of the monomer.

For the above chemical reactions, the authors proposed the kinetic equations to estimate the concentration of the individual species at a given instant of time as follows [44]:

$$\frac{d[In]}{dt} = -K_d I(z)[In] \quad (2-9)$$

$$\frac{d[R \cdot]}{dt} = 2K_d I(z)[In] - 2K_t [R \cdot]^2 - K_{t,O_2} [R \cdot][O_2] \quad (2-10)$$

$$\frac{d[DB]}{dt} = -K_p [R \cdot][DB] \quad (2-11)$$

$$\frac{\partial [O_2]}{\partial t} = -K_{t,O_2} [R \cdot][O_2] + D_{O_2} \frac{\partial^2 [O_2]}{\partial z^2} \quad (2-12)$$

Equation 2.12 is a partial differential equation in which the authors modeled the diffusion of oxygen within the resin sample along the vertical direction. The authors assumed that the oxygen might diffuse from the uncured top layers only to the bottom-curing front. The effect of lateral diffusion of oxygen was not considered in this research.

Equations 2.9-2.12 can be solved to estimate the instantaneous concentration of the individual species. However, the concentrations of the different species themselves cannot help in estimating the shape of the cured part, unless there is a theory that links the cured part height with the concentrations of one or more of the species. To bridge this gap, Carothers and Flory [51-53] described a gel as an infinitely large molecule that is insoluble. Flory used this definition to estimate the degree of cure necessary for the photopolymer resin to begin gelation [53]. It was hypothesized that gelation results when the conversion of monomers,  $\alpha$ , reaches a specific critical value. Conversion is calculated as shown in Eq. 2-13.  $[DB]$  is the concentration of double bonds at a given instant in the resin and  $[DB]_0$  is the initial concentration of the monomer in the resin sample.

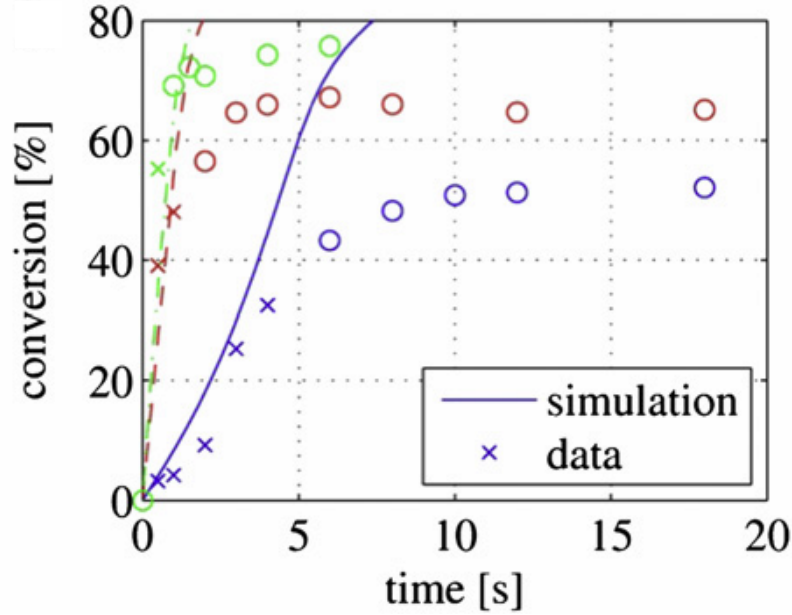


$$\alpha = \frac{[DB]_0 - [DB]}{[DB]_0} \quad (2-13)$$

Using the conversion cut-off criterion, the researchers [44] were able to predict the gel time or the time required by the photopolymer resin to be cured. Assuming the incident intensity of UV light to be constant, the method of gel time predictions can be extended to estimate the height of the cured part.

The photopolymer resin system used in the study was trimethylolpropane triacrylate (TMPTA), and a photoinitiator, 2,2-dimethoxy-1,2-diphenylethan-1-one (DMPA). The researchers used different concentrations of the photoinitiator (DMPA) for their studies. They used Fourier-transform infrared (FTIR) spectroscopy to determine the double-bond conversion of the TMPTA over a range of times throughout the curing process. Three different initiator weight fractions were used for the study, 0.5 wt%, 5 wt% and 10 wt%.

Figure 12 shows the FTIR experimental data (crosses and circles) and the simulation results (lines) obtained from using the chemical kinetic model presented in Eqs. 2.9 – 2.12 with the fitted rate constants. The blue solid curve and symbols represent 0.5 wt% DMPA, the red dashed curve denotes 5 wt% DMPA, and the green dashed-dot curve is for 10 wt% DMPA. The crosses represent the data used to fit the curves.



**Figure 12 Conversion data by FTIR experiments, along with the model-predicted conversions [44]**

The authors concluded that the model could be used to predict the gel time by using conversion cut-off values (Eq. 2.13) between 10 to 30 %. Hence, for a given magnitude of constant intensity, the conversion curves can be used to estimate the time required to start the curing process. This idea was further extended to estimate the time required to gel at a specific depth in the resin. Boddapati et al. [44] showed that the kinetic model can be used to estimate the gel times at different depths inside the resin by comparing the results with the experimental data obtained from microrheology [54]. Hence, if the irradiation intensity is kept constant, it is possible to find the relation between the cured part height and the total exposure received by the resin. However, the model was not intended to estimate the shape of the cured profile. Table 1 shows the advantages and gaps of the two modeling approaches used in literature with relevance to the ECPL process.

**Table 1 Advantages and limitations of existing photopolymerization modeling approaches (concerning the ECPL process)**

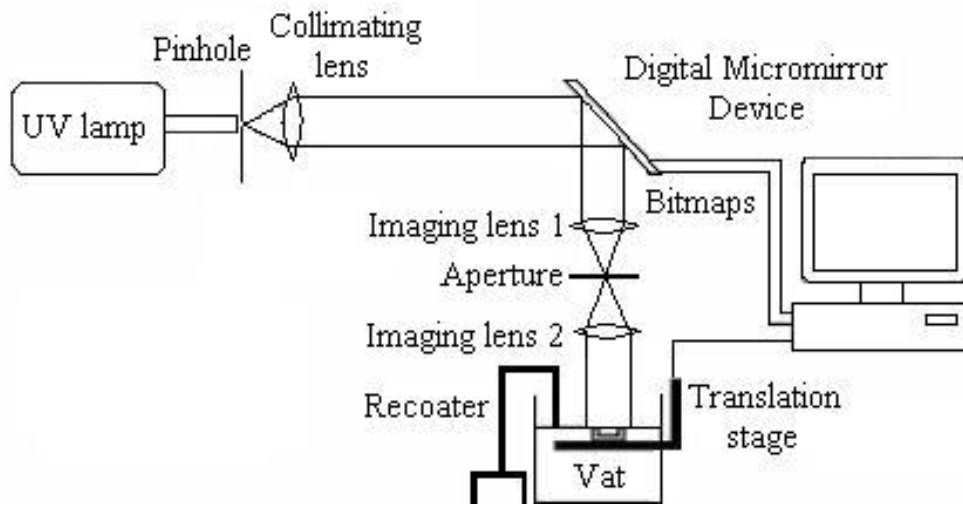
	<b>Material Modeling Approaches</b>	<b>Advantages</b>	<b>Limitations</b>
1.	Empirical Models	Simple model based on few experiments.	Not validated for estimating shape
2.1	Chemical Reaction model - Yanyan Tang [38]	Models the photochemistry process using heat and mass transfer for scanning stereolithography	Applicable for conditions where rapid polymerization takes place, hence does not model the effect of inhibitor diffusion. Not validated for estimating shape
2.2	Chemical Reaction model - Boddapati [39, 44]	Models the chemical reaction kinetics including the diffusion effect of dissolved inhibitor	Used to predict gel time and height, but not shape of the cured part

From Table 1, it is clear that of the relevant models available in literature, which can provide a relation between the input exposure and the final cured geometry, have not been used to estimate the shape of the cured parts in a photopolymerization process.

Since, the overall objective of this research is to be able to fabricate precise micron-scale structures using the ECPL process, it is necessary to formulate an appropriate algorithm which can estimate the necessary inputs to fabricate a part of the desired shape and dimensions. The following section presents the background literature in the area of process planning for micro-stereolithography related processes.

## 2.2 Process planning

Process planning is a method to convert design information into the process steps and instructions to fabricate products in an efficient and effective manner. The process plan is a bridge between the product design and manufacturing. Several researchers have contributed in the development of the process planning method for micro-stereolithography processes.

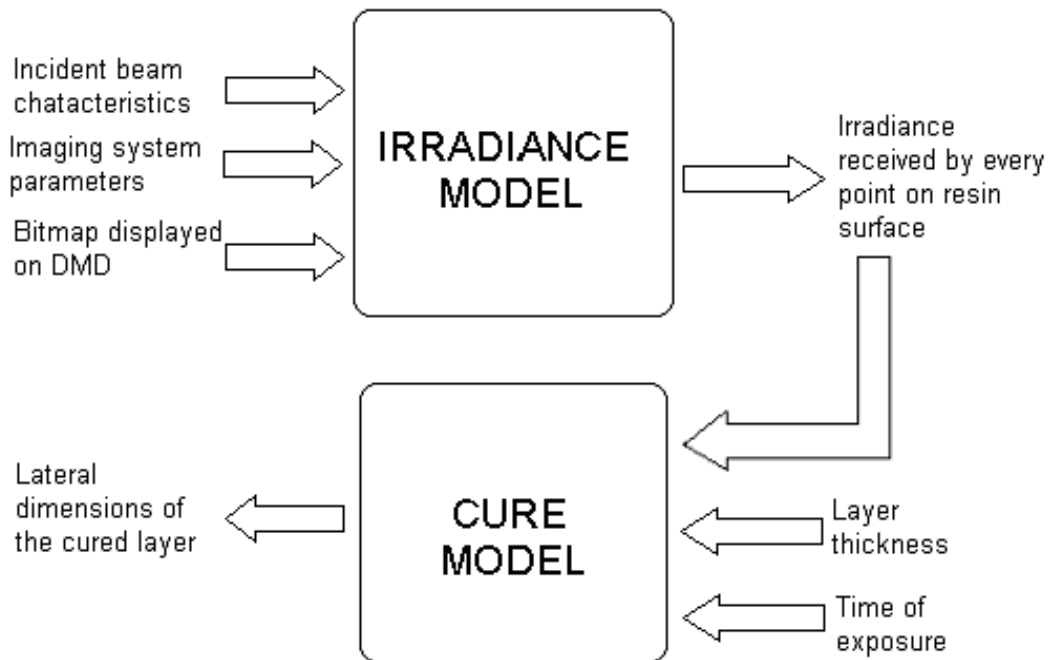


**Figure 13 Schematic of the MPSLA system used by Limaye [43]**

Limaye and Rosen [42, 43] proposed a process planning method to control the lateral dimensions of the cured part in a conventional mask-based stereolithography process (then referred to as Mask Projection micro-SLA, or MP $\mu$ SLA). The schematic design of the MP $\mu$ SLA system is shown in Figure 13. As explained in 1.1.2, the process differs from the ECPL system in that the entire part is built in form of multiple layers and only one layer is cured at a time.

A Layer Cure Model and an Inverse Layer Cure Model for MP $\mu$ SLA were developed. The Layer cure model was formulated to compute the lateral dimensions of a

layer in terms of the process parameters. The Layer Cure Model (schematic shown in Figure 14) comprised of two models: the Irradiance model and the Cure model. The Irradiance model would relate the irradiance received at every point on the resin surface by adopting ray tracing. Cure model computes the cure profile of a layer in terms of the irradiance incident on the resin surface based on the empirical Beer-Lambert's model.



**Figure 14 Schematic of the layer cure model from Limaye [43]**

The Inverse Layer Cure model, shown schematically in Figure 15, was intended to compute the values of the process parameters that would cure a layer of the desired dimensions. The inputs to the Inverse Layer Cure Model are lateral dimensions of a layer and the desired layer thickness. Using a pixel mapping model, the bitmap to be displayed on the DMD in order to form an aerial image of the dimensions equal to those of the

desired layer is generated. “Pixel-micromirror mapping database” relates the location of a micromirror on the DMD to the location of the irradiation caused by switching the corresponding micromirrors ‘ON’. Rays are traced from each micromirror on the DMD to the resin surface using ray tracing. The resulting outputs from this model are the binary bitmaps to be projected on the DMD and the times of exposure for each of those bitmaps.

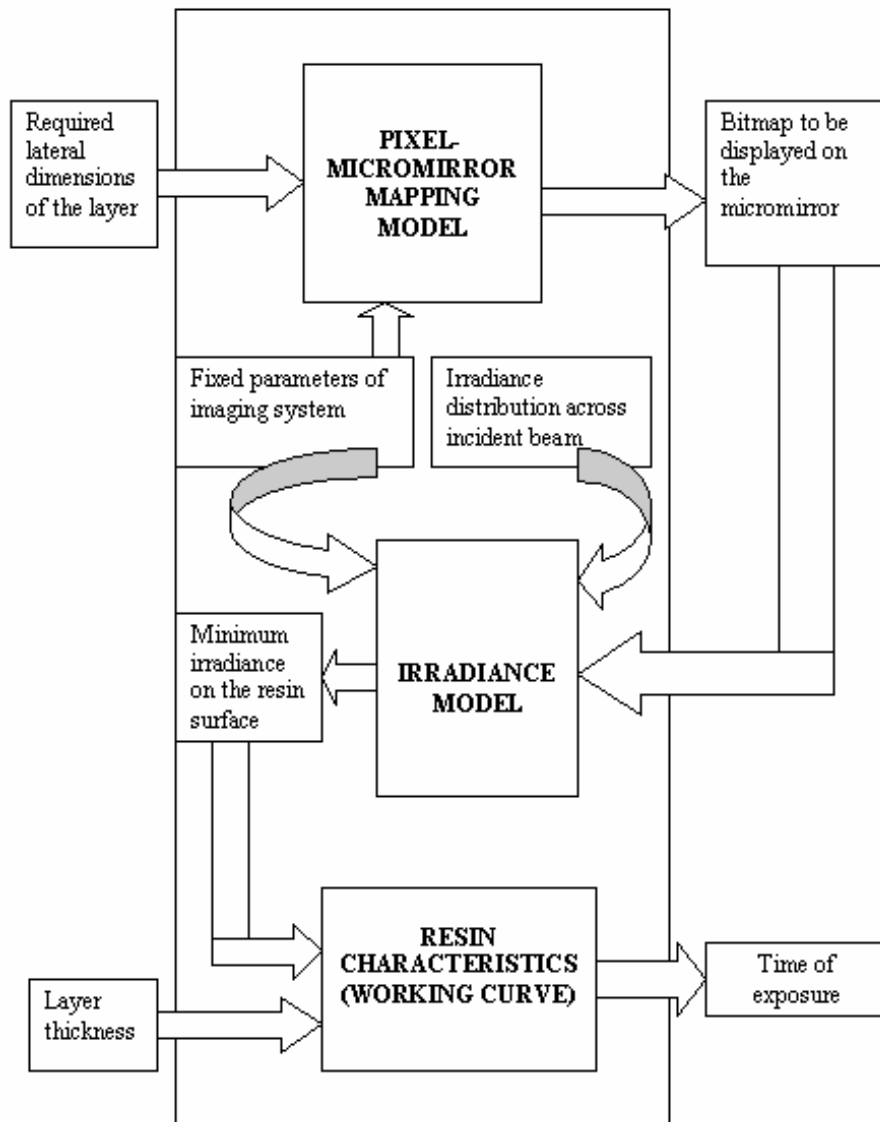


Figure 15 Schematic of the Inverse layer cure model from Limaye [55]

Limaye's process planning approach is applicable in determining the size of the binary bitmaps to be projected on the DMD to cure a layer of given dimensions. However, since the ECPL process does not necessarily have uniform layers to cure, a process plan was required to control the height of the cured part. Jariwala, et al. [56] introduced the idea of using the energy exposure model to estimate the height of the cured part. The algorithm of process planning is explained in detail in X. Zhao's Master's Thesis [14], which used the fabrication system similar to the ECPL. The schematic of the system used in Jariwala et al. [56] and Zhao X. [14] is shown in Figure 16 and was then referred to as the Thick-Film Mask Projection Micro Stereolithography (TfMPSLA). The principle of the TfMPSLA is similar to the ECPL system, except that it used binary bitmaps for exposing the light in to the resin.

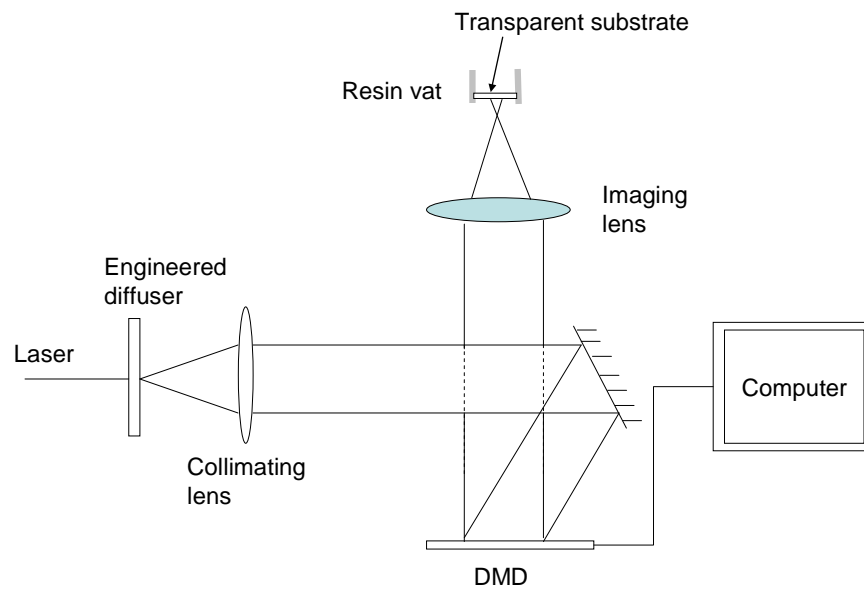
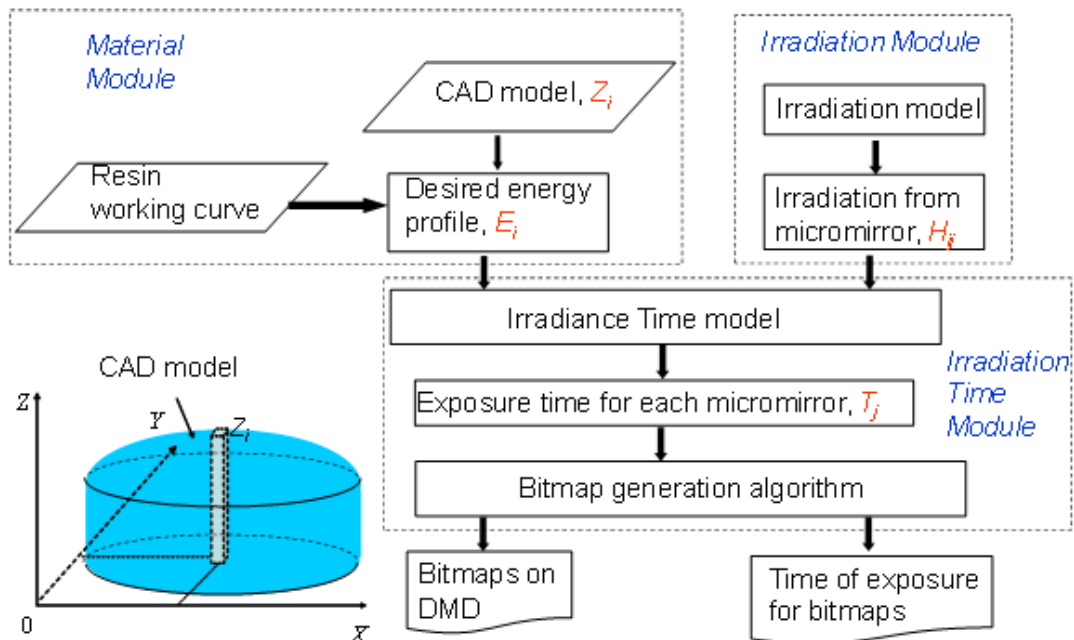


Figure 16 Schematic of the TfMPSLA system [56]

The flow-chart of the process plan is shown in Figure 17. The process plan involved discretizing the given part geometry into columns and using least squares optimization to find the exposure time for each micromirror. K-means algorithm was used to cluster the micromirrors into bitmaps to be projected with similar exposure times. Elaborate experiments based on the above process planning method were conducted and presented in Jariwala, et al. [33].

## Flow Chart of Process Plan



**Figure 17** Flow-chart of the process plan from Jariwala et al. [33]

The process plan was validated only for basic geometrical parameters like width and height of the features with simple optical metrology systems. All the results clearly showed that the edges were under-cured. It was hypothesized that the inaccuracies were largely the result of oxygen diffusion and inhibition during the polymerization process.



One of the samples studied in the paper is shown below. Figure 18 shows the CAD model of the sample desired part shape.

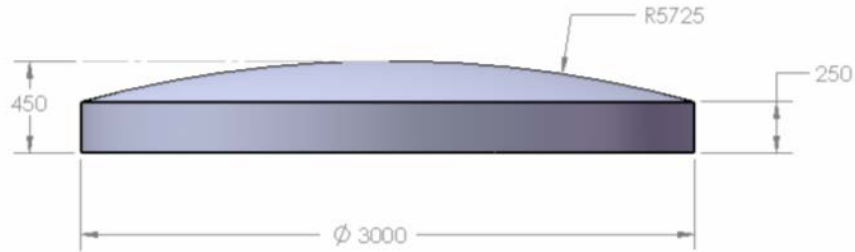
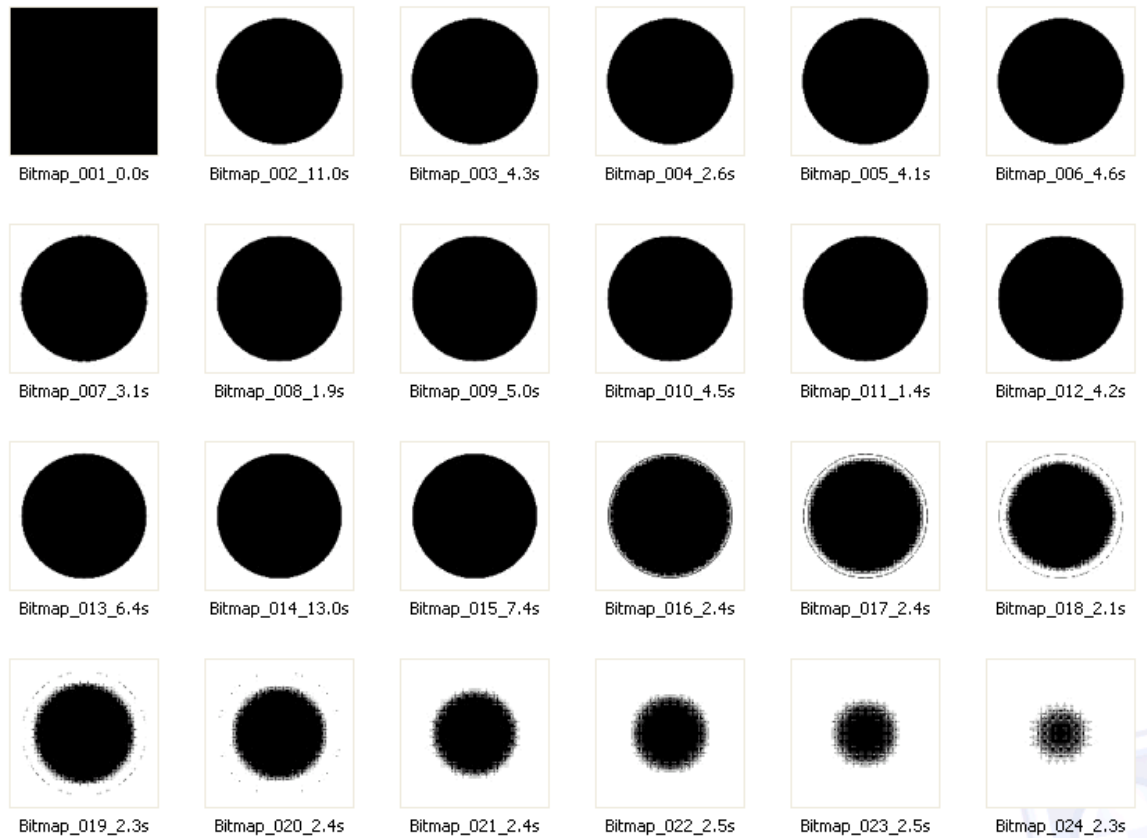


Figure 18 CAD model of the desired part shape [14]

The process-planning algorithm was used to process the input CAD geometry and generate a set of binary bitmaps of gradually reducing diameter as shown in Figure 19.

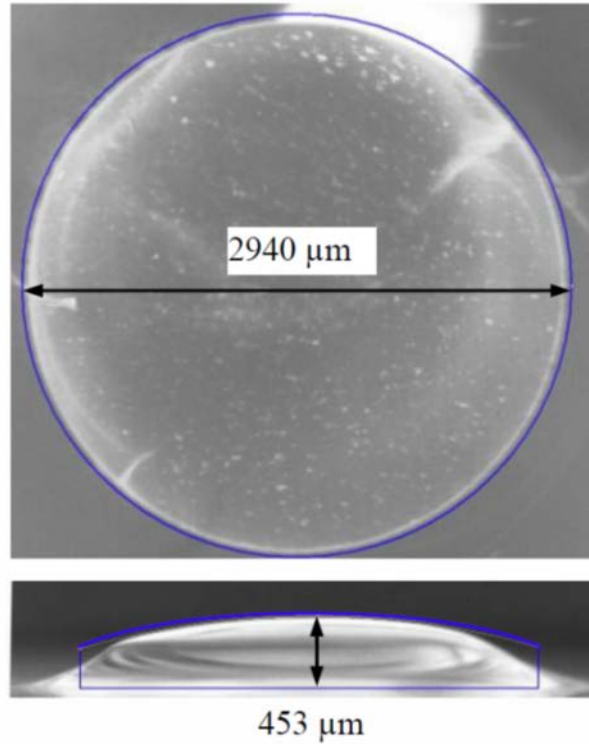




Bitmap\_025\_2.4s

**Figure 19 Bitmaps generated by process plan used by Zhao X. [14]**

The bitmaps shown in Figure 19 were used to fabricate experimental samples from a PEGDA hydrogel formulated as previously described by Mann et al. [57]. The photoinitiator 2,2-dimethoxy-2-phenyl-acetophenone (Sigma, St. Louis, MO) dissolved in 1-vinyl-2-pyrrolidinone (Sigma, St. Louis, MO) was added to Poly(ethylene glycol) diacrylate (PEGDA) (Sigma, St. Louis, MO) to form the PEGDA hydrogel. Figure 20 shows two microscopic images of a representative fabricated lens.



**Figure 20 Experimental observation of the final cured part using the process plan from Zhao X.[14]**

It is clearly seen from Figure 20 that the experimental results might have significant human error associated in measuring the cured part dimensions. The accuracy of the process plan in achieving the desired part shape was not quantified. Moreover, it can be observed that the part edge is slightly under-cured when compared to the desired part geometry. It was hypothesized that the under curing at the part edges might be a result of greater oxygen inhibition at the edges than at the center of the cured part. To mature the ECPL technology into a reliable manufacturing process, there is a clear need to define the precision of the process and develop process-planning algorithm that could cure a desired shape with dimensional control on shape as well as the entire profile.

The research objective can thus be abstracted as follows:

*To formulate a process planning method to build sub-millimeter lens shaped structures  
from the ECPL process*

### **2.3 Research questions and hypotheses**

In order to accomplish the research objective, it is first necessary to have a robust design and assembly of the ECPL fabrication system. Secondly, it is also necessary to understand the ECPL system model to identify which factors govern the process of shape generation in the ECPL process, apart from photopolymerization, which includes oxygen inhibition. Since it is already known from literature and from experimental observation that oxygen inhibition may significantly affect the dimensions of the cured part, an appropriate material response model needs to be developed. This material response model can be used to relate light energy to the shape of the final cured part in the ECPL system. Finally, a refined process-planning algorithm is required which can invert the material model and provide the necessary process inputs to cure a part of the desired dimensions.

#### **2.3.1 Process monitoring**

The ECPL process is designed to fabricate high-resolution lens shaped structures. Since this is a novel fabrication process, there has been no attempt in literature to quantify the repeatability of this process. The effect of process variations on the shape of the final cured parts was never quantified for an ECPL system. Hence, it is necessary to design a system that can provide a real-time window into the part fabrication process,

without altering the process. Such a monitoring system can help identify the sources of variations affecting the shape of the cured part due to variations in process conditions.

**RQ.1.) How to conduct an in-situ real time monitoring of the ECPL process without affecting the fabrication process?**

Hypothesis: *A system that can track the change in speed of light through a medium can be used to visualize the extent of the polymerization process.*

Explanation: Variations in a manufacturing process can occur during fabrication as well as post-processing. It is known that polymerization leads to cross-linking of the monomer, thus changing the density of the cured part. Since, the speed of light is slower in a denser medium, it should be possible to identify the extent of curing by tracking the change in speed of light through the curing photopolymer. It is also known from literature that interferometry can be used to track the change in speed of light in a medium.

### **2.3.2 System modeling**

In order to develop a reliable manufacturing process, it is necessary to identify the various factors that affect the final product. A systematic study of the ECPL process model is required to identify and quantify the various factors that might influence the shape of the cured part fabricated from the ECPL system.

**RQ.2.) What factors influence the generation of final shape/geometry of the cured part in the ECPL process?**

Since parts are fabricated in the ECPL system using photopolymerization, it is obvious that the cross-linking due to polymerization is a primary effect influencing the

shape of the cured part. However, the growth of the polymerization front may depend on the nature of the incident light at the resin substrate. Before modeling the ECPL system, it is necessary to identify how photo curing takes place. The parts fabricated in the ECPL process are subject to post-processing which might also influence the shape of the final cured part. A combination of simulation and experiments will be used to answer this research question.

In order to address the research question, the research question was further split into the following sub-research questions and hypothesis:

**R.Q.2.1.) How does optical self-focusing affect the curing process in ECPL?**

Hypothesis: *Optical self-focusing is caused when light travels from the dense cured part into the relatively less dense uncured resin. Optical ray tracing simulations through the photopolymer resin can be used to verify if self-focusing leads to curing of parts with gradually reducing dimensions from near the substrate to the top free surface of the cured part.*

Explanation: Following the Snells' Law, rays of light bend away from the surface normal as they travel from a denser medium to relatively lesser dense material. During curing in the ECPL process, light has to travel from the previously cured dense (cross-linked) photopolymer into the uncured less dense photopolymer resin. It is reasonable to expect that, if the previously cured shape was spherical or lens-shaped, the rays of light emerging from the cured shape will undergo a focusing effect. This may cause the cured

part to be of successively lesser width than the base as the curing propagates. The hypothesis will be tested in Ch. 4.

**R.Q.2.2) How does post-processing affect the geometry of the final product resulting from the ECPL process?**

*Hypothesis: Post-processing steps like washing and post-curing affect the dimensions of the cured part resulting from the ECPL process. Confocal fluorescence microscopy can be used to determine the extent of swelling or erosion caused by post-processing on the final cured part.*

Explanation: The final product resulting from the ECPL process is subject to several post-processing steps like removal of uncured material, washing and post-curing. All these steps may significantly affect the geometry of the cured part. Depending on the choice of the solvent, the cured part may swell during the washing process. Also, the mechanical action of washing process may cause erosion of the final cured shape.

### **2.3.3 Material modeling**

Review of existing literature suggests a lack of appropriate material models that can explain the photopolymerization phenomena governing the ECPL process. Preliminary experimental results (Figure 56) suggest that existing empirical models based on Beer-Lambert's law might be inadequate to explain the complex photo-polymerization process which is responsible for the generation of the part shape in the ECPL process.

**RQ.3.) How to model the photo-polymerization process to include the effects of oxygen inhibition and diffusion for curing using the ECPL process?**

Hypothesis: *Oxygen inhibition and diffusion are factors that cause a deviation of the material response from the known  $E_c - D_p$  model. This change in the resin behavior can be modeled by modifying the  $E_c - D_p$  model to incorporate the under curing observed at the edges. Specifically, the critical energy, ' $E_c$ ' and the penetration depth, ' $D_p$ ' will be modified to vary as a function of the total exposed area.*

#### **2.3.4 Process planning**

Since, the existing process planning methods are based on simplistic material models, it is necessary to formulate a revised process-planning algorithm (based on the material model developed from earlier research question) that can be used to generate the process inputs.

**RQ.4.) How to formulate an optimization problem so as to generate accurate system level inputs in order to cure a part of desired shape and size in ECPL process?**

This research question was further articulated as a sub-research question as follows:

**How to estimate the micromirrors and corresponding time duration during which they must be switched ON, in order to obtain the desired exposure profile at the substrate level? How to convert  $E_{p,q} (mJ/cm^2) \rightarrow T_{i,j} (s)$**

Hypothesis: *The desired process inputs (micromirrors and time duration for switching 'ON') for curing a desired geometry can be estimated by optimizing the exposure, ' $E$ ' required at the substrate level.*



Explanation: The process-planning algorithm is split into two problems. The first problem is to find the optimum exposure profile necessary at the substrate level, which can cure the desired part shape. This can be obtained from the material model. The second problem is to estimate the process inputs (bitmaps and time of exposure) required to achieve the desired exposure at the substrate level and is addressed by the sub-research question. It was discovered that this process planning approach has several drawbacks and fails to predict the process inputs. Hence, a revised hypothesis was proposed:

Revised Hypothesis: *The process inputs for the ECPL process (like bitmaps and corresponding exposure time) for a given desired part geometry can be estimated by optimizing the cured part geometry using the material model based on chemical kinetics (which was previously validated).*

Explanation: The primary difference between the original hypothesis and the revised hypothesis is that the revised hypothesis suggests optimization of the cured profile and not the exposure. This leads to constructing a more accurate process planning method, as verified through simulations and experiments.

## **2.4 Chapter Summary**

This chapter presented the background knowledge relevant to studying the ECPL process. The research gaps from existing literature were identified and presented. It was found that the existing literature lacks adequate material models that could precisely explain the shape of the cured part when a photopolymer resin is exposed to light. In order to accomplish the research objective, research questions and hypotheses were formulated.

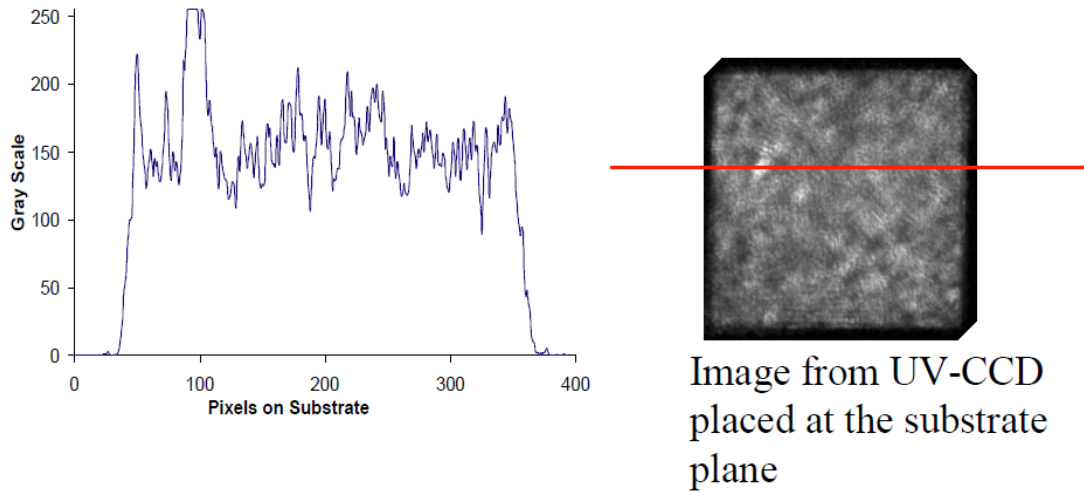
## CHAPTER THREE

### DESIGN AND ASSEMBLY OF THE ECPL FABRICATION SYSTEM

In this chapter, the design and assembly of the Exposure Controlled Projection Lithography fabrication system is presented. With reference to Figure 8 in Section 1.2, the system comprises of the UV source, beam-conditioning system, DMD™, projection system and the resin chamber. The detailed design of the ECPL is elaborated in this chapter with preliminary experimental results.

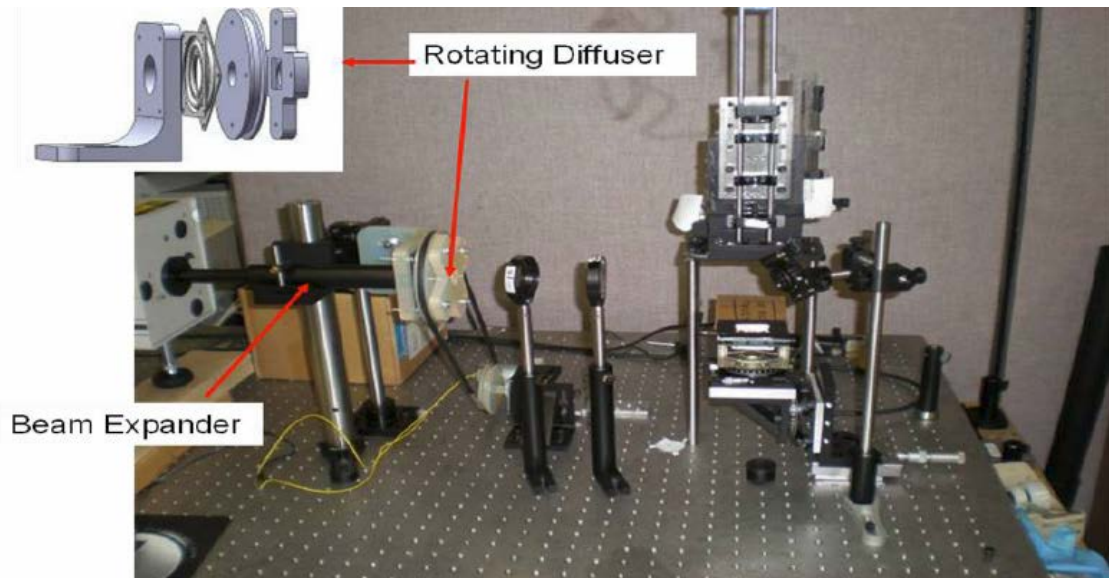
#### 3.1 Existing system design

The ECPL process was developed as a modification from the Thick Film Micro Stereolithography (TfMP $\mu$ SLA) process as designed and developed by Jariwala et al. [56]. The schematic of this system was presented in Figure 16. The primary drawback of this system was that the resulting irradiance profile was not uniform. By placing a UV CCD at the substrate level, the irradiance profile plot was obtained as shown in Figure 21.



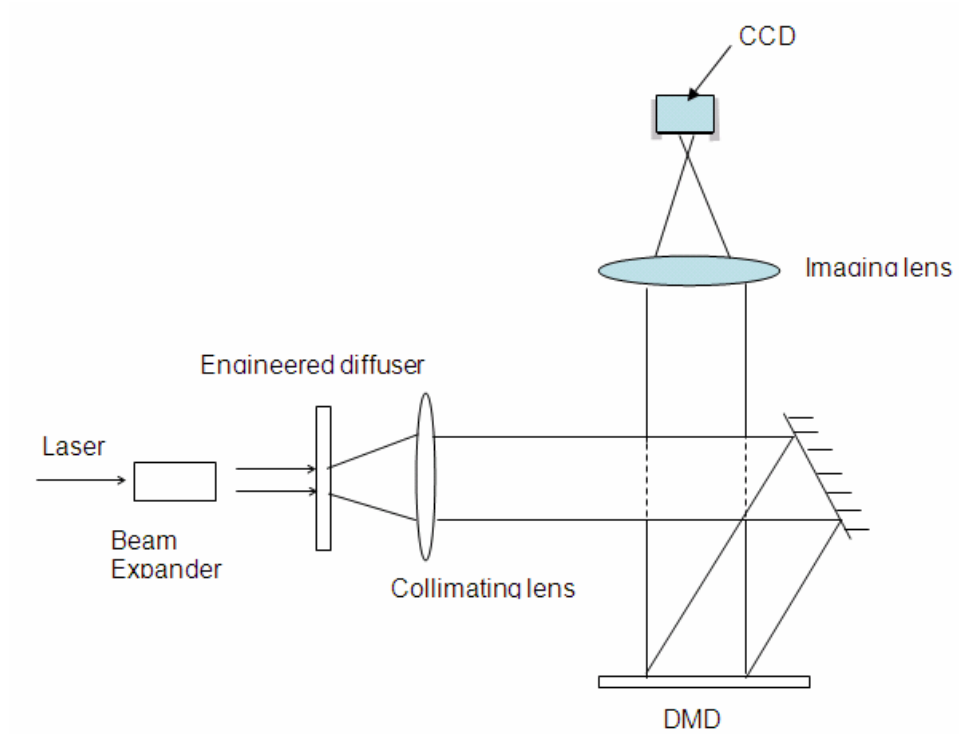
**Figure 21 Irradiance line profile obtained from UV CCD [14]**

To homogenize the exposure profile, a rotating mechanism for the engineered diffuser was installed, and Figure 22 shows the photograph of the modified system.



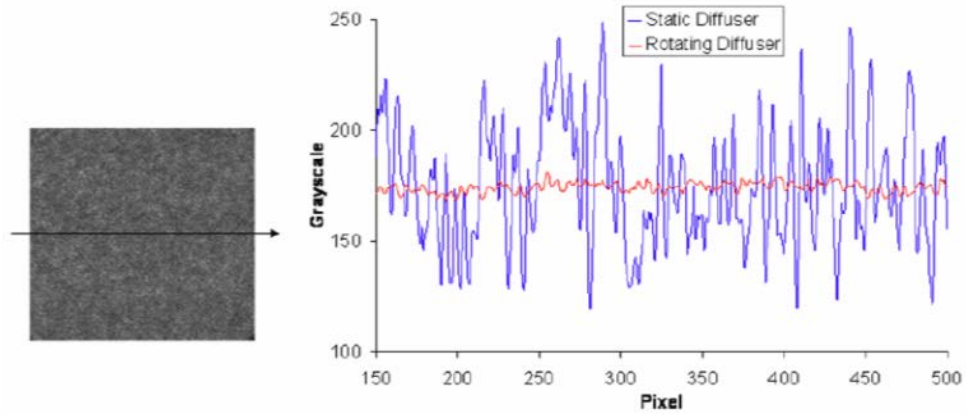
**Figure 22 Modified TfMP $\mu$ SLA experimental system**

The homogeneity of the light beam was tested by replacing the resin chamber with a UV CCD camera. Figure 23 shows the schematic of how the camera was placed in the fabrication system for measuring the light intensity profile.



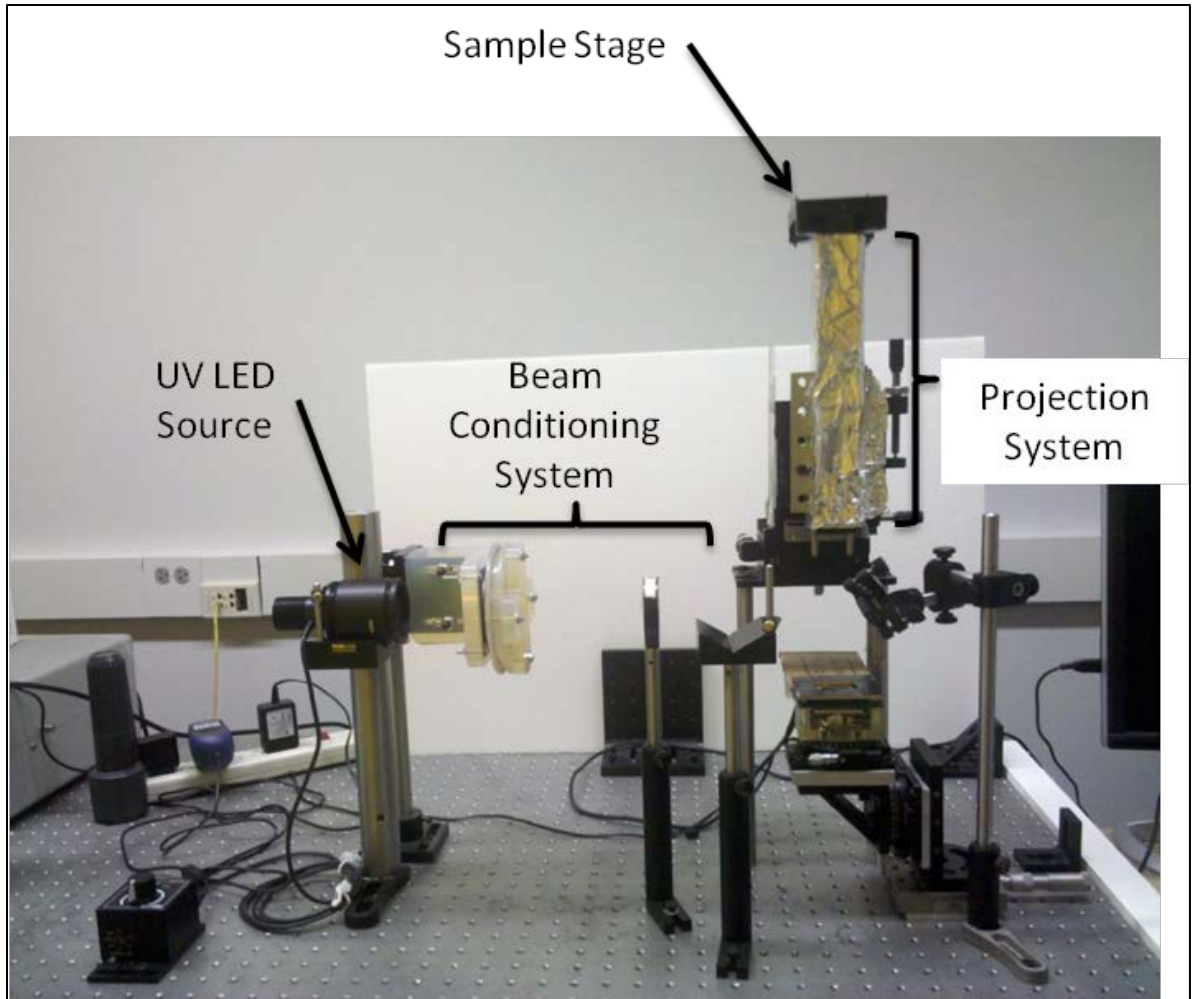
**Figure 23 Schematic showing the location of the UV CCD [14]**

The irradiance profile obtained after rotating the diffuser shows substantial improvement in achieving beam homogeneity as shown in Figure 24.



**Figure 24 Irradiance profile plot obtained by static and rotating diffuser [14]**

The modified TfMP $\mu$ SLA system was used to develop a basic process planning algorithm in Jariwala et al. [56]. Unfortunately, the He-Cd laser used in the setup reached its end of life before additional research could be conducted and hence the system was augmented with a collimated UV LED light source as shown in Figure 25.



**Figure 25 Photograph of the modified experimental setup**

While the beam conditioning system had a greatly improved light source, it incorporated an older generation Digital Micromirror Device (DMD™) chip that had extremely limited interfacing options and was limited to projecting binary images only. In order to add greater flexibility, reliability and throughput to our fabrication facility, a third generation ECPL system that incorporated a newer, higher resolution DMD chip with the capability to project gray-scale images was assembled. This newer system design was referred to as the Exposure Controlled Projection Lithography (ECPL) – a

*system, which controls the cured part profile by exposure.* The detailed design of the ECPL system is explained in the following section.

### **3.2 Design of the ECPL fabrication system**

The ECPL system was developed in three modules as follows:

1. Selection of the UV light source and design of the beam conditioning system
2. Design of Projection System with the DMD™
3. Design of the Resin Chamber

#### **3.2.1 Module – 1: Selection of the UV light source and design of the beam conditioning system**

The primary requirement for the design of this module was to maximize the energy throughput from the light source to the substrate while also homogenizing the beam profile.

**UV light source:** Referring to Figure 8, the major source of loss in power was anticipated from the beam conditioning system. To offset for the potential losses, primarily due to homogenization, a high power UV curing lamp source was selected as a light source. The Omnicure® S2000 UV spot curing system from Lumen Dynamics was chosen for this study. This is a commercial high-power mercury arc lamp with integral feedback control over the total irradiation intensity. Specifically, it consists of a High Pressure 200 Watt Mercury Vapor Short Arc. The light from the lamp is delivered through a 5mm light guide. The light spectrum resulting from this source is in the range of 320-500nm. Figure 26 shows the resulting beam profile from the UV light source after exiting from the 5mm

light guide. The profile is projected on a white cross-marked paper to expose the fluorescence. As seen in the photograph, a reflective neutral density filter with 50% transmission was placed at the end of the light guide to reduce the intensity for ease in visualization of the donut shaped intensity profile. Since the ECPL fabrication process is entirely controlled by light, it is necessary to have an input light source of uniform intensity. Hence, a sub-system is necessary to convert the donut shaped light profile from the light guide into a homogeneous beam.



**Figure 26 Photograph showing the intensity profile resulting from the UV light source from the light guide**

**Beam Conditioning Module:** The primary function of the beam-conditioning module is to homogenize the light beam resulting from the light source and project it on the DMD™ chip. Homogenizing a light beam typically requires one or a combination of diffusers and/or micro lens arrays [22]. The choice of these components depends on the



input intensity profile and the divergence angle of the light source. Beam homogenization is vast area of research and countless companies offer optical products and provide specialized design consulting primarily to obtain a uniform beam profile from a given light source. During the course of this research, we manually experimented with using the Engineered Diffuser™ from RPC Photonics, microlens arrays and light pipes from Edmund Optics and ground glass diffusers from Thorlabs, Inc. The compromise has always been between beam homogeneity and higher energy throughput. For example, diffusers provide a uniform light intensity profile. However, the light beam gets divergent after exiting from the diffuser. This causes a significant amount of loss of light energy. This loss can be eliminated by using a collimation lens, which eventually tends to reimage the diffuser and makes the light beam less homogeneous. The document on DLP™ System Optics [58] by Texas Instruments explains the advantages of a solid or hollow light integrator as compared to lens-array type integrators. Since we also had access to a commercial DLP projector, we attempted to mimic the optical schematic of a typical projector. Figure 27 [58] shows the schematic of the optical system in a typical DLP projector. Of relevance to this study is the optical arrangement including the condenser lens, optical integrator and the collimating lenses.

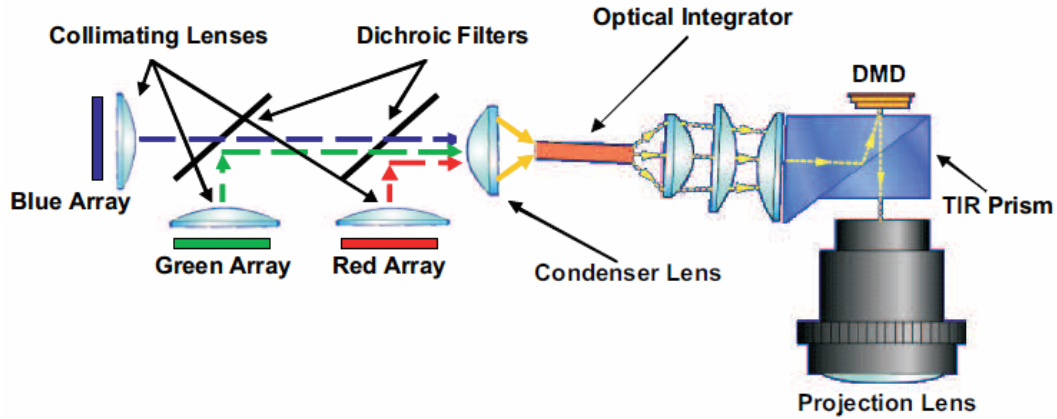
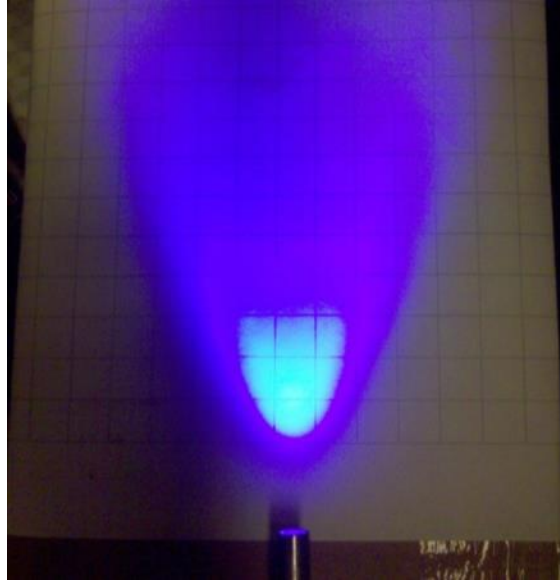


Figure 27 Schematic of the optics within a DLP projector by Texas Instruments [58]

We had planned to use a ViewSonic DLP projector for the DMD™ chip. This projector used a hollow tunnel shaped light integrator. A tunnel integrator is rectangular in shape, which comprises of internally reflecting surfaces. When diverging light is passed through the integrator rod, the resulting light is spatially homogenized due to multiple internal reflections. Figure 28 shows a photograph of several integrator rods. In order to utilize the integrator rods to obtain satisfactory performance, it is necessary to ensure that the input light conditions are suitable for the integrator rod's operation.

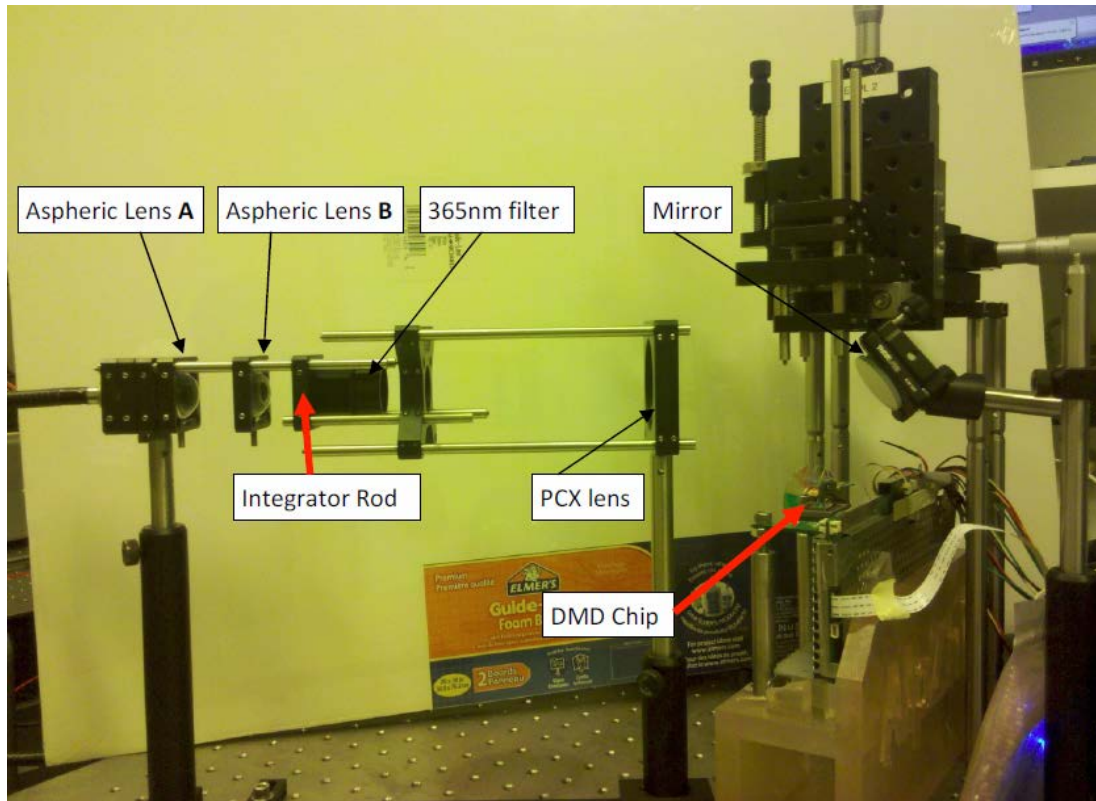


Figure 28 Photographs of Integrator Rods [59]



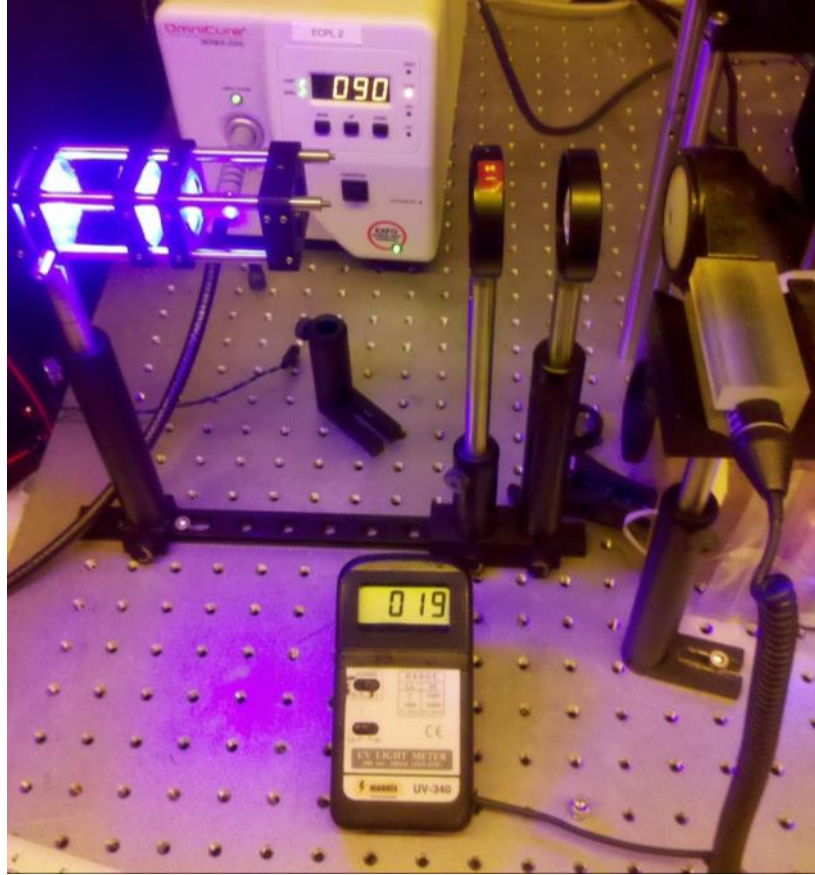
**Figure 29 Photograph showing the divergence of the light resulting from the light guide**

The desired input light beam for an integrator rod is convergent. However, the light beam resulting from the light guide is divergent (half angle of around 12 degrees) as shown in Figure 29. Hence, a series of condenser lenses, specifically short focal length aspheric lenses, were required to transform the beam into a convergent light beam. This collimated light was then directed through an integrator rod, which homogenizes the light intensity. The light exiting from the integrator rod is divergent and hence a plano-convex lens was used to collimate it. A bandpass filter of  $365.0 \pm 2 \text{ nm}$  was incorporated in the system. Figure 30 shows the photographs of the assembled beam conditioning system. The 5mm liquid light guide from the UV lamp is seen in partial view on the extreme left.



**Figure 30 Photograph showing the front view of the beam conditioning system; with the mirror to fold the light on the DMD Chip**

The beam conditioning system was assembled while maximizing energy throughput as well as beam homogeneity. Figure 31 shows the arrangement used to measure the resulting light intensity from the beam-conditioning system. A UV radiometer was used to measure the intensity of light. A special fixture was designed and fabricated, using commercial SLA machine, to hold the sensor for the radiometer. The position of individual lens elements was varied to obtain better beam quality.



**Figure 31 Photograph showing the experimental setup used to assemble the beam conditioning system**

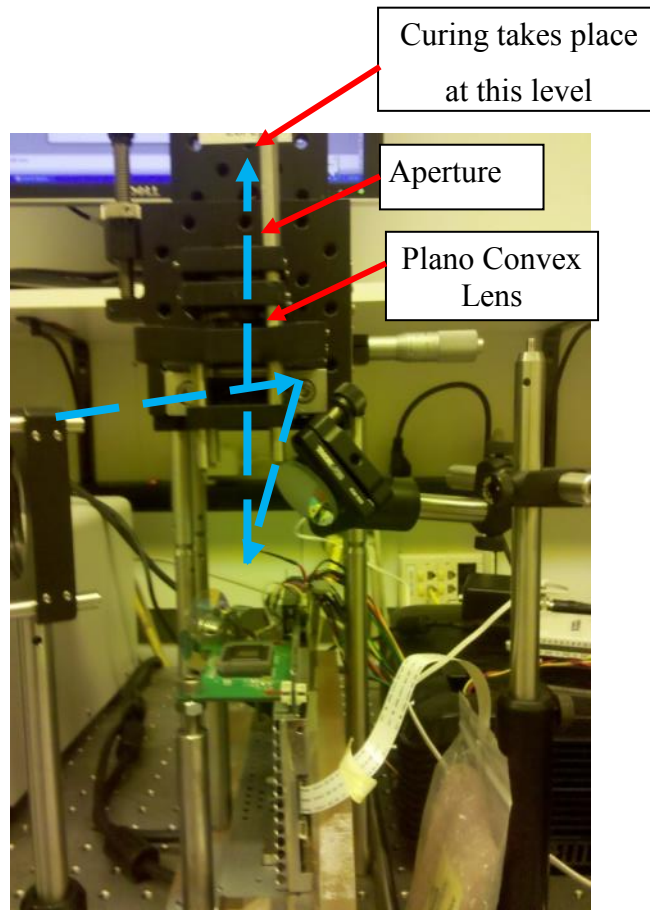
### **3.2.2 Module – 2: Design of projection system with the DMD™**

The Digital Micromirror Device (DMD™) is a product of Texas Instruments and is an array of individually addressable, bistable micro mirrors, which can be selectively oriented to display any bitmap. Every pixel on the bitmap controls one and only one micromirror on the DMD™. The micromirrors are  $12.65 \mu\text{m}$  square and the spacing between adjacent micromirrors is  $1 \mu\text{m}$ . The micromirrors in their neutral state are parallel to the DMD™ chip.

In its “ON” state, a micromirror swivels about its diagonal by  $10^\circ$  in one direction and in the “OFF” state, swivels by the same amount in the opposite direction. The DMD™ chip used in this study was obtained from a ViewSonic PJD 6221 projector. The bitmap displayed on the DMD™ serves as the object for the projection system, which is imaged on the resin chamber. Powerpoint® presentation software was used to create the images on the DMD™. The system is so designed such that a white image on the DMD™ reflects the light away from the projection system, resulting into no curing. Similarly, a black image results in projecting the image into the projection system, thus resulting in curing.

A special fixture was designed to hold the DMD chip with the electronics board from the DLP projector. The objective of the holder was to ensure that the chip remained parallel to the optical table and allowed for interconnects to and from the electronics board. A commercial SLA machine from 3D Systems™ was used to fabricate this design.

**Projection System:** The primary function of this system is to enlarge or reduce the image presented on the DMD™ and project it on the resin chamber. For this study, we used a single plano convex lens to achieve a magnification of 0.47X. The light resulting from the beam conditioning system is not perfectly collimated. Hence, to reduce the image blur caused by inclined rays of light, an aperture was placed after the lens to block the transverse rays. Figure 32 shows the close-up photograph of the DMD™ with the projection system.



**Figure 32 Photograph showing the mirror, DMD Chip and the projection system**

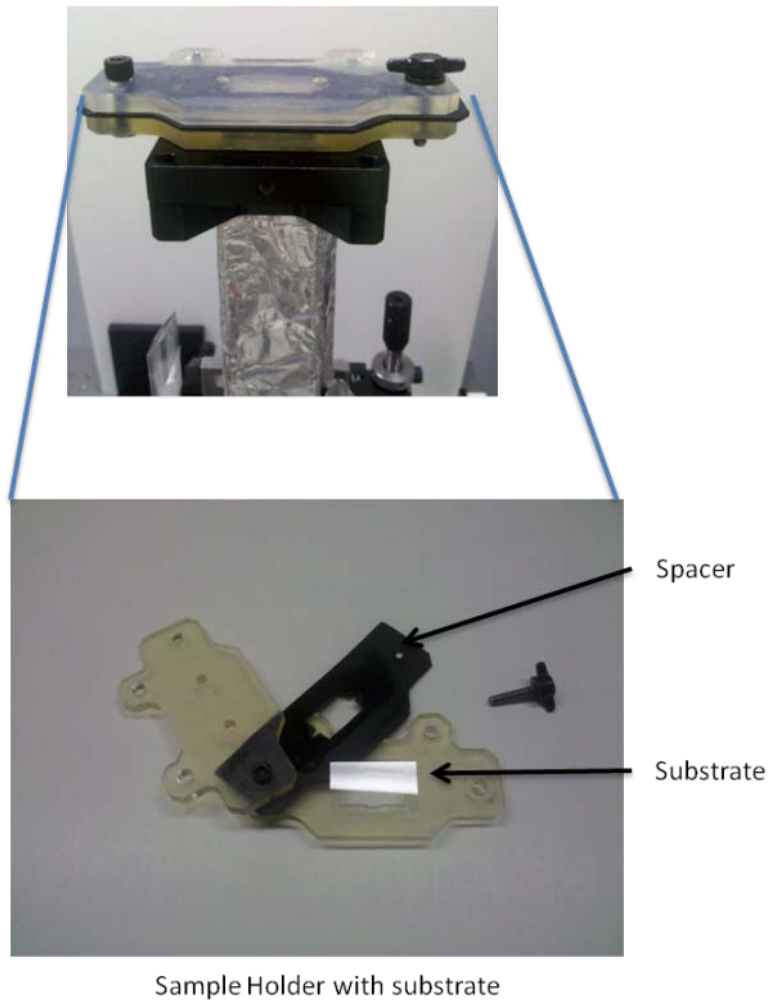
It is to be noted that the design presented above is by no means intended to suggest being one providing a well-collimated homogenous UV beam. The system was designed and assembled considering limited resources, while maximizing performance by numerous trial-and-errors. As the ECPL technology matures, a rigorous custom optical system design will be necessary to ensure a high degree of homogeneity, collimation and energy throughput.

### **3.2.3 Module – 3: Design of the resin chamber**

The resin chamber is the primary reaction cell used to hold the liquid photopolymer during the fabrication process. The design considerations for the chamber are that it should have a transparent base to allow light to enter the photopolymer. The chamber should be small enough so as not to allow large waste of uncured photopolymer. Moreover, the resin chamber should be rigidly mounted to ensure positional consistency from one experiment to another. The resin vat used in Jariwala et al. [56] was a rectangular container, such that the glass slide would act as the base when completely assembled. The glass slide would then be the substrate on which the parts would be fabricated.

There is a lot of waste of the uncured photopolymer resin as compared to the volume of the parts cured. There may be variations in the total volume of resin loaded in the vat, which may affect the precision of the fabrication process. In addition, the top resin surface is in contact with the surrounding ambient air, which may lead to oxygen diffusion during the curing process. Hence, an enclosed resin chamber was designed in form of a sandwich structure, as shown in Figure 33.

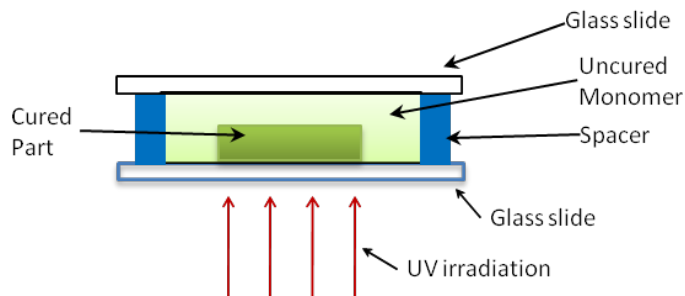




Sample Holder with substrate

**Figure 33 Photograph of the second-generation resin chamber**

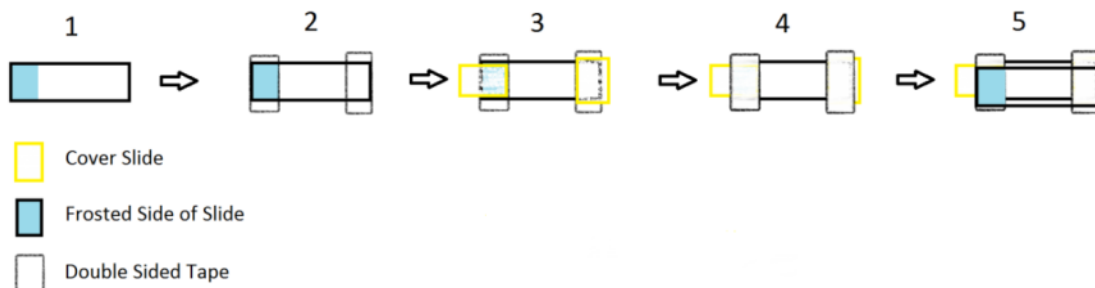
To further reduce the amount of lost material and ease in assembly of the resin chamber, a new design was implemented. The resin chamber thus designed, consisted of two glass slides stuck closely together with a spacer (microscope slide cover slip) of known thickness placed along two edges as shown schematically in Figure 34. The resin is loaded between this sandwich structure of glass slides and is held by capillary force. The base glass slide acts as the substrate upon which the film is cured.



**Figure 34 Schematic of the Resin Chamber**

The procedure to create a resin chamber is depicted in Figure 35 and is elaborated as follows.

1. Remove a clean frosted glass slide from the box and orient the frosted side to the left.
2. Apply a double-sided sticky tape to both ends of the slide, pressing down lightly to ensure the seal.
3. Attach two cover slides (which acts as a spacer), one to each sticky tape piece with the orientation shown in the figure.
4. Place double-sided sticky tape over both pieces of cover slide, pressing down lightly so that the seal does not have air gaps.
5. Place a second frosted slide over the sticky tape slightly lower than the first slide to create a small lip in which to inject the resin into the cavity between the slides.



**Figure 35 Figure showing the steps in constructing the resin chamber**

Once the desired pattern is exposed, the resin chamber is disassembled, the uncured monomer removed and the glass slide with the cured part is washed to remove traces of uncured monomer.

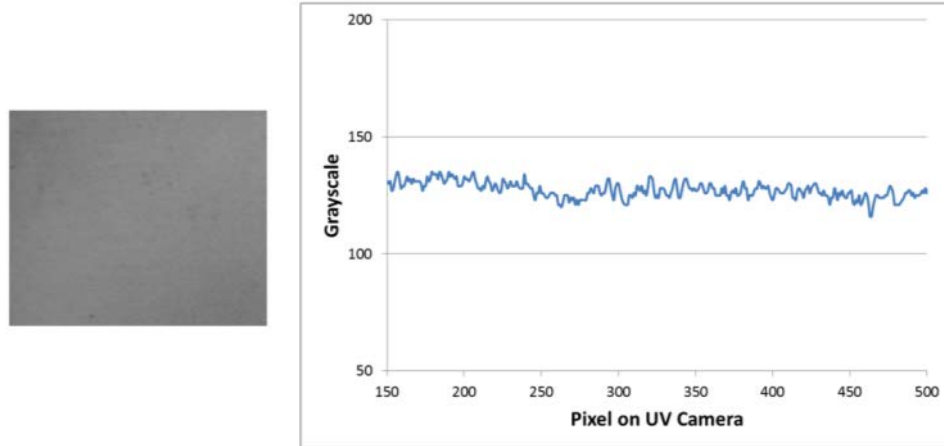
The specifications of the ECPL system are presented in Table 2.

**Table 2 Specifications of the components used in the ECPL system**

<b>Component</b>	<b>Description</b>	<b>Model/Manufacturer</b>
UV Lamp source	High pressure 200W Mercury Vapor Lamp Broadband: 320-500nm Light guide diameter = 5 mm	Omniculture S2000 / Lumen Dynamics
Collimating lens	Fused silica Plano convex lens Effective focal length = 150.0mm Diameter = 50.8mm	Thorlabs Catalog # LA4904-UV
Mirror	Round UV Aluminum mirror Diameter = 25.4mm	Thorlabs Catalog # PF10-03-F01
DMD	1024 X 768 array of micromirrors	Obtained from ViewSonic DLP PJD 6221 projector
Imaging lens	Fused silica Plano convex lens Effective focal length = 50.0mm Diameter = 25.4mm	Thorlabs Catalog # LA4148-UV

### **3.3 Experimental procedure**

An ECPL system was installed as per the specifications in the Table 2. This system was used to conduct preliminary experiments, which lay the foundation for the research investigation in the subsequent chapters.



**Figure 36 Camera image of the irradiation (on left) and average irradiation plot (on right)**

Using the method described in Section 3.2.1, the UV-CCD camera (Table 3) was used to confirm the homogeneity of the irradiation profile. The irradiation profile plot is shown in Figure 36 and the beam was found to be homogenous within  $\pm 5\%$ .

**Table 3 Technical Specifications for the UV CCD Camera used in this research**

Model:	Sony XC-EU50 (Near UV Sensitive B/W Camera)
Effective Pixels	768(H) x 494 (V)
Cell Size	8.4 x 9.8 $\mu\text{m}$
Applicable wavelength range	300-420nm

The fabrication process involves having the operator load the resin chamber and place it at the substrate level. This loading and unloading process can misalign the optical system, which may lead to process variations. The DMD Chip, which is a part of the DLP projector, is driven using the Powerpoint® Software. Binary or gray-scale images can be projected. For preliminary experiments, binary images were used. The resin chamber was filled with the photopolymer resin, which was held in the chamber due to capillary forces.

### 3.3.1 Photopolymer material

The basic requirements for the resin formulation were to have a clear transparent cured product, which is sensitive to UV radiation and, the chemical kinetics behavior known. A tri-functional acrylate monomer - trimethylolpropane triacrylate (TMPTA, SR-351) obtained from Sartomer was used as obtained, with the photoinitiator 2, 2-dimethoxy-1, 2-diphenylethan-1-one (DMPA, IRGACURE-651) obtained from Ciba Specialty Chemicals, as the resin composition. Since the ECPL process was being designed and developed primarily for fabrication of micro-optics, it was necessary to ensure that the resin used in the system would be photocurable as well as allow transmittance of light, after complete curing. The UV-VIS transmission spectrum of a completely cured tri-functional acrylic resin is shown in Figure 37. The photopolymer exhibits transmittance in excess of 90% throughout the visible spectrum.

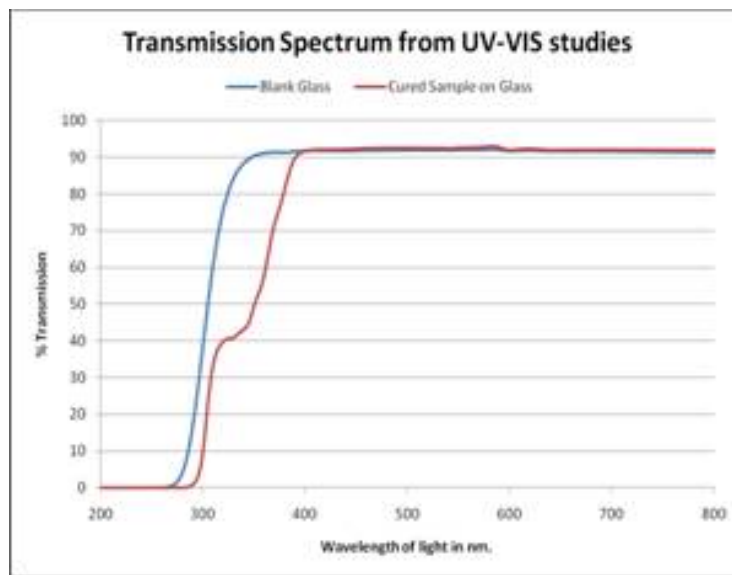


Figure 37 Optical transmittance of cured photopolymer (red) and that of blank glass slide (blue), used for comparison

The ECPL process relies on developing a material formulation that was sensitive to UV radiation and would cure such that it would yield a sharper gel boundary. A sharper gel boundary may help ensure higher degree of repeatability. Lee et. al [60] presented a relationship between the cure depth and the photoinitiator concentration, which suggested that a higher photoinitiator concentration sample may yield in a sharper gel boundary. According to the technical datasheet for the photoinitiator [61], the maximum solubility of the photoinitiator in the monomer, TMPTA is 26 (g/100 g of solution). To ensure a homogenous solution, a solution of 20% by wt. of DMPA in TMPTA was selected for most of the experiments in this thesis. This specific formulation required less than 30 seconds to cure a thick layer of resin. In principle, a resin formulation with higher sensitivity could have been appropriate for ECPL. However, a fast curing resin system would impose a higher demand on accurate timing control on the DMD (which currently has only a resolution of only 0.1s, limited by the PowerPoint® software used to control the DMD). Hence, the current resin formulation was used.

In order to avoid variations resulting from varying chemical composition, a consistent batch of resin was used. The variations introduced by resin composition can be eliminated by adopting a consistent method for preparation of a batch of resin for characterization and fabrication experiments.

### **3.3.2 Exposure control**

The exposure times can be controlled by two means – using the timing control on the UV lamp source or switching the bitmaps using the slide show transition from the Powerpoint® presentation software. For most of the experiments, it was easier to control

the exposure times using the timing control on the UV lamp source. The minimum resolution for controlling the exposure through the UV light source is 0.1s.

### **3.4 Experimental results**

Square shaped binary bitmaps were projected on the DMD chip and the exposure time was systematically varied. The samples were washed in water and post-cured for 10 minutes to cross-link any uncured monomer. A laser confocal microscope (3D LEXT Confocal microscope from Olympus, accessed from the Georgia Tech Marcus Organic Nanotechnology cleanroom) was used to measure the three-dimensional profiles of the cured parts. Figure 38 shows the measured cured part height as a function of exposure time. Five samples were fabricated for each exposure time. It is clearly seen that the system generates a variation in the cured part height  $\sim 9\mu\text{m}$  for a nominal height of  $55\mu\text{m}$ , which amounts to around  $\pm 8\%$ , while keeping all control factors constant. There must be some inherent system variations, which yield these variations in the cured part heights. Since, the motivation for developing the ECPL process was to fabrication precision microstructures, including micro-optic elements, it is necessary to investigate the sources of these variations and eliminate them. It is desired to develop a robust ECPL system, which can fabricate samples with a high degree of repeatability.

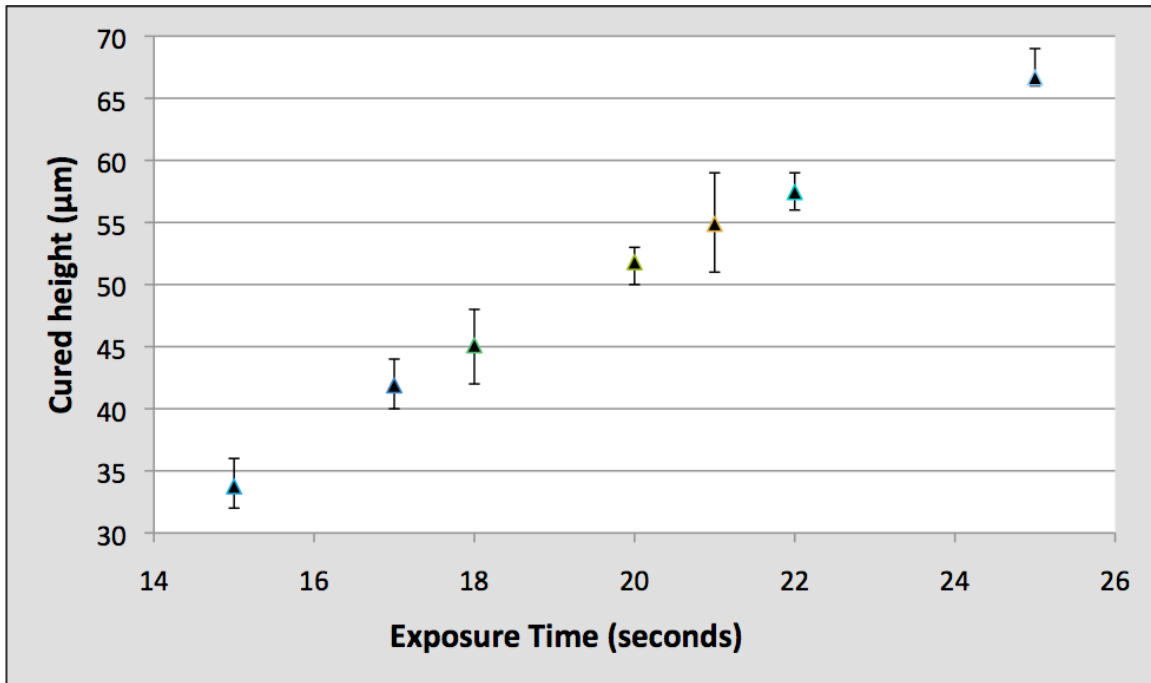


Figure 38 Plot showing the cured part height as a function of exposure time

### 3.5 Chapter summary

This chapter presented the designs of three generations of the EPCL system assembled and installed over the course of this research, highlighting incremental advances from the earlier system. The challenges associated in designing the ECPL system were discussed. A commercial DLP projector was used to provide the DMD chip in the gray-scale ECPL system. The design specifications of this latest gray-scale ECPL system were presented. Preliminary experiments were conducted using the system, which suggested the presence of several noise factors in the fabrication process.

Process variations can be caused due to numerous factors present both during fabrication and during post-processing. To identify the majors factor causing the variations, it is necessary to isolate if the variations in the process are during the



fabrication process or during post-processing. The following chapter will present the design and preliminary results from a novel real-time process monitoring system. This system will be used to identify and eliminate the process variations.

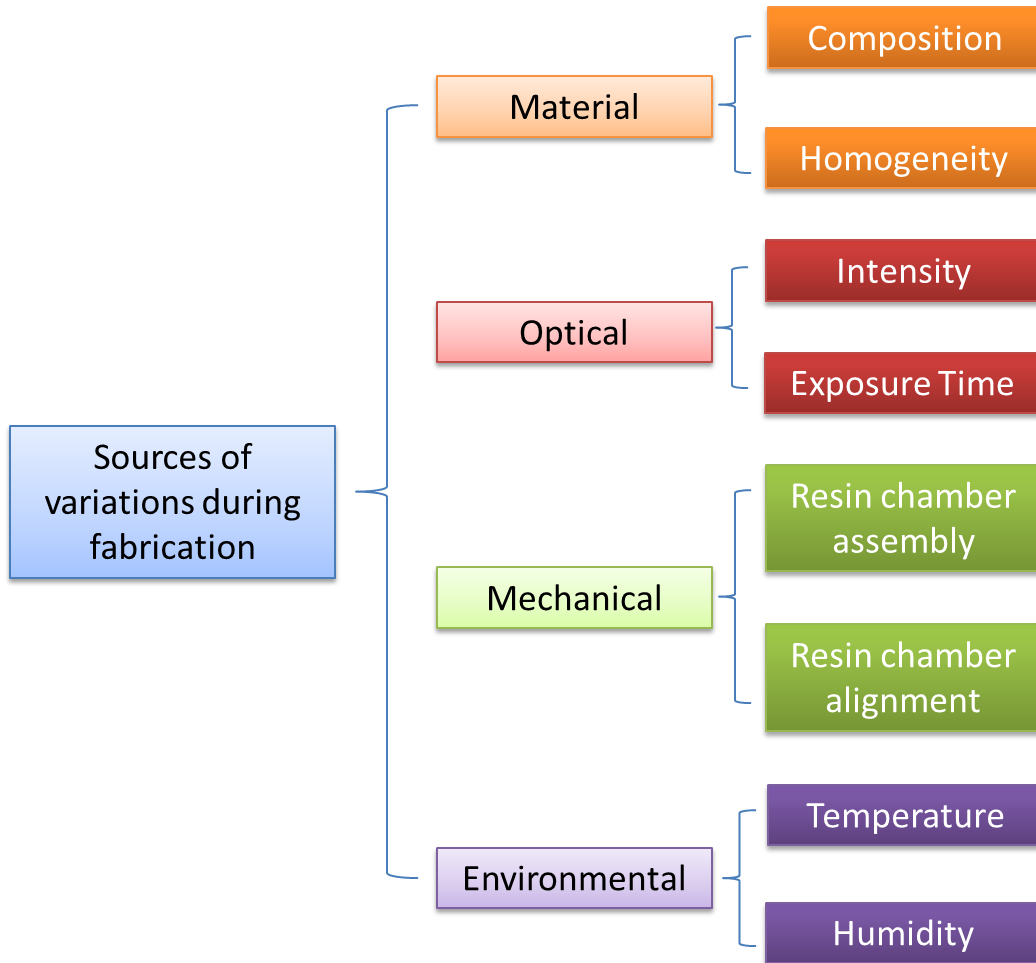
## CHAPTER FOUR

### ECPL PROCESS MONITORING SYSTEM

This chapter presents the design of the novel real time interferometric monitoring system used for the ECPL system. This chapter also presents the first research question and validates its hypothesis.

#### **4.1 Motivation for development of a real-time cure monitor**

The primary reason for implementing a real-time in situ polymerization monitor was to identify if there are inherent variations in the ECPL process, caused during the fabrication process. Another motivation for investigating a real-time in-situ monitoring technique was to be able to conduct metrology during the curing process and quantify the effect of post-processing on the shape and dimensions of the final cured part, resulting from the ECPL process. Figure 39 shows the various sources of errors that can be introduced during the fabrication process.



**Figure 39 Potential causes of variations during fabrication in the ECPL process**

The primary causes of variations can be optical or mechanical. Assuming that the optics is rigidly fixed on the optical table, the optical variations may be caused due to changes in light intensity or improper control of the exposure time. Variations in the light intensity introduced by the UV lamp during curing are possible as the lamp warms during the curing process and ages. The light intensity from the UV lamp source can vary and this can affect the accuracy of the system. The variations in the light intensity can be measured using a UV camera. However, installing and uninstalling a camera at the

substrate can affect the alignment of the system, further accentuating the errors in the fabrication system.

As explained earlier, the exposure times can be controlled by either using the timing control on the UV lamp source or switching the bitmaps using the slide show transition from the Powerpoint® presentation software. The switching time on the DMD™ chip can be set using the Microsoft® Powerpoint® presentation software and is not in complete control of the user. From experimental observations, it was found that the software cannot reliably replicate the slide switching times and the error is around +/-2 seconds. Since the typical curing time for most experiments was 15 seconds, this error would represent variations to the extent of 13% in curing time. Hence, for most of the experiments, we controlled the exposure times using the timing control on the UV lamp source. The minimum resolution for controlling the exposure through the UV light source is 0.1s.

Further study of the process involves development of semi-empirical material models and process planning based on actual curing experiments. If the experimental results have inherent error (due to process variations), these errors will translate into the process plan and can limit the accuracy of the process plan. Hence, it was necessary to develop a real-time monitor of the photo-curing process that could monitor the photopolymerization process in real-time. Ideally, the monitoring system would help visualize the growth of the cured part in real-time. It would also help identify samples, which may not have been properly cured – due to improper location of the resin chamber,

variations in the intensity and time of exposure, improper resin chamber structure. This leads to the first research question:

### **Research Question #1**

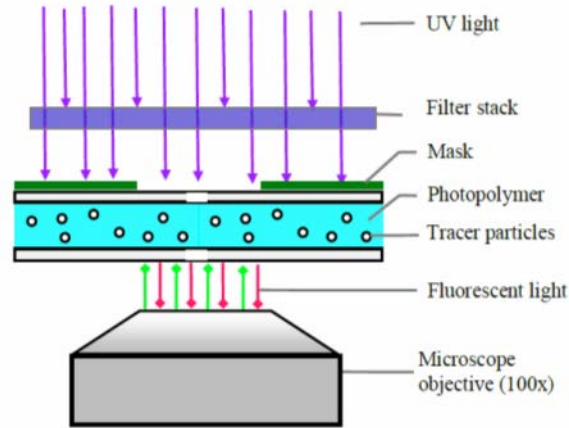
*How to conduct an in-situ real time monitoring of the ECPL process without affecting the fabrication process?*

## **4.2 Existing monitoring techniques**

Several real-time measurement techniques for studying photopolymerization have been explored by past researchers. These techniques differ in a way that they rely on either reaction kinetics (spectroscopy and calorimetry techniques) or the changes in mechanical properties (rheology and interferometry) to monitor the progress of photopolymerization [62-64]. Techniques that rely on reaction kinetics are suitable for estimating the progress of polymerization by estimating the change in the concentration of individual species over time. This method is applicable only for investigating the progress of reaction for an entire volume of the photopolymer resin and thus cannot provide any spatial information.

Microrheology is an extension of rheology at microscopic length scale and it studies the deformation and flow of matter. Microrheology measurements rely on the Brownian motion of micron-sized particles embedded in the sample. By tracking these particles, it is possible to assess the viscoelastic properties of the surrounding medium. Slopek [45, 54] investigated the use of passive microrheology method for monitoring the growth of photopolymerization in real-time. A detailed diagram of the experimental

system is shown in Figure 40. He also showed that by accurate manipulation of the fine focus on the microscope, measurement of polymerization with high spatial resolution could be conducted.



**Figure 40 Schematic of the experimental setup used by Slopek [45]**

The primary advantage of this technique over those based on reaction kinetics is that it can provide one-dimensional spatial information, i.e., it can be used to estimate the time required to obtain a gel at a pre-defined height within the resin chamber. However, this system cannot be used to track the growth of polymerization throughout the entire resin chamber. To use this system, the resin has to be filled with microscopic tracer particles. This is acceptable for lab-based studies of different photopolymer resins. However, in the ECPL system, it is not acceptable to contaminate the resin with any particles, as the final product has to function as an optical element (and embedded particles might cause scattering and hence loss of light).

Interferometry based techniques do not require adding any foreign particles in the resin and is a non-contact real-time monitoring system. Several researchers have

employed interferometry to monitor photopolymerization reactions, using either Michelson [65, 66] or Mach-Zehnder [67, 68] interferometer configurations. However, these systems were used primarily to estimate the distortion due to shrinkage. Moreover, these prior schemes have all used elaborate, delicate optical systems with multiple mirrors and beam-splitters, making them expensive and time-consuming to set up. Nevertheless, the principle of interferometry can be applied towards measuring the progress of photopolymerization by redesigning the resin chamber, such that it only measures the change in material properties due to polymerization and not shrinkage. Another potential benefit of using an interferometric system is that it can be easily extended to investigate the progress of polymerization across the entire irradiated area. Using an interferometric principle for monitoring the progress of photopolymerization has the potential to be used as a true three-dimensional monitoring tool and hence is explored in further depth in the following sections. This leads us to the hypothesis to the research question as...

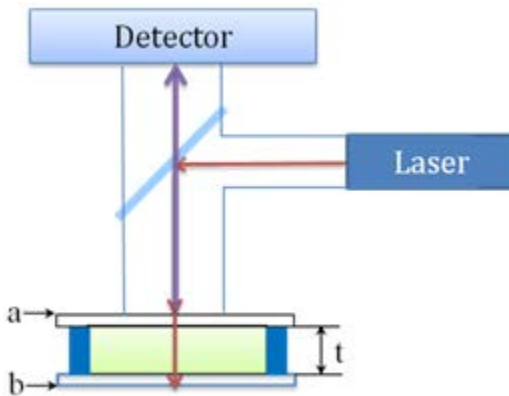
#### **Hypothesis for Research Question #1**

*A system that can track the change in speed of light through a medium can be used to visualize the extent of the polymerization process.*

### **4.3 Theory & Principle of an Interferometric Monitoring System**

The basic principle of the interferometric monitoring system developed in this study is based on the Mach-Zehnder interferometer. A coherent laser beam from a low-power red diode laser (670 nm wavelength) is directed at right angles into the photopolymer resin having a physical thickness  $t$  that is transparent at the wavelength of

the laser. Interference occurs between the light reflecting from the front surface of the sample chamber (a) and the light reflecting from the back surface of the chamber (b) as shown schematically in Figure 41.



**Figure 41 Schematic of the monitoring system based on interferometry**

Depending on the details of the experiment – the wavelength of the laser, the thickness of the material, the refractive index of the material at the wavelength of the laser – the interference can be either constructive, leading to an increase in the intensity of the reflected beam, or destructive, leading to a decrease in the intensity of the reflected beam. If the material being examined is reactive upon UV irradiation, as the photopolymer resins are, the refractive index of the material will increase as density of the resin increases as it polymerizes. The intensity of the reflected laser beam will therefore exhibit a periodic modulation of maxima and minima as the front-surface and back-surface reflections go in and out of phase with one another.



The optical path length of light in any medium is given by:

$$L = nl = nt / \cos \theta \quad (4-1)$$

where  $L$  is the optical path length,  $n$  is the refractive index of the medium through which the light travels,  $l$  is the physical path length of the light in the medium,  $t$  is the physical thickness of the medium, and  $\theta$  is the angle of incidence of the light, as measured from the normal to the plane of the sample. From Figure 41**Error! Reference source not found.**, the total round optical path length resulting from traveling through the top glass slide, reflecting from the bottom glass slide, and traveling back to the top of the top glass slide can be calculated as:

$$L_t = (4n_g t_g + 2n_s t_s) / \cos \theta \quad (4-2)$$

where  $L_t$  is the total optical path length for light travelling though the sample and back.  $n_g$  &  $n_s$  are the refractive indices of glass slide and the sample and  $t_g$  &  $t_s$  are the thicknesses of the glass slides (assuming that thickness of both the top and bottom glass slides are same, which is indeed the case for our experiments) and the thickness of the spacer, respectively (which is the same as the thickness of the photopolymer resin in the sample cell). If the refractive index of the sample material changes during the measurement, as is expected for the photopolymer material being irradiated, the resulting change in the optical thickness of the material is then given by:

$$\Delta L_t = 2\Delta n_s t_s / \cos \theta \quad (4-3)$$

Since the refractive index of the glass slides does not change, this does not contribute to the change in interference condition during the reaction. Moreover, since the laser beam is normally incident on the resin chamber, Eq. 4-13 can be simplified to a good approximation as:

$$\Delta L_t = 2\Delta n_s t_s \quad (4-4)$$

This can be expressed as a fraction of the laser wavelength, or the Wave Shift, by

$$\text{Wave Shift} = \Delta L_t / \lambda \quad (4-5)$$

For our purposes, the direction of the intensity change (increase versus decrease) is unimportant, since each measurement starts at a completely arbitrary reflected intensity and we have no control over the initial interference condition of the front-surface and back surface reflected laser beams.

The overall intensity of the reflected laser beam follows a cosine curve as a function of the Wave Shift, with a maximum intensity when the wave crests of the electric field vectors of the front-surface reflection match up with the wave crests of the electric field vectors of the back-surface reflection, and minimum intensity when the two sets of wave crests are exactly out of phase with one another. It is therefore more useful to express the Wave Shift of Equation 4-5 as a Phase Shift,  $\phi$ , with units of  $2\pi$  radians of phase difference between the wave crests of the two beams.

$$\phi \text{ (radians)} = \frac{2\pi\Delta L_t}{\lambda} = \frac{2\pi(2\Delta n_s t_s)}{\lambda} = \frac{4\pi\Delta n_s t_s}{\lambda} \quad (4-6)$$

In general, for any arbitrary phase shift  $\phi$  (not necessarily a maximum or a

minimum of the reflected laser beam intensity), the refractive index change responsible for the phase shift can be given by:

$$\Delta n_s = \frac{\lambda \phi}{4\pi t_s} \quad (4-7)$$

and for the specific case where  $\lambda = 670 \text{ nm} = 0.670 \text{ microns}$  (for a typical red diode laser),

$$\Delta n_s = 0.053\phi/t_s \quad (4-8)$$

where  $\phi$  is expressed as the measured total number of  $\pi$  radians of phase shift and  $t_s$  is the physical thickness of the photopolymer sample in microns.

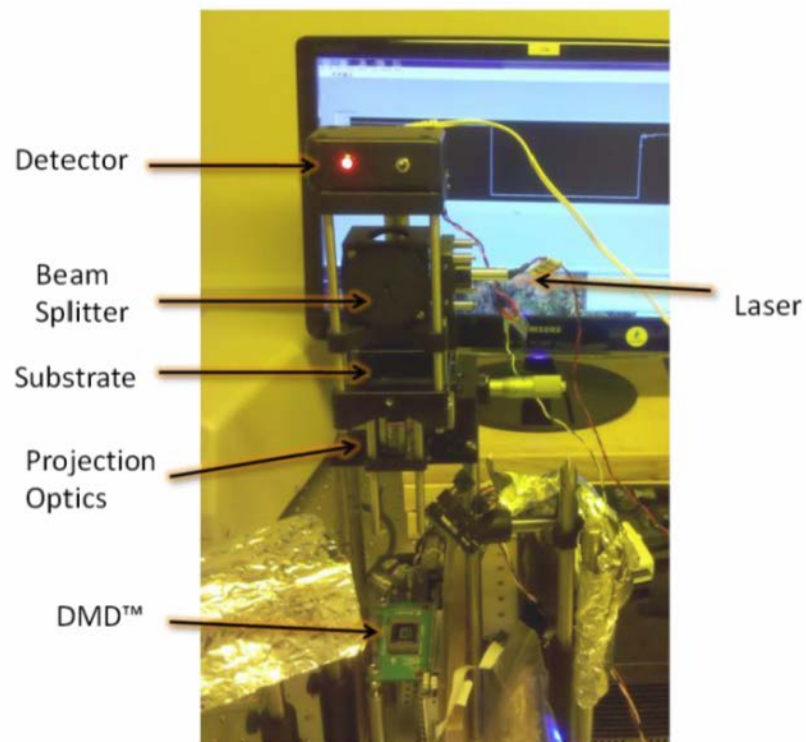
Alternatively, the same relationship can be expressed as:

$$\phi = 18.87\Delta n_s t_s \quad (4-9)$$

We thus find a linear relationship between the total phase shift and the change in the refractive index that occurs during the reaction. Because the photopolymer curing reaction propagates vertically through the resin sample as the irradiation proceeds, the change in refractive index can be attributed to the height of the cured polymer within the resin sample. Thus, the observed phase shift can be used as a direct measure of the height of the cured region of polymer as the reaction proceeds. It is to be noted that this analysis assumes that the physical thickness of the sample chamber does not change during the irradiation. This assumption is appropriate in our case, given the rigidity of the glass slides used to form the sample.

#### 4.4 One dimensional monitoring system design

The ECPL system was augmented with the cure monitoring system based on interferometry, as explained in previous sections. A glass microscope slide inclined at 45 degrees was installed to serve as a beam splitter to direct the laser beam into the sample chamber. A custom-made detector module incorporating a Texas Instruments OPT-101P photodetector chip was used as the detector. The photograph of the assembled system is shown in Figure 42. This chip includes built-in circuitry that enables it to provide a linear voltage output in response to changes in the detected light intensity, making it ideal for our purposes. The output was coupled to a lab computer via a National Instruments A-to-D module.



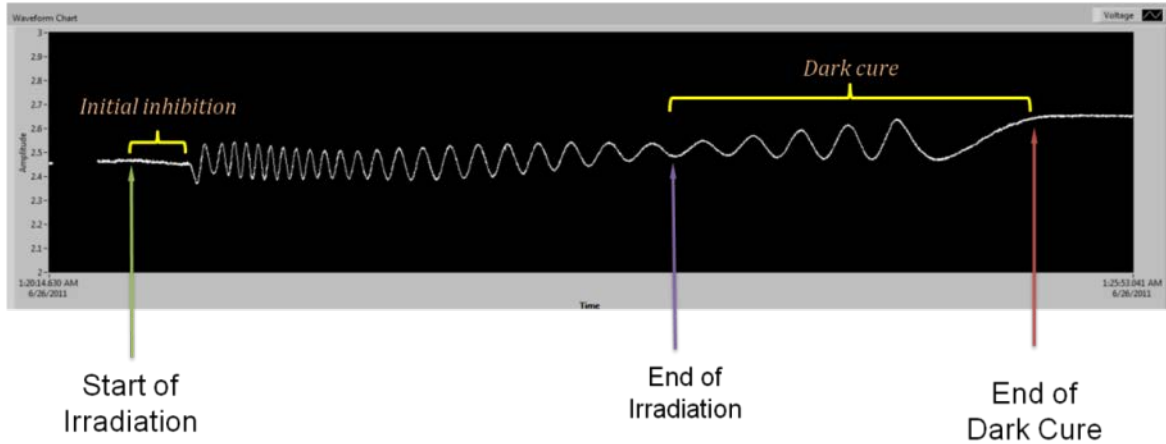
**Figure 42 Photograph showing part of the ECPL system, with the components of the interferometric monitoring system**

#### **4.4.1 Experimental Procedure**

The resin in the reaction chamber was cured by the UV irradiation patterned by the bitmaps on the DMD™. The exposure intensity and time was controlled by directly setting the intensity levels and the shutter time on the UV light source. As specified earlier, a tri-functional acrylate monomer - trimethylolpropane triacrylate (TMPTA, SR-351) obtained from Sartomer was used as obtained, with the photoinitiator 2, 2-dimethoxy-1, 2-diphenylethan-1-one (DMPA, IRGACURE-651) obtained from Ciba Specialty Chemicals, as the resin composition. The DMPA concentration in the monomer was 5% by wt.

#### **4.4.2 Typical Interferogram**

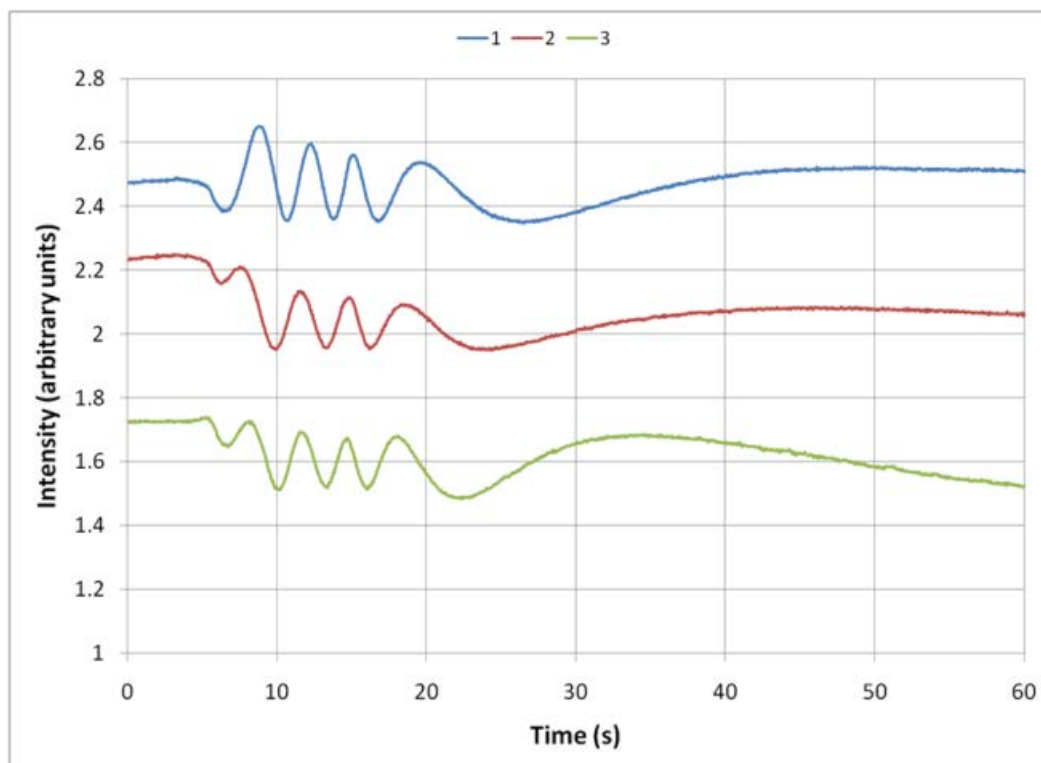
A representative example of the data provided from the interferometric cure monitoring system is shown below in Figure 43 for a 250-micron thick sample. A number of salient features is evident from the figure. An initiation period is clearly visible at the left side of the trace as dissolved oxygen and inhibitors in the photoinitiator are scavenged before the polymerization process can get underway. Then, toward the right side of the trace, a continuing densification that we ascribe to dark reaction is apparent after the irradiation has stopped, followed by eventual equilibration. About 27.5 full oscillations of the intensity are visible, corresponding to a total phase shift of approximately 173 radians. These oscillations are a result of the changes in refractive index as the photopolymer is being cured in height. By monitoring the number of oscillations during the curing process, we can estimate the height of the cured part.



**Figure 43 Results from the one-dimensional interferometric monitoring system for curing a 250 thick sample. Horizontal axis corresponds to timer ad the Y-axis shows the output voltage detected from the photo detector**

#### 4.4.3 Experimental Results

The primary motivation of developing the real-time monitoring system was to identify if there are any process variations present during the curing process. Keeping all control factors constant, several experiments were conducted while recording the signals from the interferometric cure monitoring system. The results from three experiments conducted under identical conditions are shown in three different colors in Figure 44.



**Figure 44 Plot of the intensity signals from the interferometric system obtained by curing three consecutive experiments with same experimental conditions**

It is to be noted that the charts are plotted on arbitrary intensity units and only the number of oscillations in the signal are of importance (the three curves differ somewhat in shape because the initial phase relationship between the front and back reflections differs slightly from sample to sample). The key result is that all the three samples yielded essentially the same number of oscillations, and therefore the same total phase shift and the same overall change in refractive index, over the course of fabrication. Although the signals from the monitoring system are not exactly the same, they do indicate that there is no presence of any significant variation during the polymerization process.

#### **4.5 Development of Post-Processing Method**

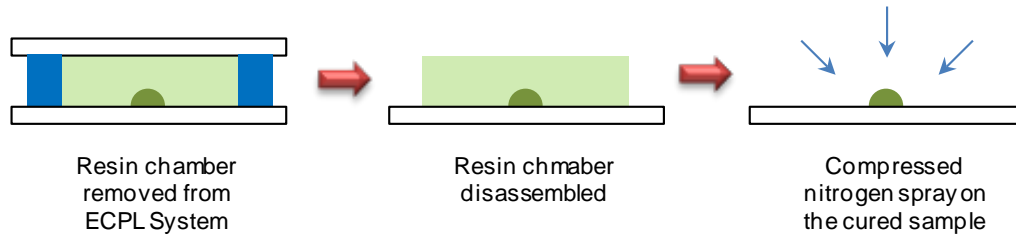
From Figure 44, there is no clear evidence of substantial variations during the fabrication process, which might affect the photopolymerization process. This suggests that the variations in the part dimensions (Figure 38) should be a result of variations in some other step of the ECPL process. It was hypothesized that the washing procedure is primarily responsible for the dimensional variations as observed from experiments.

With reference to Figure 8, after the resin chamber is exposed to the projected pattern from the DMD™, the glass slide from the resin chamber undergoes a washing/developing process. This step is necessary to remove the uncured monomer from the slide and the partially cured sample. The challenge associated with this step lies in precisely differentiating the gel boundary from the uncured monomer. An extremely gentle washing process can lead to traces of uncured monomer lying on the substrate. On the other hand, a harsh washing method can lead to damage of the partially cured gel boundary, thus leading to deteriorated surface finish. The cured part has cross-linked due to irradiation received only from the bottom of the substrate. Hence, the free surface of the sample, which is in contact with the uncured monomer, is in the form of a partially cured gel. It was thus necessary to develop a rigorous washing method to clean the samples after exposure.

Figure 45 shows the existing washing process used to remove the uncured monomer from the slide with the cured sample. After the resin chamber is exposed for the desired exposure time with the bitmap pattern, the chamber is removed from the ECPL system, disassembled and a high-pressure compressed nitrogen gas is used to remove the



uncured monomer from the glass slide and from the cured part. As expected, this harsh washing process can significantly damage the part profile, while also causing sample-to-sample variations.



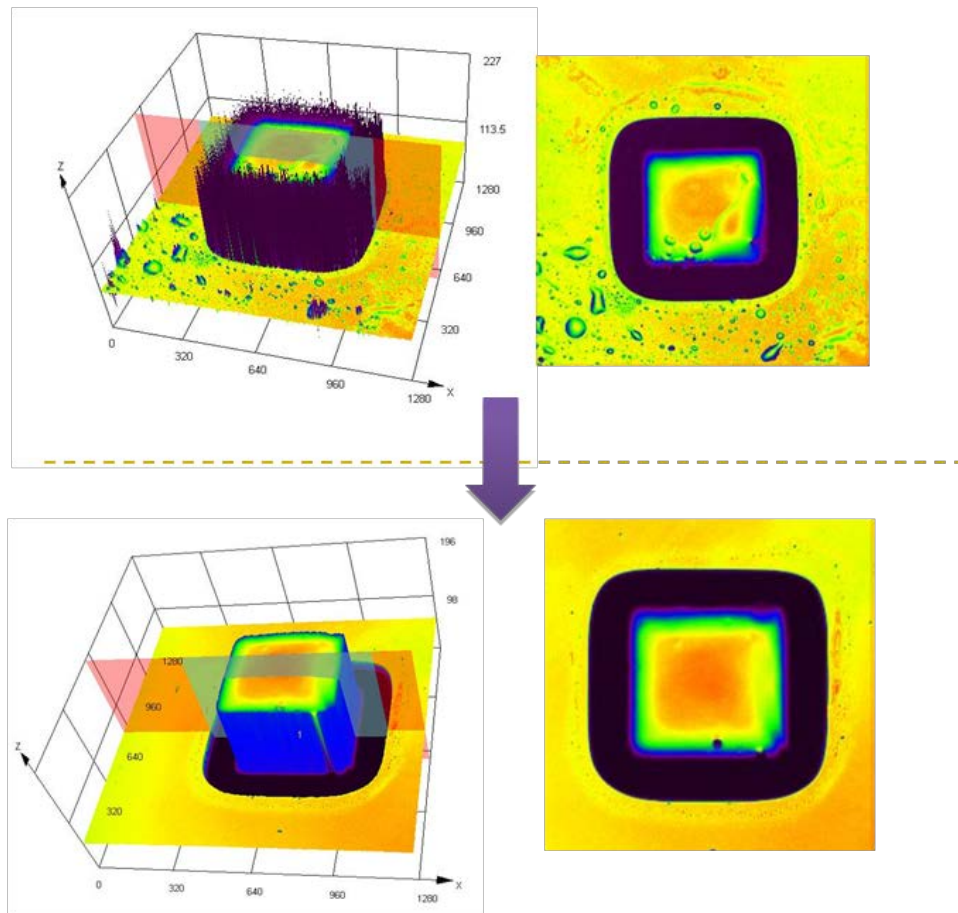
**Figure 45 Schematic of the steps involved in washing process (Dark green region shows cured part, blue arrows indicate the random direction of the compressed nitrogen gas on the cured sample)**

In order to develop a better washing procedure, the following criteria were used in designing a washing protocol:

- The washing protocol should completely remove all traces of monomer from the surface of the substrate/glass slide. This can be tested by inspecting the sample under a microscope.
- The washing protocol should not adversely affect the surface of the cured part. This can be tested by obtaining the surface profile of the cured part, preferably using non-contact metrology methods, like the laser confocal microscope.

To meet the above requirements, we considered using chemical solvents (instead of compressed nitrogen) to clean the cured sample. For a typical stereolithography process, iso-propyl alcohol is used to wash the parts and remove any uncured photopolymer resin. This solvent works well for this application, since the material used in typical stereolithography process is a combination of acrylates and epoxies. However, in our

case, the cured part is fabricated from an acrylic base photopolymer, which does not cross-link densely and hence swells when organic solvents are used. After a certain period, the solvent vaporizes causing the samples to distort and curl. The various solvents tried were water, acetonitrile, hexane, ethyl acetate, ethyl acrylate and a solution of water and soap. Through trial and error, it was found that a solution of water and Triton-X (obtained from The Dow Chemical Company) was most effective in removing all traces of uncured monomer. Figure 46 shows the images of the cured samples obtained from 3D laser confocal microscopy for samples before and after washing.



**Figure 46** Images of cured sample from 3D laser confocal microscopy. Using old method (above) and refined method (below)

Traces of uncured monomer left on the substrate are observed using the older washing method. Moreover, the top cured surface is not flat. By using a refined washing method, there are no traces of uncured monomer on the substrate and the cured surface is relatively clean. The repeatability of the process was tested by fabricating several samples and measuring the cured part profile using a laser confocal microscope. Figure 47 shows the cured part profiles from different samples fabricated by the ECPL system and washed using the refined washing procedure. The maximum variation in part height is  $\pm 1 \mu\text{m}$  for a nominal cured part height of  $120\mu\text{m}$ , which represents a total part height variation of 0.8%.

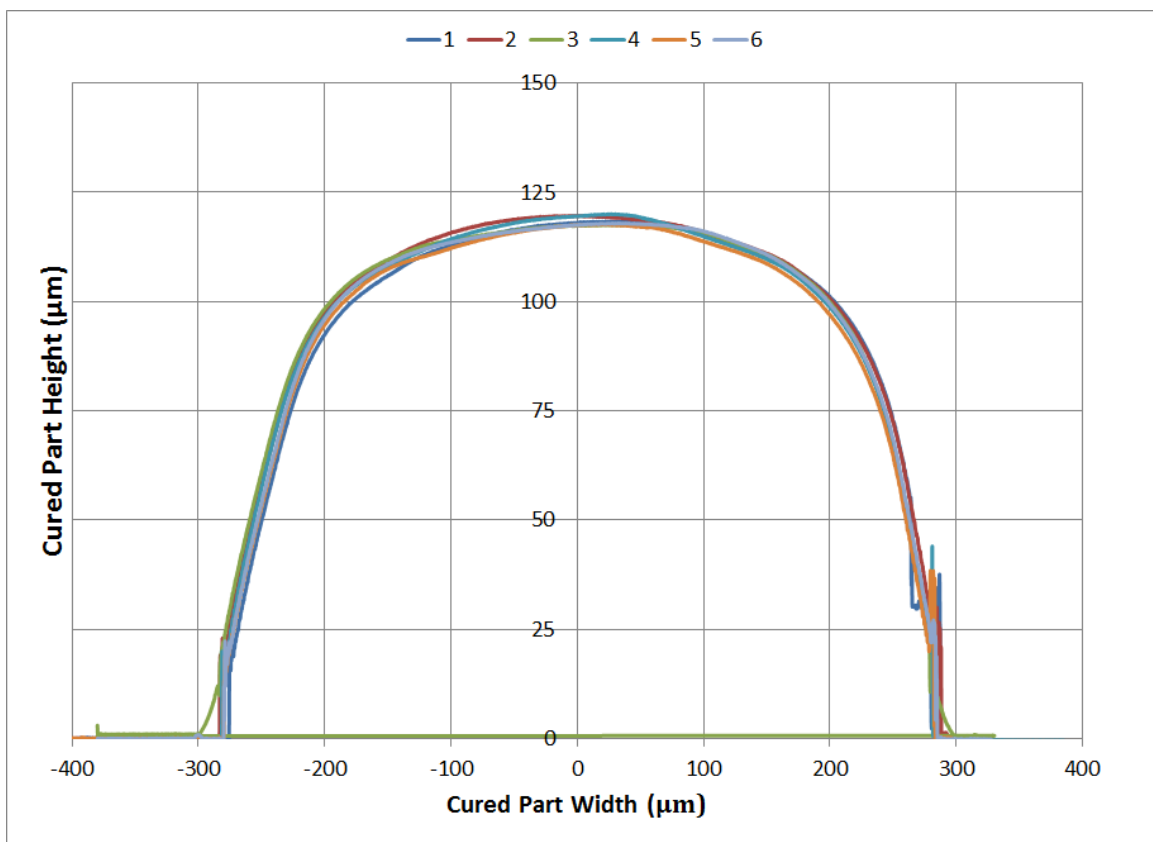
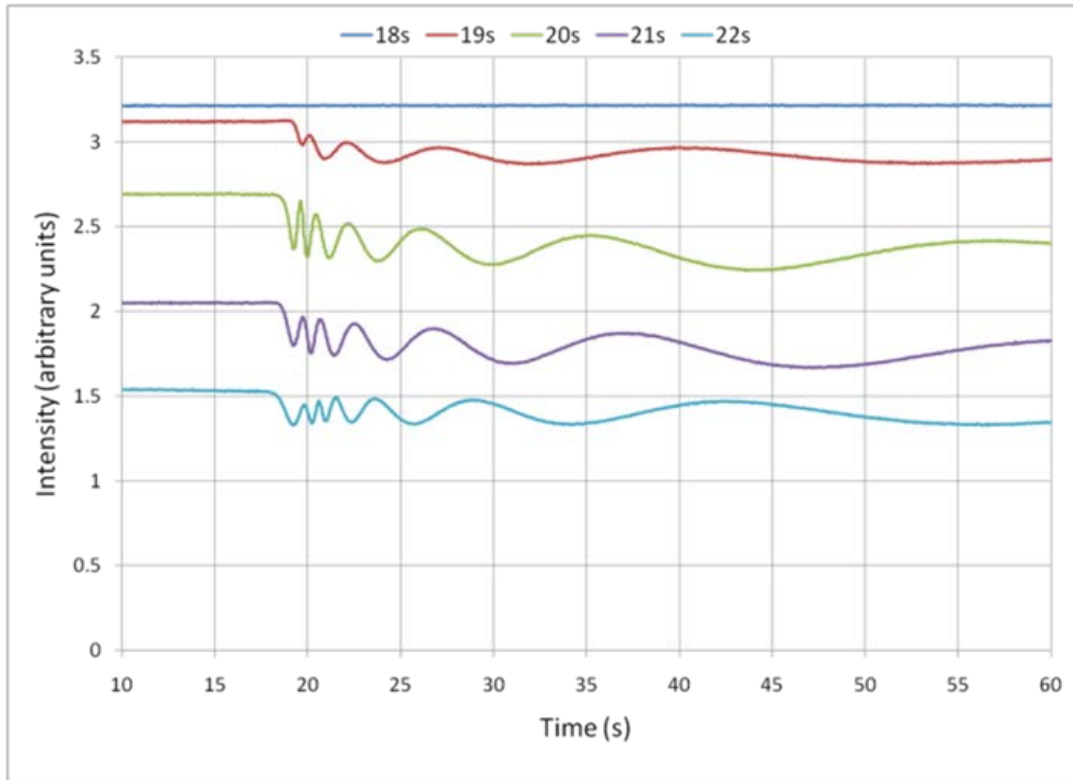


Figure 47 Plot showing superimposed profiles from six discrete experiments

## 4.6 In-situ part height metrology



**Figure 48 Results from the monitoring system based on interferometry (each color represents a specific exposure dose)**

The real-time interferometric cure monitoring system was further used to visualize the photopolymerization reaction and study the polymerization phenomena in detail. Figure 48 shows the result from the monitoring system by varying the exposure dose, by varying the exposure time. It is to be noted that the charts are plotted on arbitrary intensity units and only the number of oscillations in the signal is of importance.

An interesting result of these experiments is that the initial inhibition period of ~19 seconds remains more or less constant under our conditions over the various experiments conducted with the same batch of resin. The number of fringes also increases with increasing total exposure dose, as would be expected from the increased total

densification as the cured part height increases. The intensity of the UV light was around  $1.2\text{W/m}^2$ . Thus, an inhibition of 19s corresponds to the critical energy of  $\sim 2.3\text{mJ/cm}^2$ .

One of the primary objectives for incorporating this live monitoring system was to assist in estimation of the height of the cured part in real time. Figure 49 shows the preliminary correlation that was observed between the measured height of the cured part after washing and flood cure (by confocal microscopy) and the corresponding total phase angle. The errors in the experimental data points along the vertical cured height axis are  $\pm 1\mu\text{m}$ . The errors in the experimental data points along the horizontal axis of measured phase angle were  $\pm 5$  degrees, assuming human error in counting the fringes.

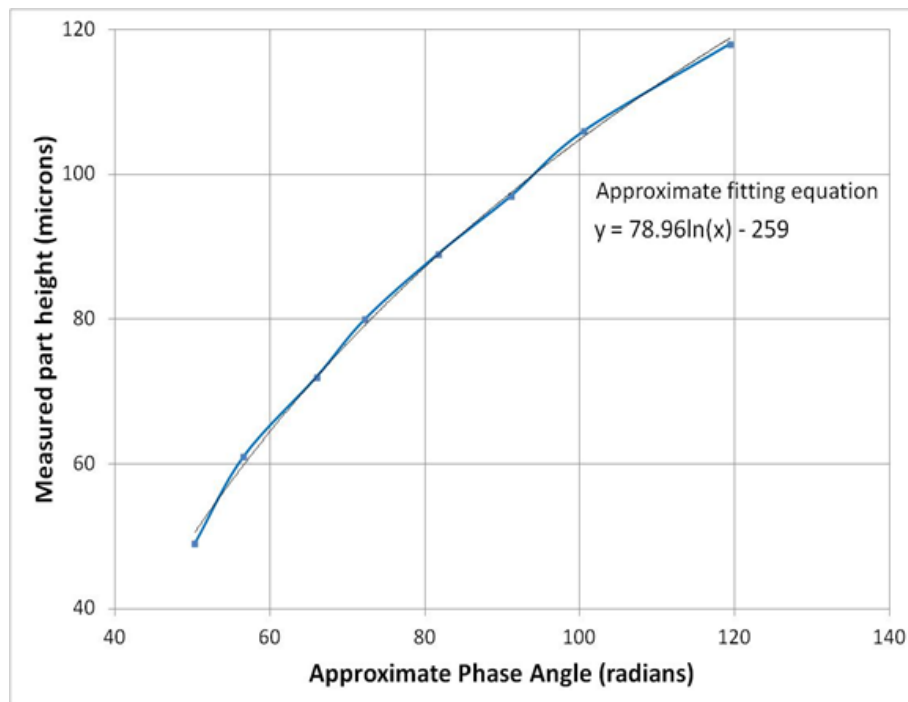


Figure 49 Results showing the height correlation with total phase angle

Blue dots represent average readings of 20 actual experimental data points. It should be noted that the final cured part was washed in an aqueous solution followed by blowing with nitrogen gas and post curing by flood exposure with 365nm light prior to measuring its height. A logarithmic fit was found to match the experimental data points with an R-squared value of 0.9984. The fitting equation describing the relation between the phase angle,  $\phi$  and the measured part height,  $h$  was found to be the following:

$$h = 78.96 \ln(\phi) - 259 \quad (4-10)$$

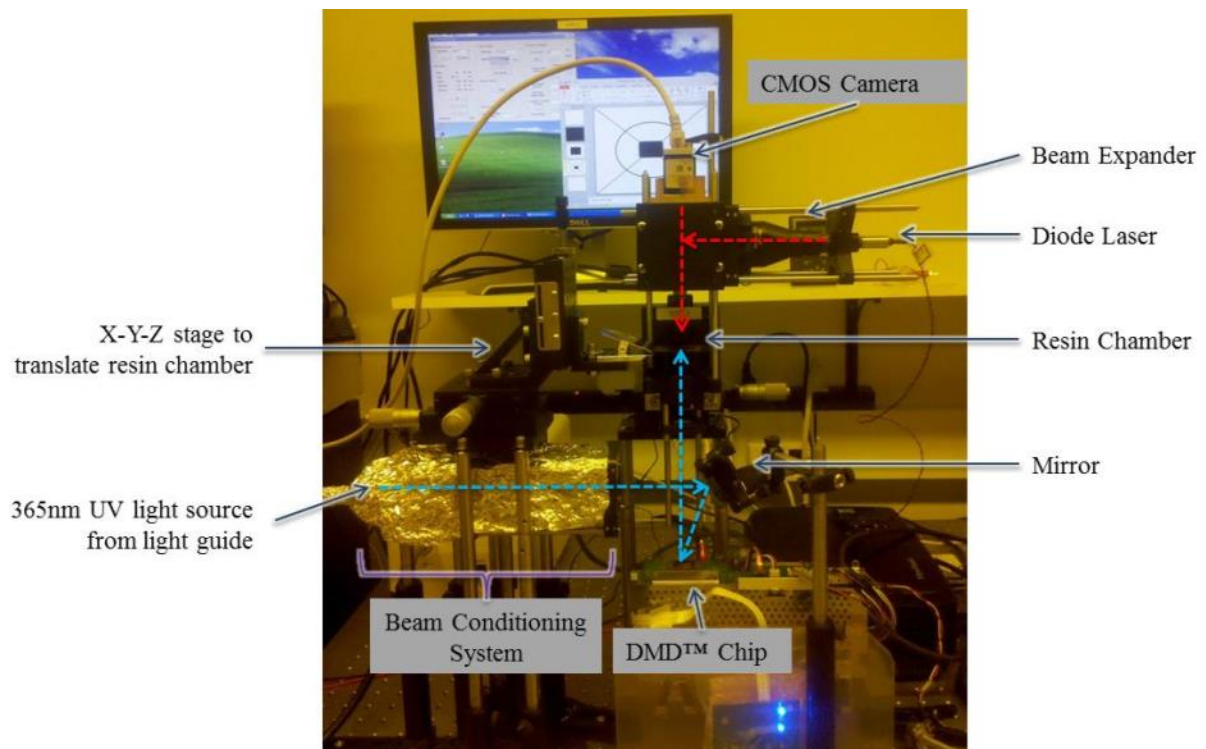
The experimental one-dimensional monitoring system provided results that indicate the capability of the system to monitor the polymerization reaction.

We were interested to learn if the cured part width also varies with the exposure time. The one-dimensional system can be extended such that it can interrogate the polymerization reaction in two-dimensions and this can provide insights into the polymerization process in two dimensions. Hence, the one-dimensional system was modified into a two-dimensional system, which is explained in the following sections.

#### **4.7 Two dimensional monitoring system design**

The ECPL system described in Section 4.4 was modified to incorporate a diode laser (ThorLabs Part # CPS180) with a 5x beam expander (ThorLabs part #BE05M-A), a beam splitter (ThorLabs Part # BSW 16) to direct the laser beam into the sample chamber, and a 5MP CMOS Camera (Basler Ace acA2500-14gm) from Graftek Imaging, Inc.

Figure 50 shows the photograph of the ECPL system with the two-dimensional monitoring system. The dashed blue arrows show the direction of the UV light used to cure the parts and the dashed red arrows show the direction of the laser beam used for real-time interferometric monitoring of the cured part. The laser beam inclines at right angles to its original path when it intersects with a beam splitter (enclosed in a cube component and hence not seen in the photograph).



**Figure 50 Photograph showing the ECPL system with the two-dimensional monitoring system**

A user interface for decoding the data obtained from the camera was developed in National Instruments' LabView Software. The user interface allows the user to save the live video file in .avi format, as well as show the intensity variation of any given pixels in real time. In order to test the utility of the live monitoring system for predicting the part width and height in two-dimensions, the following test was conducted.

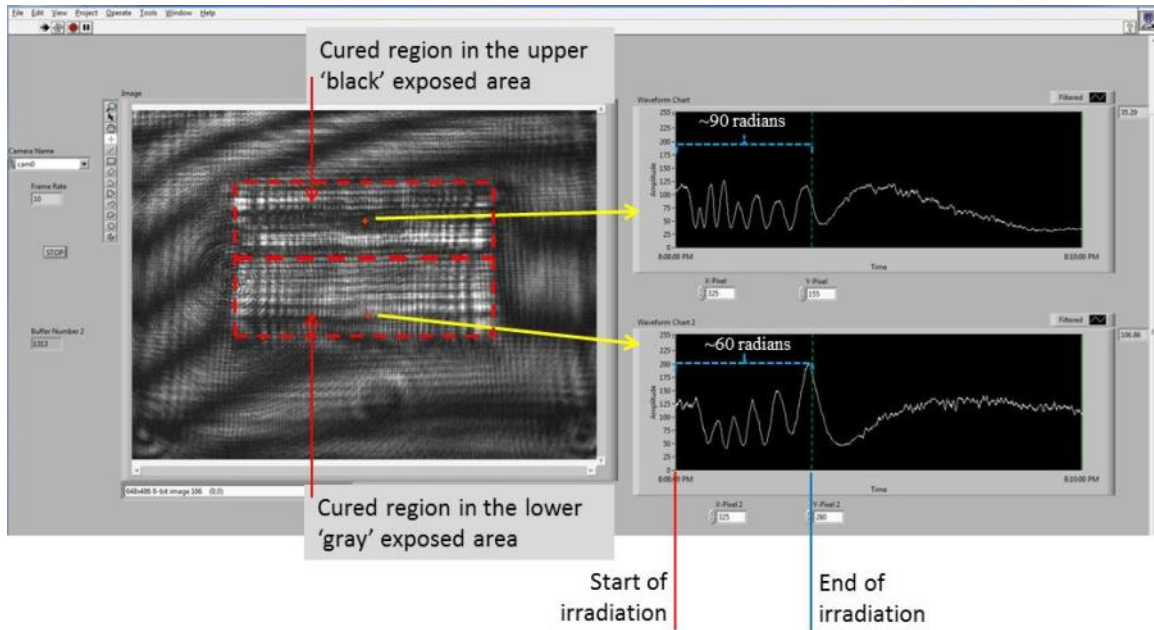
A rectangular part with a stepped intensity profile was cured by projecting a grayscale image on the DMD™, as shown in Figure 51. The top half of the projected image is completely black, whereas the lower half is a shade of gray. The lower gray region results in relatively lower intensity of UV irradiation being projected in the resin chamber.



**Figure 51 Bitmap projected on the DMD**

Figure 52 shows the snapshot from the LabView user interface after curing with the image shown in Figure 51. Pixels under consideration are shown as red colored stars. From Eq. 4.9, it follows that a region exhibiting larger change in refractive index should cause a larger phase shift.

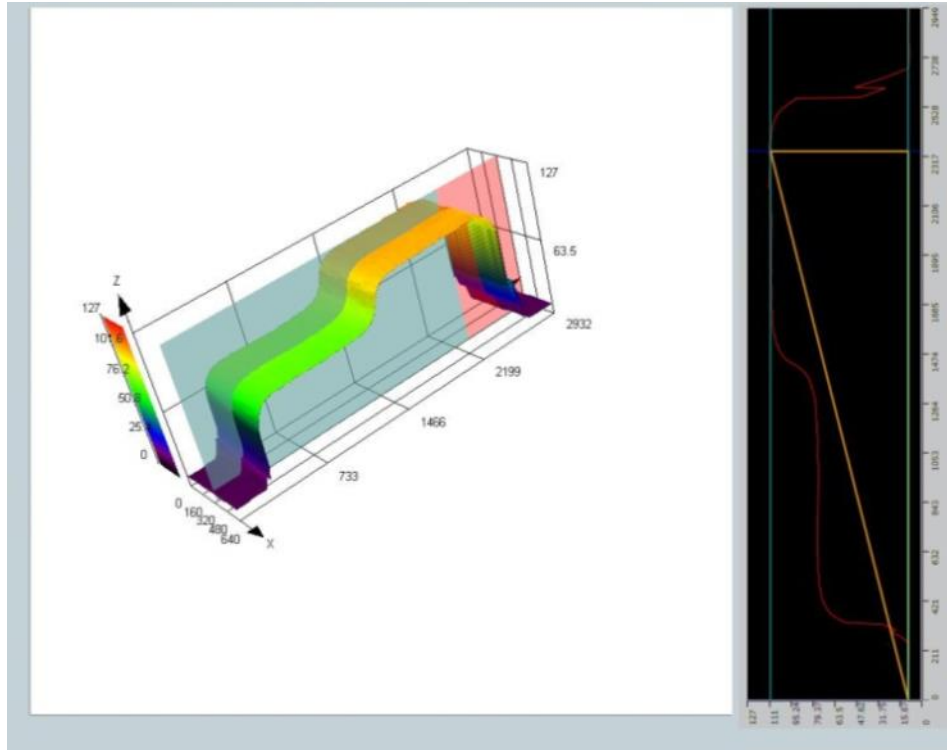




**Figure 52 Snapshot of the user interface developed for 2D monitoring system, showing the results after curing the bitmap with stepped intensity profile**

Since the irradiated intensity is comparatively higher in the top region of the irradiated area, a larger degree of cure is expected and hence a greater change in refractive index. This is confirmed by counting the number of full oscillations from the pixel intensity plots in Figure 52. There are approximately 7 full oscillations for the pixel located in the top region, compared to around 5 oscillations for a pixel in the bottom region; corresponding to approximately 90 radians and 60 radians, respectively.

From the calculated phase angle and Eq. 4-10, we can predict that the height of the part in the upper region (which received higher intensity) should be around  $105\mu\text{m}$  and the height of the part in the lower region (which received lesser intensity) should be around  $64\mu\text{m}$ .



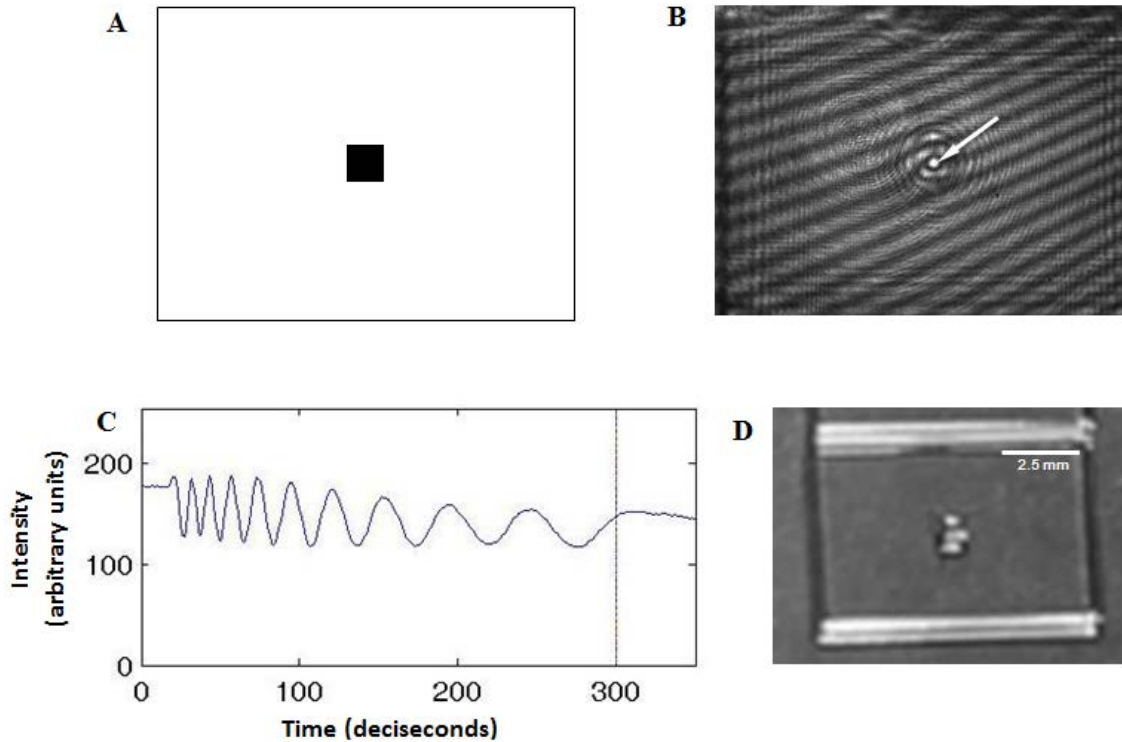
**Figure 53 Results from the confocal microscope for the sample cured with stepped intensity profile**

The cured sample was washed and the height was measured on a 3D confocal microscope. Figure 53 shows a narrow region of the part profile as scanned and measured by the microscope. The height of the upper region of the cured rectangle was found to be around  $100\mu\text{m}$  and the lower region was around  $66\mu\text{m}$ .

#### **4.8 Experimental validation for cure monitoring system**

The laser diode used in the above experiments might have a smaller coherence length than the cell width being studied. It is possible that the observed fringes will be a result of phenomena other than polymerization. Hence, a series of experiments were carried out to confirm that the fringe patterns were in fact due solely to the growth of

photopolymer in the irradiated region and not to other reactions or bulk shrinkage of the sample cell. These results are shown in Figure 54 and Figure 55.



**Figure 54** Cure monitoring of centered bitmap photopolymerization. (A) Bitmap and DMD frame; (B) Two-dimensional cure monitor image showing cured shape in center and location of center pixel monitored for time evolution of polymerization (arrow); (C) Time evolution of small-aperture interference pattern at center pixel during center photopolymerization; (D) Photograph of polymerized shape after washing and flood-cure

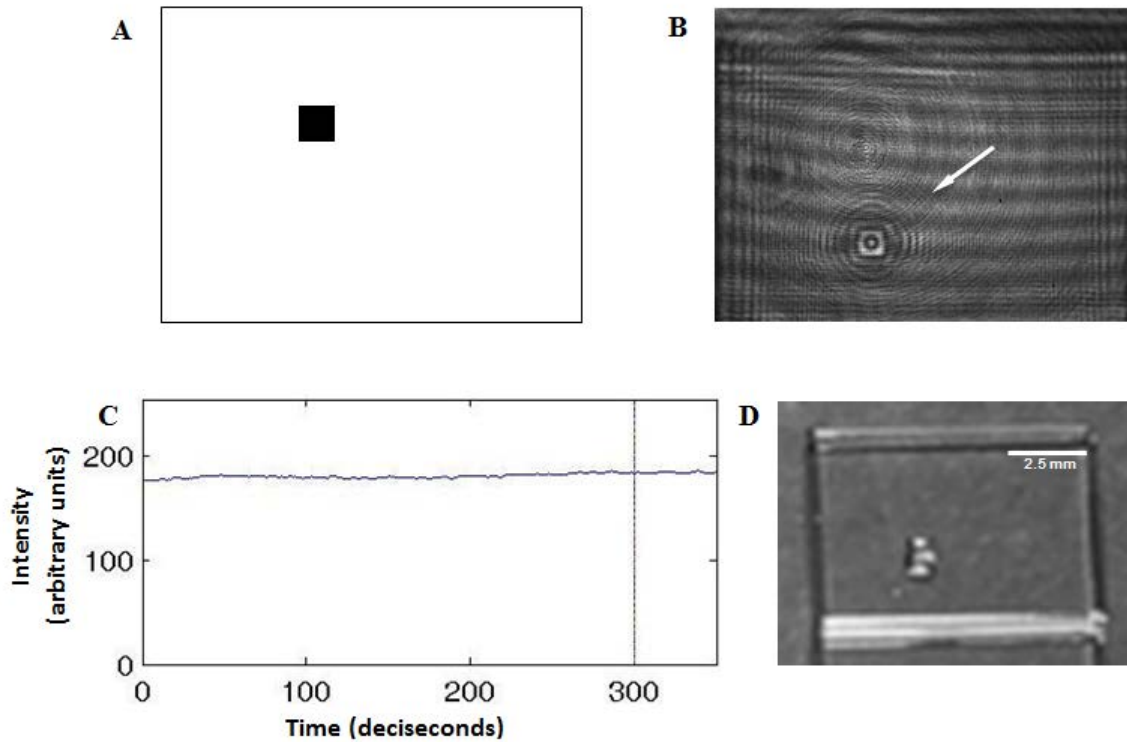
First, a square bitmap was projected into a 250-micron thick sample cell, with the bitmap centered in the DMD™ frame as shown in Figure 54 (A), and irradiated at low irradiance for 300 seconds; this was sufficient to cure the sample to a height of approximately 120 microns, or roughly halfway through the thickness of the cell. With the aperture of the cure monitor fully open, so the beam covered the entire frame of the

irradiated area, the interference pattern shown in Figure 54 (B) was observed at the conclusion of the irradiation. This interference pattern is rather complex, and requires some explanation. The key feature is the nominally square “hump” surrounded by circular fringes in the center of the frame; this is the interference image of the actual cured shape immediately after the irradiation, and it can be seen to grow while the irradiation is in progress. The other, larger circular patterns, and the bold diagonal linear fringes, result from the microscope slides that comprise the sample cell. These features were observed in the two-dimensional cure monitor image of a single fresh microscope slide, due to variations in the thickness of the slide on the scale of the wavelength of light. It is also noted that while two-dimensional cure monitoring is very useful (as shown in Section 4.7) for visualizing the formation of the complete shape in real time, the analysis of the fringe patterns produced is difficult. This is because different parts of the expanded laser beam may be refracted at various angles by the growing polymer shape resulting in interference with the incoming light.

Hence, to monitor the time evolution of the growing part, a single pixel in the center of the frame (indicated by the arrow in Figure 54 (B)) was chosen. The cell was moved laterally to expose a fresh region of resin, and the irradiation was repeated with the beam aperture closed down to produce a laser spot only a few millimeters in diameter. This produced the clean fringe pattern shown in Figure 54 (C), clearly reflecting the growth of the polymer as a function of irradiation time.

The same cell was then translated again to expose a fresh region of resin, the beam aperture was again opened fully, and the irradiation was carried out exactly as

before but with a new bitmap that was positioned off-center, as shown in Figure 55 (A) and (B). (With the configuration of the optical projection system used in this research, the inverted image of the DMD™ chip is projected into the sample cell, so the square at upper left in the bitmap results in curing a square at lower left in the resin.)



**Figure 55** Cure monitoring of off-center bitmap photopolymerization. (A) Bitmap and DMD frame; (B) Two-dimensional ICM image showing cured shape at lower left and location of center pixel monitored for time evolution of polymerization (arrow); (C) Time evolution of small-aperture interference pattern at center pixel during off-center photopolymerization; (D) Photograph of polymerized shape after washing and flood-cure

The cell was then again translated laterally, the beam aperture was again closed down *without moving the laser beam from the center of the sample*, and the off-center bitmap irradiation was again carried out while we monitored *the same center pixel that*

*had been used before* (at the arrow in Figure 55 (B)). Even though the irradiation clearly results in polymerization, as shown by Figure 55 (B), Figure 55 (C) shows that no fringes whatsoever appear in the center of the frame, only a few millimeters away. This demonstrates convincingly that in the developed cure monitoring system, under the presented conditions, there is no bulk shrinkage of the resin in the sample cell, and that the interference fringes we observe result *only* from the growth of polymer in the irradiated regions.

Finally, the cell was dismantled, unreacted resin was removed by washing, and the cured shapes were subjected to an overall flood cure at 365 nm to fully harden them. The center and off-center shapes are shown in Figure 54 (D) and Figure 55 (D), respectively (the cured parts are difficult to photograph because they are transparent, and are shown here at an oblique angle that also shows some reflections from the tops and sides). The salient point is that these photographs clearly show that polymer has been formed exactly where the two-dimensional cure monitoring images show that curing has occurred, and that interference fringes develop over time only in the regions where polymerization is occurring and nowhere else in the frame of the DMD.

#### **4.8.1 Current limitations of the monitoring system**

Ideally, the real-time monitoring system could be used to track the height of the cured part in real time. This system may be used to directly control the process in real-time. However, with the current state of development, there are some inherent limitations of this system. Although the experimental height measurements closely match predictions from the monitoring system, there are minor deviations observed. These deviations can

be attributed to the approximate measurement of the phase angle. It is recommended that future work be conducted towards developing an automated reliable method to calculate the phase angle from the interferometric monitoring system.

Secondly, the monitoring system cannot accurately estimate the width of the cured sample. With reference to Figure 52, we observed stray fringes even in regions outside of the cured region (shown in dashed red line). This might be due to multiple internal reflections from the two slides of the resin chamber. The resin chamber needs to be precisely assembled to avoid multiple internal reflections from the two slides of the resin chamber. This can be avoided by ensuring that the two glass slides enclosing the resin chamber are maintained parallel to each other. Moreover, the cured part itself might cause distortion of light. Further research will be necessary to identify these factors, quantify their effect and develop a better monitoring system, which may help in providing direct feedback control to the process.

#### **4.9 Chapter summary**

The ECPL system, as designed, was prone to fabrication errors. To identify the source of these errors, a real-time monitoring system was developed. The first research question was studied and the hypothesis was validated that an interferometric system can be used to monitor the polymerization process in real-time in the ECPL process. The ECPL system was augmented with this in-situ real-time monitoring system. This monitoring system helped to confirm that the sources of variations are present in the post-processing step. The post-process was experimentally improved, which reduced the overall variations in the ECPL system to less than 1%. It was found that although the

interferometric monitoring system could predict the part heights, it cannot be yet used to determine the width or the three dimensional profile of the cured part. Further research is recommended to extend the application of this monitoring system to assist in feedback control of the system.

In order to control the fabrication process, it is necessary to identify the factors contributing to the shape of the cured part, not just the height. The next chapter presents the ECPL process model and presents a qualitative overview of the factors affecting the shape of the cured part.



## CHAPTER FIVE

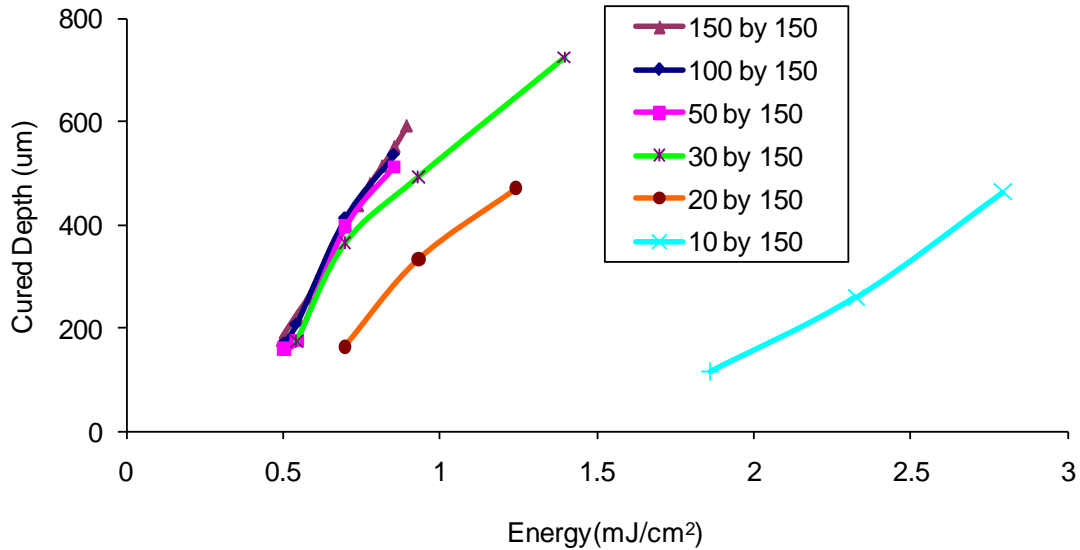
### ECPL PROCESS MODEL

It is reasonable to assume that the photopolymerization process is primarily responsible for the generation of the cured shape in the ECPL process. However, in the ECPL process, the cured part is not considered a final product until it undergoes intermediate processing (like washing and post-processing). These processes can significantly alter the shape and dimensions of the cured part, so, it is necessary to identify and quantify the effects of these processes on the shape of the cured part. If the intermediate processes cause a significant effect on the shape of the cured part, then their influence must be incorporated in the process plan. This chapter presents the overall system model to identify the sources of variations. Experimental and simulation approaches are then presented to quantify the potential factors, which may affect the shape and dimensions of the final cured part.

#### 5.1 Introduction

Experiments were conducted to explore the effect of oxygen diffusion and it was found that the cured height is not only dependent on the exposure on the resin; it is also dependent on the area on which the resin receives irradiation. In other words, the cure depth is dependent on both the exposure energy and the size of the bitmap displayed on DMD. Figure 56 shows the working curves for PEGDA hydrogel using varying rectangular bitmaps, whose sizes range from 150 by 150 to 10 by 150 pixels. It is evident

that the cured depth seems to vary with the bitmap size. With the same exposure, the large bitmap yields large cured depth.

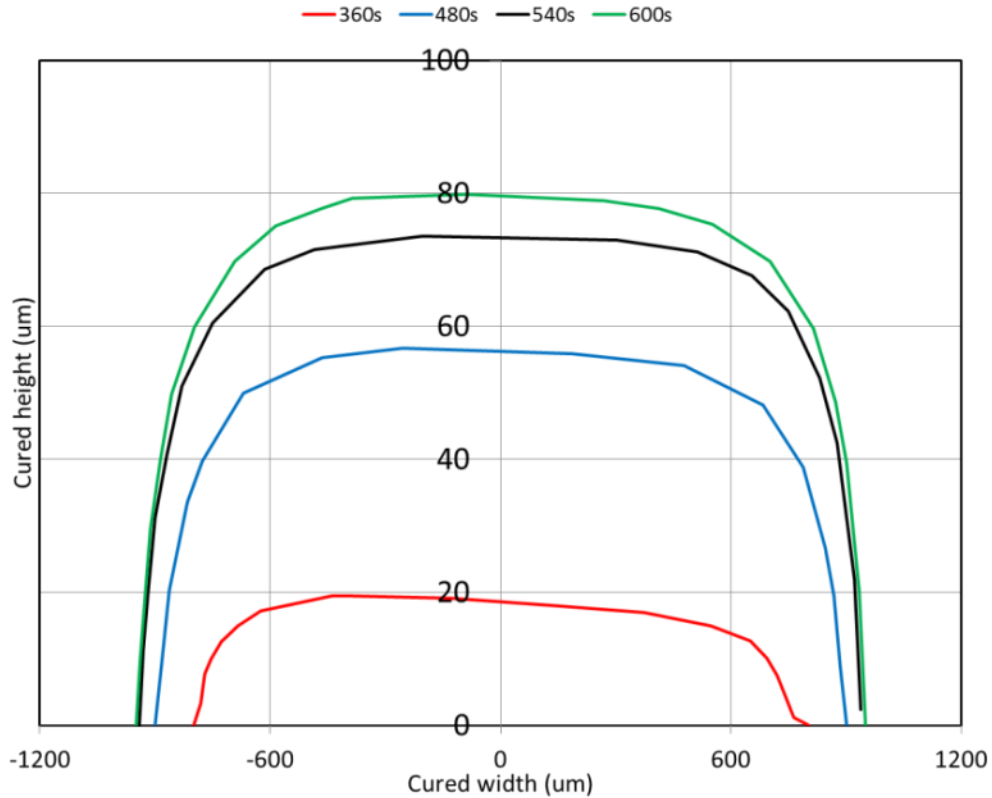


**Figure 56 Working Curves for PEGDA hydrogel using varying shapes of bitmaps**

It is clear that there is a need for better models to predict the shape and size of the parts resulting from the ECPL system. These models could then be incorporated in developing a process plan to fabricate samples of desired geometry.

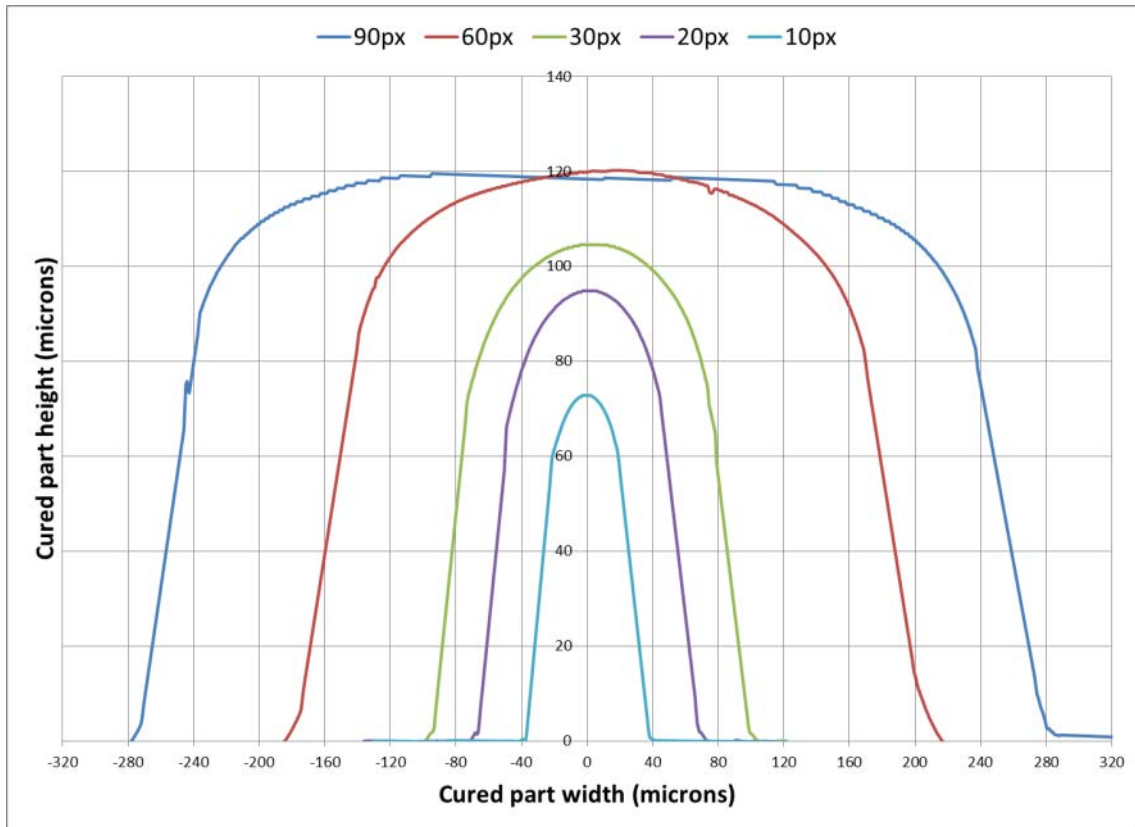
Additional experiments were also conducted to quantify the shape of the cured part for a pre-defined constant bitmap size. Figure 57 shows the cured part profiles resulting from the ECPL system for different exposure times. The photopolymer composition as described in section 4.4.1 (TMPTA with 5wt% DMPA) was used. The total exposed region was 2 mm. It can be seen that the cured parts exhibit a strong curvature at the edges and that the width increases as the exposure time is increased. This further suggests that greater oxygen inhibition at the edges might be a factor causing the

shape of the cured parts to vary with exposure time. It might also be that post-processing influences the shape of the final cured part resulting from the ECPL process.



**Figure 57 Experimental results showing the cured part profiles for different exposure times**

Figure 58 shows the cross-sectional profile of the cured parts as obtained from 3D laser confocal microscopy. The different profiles are generated by curing lines of varying widths projected on the DMD chip. In the legend, 'px' refers to the number of micromirrors (pixels) switched ON the DMD. The images were centrally placed on the Microsoft Powerpoint® presentation software. All samples were exposed at the same intensity for an exposure time of 30s. Figure 58 suggests that the height of the cured part gradually decreases as the overall projected image size is reduced.



**Figure 58 Cured part profiles obtained by varying exposed line widths**

The above observations suggest that there might be several factors influencing the shape of the cured part and these have to be investigated in order to develop reliable models and process planning algorithm. This leads us to the second research question...

### **Research Question #2**

*What factors influence the generation of final shape/geometry of the cured part in the ECPL process?*

The following sections of this chapter will present the hypothesis and validate it using simulations and experiments.

## 5.2 ECPL process model

In order to study the ECPL fabrication system, a simplified process model for curing a part in the ECPL system is presented in the form of discrete phases in Figure 59. The three phases involved in obtaining a finished product from the ECPL system are, 1.) Apply Energy; 2.) Process and 3.) Post-Process.

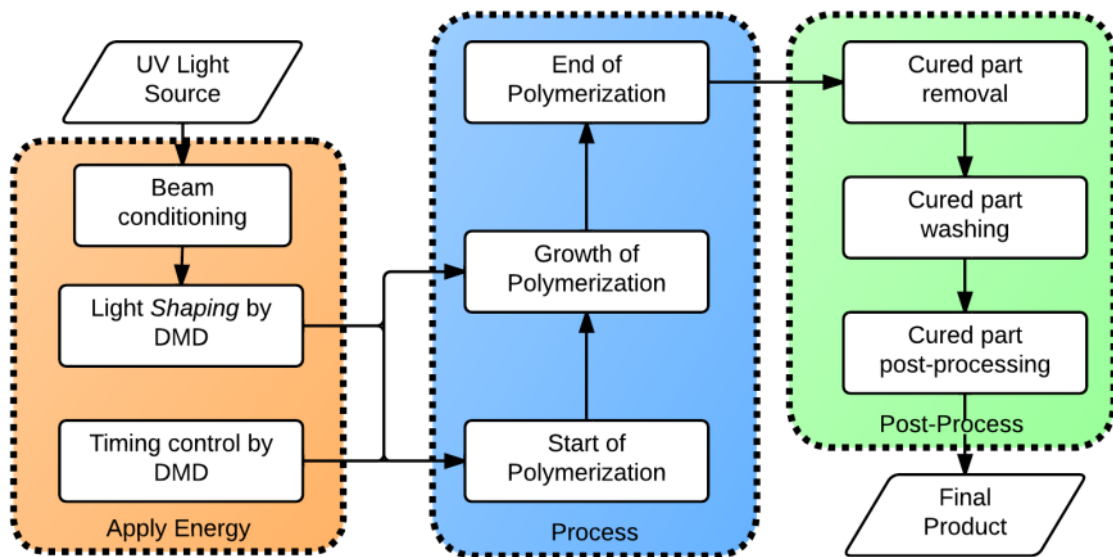


Figure 59 Block diagram of the ECPL Process Model

With reference to Figure 59, the 'Apply Energy' phase represents the manipulation of light source from the blocks shown as 'UV source' to the 'Resin chamber' in Figure 8. In this phase, the intensity of light ( $\text{mW}/\text{cm}^2$ ) is governed by the light source, the light beam is patterned by the DMD<sup>TM</sup> chip in form of bitmaps and the timing controls is achieved by switching the bitmaps on or off, also by the DMD<sup>TM</sup> chip itself. As presented in Chapter 3, the beam was found to be homogenous within  $\pm 5\%$  and will be assumed to be homogenous for further research in this thesis.

The 'Process' phase primarily includes the photopolymerization process. This process is split in 3 sub-phases to explain the nature of complex phenomena occurring during polymerization. The start of the polymerization reaction obviously depends on the input beam shape and the time during which the bitmap is switched on. However, the growth of polymerization does not only depend on the supply of energy, but also on the previously cured part shape. The energy to cure deeper depths has to penetrate through the already polymerized region into the liquid resin. Light may undergo self-focusing as it continues to cure deeper into the sample. Moreover, light characteristics might vary as it travels from the cured region into the uncured region. As explained in Chapter 4 and shown in Figure 43, the polymerization reaction can continue even after the input light energy is switched off. This continual reaction is referred to as the dark reaction and is crucial to account for this process for achieving precise control over the polymerization process.

The 'Post-Process' phase is the phase after which the cured part transforms into a finished product. The cured part is submerged within uncured resin in the resin chamber. The uncured resin is removed; the part is gently washed and post-cured. Figure 38 showed how using a traditional washing process can adversely affect the overall part dimensions. The washing process was then developed in Section 4.5, resulting in a high degree of repeatability as shown in Figure 47. Despite all these prior efforts, it is unclear if the part actually undergoes any modification during the washing process.

From the above analysis, we may conclude that the shape of the final product is a result of the transient polymerization process controlled by the light conditions, and the

washing process. Identification of contributions from each of these factors is necessary for reliable process modeling and eventual process planning. Each of the three phases shown in Figure 59 will be studied in greater depth in the following Section.

### **5.3 Phase - I: Apply energy**

The UV light energy is the primary source of energy to the ECPL process. The total amount of energy input into the process is controlled in both space and time. The exposure time is set on the UV lamp and bitmaps projected on the DMD control the exposure spatially. The total amount of UV energy incident per unit area is referred as exposure (units of energy/area). Incident light energy is a product of irradiation (light energy / unit area / unit time) and time. For a constant exposure time, the distribution of irradiance at the substrate level will govern the total dose of energy provided to the resin. Hence, it is necessary to find a relationship between the irradiance distribution on the DMD chip and the substrate of the resin chamber. The only optical element present between the DMD chip and the resin substrate is the projection system, which magnifies or reduces the image of the micromirrors. The following section presents how optical ray tracing was used to develop an irradiance model.

#### **5.3.1 Irradiance model**

The irradiance model models the irradiance received by the resin in terms of the process parameters. The irradiance distribution on the resin depends upon the power distribution across the light beam incident on the bitmap and upon the optical aberrations caused by the imaging lens. The ray tracing method is adopted from Limaye & Rosen

[42]. Figure 60 shows the schematic of the ray-tracing algorithm for projection of light rays from the DMD onto the flat substrate.

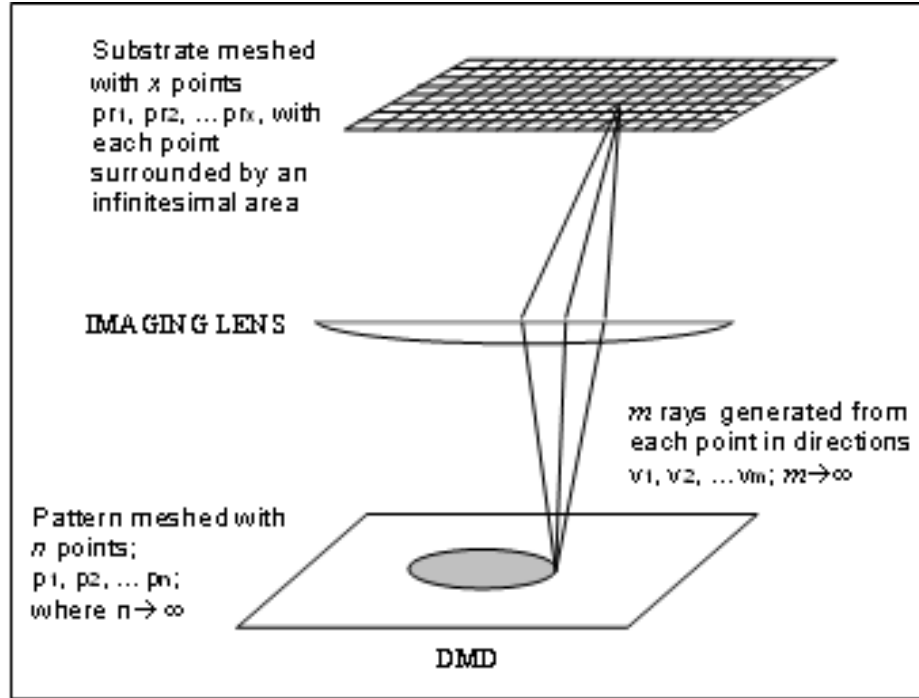


Figure 60 Schematic of ray tracing algorithm [42]

The irradiance distribution across the beam incident on the DMD is assumed uniform and the value is measured using a radiometer. This irradiance is one of the inputs to the irradiance model.

The irradiance,  $H(pr_i)$  at a point at the resin substrate can be given by:

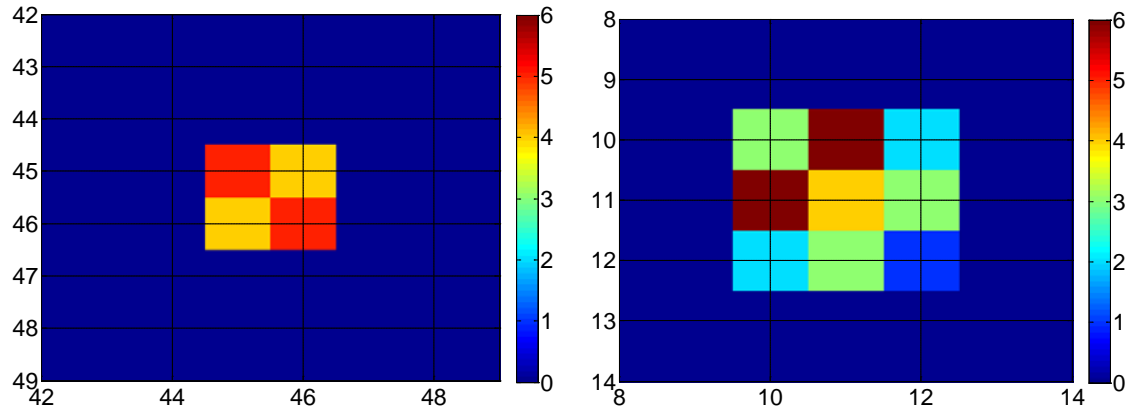
$$H(pr_i) = c \sum_{j=1}^n \sum_{k=1}^m \delta(p_j, v_k, pr_i) \quad (5-1)$$

where  $c$  is the power of single ray and is constant.  $\delta$  is a function introduced to evaluate whether a particular ray will strike an infinitesimal area centered on a given point on the



resin or not.  $p_i$  corresponds to the number of points:  $p_1, p_2, \dots, p_n$ , where  $n \rightarrow \infty$  on the DMD.  $v_k$  ( $v_1, v_2, \dots, v_m$ , where  $m \rightarrow \infty$ ) represents the direction vector in which the rays are emitted from the point on the DMD and  $pr_i$  ( $pr_1, pr_2, \dots, pr_x$ , where  $x \rightarrow \infty$ ) is a point on the substrate. Rays of light emerging from the DMD<sup>TM</sup> chip showed divergence with a half cone angle of 0.75 degrees. This angle was measured by measuring the width of the fluorescence on a blank white paper placed at several distances from the DMD<sup>TM</sup> chip. To take into account the effect of this minor divergence, a cone of rays is emitted from each pattern point.

In effect, the irradiance model helps estimate the effect of optical aberrations in the projection system. The irradiance model was simulated in MATLAB®. Individual micromirrors can be simulated as turned ON or OFF and the irradiance produced by them at the resin substrate can be estimated. For the sake of simulations, each micromirror was discretized into a matrix of 3 x 3 points, whereas the resin substrate was discretized into a mesh of 901 x 901 pixels each spaced 1  $\mu\text{m}$  apart. Figure 61 shows the irradiance produced by the micromirrors placed at the center and the edge after resampling the data with pixel size of 10  $\mu\text{m}$  with nearest neighbor interpolation method (for sake of figure clarity). The effects of spherical aberrations can be clearly observed from these charts.



**Figure 61 Irradiance produced at the resin substrate by switching a single micromirror. a) Central Micromirror switched on; b) Edge Micromirror switched on**

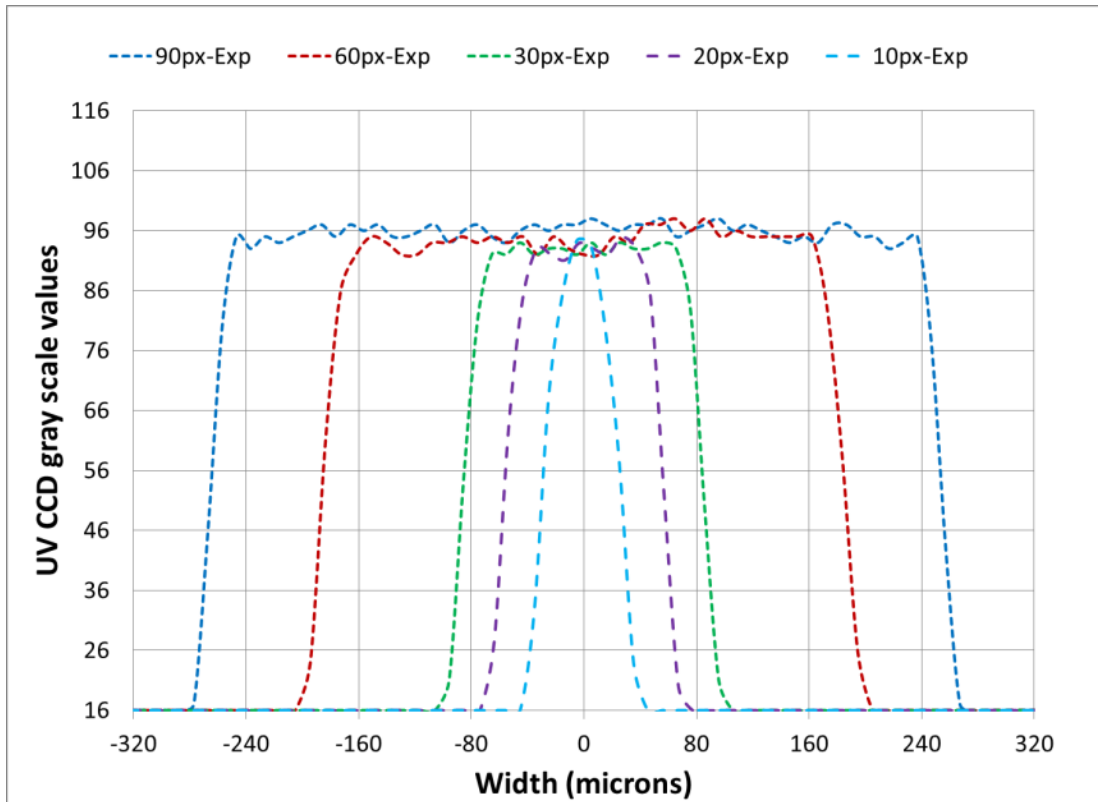
### 5.3.2 Calculation of single ray power

The constant,  $c$  in Eq. 4-11, power of a single ray, is obtained as follows. A radiometer, similar to the one shown in Figure 31, can measure the average irradiance of a beam in the units of  $\text{mW}/\text{cm}^2$ . Assume the average irradiance to be  $H_{avg}$  ( $\text{mW}/\text{cm}^2$ ). The number of rays striking a unit area on the resin substrate can be estimated by using the Irradiance Database, obtained by optical ray tracing. Assuming this number of rays to be  $N_{avg}$  ( $\text{cm}^2$ )<sup>-1</sup>, the constant, ' $c$ ' can be determined to be  $H_{avg}/N_{avg}$  ( $\text{mW}$ ). The Irradiance model was simulated in MATLAB® and 11104821 number of rays were calculated to hit the resin substrate over an area of approximately  $720 \mu\text{m} \times 720 \mu\text{m}$ . The average irradiance measured from the radiometer at the substrate level was  $0.8\text{mW}/\text{cm}^2$ . Thus, the power of a single ray,  $c$  is estimated as  $3.7179 \times 10^{-10} \text{mW}$ .

### 5.3.3 Experimental validation

A UV camera (with specifications listed in Table 3) was placed at the resin substrate level. The averaged exposure profiles as captured from the UV-CCD camera by

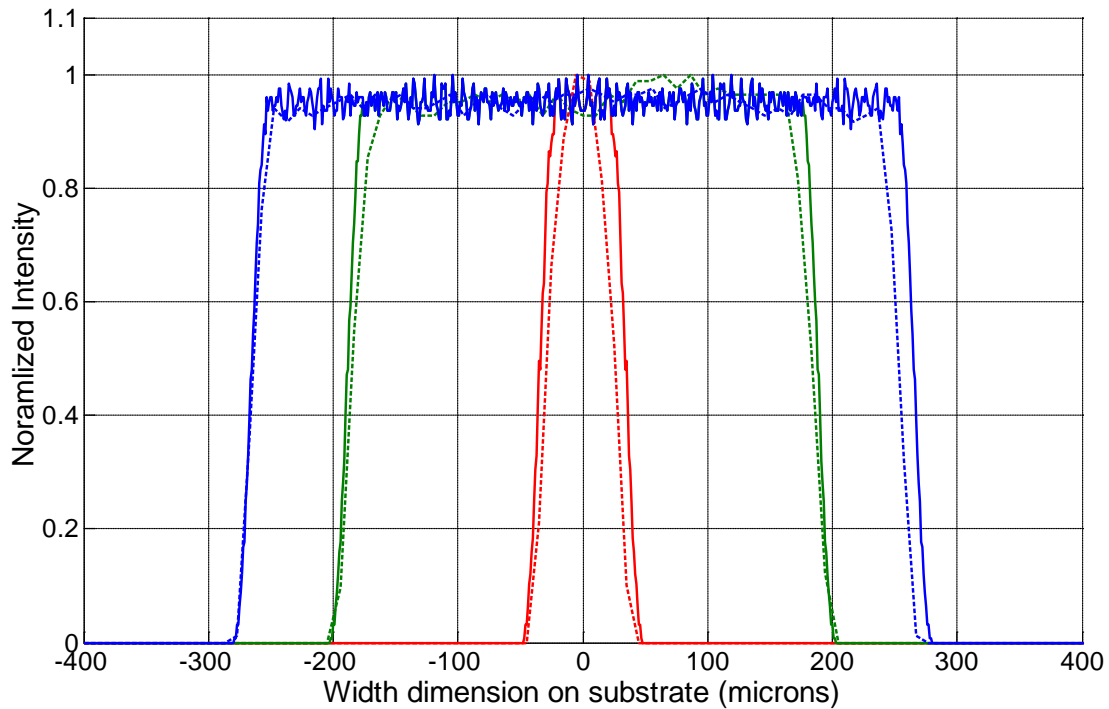
varying the size of the projected lines are as shown in Figure 62. A single image was captured from the UV camera and gray scale values were then averaged over the entire length of the exposed region. Figure 62 shows that varying the width of the projected area does not significantly affect the maximum intensity of the cured part.



**Figure 62 Exposure profile by varying projected line widths on DMD chip**

Figure 63 shows the plot of the exposure profiles from the camera (in dashed lines, same as Figure 62) superimposed with the simulated exposure profile using the irradiance model (in solid lines). The plots show that the irradiance model based on ray tracing can estimate the actual exposure profile on the substrate level. It is to be noted that there are some deviations from the model, which may be attributed to misalignment

of optics, inexact setting of the aperture opening on the system hardware and inexact reproduction of the actual exposure profile on the UV CCD. The resolution of the simulation model was  $1\mu\text{m}$  and that of the UV CCD Camera is  $\sim 10\mu\text{m}$ , which might explain the discrepancy between the experimental and simulation results.



**Figure 63 Comparison of simulation results from Irradiance model (solid lines) with data from Camera (dashed lines). Red corresponds to 10pixels; green to 60pixels and blue to 90pixels**

The UV CCD camera was also used to quantify the accuracy and precision of the timing control of the DMD™ chip. The chip is a part of the projector and is controlled by using the Powerpoint® presentation software. Several bitmaps were designed and placed on the individual slides. These slides were projected sequentially using the software's

slide transition feature. It was experimentally observed that the error in switching of the slides was less than  $\pm 0.1s$ .

From the above study, an irradiance model was found suitable to model the exposure profile, i.e. the light shaping effect due to the DMD™ chip. Figure 64 summarizes the results obtained from the above study.

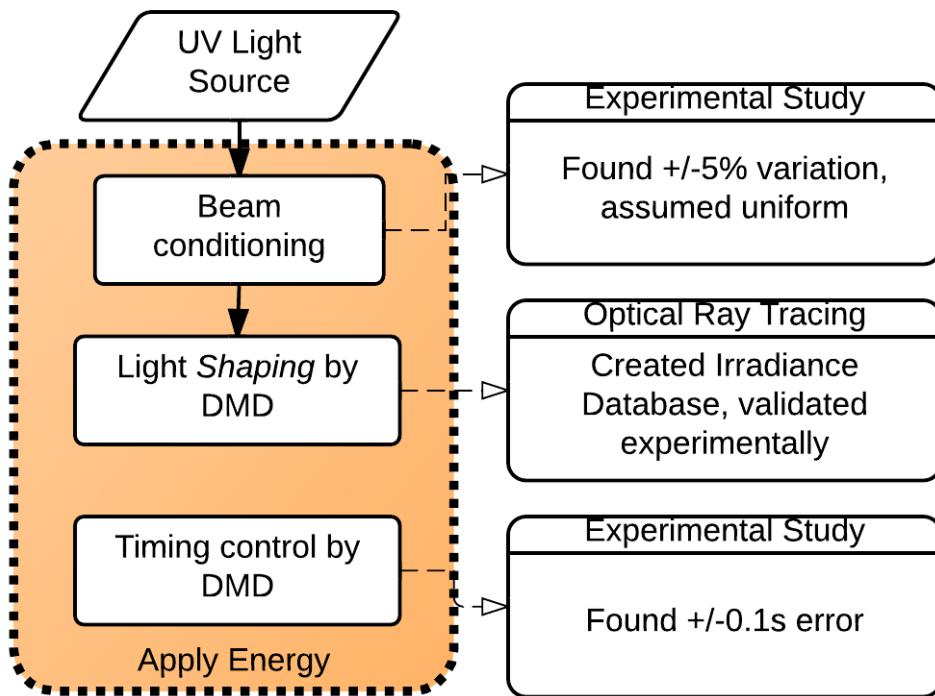


Figure 64 Results of investigation on the factors affecting the cured part due to Apply Energy Phase

#### 5.4 Phase – II: Process

The ‘Process’ phase primarily includes the photopolymerization process. This process is induced by the UV light energy incident at the resin substrate. In order to study how the photopolymerization process influences the generation of the cured part shape,

several test samples were fabricated on the ECPL system with different exposure doses. The polymerized parts were cured on the glass slide. After curing, the glass slide was removed from the resin vat and additional uncured resin was removed using the developed washing procedure described in Section 4.5. A 3D laser LEXT confocal microscope was used to measure the cured part profile using the glass slide as the reference. The experimental data was fitted to the empirical model, presented in Eq. 2-4 and repeated here for convenience.

$$z \approx D_{pS} \ln \left[ \frac{D_{pL} E}{D_{pS} E_c} + 1 - \frac{D_{pL}}{D_{pS}} \right] \quad (5-2)$$

where  $D_{pL}$  is the depth of penetration for liquid resin and  $D_{pS}$  is the depth of penetration for a cured layer. The parameters  $E_c$ ,  $D_{pL}$  and  $D_{pS}$  are usually fit to experimental data at a specific resin composition and cure intensity, and were found to be 1.2315 mJ/cm<sup>2</sup>, 68.6063 μm and 34.0702 μm, respectively.

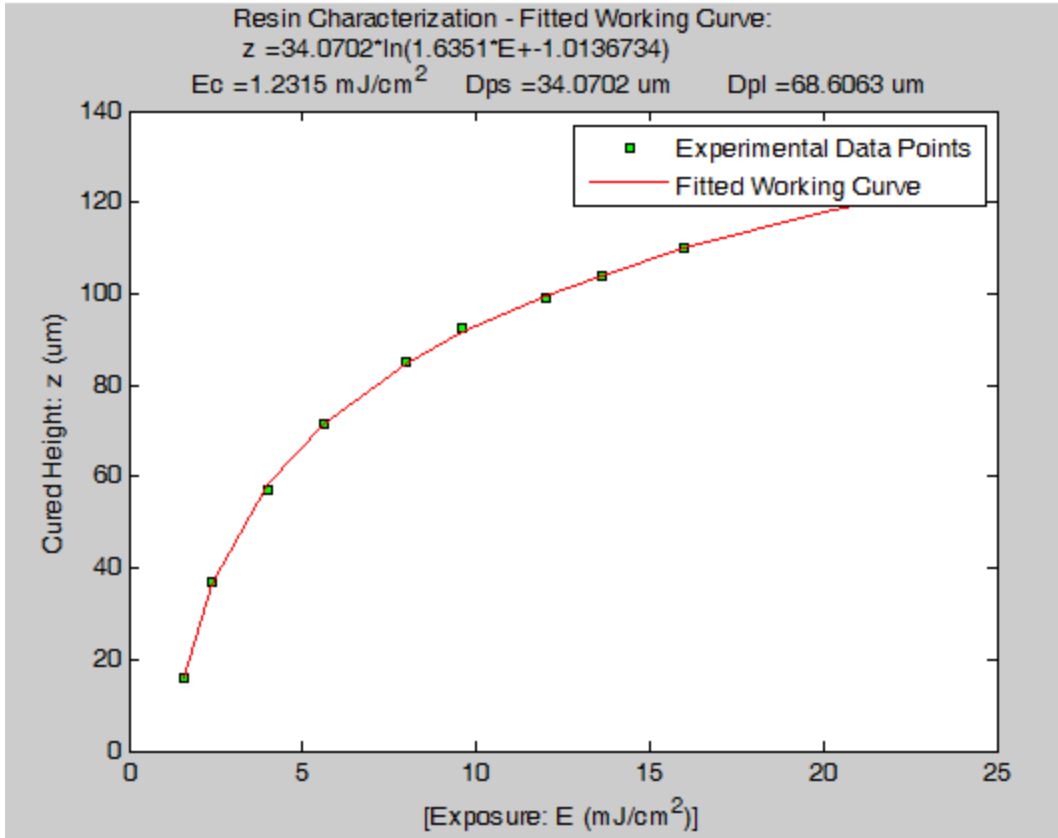
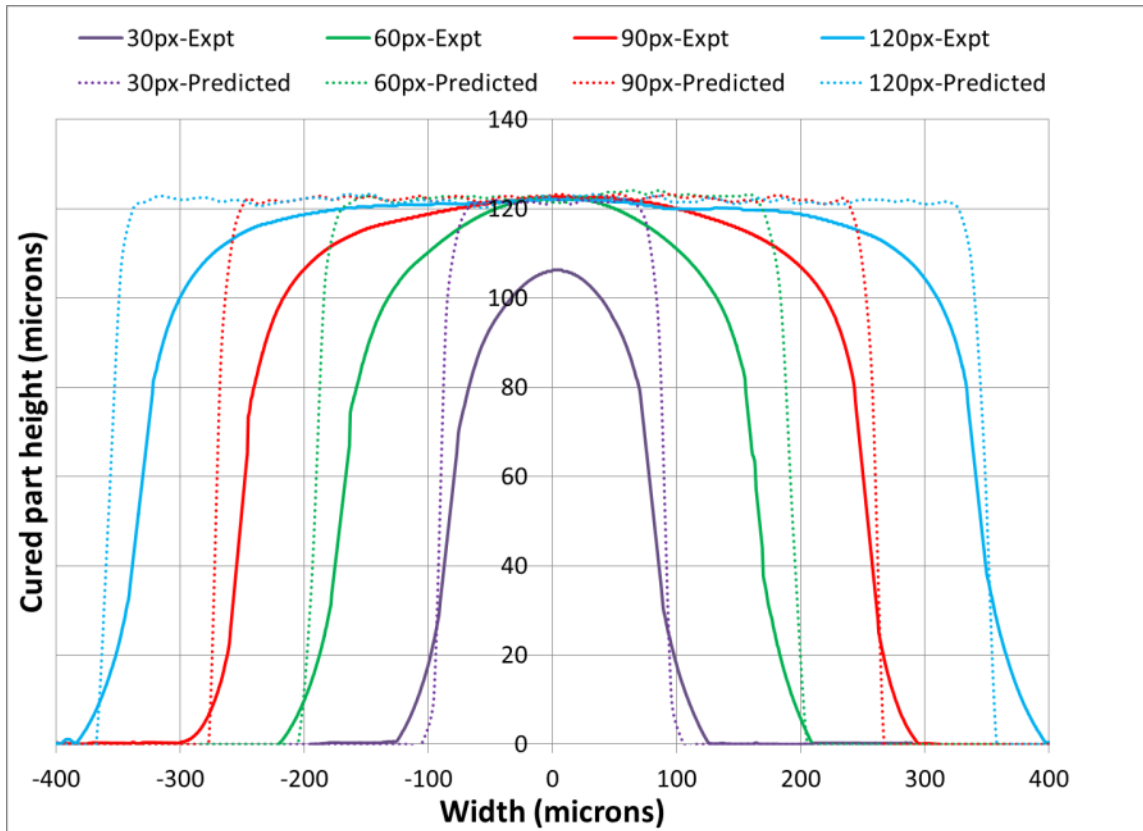


Figure 65 Experimentally obtained data shown in green dots fitted on a working curve (in red)

Figure 65Figure 84 shows the plot of the working curve with the experimental data points superimposed and shown as green dots. Using the fitted constants, given the exposure dose, the cured part height can be predicted by Eq. 5-2 as follows [14]:

$$Z = 34.0702 * \ln(1.6351 * E - 1.0137) \quad (5-3)$$



**Figure 66 Plot showing the inadequacy of the existing empirical model to explain the cured part profile. The solid lines show the experimentally observed cured part shapes and the dotted lines depict the predictions using empirical model based on Beer-Lambert's law from Eq. 5-3**

Test samples were fabricated by projecting lines of varying widths on the DMD™ chip. Specifically, line shaped parts were cured by projecting 30, 60, 90 and 120 micromirrors (or pixels). The UV CCD camera was used to image the intensity profile resulting from projecting the lines, in a similar way in which the plot shown in Figure 62 was obtained. This intensity profile, which is in terms of the gray scale values of the camera, is normalized to obtain the irradiance (energy/time/unit area). The product of irradiance and time is the total incident exposure dose (energy/unit area), 'E'. Eq. 5-3 was used to predict the shape of the cured part profile for each of the line widths.



The predicted part profiles are shown as dotted lines in Figure 66. The 3D LEXT Confocal microscope was used to measure the cross-sectional part profile of the cured samples. These profiles are shown as solid lines in Figure 66. It can be seen from the figure that the existing empirical model (which is based on Beer-Lambert's attenuation law) fails to explain the presence of a consistent edge curvature. We also notice additional curing beyond the region of exposure close to the substrate. This can be a result of the uncured monomer not being removed due to surface tension between the cured sample and the glass slide, which might have been post-cured and become a part of the previously cured part. However, the primary unanswered question about the polymerization process is – *what causes formation of edge curvature on the cured part resulting from ECPL process?* This question can be restated as – *why do parts fabricated from the ECPL system exhibit a deviation from the empirical material response, primarily at the edges?*

One explanation to the above question can be that the growth of polymerization does not proceed along the normal to the substrate surface. It was hypothesized that the light path continually varies as it causes curing and this might lead to self-focusing effect causing a reduction of exposure width as light travels deeper into the resin, during the curing process. This leads us to the sub-research question:

### **Research Question & Hypothesis #2.1**

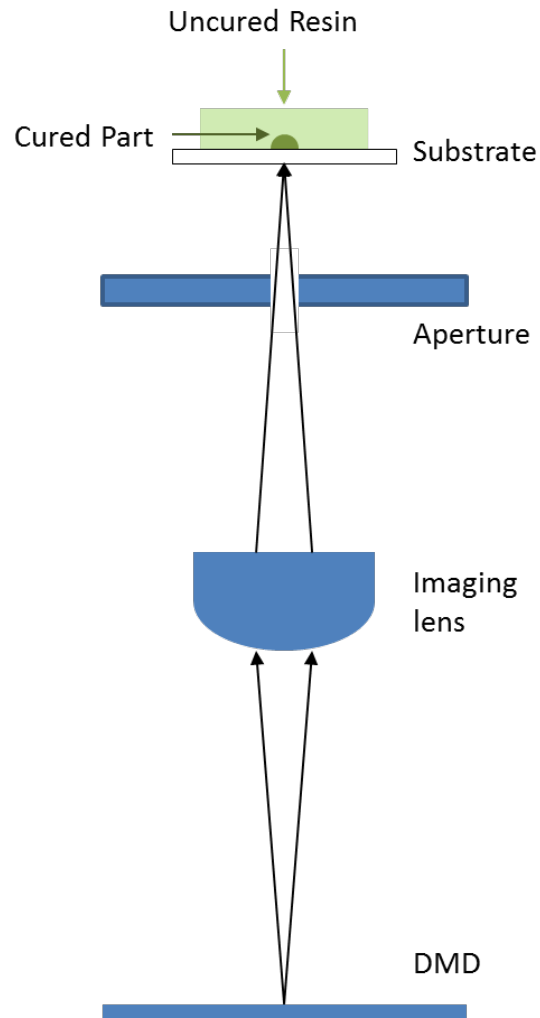
#### **How does optical self-focusing affect the curing process in ECPL?**

Hypothesis: *Optical self-focusing is caused when light travels from the dense cured part into the relatively less dense uncured resin. Optical ray tracing simulations through the*

*photopolymer resin can be used to verify if self-focusing leads to curing of parts with gradually reducing dimensions from near the substrate to the top free surface of the cured part.*

#### **5.4.1 Investigation on effects of optical self-focusing**

To determine if optical self-focusing is a factor influencing the shape of the cured parts resulting from the ECPL process, an optical test simulation was conducted in LightTools software. The projection system, as shown in the ECPL block diagram in Figure 8, was modeled in LightTools. The dimensions from the experimental system were used for placing the imaging lens, aperture and the glass substrate in the optical model within the software. Figure 67 shows the schematic of the projection system modeled in the software. The detailed specifications were presented in Table 2.



**Figure 67 Schematic of the optical projection system modeled in LightTools**

The objective of this optical simulation is to understand if rays of light bend significantly, as they translate from the cured shape into the uncured monomer. The simulations will be performed by assuming the following:

At time,  $t = 0$ , there is no curing. After an incremental time,  $\Delta t$ , around  $50 \mu\text{m}$  of the resin will be cured.

For sake of comparison, two receiving surfaces were used – one placed on the interface of the resin and the substrate and the other was placed at 10 microns into the resin. Optical simulations will be conducted with and without the presence of the cured part submerged into the resin. The distances of all the optical elements and their individual refractive indices are already known. The primary task before simulating the system is to model the refractive indices of the cured and uncured resin.

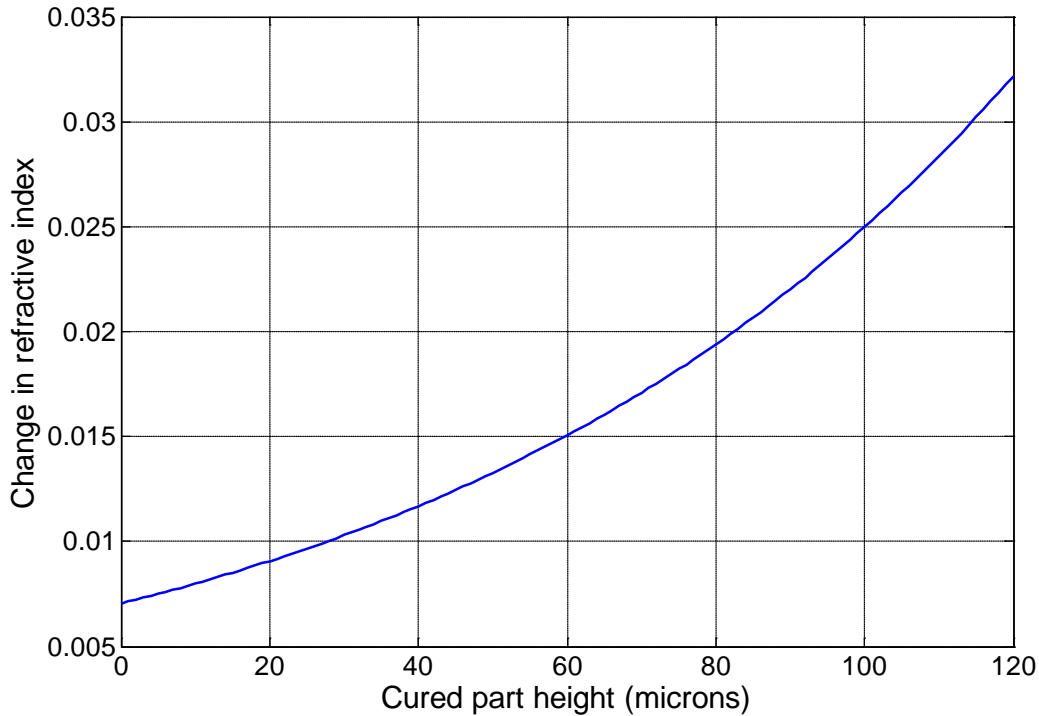
The refractive index of the uncured photopolymer resin, SR351 is known from published technical literature as 1.4723. *How do we determine the refractive index of the partially cured sample?* Here again, the interferometric photopolymerization monitoring system (discussed in Chapter 4) can be used. Equation 4-10 can be rearranged to estimate the observed phase shift for a given height as follows:

$$\phi = e^{\left(\frac{h+259}{78.96}\right)} \quad (5-4)$$

where the cured part height,  $h$  is in  $\mu\text{m}$  and the phase angle,  $\phi$  is in radians. Using this equation, the phase angle corresponding to a cure of a  $10\mu\text{m}$  high part is 30 radians. From Eq. 4-8, we can estimate the refractive index change caused during curing a  $10\mu\text{m}$  part height to be 0.00795 (for a spacer thickness of  $200\mu\text{m}$ ) as used in this study. This implies that if the refractive index of the uncured resin is considered as 1.4723, the refractive index of the cured part can be assumed as 1.47025. Equation 4-8 and 4-10 can also be rearranged to form a relationship between the cured part height and the change in refractive index as follows:

$$\Delta n = \frac{e^{\left(\frac{h+259}{78.96}\right)}}{18.87 * t_s} \quad (5-5)$$

Using Eq. 5-5, for a spacer thickness,  $t_s$ , of 200  $\mu\text{m}$ , the relationship between the cured part height,  $h$ , and the change in refractive index,  $\Delta n$ , can be plotted as shown in Figure 68.



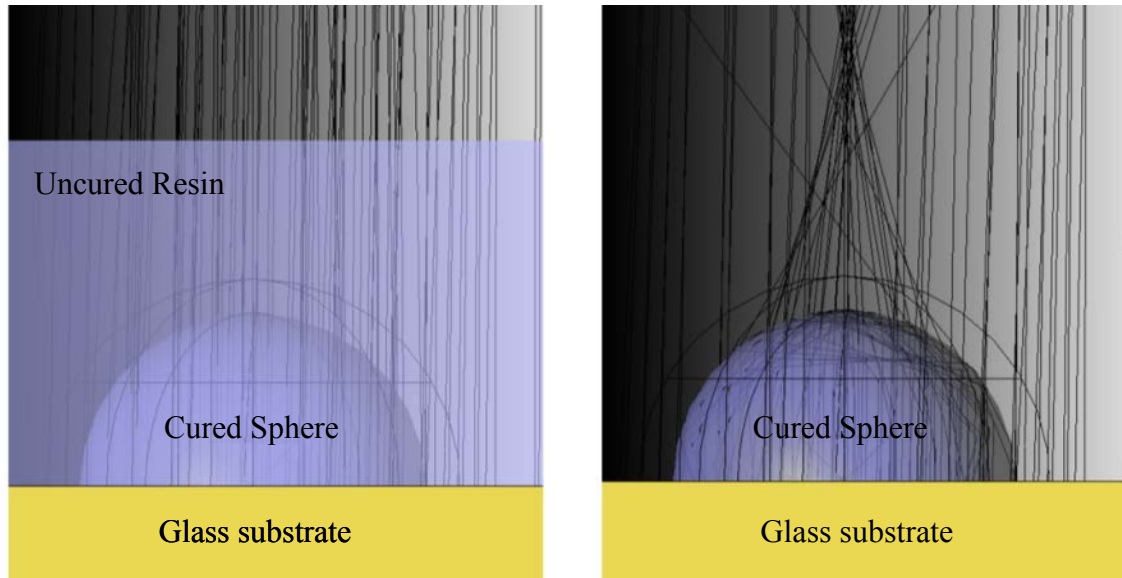
**Figure 68 Change in refractive index as a function of cured part height**

A spherical geometry with a radius of 50 $\mu\text{m}$  was modeled in SolidWorks® and integrated into LightTools as the cured part through which the light rays would pass. From Eq. 5-5, the change in refractive index at height of 50 microns is 0.0133. Hence the refractive index to the cured part was assigned to be 1.4856 (1.4723+0.0133) and was placed right next to the glass substrate, as shown in Figure 67. As seen from Figure 68,

the refractive index of the cured part within the monomer during curing will be a gradient and not homogenous throughout the partially cured part. This is because the curing occurs as a gradient gradually increasing in density from the base of the curing region to the free surface of the growing cure front. The motivation of this study is to investigate if optical self-focusing could cause significant deviations in the light path within the resin. Hence, it is reasonable to assume a constant homogenous refractive index for the previously cured part. The refractive index of the glass substrate was assumed as 1.5.

The simulation on LightTools software was conducted by switching ON an equivalent area corresponding to 20 x 20 micromirrors at the DMD™ surface. The effect of self-focusing, if present, will be greater due to transverse rays, than axial rays. Hence, the simulated area was placed 1mm away from the center of the DMD surface, which is at a distance of around 75 micromirrors from the center. A spherical shaped receiver was placed such that its spherical surface was at a radial distance of 10 μm from the modeled cured surface. The receiver surface was discretized into 5 μm per pixel.

Figure 69 shows the results obtained from the optical ray-tracing simulations. The modeled cured part (R.I. of 1.4856) was assumed immersed into the resin (R.I. of 1.4723) for the observations on the left. This is the typical condition during curing on the ECPL system. The figure on the right shows the effect of removing the resin and continuing the optical ray tracing in air. The results match intuition that the rays would tend to focus. Of interest is the fact that self-focusing does not cause a significant deviation in deflecting the light path since the difference of refractive index between the cured and the uncured sample is very less.



**Figure 69 Comparison of light path when curing through a cured part. Left: in presence of resin. Right: in absence of resin**

In order to quantify the influence of the cured sample on the direction of the light into the resin, three ray-tracing simulations were performed as follows:

1. Without the cured part in the resin
2. With cured part in the resin
3. With cured part in air

The normalized intensities striking the spherical receiver surface is potted in Figure 70. It can be clearly observed that there is minimal influence of the cured part on the light intensity available at the spherical receiver for case with and without the cured part in the resin. However, this is not the case when the surrounding medium is assumed air, which is indeed not practical, but was conducted to validate the simulation method. This study confirms that optical self-focusing is not a cause for formation of edge curvatures on the cured parts resulting from the ECPL process.

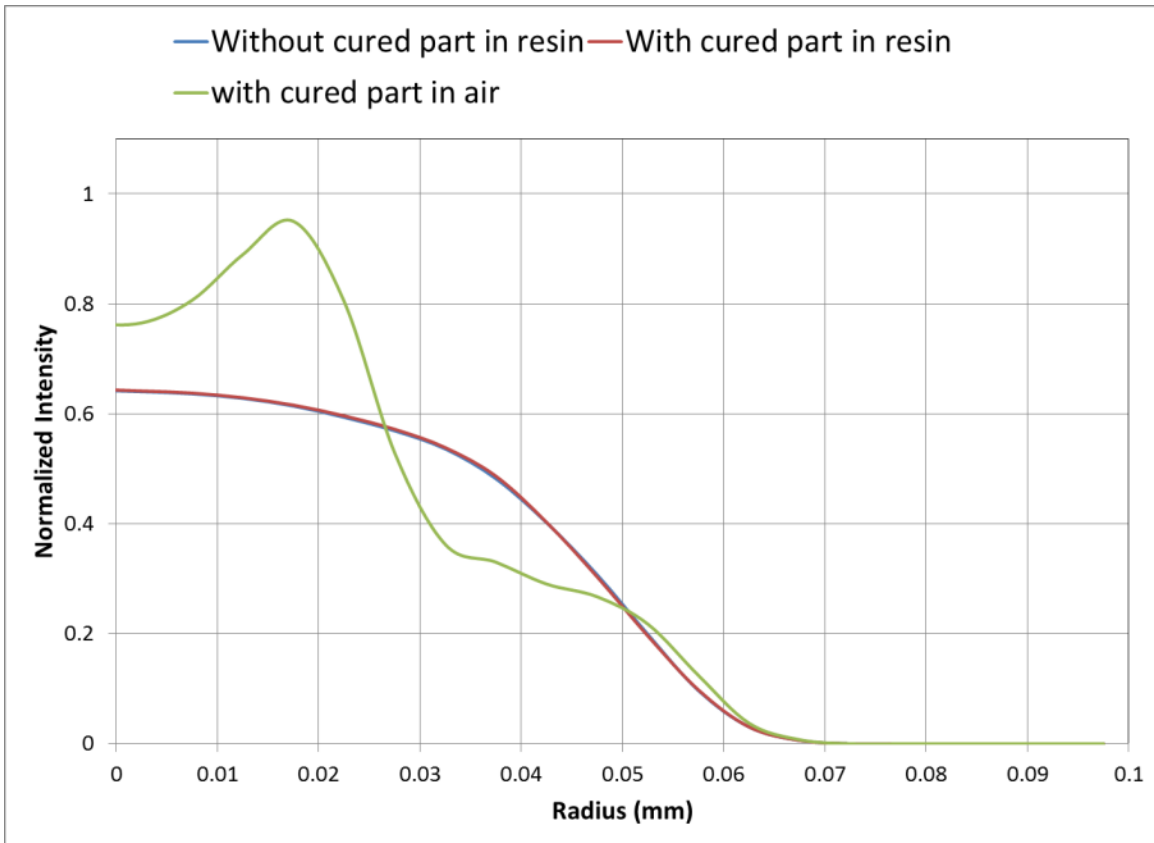
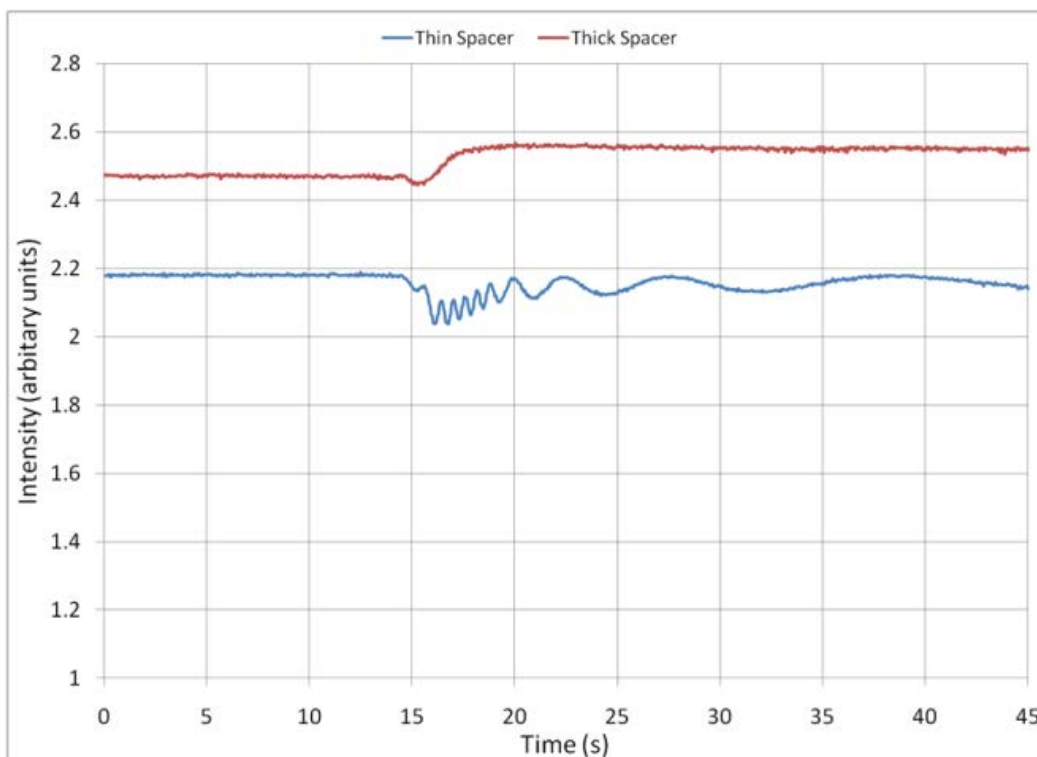


Figure 70 Intensity plots obtained from LightTools ray-tracing simulation from the spherical receiver (red and blue curves overlap)

#### 5.4.2 Investigation on presence of oxygen inhibition

Experiments were conducted using the interferometric monitoring system to understand the effects of chemical inhibition (caused by dissolved oxygen and inhibitors) on photopolymerization. Specifically, the spacer thickness was varied, thus varying the thickness of the sample chamber,  $t$ , as shown in Figure 41.





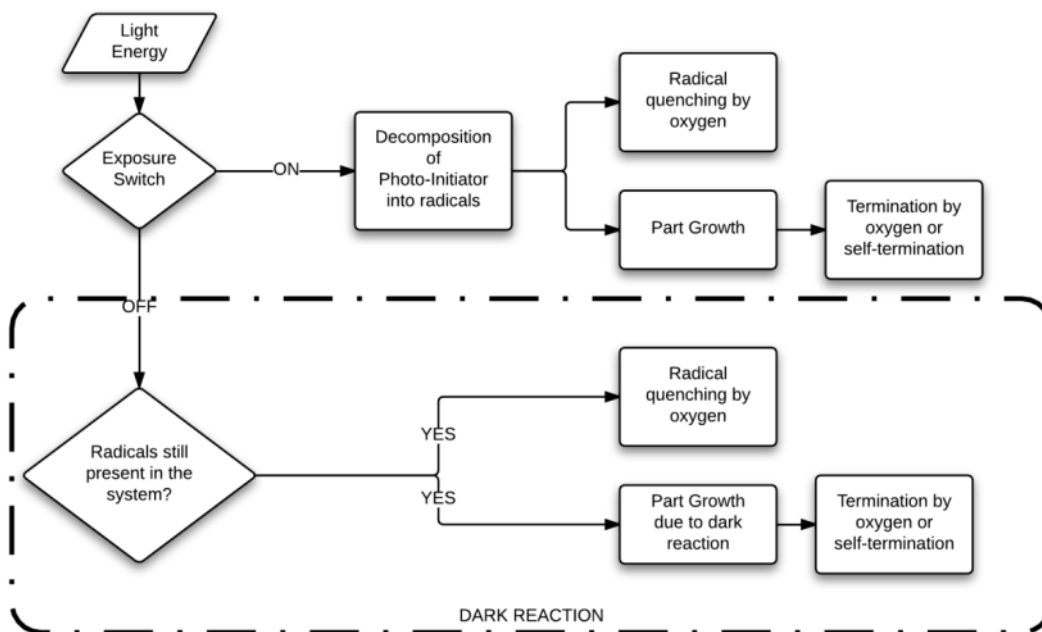
**Figure 71 Results showing the effect of spacer thickness**

The two plots were obtained from two different experiments, where the samples were irradiated at the same intensity for 25 seconds. No curing was observed when using a thicker spacer (1.4mm), whereas a different sample of the same resin was cured easily to a height of around 106 $\mu$ m (as measured from a laser confocal microscope) when using the thinner, 200 $\mu$ m spacer. This phenomenon was never considered when using the conventionally accepted empirical model based on the Beer Lambert's law for photopolymerization. This effect can be ascribed to continued inhibition of the photopolymerization reaction by rapid diffusion of dissolved oxygen into the irradiation zone from the larger reservoir of air-saturated resin in the thicker sample.

Hence, it is reasonable to assume that oxygen inhibition might be a significant factor worth considering for modeling purposes. Further chapters will elaborate on how this effect can be modeled.

### **5.4.3 Investigation on presence of dark reaction**

For reliable process planning of a manufacturing process, it is necessary to ensure that the input parameters can consistently control the output. In other words, the output cured part shape should be directly related to input exposure. If there is presence of significant dark reaction as observed in Figure 43, it will be difficult to control the process, as curing can continue even after the input exposure is switched off. Figure 72 shows the schematic of the photopolymerization process in form of block diagram and presents the source of dark reaction. In essence, dark reaction is caused due to excess of live radicals present in the system, which continue the cross-linking process even after the exposure is turned off. The existence of dark reaction poses a challenge to the overall control of the ECPL process, as the controlling parameter is not only the exposure, but also the number of radicals present in the system. This can further complicate the overall process planning strategy. Although there is no well-defined method available in literature (to the best of author's knowledge) to eliminate dark reaction, simple experimental studies can be performed to obtain the cure recipe that can yields the least amount of dark reaction.

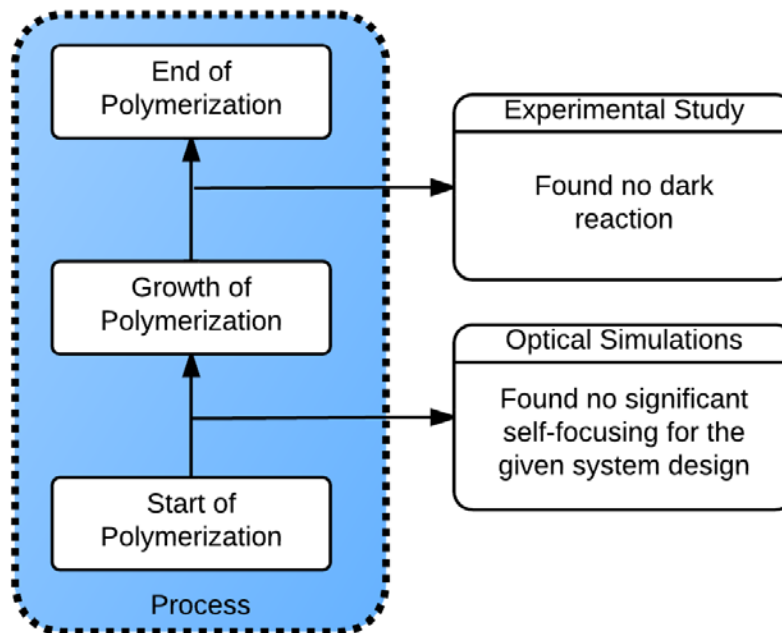


**Figure 72 Block diagram of the photopolymerization process for ECPL; highlighting the source of dark reaction**

The probability of dark reaction is directly dependent on the number of radicals present in the system. The numbers of radicals depend on the light intensity, time of exposure, photoinitiator concentration and the presence of inhibitor in the photopolymer system. For simplicity, while keeping other factors constant, the light intensity (at the substrate) was varied and the presence of dark reaction was monitored using the interferometric monitoring system (described earlier in Ch. 4). Table 4 shows the table of values for the different range of intensities used to conduct experiments and measure the time for dark reaction. It was observed that higher intensities typically yield a longer dark reaction. Hence, lower intensities were preferred from this study.

**Table 4 Design of Experiments table to determine the cure recipe to avoid dark reaction**

Run #	Intensity (mW/cm <sup>2</sup> )	Exposure Dose (mJ/cm <sup>2</sup> )	Settling Times (seconds) (Time of dark cure)			
			#1	#2	#3	Average
1.	0.8	8	2	1	3	2
2.	1.6	8	10	12	9	10.3
3.	2.4	8	15	18	12	15



**Figure 73 Results of investigation on the factors affecting the cured part due to Processing Phase**

#### 5.4.4 Investigation on effects of shrinkage

The photopolymer resin experiences shrinkage upon changing from liquid to solid during the curing process [69]. Shrinkage accompanying photopolymerization in the

stereolithography process has been studied in depth in existing literature [70-73]. Most of the research efforts were spent towards characterizing shrinkage and the effects of resulting residual stresses on conventional stereolithography processes. In conventional SLA processes, the parts are built in layers and the subsequent layers are built on a layer undergoing shrinkage. Hence the overall part geometry is substantially affected by warpage resulting from residual stresses from each layer. On the contrary, in the ECPL process, the entire part is built gradually by curing through the previously cured part. Hence, it is reasonable to expect that there will be a relatively lesser effect of residual stresses being generated during curing.

For the photopolymer material under consideration in this research, the maximum total volumetric shrinkage was experimentally found to be 12% [74]. Hence, the linear shrinkage or the amount of shrinkage along one dimension is expected to be around 2.3%. This means that for curing a lens of 100 $\mu$ m diameter, the cured part will lose around 2 $\mu$ m. This value is within the fabrication error of the ECPL system, which was found to be  $\pm 1\mu$ m. It may be worthwhile to explore detailed shrinkage models and estimate its impact on the effect of the cured part shape for improving the ECPL process. However, at the current stage, the focus of the current research effort was to understand the factors responsible for larger errors as shown in Figure 57 and Figure 58. Hence, further investigation on the effects of shrinkage is not pursued in this work.

So far, we have found that optical self-focusing does not affect curing in the ECPL process for the given system design. The presence of oxygen inhibition was

confirmed using experiments. The only probable factor that can affect the shape of the cured part can be the post-processing steps, which leads us to sub-research question...

### **Hypothesis for Research Question #2.2**

**How does post-processing affect the geometry of the final product resulting from the ECPL process?**

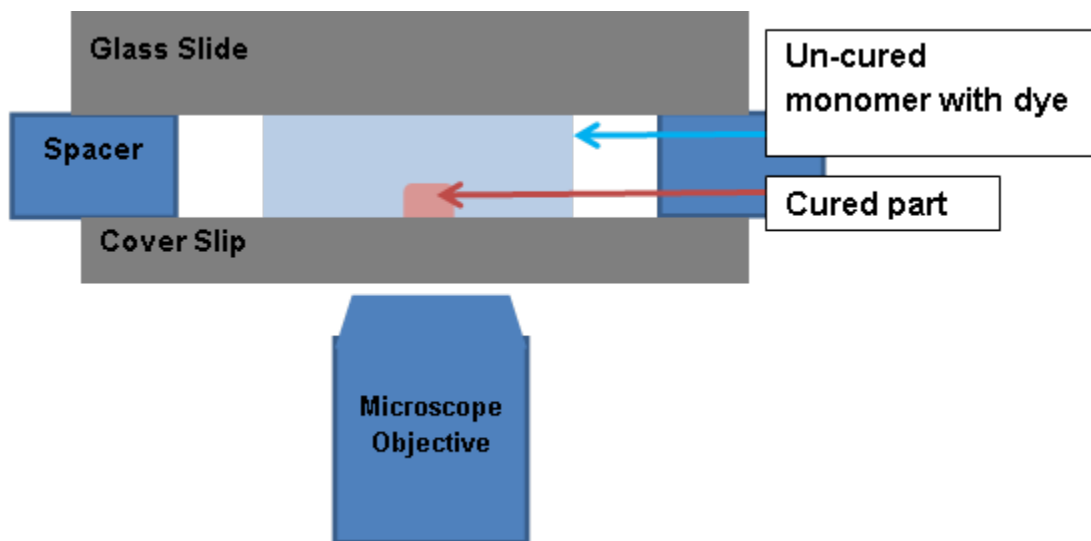
*Hypothesis: Post-processing steps like washing and post-curing affect the dimensions of the cured part resulting from the ECPL process. Confocal fluorescence microscopy can be used to determine the extent of swelling or erosion caused by post-processing on the final cured part.*

## **5.5 Phase – III: Post-Process**

The technique of laser fluorescence confocal microscopy was used to study the effect of post-processing on the parts fabricated from the ECPL process. This technique is based on the principle of imaging fluorescent substances using a microscope [75]. Fluorescent substances fluoresce when activated with a light of specific wavelength. When samples are imaged with a fluorescence microscope, the fluorescent region appears bright and the non-fluorescent region appears dark. This technique is widely used for examining biological samples. This technique was also demonstrated for use in measuring three-dimensional features of microstructures in literature [76].

The advantage of this technique is that samples can be imaged before washing or post-processing. Fluorol-555 from Exciton [77] was used as a dye for this study and the samples were imaged using a Zeiss LSM 510 UV Confocal microscope. The microscope

is so configured to image the samples from the bottom, i.e; the objective is placed underneath the sample to be imaged, as shown in Figure 74. Samples were cured on a microscope cover slip, instead of a glass slide, since the objectives used in the microscope had a very high numerical aperture and hence a very shallow working distance.



**Figure 74 Schematic describing location of the sample in the fluorescence confocal microscope**

The four types of samples investigated using these techniques are outlined as follows:

Sample # 1: As cured: Samples cured on the ECPL system were not washed. After curing, a solution of the blank monomer loaded with the fluorescence dye was loaded on top of the uncured monomer. Sufficient time was allowed for the dye to diffuse into the uncured monomer surrounding the cured part. The idea behind using this method was that the dye would diffuse into the uncured monomer, but will not penetrate into the cured part. This boundary between the cured and the uncured region could be captured from the

fluorescence confocal microscope. This test will help establish a baseline of the cured part profile. Subsequent post-processing may adversely damage the cured sample and hence the following tests were conducted to identify the extent of damage, if any.

Sample # 2: After wash: Samples cured from the ECPL system were washed in TritonX solution. Similar to earlier procedure, a solution of the blank monomer loaded with the fluorescence dye was loaded on top of the cured sample. Comparing the boundary profile between the dye and non-dyed regions would show if washing the sample in TritonX solution caused any adverse effect on the part shape.

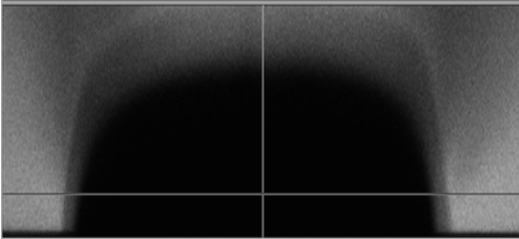
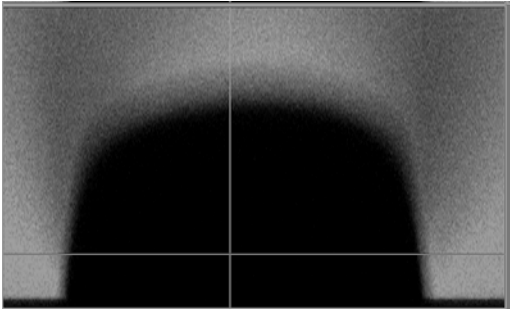
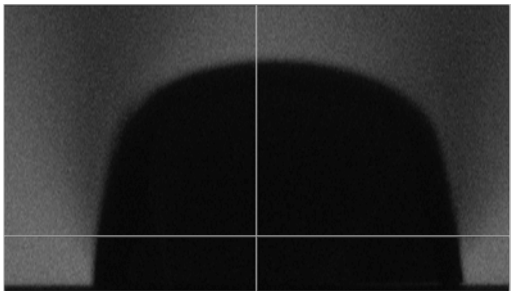
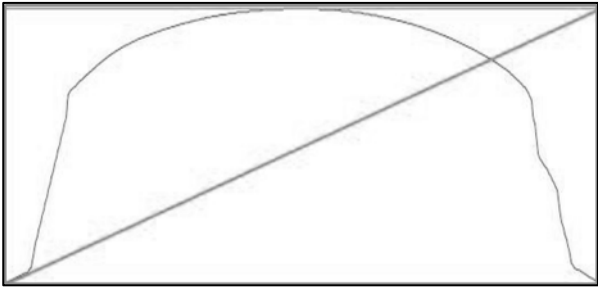
Sample # 3: After post-processing: After the cured samples were washed, they were post-cured for 10 minutes under a 365nm UV LED lamp. A solution of the blank monomer loaded with the fluorescence dye was loaded on top of the cured sample. Comparing the boundary profile between the dye and non-dyed regions would show if post-curing process caused any adverse effect on the part shape.

Sample # 4: This is similar to the above sample. However, no dye was added to the post-cured shape. The sample was simply observed using a 3D Laser Scanning Confocal microscope in air. Ideally, the part profile from the earlier test and this should be the same. However, the actual dimensions may differ. This is because the fluorescence confocal microscope was not calibrated to yield actual part dimensions. Nevertheless, this test would help ascertain that the profile shape obtained from the fluorescence microscopy is indeed the actual part profile.



A line shaped part was cured by projecting a line image of 30pixels (micromirrors) on the DMD™ chip of the ECPL system. All images were taken nearly at the center of the cured line. Table 5 shows the images obtained from the fluorescence confocal microscope. The images are for relative comparison only and are not to scale.

**Table 5 Table showing the images from the experiments conducted to study the influence of post-processing on cured part shape (for a sample with 30s exposure)**

<b>30s exposure</b>	
Sample #1: Original: (without post-processing)	Sample #2: After washing (no post-curing)
	
Sample #3: After wash & Post-Cure	Sample #4: After wash & Post-Cure (no Dye): (from LEXT 3D Confocal microscope)
	

Several samples were tested using the above technique. As evident from the images in Table 5, the boundary of cured part profile is not distinct. The images show three regions: a completely black region, an intermediate gray region immediately surrounding the black region, an outermost dark gray region. Presence of the intermediate gray region suggests that dye diffuses into the partially cured gel region. The images of the washed

and post-cured parts show a sharper contrast between cured and uncured parts. This indicates that post-curing is hardening the gel region thus disallowing the dye to diffuse into the part. The part profile from fluorescence confocal microscopy (Sample #3) matches the part profile from the 3D laser confocal microscope (Sample #4). However, the part width as measured from the laser confocal microscope is relatively larger. This is quite probable due to calibration errors, which result from the changes in refractive index from cover slip to cured part in the case of fluorescence microscopy images.

Several samples were fabricated using the technique elaborated above. Figure 75 shows the plot of results for two representative samples exposed for 10s and 30s. The part heights were measured at the center of the cured parts. Due to the presence of the intermediate gray region, two heights were measured – maximum and minimum, corresponding to the edges of the intermediate gray region. As seen from Figure 75, the maximum heights for both the cases of 10s and 30s exposures do not change between subsequent post-processing steps. We can thus conclude that the washing and post-curing do not have a significant effect on the height of the cured part.

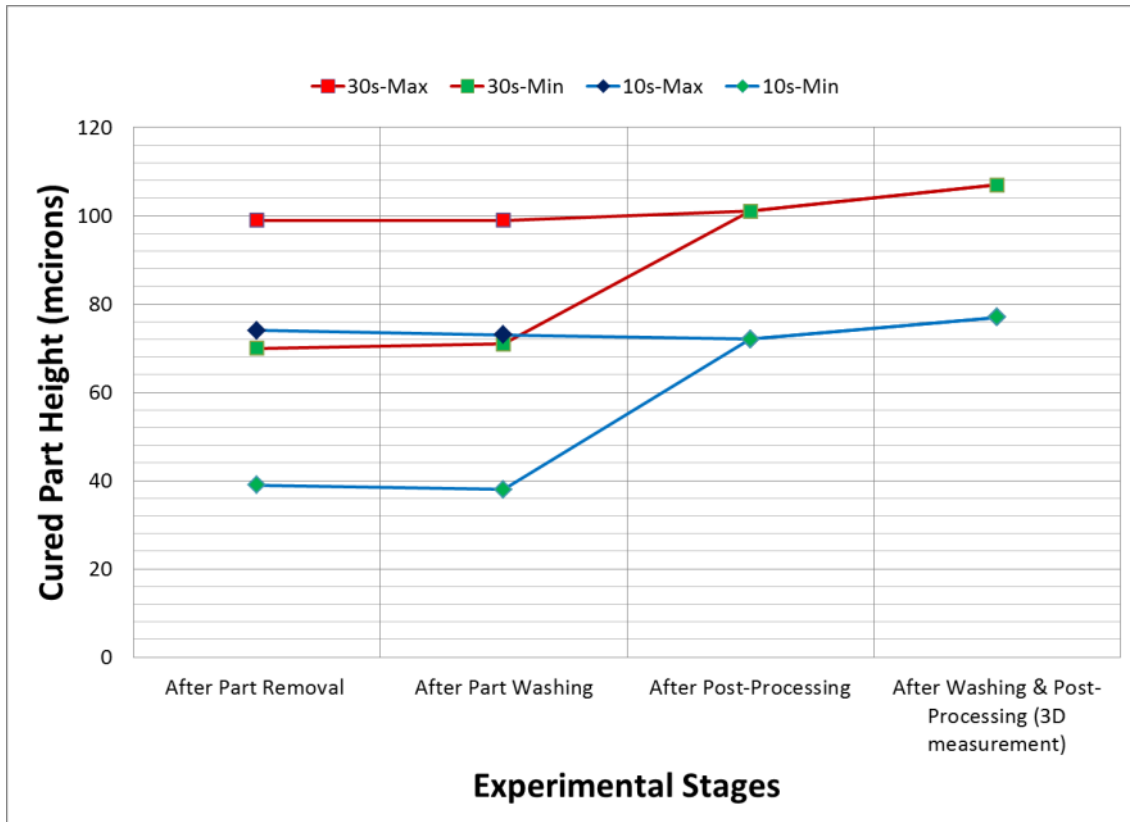
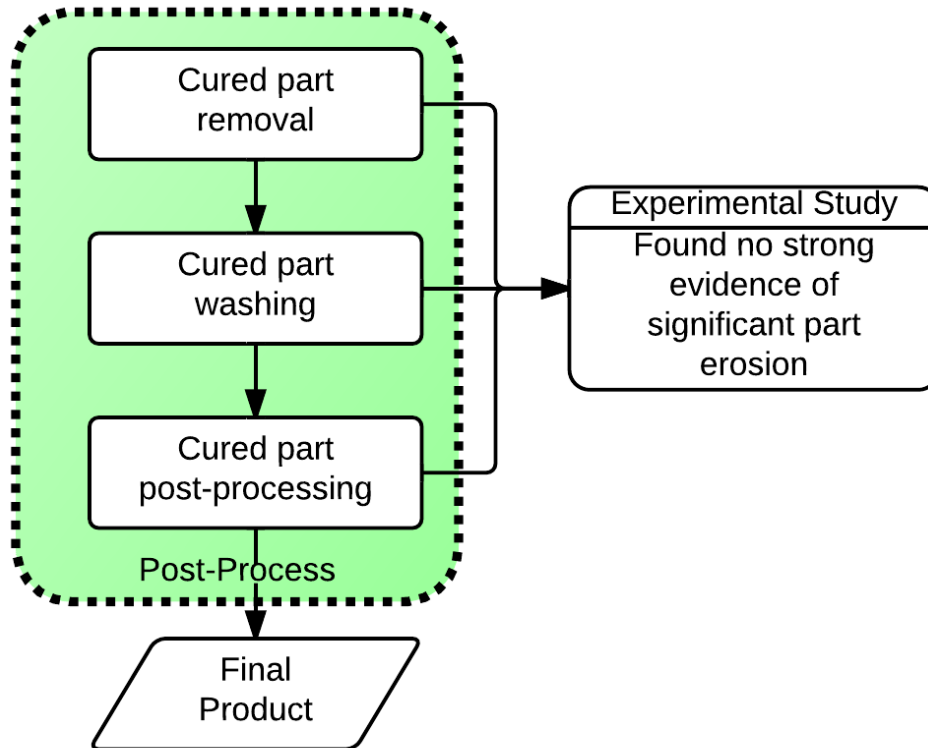


Figure 75 Plot of measured heights for samples exposed for 30s and 10s

From the above study, we concluded that there is no significant difference between the height of the cured part before and after washing process. This implies that the developed washing process does not cause substantial variations in the part height. Figure 76 summarizes the results obtained from the above study.



**Figure 76 Results of investigation on the factors affecting the cured part due to Post Processing Phase**

## 5.6 Chapter Summary

In this chapter, systematic investigations were conducted to identify the factors that affect the shape of the cured part. The second research question was presented in this chapter, which was divided into two sub-research questions. The ECPL process model was presented which elaborated the fabrication process in the ECPL system in the form of three distinct phases. Each of these phases was studied using experiments and simulations. As expected, the exposure profile was identified as a primary factor affecting the width of the cured part. An irradiance model (which was available in literature) was adapted for the current ECPL system and validated using experiments. The hypothesis to

research question 2.1 was tested using optical ray tracing simulations. It confirmed that optical self-focusing does not significantly affect the shape of the cured part in the ECPL system as assembled and presented in Chapter 3. The hypothesis for research question 2.2 was tested experimentally. Experimental studies concluded that the washing process developed in Chapter 4 is well suited for parts fabricated from ECPL and does not cause a significant erosion effect on the height of the cured parts. It was found that oxygen inhibition affects the polymerization process and its effect will be modeled in the next chapter.

## CHAPTER SIX

### FORMULATION OF A PHOTOPOLYMERIZATION MODEL

This chapter presents how the modifications were performed to the existing models from literature in order to develop an appropriate material response model, which may be suitable for process planning purposes. Existing kinetic models were modified to incorporate the effect of oxygen inhibition and diffusion. The free-radical photopolymerization reactions with oxygen inhibition and diffusion were modeled and simulated using a finite element software package to predict the cured part geometry for a given exposure profile. It was found that the available rate constants for the kinetic models from existing literature were not applicable for the experimental conditions in the ECPL process. Hence, parametric search was conducted to find an appropriate range of values of the rate constants. The Jacob's model ( $E_c - D_p$  model), which is derived from the Beer-Lambert's law, was found to provide good correlation with the experimental results in one dimension. The simulation results from the kinetic model were used to develop an empirical material model, which could account for edge curvature formed due to oxygen inhibition and diffusion during the photopolymerization process.

#### **Chemicals used in this study**

For the purposes of the study conducted in this chapter and for the rest of the thesis, the photopolymer mix of TMPTA with DMPA as specified in Section 4.4.1 was used. It should be noted that 125 ppm of Hydroxy Quinone (HQ) or 175 ppm of Hydroquinone Monomethyl Ether (MEHQ) are included in the monomer formulation of TMPTA to

inhibit polymerization from hydroxy radicals while in storage, and the inhibitor was not removed from the experiments. The above ppm concentrations are equivalent to the molar concentration of oxygen in the sample, but the exact amount of inhibitor in the monomer at the time of use can vary, and it has been shown that these inhibitors do not impede the photopolymerization as strongly as oxygen does [45]. All experiments were neat solutions (containing no additional solvent) of TMPTA prepared by varying initiator concentration by wt% of TMPTA.

### **Why is oxygen needed in the sample?**

Researchers have shown that the presence of oxygen strongly enhances the inhibitory efficiency of MEHQ on free-radical polymerizations [78-80]. Several methods have been proposed to overcome oxygen inhibition in photopolymerization. However, none of them appears to be fully satisfactory in terms of efficiency.

### **6.1 One-dimensional modeling & simulation results**

This section will present the chemical kinetics' based photopolymerization model, which was available in literature. This model was simulated using the COMSOL® simulation software package. The researchers, who presented the model, also provided a sample set of optimized rate constants, which act as material parameters. Detailed studies conducted on the simulation results from the model revealed that the published optimized rate constants failed to explain the oxygen inhibition phenomena present during the photopolymerization process for curing of acrylates in air. Experimental results available from literature were used to optimize the rate constants. The use of revised rate constants

for polymerization simulation successfully explained the influence of oxygen inhibition and diffusion during polymerization.

As presented in Chapter 2, several researchers have modeled the photopolymerization process by modeling the chemical kinetics. These models are derived from bulk experiments, where the concentration of the individual species in a given volume of the photopolymer resin is tracked as a function of time and exposure. In order to predict the shape of the parts cured from the ECPL process, there is a need to develop a material model, which can provide an insight into the photopolymerization process in three-dimensions.

Recently, Boddapati et al. [44] developed a model to predict the gel time for multifunctional acrylates using a kinetics model. This model incorporated the effects of oxygen inhibition and diffusion in one dimension, which was parallel to the direction of UV irradiation. Equations 2.9-2.12 were solved using MATLAB® and the rate constants were optimized to fit the experimental data. There were four unique rate constants in the kinetic model, with the diffusivity of oxygen in the photopolymer resin. For ease of reference, the kinetic model is presented as follows. The concentrations of photoinitiator [In], radicals [ $R \cdot$ ], unreacted double bonds [DB], and oxygen [ $O_2$ ] were modeled in the kinetic model. The reactions considered by them were as follows[44]. When the photopolymer resin receives light energy, the photoinitiator absorbs it and decomposes into two radicals with first order rate constant of,  $K_d$





The initiator decomposition rate  $K_d$  is well known in literature and is modeled as a function of the local intensity, which varies with depth (following the Beer-Lambert Law) [39]

$$K_d = \frac{2.3\phi\epsilon\lambda}{N_A hc} I_0 e^{(-2.3\epsilon[In]z)} \quad (6-2)$$

where  $0 < \phi < 1$  is the quantum efficiency of the photoinitiator,  $N_A$  is Avagadro's number,  $h$  is Planck's constant, and  $c$  is the speed of light. The molar absorptivity of the resin,  $\epsilon$ , depends upon the source wavelength  $\lambda$ . The depth inside the resin is,  $z$ . The kinetic equation of the initiator can then be given as,

$$\frac{d[In]}{dt} = -K_d[In] \quad (6-3)$$

The radicals can then react with the double bonds to form longer chains, or form a dead radical or be quenched with dissolved oxygen as depicted by the following three equations.



$R_{dead}$  is species produced that destroys one or more radicals. The rate constants used are,  $K_p$  for propagation of a radical through an acrylate double bond,  $K_t$  for

termination between two radicals, and  $K_{t,O_2}$  for termination of a radical with an oxygen molecule.  $R^*$  is non-propagating radicals.

The overall rate of initiator decomposition,  $R_i$ , is modeled by multiplying the rate constant  $K_d$  by the initiator concentration  $[In]$

$$R_i = K_d[In] \quad (6-7)$$

The kinetic equations for the double bond  $[DB]$ , live radicals  $[R \cdot]$  and oxygen  $[O_2]$  can be given as follows:

$$\frac{d[R \cdot]}{dt} = 2k_d I(z)[In] - 2k_t [R \cdot]^2 - k_{t,O_2} [R \cdot][O_2] \quad (6-8)$$

$$\frac{d[DB]}{dt} = -k_p [R \cdot][DB] \quad (6-9)$$

$$\frac{\partial [O_2]}{\partial t} = -k_{t,O_2} [R \cdot][O_2] + D_{O_2} \frac{\partial^2 [O_2]}{\partial z^2} \quad (6-10)$$

The effect of oxygen inhibition and diffusion was explicitly modeled in Eq. 5.10. Due to the high diffusivity of dissolved oxygen in the photopolymer resin, it was assumed that the oxygen would primarily diffuse from uncured top layers of the sample chamber down to the curing front, competing with double bonds for radicals and significantly slowing down the rate at which the double bonds are converted, thus increasing the gel time. The researchers estimated the rate constants,  $K_p$ ,  $K_t$  &  $K_{t,O_2}$  by fitting the simulation results with the experimental data from FTIR. The physical

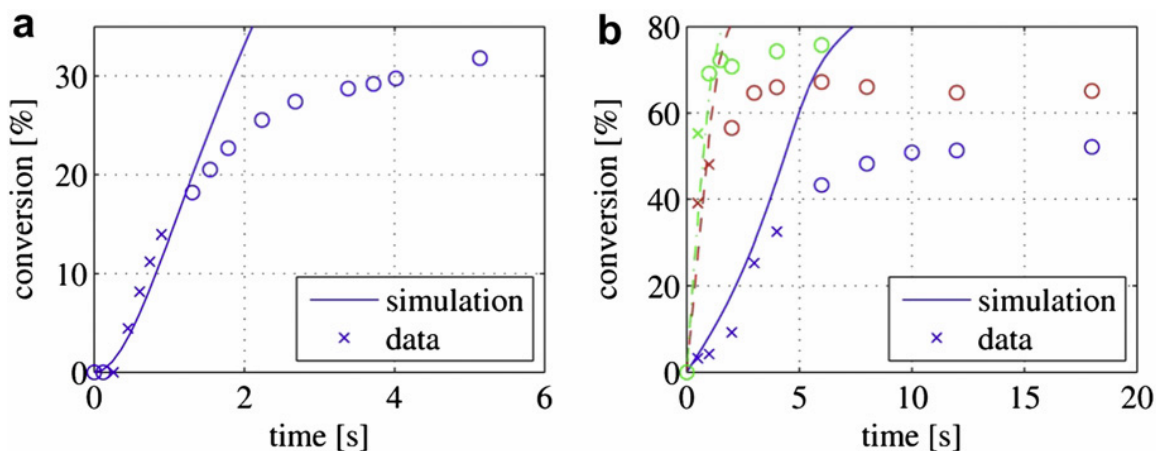
parameters, experimental conditions and the fitted rate constants in the study are presented in Table 6.

**Table 6 Physical parameters used in this study**

Parameter	Value	Units	Source
Quantum efficiency of radical, $\phi$	0.6	-	[38]
Molar absorptivity of photons at 365nm wavelength, $\epsilon$	15	m <sup>2</sup> /mol	[38, 45]
UV light Intensity, $I_0$	140	W/m <sup>2</sup>	Experimental
Molecular weight of Monomer, TMPTA	296	g/mol	Sartomer
Molecular weight of Photoinitiator, DMPA	256	g/mol	Ciba
Rate constant for propagation reaction, $K_p$	0.498	m <sup>3</sup> /mol-s	[39, 44]
Rate constant for termination reaction, $K_t$	1.31	m <sup>3</sup> /mol-s	[39, 44]
Rate constant for termination via oxygen quenching, $K_{t,O_2}$	2.11	m <sup>3</sup> /mol-s	[39, 44]
Diffusion coefficient of Oxygen, $D_{O_2}$	1e-10	m <sup>2</sup> /s	[81]
Initial concentration of Oxygen, $[O_2]_0$	1.05	mol/m <sup>3</sup>	[50]

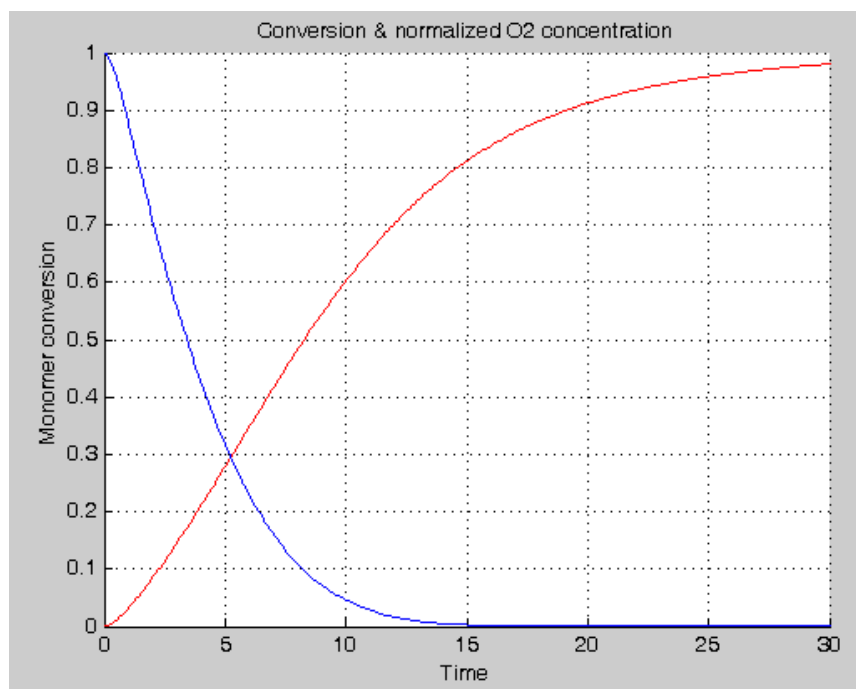
### 6.1.1 Results from the fitted rate constants

Figure 77 shows the conversion data from FTIR and the simulation results from the kinetic model. The blue solid curve and symbols represent 0.5 wt% DMPA, the red dashed curve denotes 5 wt% DMPA, and the green dashed-dot curve is for 10 wt% DMPA. As it can be seen from the charts, that the presence or absence of oxygen does not show a significant inhibition time before polymerization could start. The x's represents data points used in the fit, and the o's represent data points not used to fit the rate constants.



**Figure 77 Conversion data by FTIR, along with the model-predicted conversions a) deoxygenated conditions and b) oxygenated conditions. x's represents data points used in the fit, and the o's represents data points not used to fit the rate constants [44]**

To gain better insight into the kinetic model, the equations shown in 5.3 and 5.8-5.10 were modeled in COMSOL® software assuming one-dimensional diffusion. The physical parameters were used as listed in Table 6. The simulation results for the conversion curves matched the results in Figure 77, as expected. The same model was then simulated for the conditions under which the microrheology experiments were conducted. Specifically, the model was simulated with an intensity  $I_0$  of  $10\text{W/m}^2$  and photoinitiator concentration of 5wt%. The rate constants optimized for this set of experimental conditions were  $\{K_p, K_t \text{ \& } K_{t,O_2}\} = \{0.504, 1.31, 2.06\} \frac{\text{m}^3}{\text{mol s}}$  when the conversion cutoff is assumed as 20%.



**Figure 78 Simulation results from 1D COMSOL® simulation (Red curve shows fractional monomer conversion; blue curve shows normalized concentration of oxygen; time is in seconds)**

Figure 78 shows the simulation results from one-dimensional COMSOL® simulation at a depth of  $8\mu\text{m}$ . The red curve shows the fractional monomer conversion and the blue curve shows the normalized concentration of oxygen as a function of irradiation time. The experimental data from Slopek [45] suggests that the height of  $8\mu\text{m}$  under the given conditions must start to gel at around 3.8s. From the Figure, it is seen that this suggests a double bond conversion of around 20% is sufficient to begin the gel. It is interesting to note that by using the fitted rate constants, at a conversion of 20%, the simulated oxygen concentration in the system is still around 35% of the original concentration. It is known from literature that oxygen competes strongly for the radicals to form a stable peroxy radical. Until most of the oxygen in the reaction volume has been used up, via reaction with radicals, there is very little consumption of the monomer [47].

However, the results from Figure 78 show that there should be substantial amount of dissolved oxygen in the system when the photopolymer resin starts to gel. This suggests that there is a need to modify the kinetic model to explain the phenomena driving the photopolymerization reaction.

### 6.1.2 Need to modify the rate constants

The authors, Boddapati et. al [44], did specify that the rate constants are not unique and may vary over a significant range as long as the quantity  $K_p/\sqrt{K_t}$  is maintained constant for the experimental conditions considered in the paper. Of the three rate constants, it is very likely that the rate constant for oxygen consumption,  $K_{t,O_2}$ , must be varied significantly to explain the effect of oxygen inhibition. The rate constant for oxygen termination  $K_{t,O_2}$  is often expected to be faster than  $K_t$ , due to some combination of a higher intrinsic reactivity of oxygen with a radical as compared to the vinyl double bond or to a higher diffusivity for oxygen in the resin than the monomer itself [22,23]. Since the objective of this research is to understand the effects of oxygen inhibition and diffusion on the shape of the cured parts, it is essential to derive a better understanding of the rate constant for oxygen termination,  $K_{t,O_2}$ . The rate constants were obtained by fitting the simulation results to the FTIR experimental data, which were conducted at a very high intensity of  $140\text{W/m}^2$ . This value is 175 times higher than the intensities used in the ECPL process. When curing at a very high light intensity, the resin chamber is overwhelmed by the newly generated radicals. There is not enough time for oxygen to quench the reaction and cause any significant observable inhibition time. Hence, the rate constants obtained by fitting the simulations to high intensity experimental results might

not provide adequate insight into the polymerization phenomena, especially oxygen inhibition and diffusion.

Decker et. al [47] was one of the first research groups to confirm that the concentration of dissolved oxygen in the system had to drop by at least a factor of 300 before polymerization could begin. The researchers also suggested that the rate constant for termination of radicals by oxygen is around two orders of magnitude higher than the rate constant for termination. The following section presents how an appropriate experimental data set was used to optimize the rate constants.

### **6.1.3 Estimating kinetic rate constants**

In order to find the suitable range of rate constants, which can also explain the oxygen inhibition and diffusion effect, we need experimental data with the inhibition times from both oxygenated and deoxygenated samples. In order to find an optimized set of rate constants which would be valid for experiments conducted on the ECPL system, the experimental data from microrheology experiments conducted by Slopek [45] could be used. These experiments were conducted at  $10\text{W/m}^2$ , which is  $\sim 12$  times higher than the intensities encountered in ECPL. However, the light intensity used in the microrheology experiments is an order of magnitude closer to the conditions in ECPL and hence preferred over the FTIR experimental data set. Slopek [45] used a microrheology system to investigate the inhibition times for TMPTA with DMPA as the photoinitiator. Experiments were conducted with both oxygenated and deoxygenated samples.

Slopek confirmed that polymerization could be modeled as a simple two-step process. If the diffusion of oxygen is fast in comparison to the radical generation, a cross-linked network cannot be formed until all the dissolved oxygen in the system is consumed. The following equation was proposed for the gel time,

$$t_{gel} = t_{inhib} + t_{gel,DEOX} \quad (6-11)$$

where  $t_{gel}$  is the total time to gelation,  $t_{inhib}$  is the oxygen inhibition time during which oxygen is consumed, and  $t_{gel,DEOX}$  is the time required for gelation in the absence of oxygen. Table 7 shows the experimental data of the gel time obtained from Slopek's Ph.D. thesis [45].

**Table 7 Experimental data on gel times from Dr. Slopek [45]**

Test	Intensity (W/m <sup>2</sup> )	DMPA conc. (wt %)	Rate of Initiator Decomposition, $R_i$	$t_{gel,DEOX}$ (s)	$t_{gel}$ (s)
#1	8	2	$39.44 \times 10^{-3}$	2	12
#2	8	1	$19.72 \times 10^{-3}$	2.8	23
#3	4	2	$19.72 \times 10^{-3}$	3	26

A parametric study was conducted in order to estimate an appropriate range of rate constants. The steps utilized were as follows:

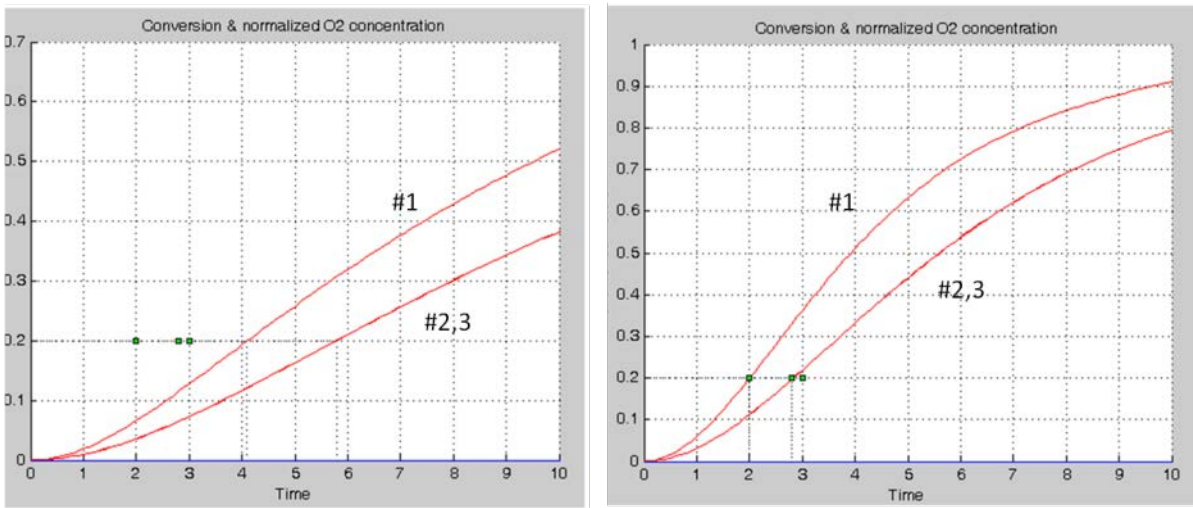
1. Obtaining the ratio,  $K_p/\sqrt{K_t}$  :

Since the authors suggested that the rates can vary over a significant range as long as the ratio  $K_p/\sqrt{K_t}$  is kept constant, the first step was to estimate the range of this



ratio suitable for the experimental conditions considered in this research. To eliminate the effect of rate constant of oxygen consumption, the data from the deoxygenated samples was considered. A double bond conversion cut-off of 20% was assumed, since this is known from literature for the tri-functional acrylate that was used for the study. A value of  $K_p/\sqrt{K_t}$  was estimated by a least squares fit between the experimental gel time for deoxygenated samples and the model predicted gel times.

The fitted ratio of  $K_p/\sqrt{K_t}$  was found to be  $1.45 (m^3/mol s)^{1/2}$



**Figure 79 Simulation plots showing double-bond conversion for deoxygenated samples. Green dots show experimental data. Left figure shows the simulation results prior to changing the rate constants. Right figure shows the results after using the new rate constants  $\{K_p, K_t\} = \{1.66, 1.31\} m^3/mol s$**

Figure 79 shows the simulation results before and after using the revised rate constants. The plot on the left is generated using the rate constants as published in Boddapati et. al [44]. The plot on the right is generated using the revised rate constants obtained after least squares fitting to the experimental data from Slopek [45], shown in green dots in the figure. The horizontal dashed line shows the monomer conversion cut-

off of 20%, which is assumed as the cut-off for gelation. Ideally, the green dots should coincide with the intersection of the dashed black line with the red conversion curve line.

2. Obtaining the rate constant for oxygen termination,  $K_{t,O_2}$ :

Keeping the ratio from above step constant, the rate constant for oxygen termination,  $K_{t,O_2}$ , was estimated by least squares fit between the experimental gel times from oxygenated samples and the model predicted gel times. The rate constant  $K_{t,O_2}$  was found to be in the range of  $125 \text{ m}^3/\text{mol s}$ .

Following the above steps, the rate constants were thus found to be,

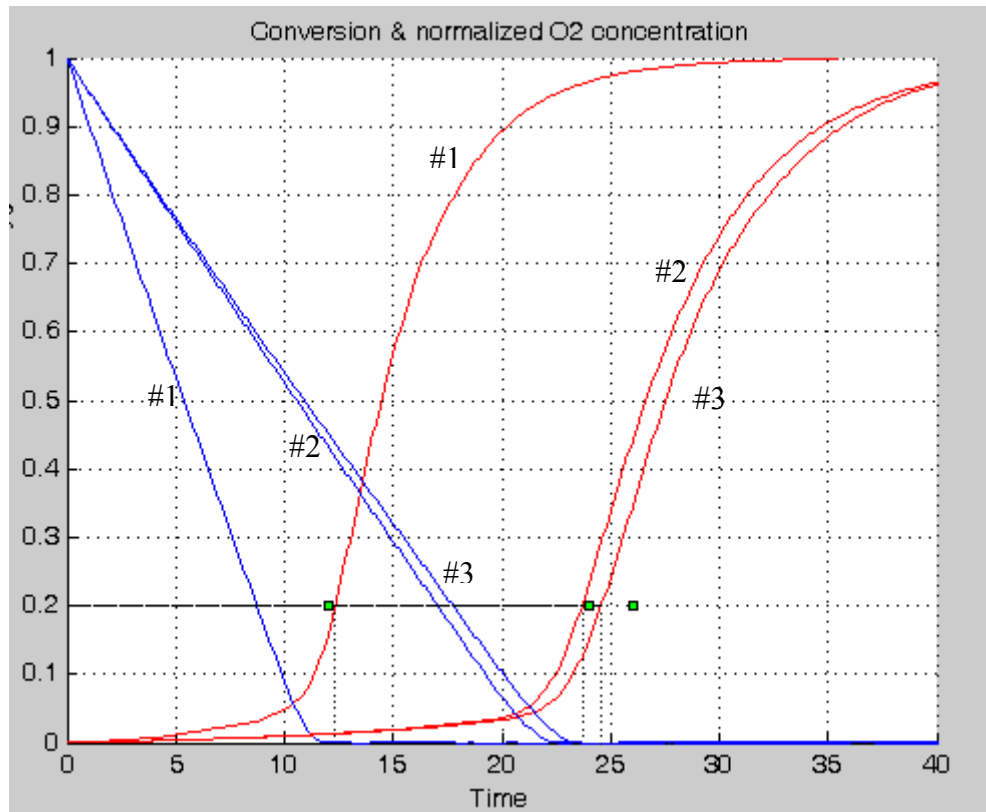
$$\{K_p, K_t \text{ \& } K_{t,O_2}\} = \{1.66, 1.31, 125\} \frac{\text{m}^3}{\text{mol s}}.$$

Figure 80 shows the simulation plots obtained by using the new rate constants. The horizontal dashed line shows the monomer conversion cut-off of 20%, which is assumed as the cut-off for gelation. Ideally, the green dots should coincide with the intersection of the dashed black line with the red conversion curve line. It is to be noted that the simulation plots with the revised rate constants do not precisely fit the experimental data. There are numerous reasons which may explain this behavior. Firstly, it is not confirmed that the conversion cutoff of 20% is indeed valid for this material at all the three experimental conditions considered in this study. Secondly, polymerization is a complex process involving heat and mass transfer of all the species. Only mass transfer of oxygen was considered in this study. Moreover, the effect of chain length is also not considered. However, despite these drawbacks of the model, it can quite closely predict the gel times and explain the substantial reduction of dissolved oxygen concentration prior to gelation.

As an alternative approach to optimizing the rate constants, it is possible to conduct actual experimental studies using FTIR to measure the rate constants. However, the FTIR procedure is typically conducted at an extremely high intensity (compared to the conditions for the ECPL process), which essentially undermines the effect of oxygen inhibition and diffusion by fast curing. The proposed rate constants were obtained under experimental constraints and no claim is made that the presented optimization method will be better than conducting actual experiments.

It has to be acknowledged that the rate constants obtained from the above procedure are not unique. They are simply calibration coefficients, which are treated as empirical constants for chemical kinetics model. However, the presented discussion provides an enhanced understanding of these rate constants. Moreover, the optimized constants provide a better fit to the experimental data than those available in literature.

The models presented above will be extended further to develop two-dimensional models to predict the shape of the cured parts.



**Figure 80 Simulation plot showing the normalized oxygen concentration (blue) and fractional double-bond conversion (red). The experimental data points are shown as green dots**

For comparison purposes, the simulation conditions used in Figure 78 were rerun using the revised rate constants, where the intensity  $I_0$  is  $10\text{W/m}^2$  and photoinitiator concentration of 5 wt%. The simulation result is shown in Figure 81. It is to be noted that with the revised rate constants, the oxygen concentration now seems to be substantially lower prior to gelation, which is assumed to occur at 20% conversion.

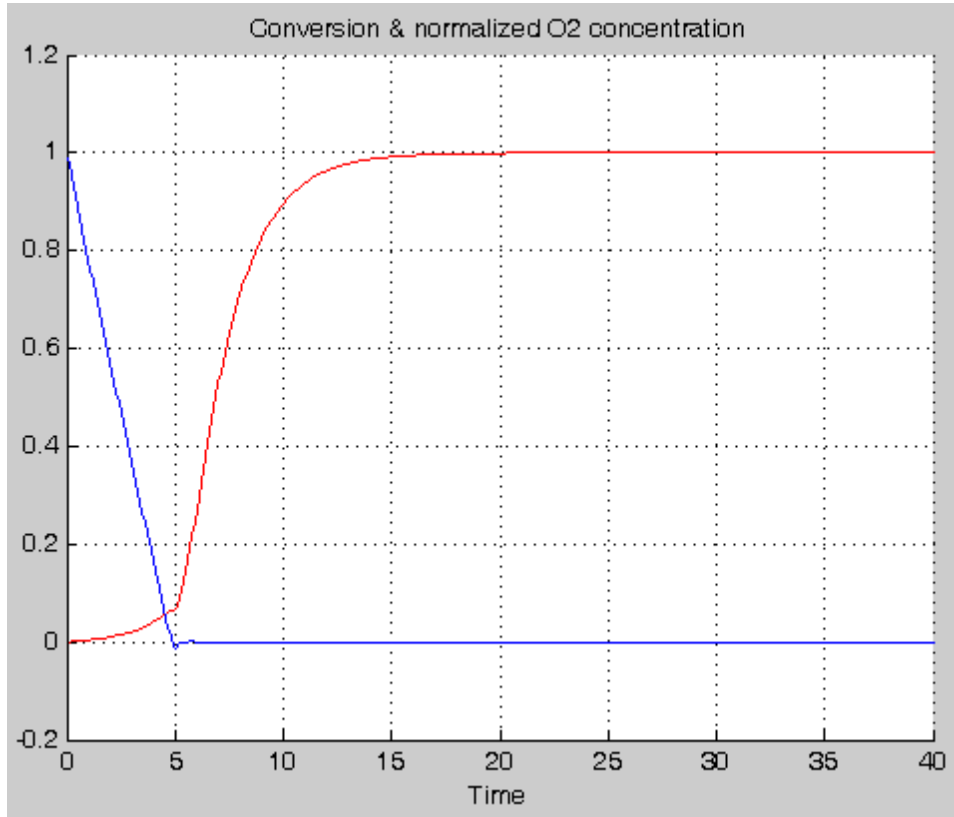


Figure 81 Simulation results from COMSOL® 1D model (using revised rate constants)  $\{K_p, K_t \text{ \& } K_{t,O_2}\} =$

$$\{1.66, 1.31, 125\} \frac{m^3}{mol s}$$

## 6.2 Two-dimensional modeling & simulation results

The one-dimensional model explained in the earlier section can be used to predict the gel time at a specific height in a sample. Since parts fabricated from ECPL are three-dimensional structures, a model was required, which could also predict the entire shape of the cured part. In order to transition from a one-dimensional model to two-dimensions, Eq. 6-10 was modified as Eq. 6-12 as follows:

$$\frac{\partial [O_2]}{\partial t} = -k_{t,O_2} [R \cdot][O_2] + D_{O_2} \frac{\partial^2 [O_2]}{\partial x^2} + D_{O_2} \frac{\partial^2 [O_2]}{\partial z^2} \quad (6-12)$$

Equations 6-1 to 6-9 and 6-12 were used and simulated using COMSOL® software with 2D conditions. The rate constants from the ordinary differential equations are modeled along with the diffusion model in COMSOL®. Application mode ‘*chdi*’ was selected in COMSOL® to simulate the diffusion process. The initial concentrations of monomer and photoinitiator were calculated as shown in Table 2, using the values shown in Table 8. The number of double bonds for monomer is considered thrice the normal weight, as it is a tri-functional monomer. Experiments were conducted with 20wt% of photoinitiator concentration.

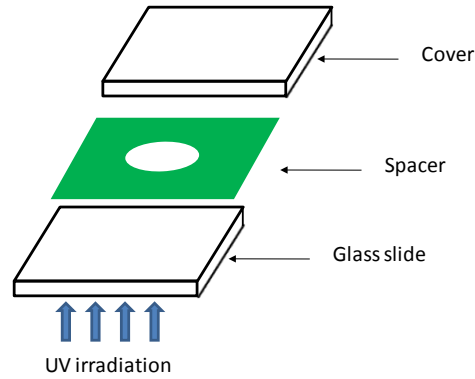
**Table 8 Calculation for concentration of double-bond and photoinitiator**

	<b>Double-Bond Concentration</b>	<b>PI Concentration</b>
Equation	$\frac{3 * (100 - wt \%)}{MW * 0.0001}$	$\frac{wt\%}{MW * 0.0001}$
Molecular Weight, MW	296 g/mol	256 g/mol
Calculated concentration	8108.11 mol/m <sup>3</sup>	781.25 mol/m <sup>3</sup>

### 6.2.1 Numerical finite element model

COMSOL® simulations were conducted to predict the height and profile of the final cured part. The working bitmap, which has a width of 90 pixels, projects an irradiation region, which is approximately 560 μm wide. A 2D finite element model was created to simulate the experimental conditions. The width of the model was taken as

1mm and the height as 200  $\mu\text{m}$ , which match the dimensions of the reaction chamber in the actual experimental setup and shown schematically in Figure 82.



**Figure 82 Schematic of the resin chamber used for simulation purposes**

The simulated finite element mesh geometry is as shown in Figure 83. The entire geometry was meshed using 1855 triangular elements. The size of the finest mesh in the irradiation area was  $8\mu\text{m}$ . The red arrows show the area that receives irradiation. The entire rectangular subdomain is assumed as filled with liquid resin mixture. All boundaries are assumed as insulated, which closely resembles the actual experimental conditions. The coordinate system is also shown in the figure.

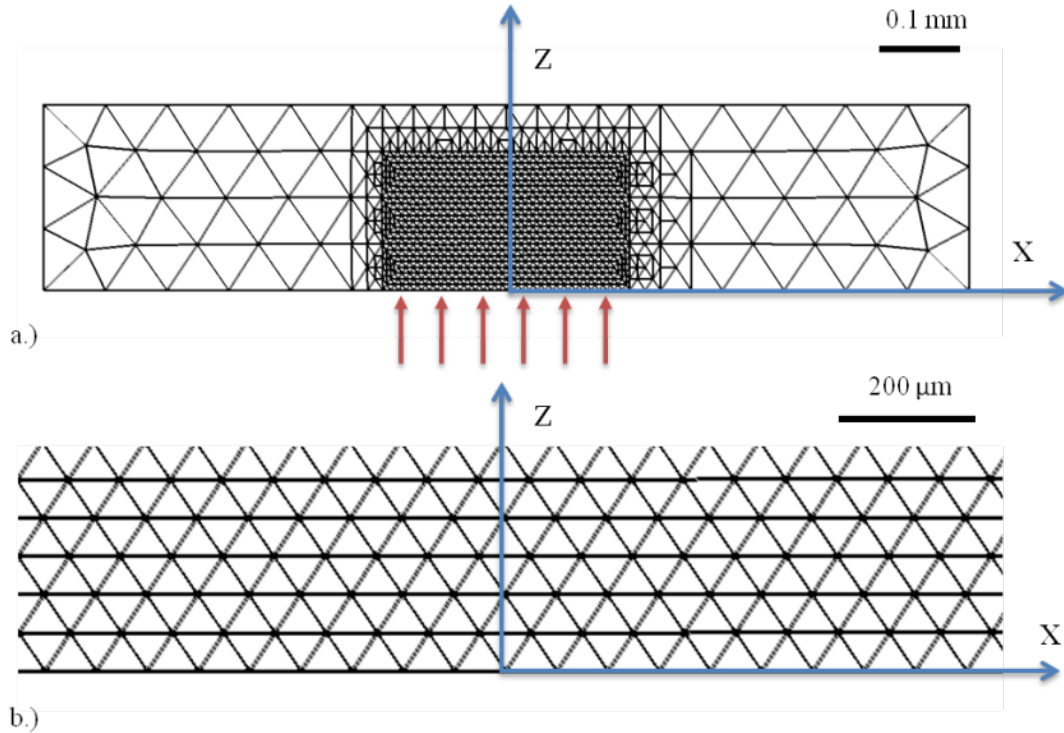


Figure 83 a.) Schematic of the FE mesh geometry simulated using COMSOL®;  
 b.) Enlarged view of the FE mesh

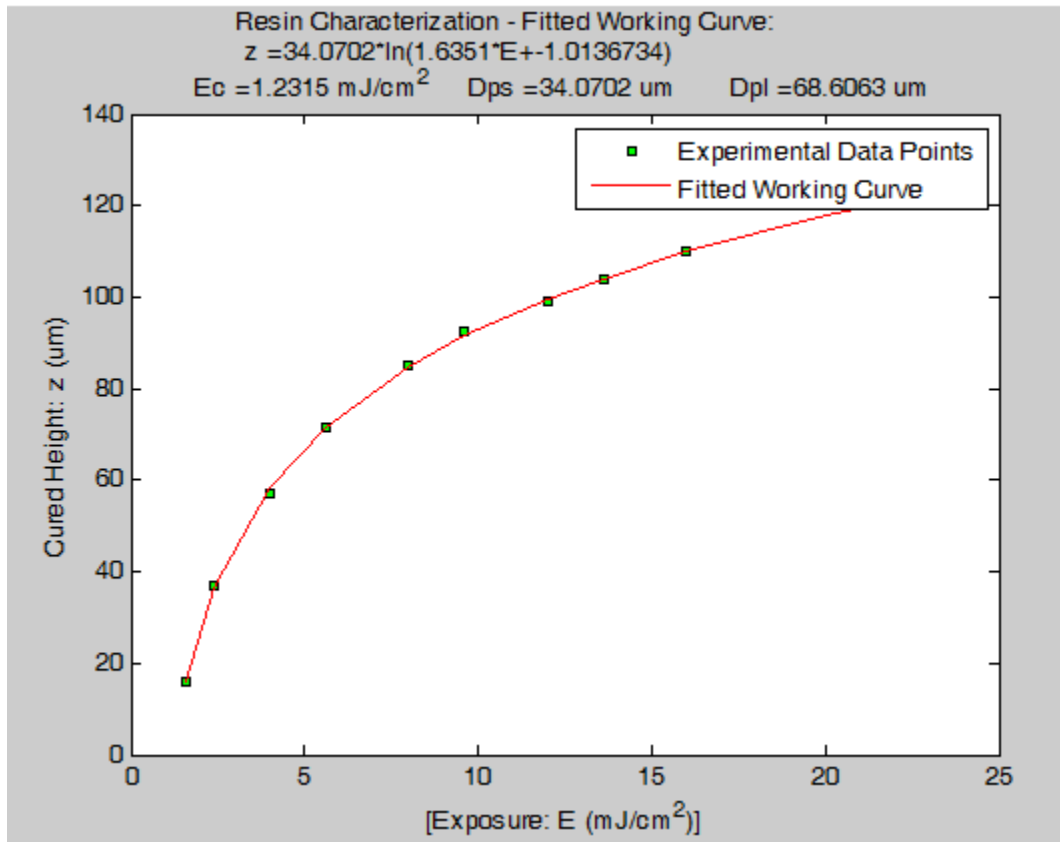
### 6.2.2 Simulation results & comparison with experiments

Experiments were conducted on the ECPL system. The polymerized parts were cured on a glass slide. After curing, the glass slide is removed from the resin chamber and additional uncured resin is removed using an air duster. A 3D laser LEXT confocal microscope was used to measure the cured part profile using the glass slide as the reference. The experimental data were fitted to the empirical model, presented in Eq. 2-4 and repeated here for convenience.

$$z \approx D_{pS} \ln \left[ \frac{D_{pL} E}{D_{pS} E_c} + 1 - \frac{D_{pL}}{D_{pS}} \right] \quad (6-13)$$



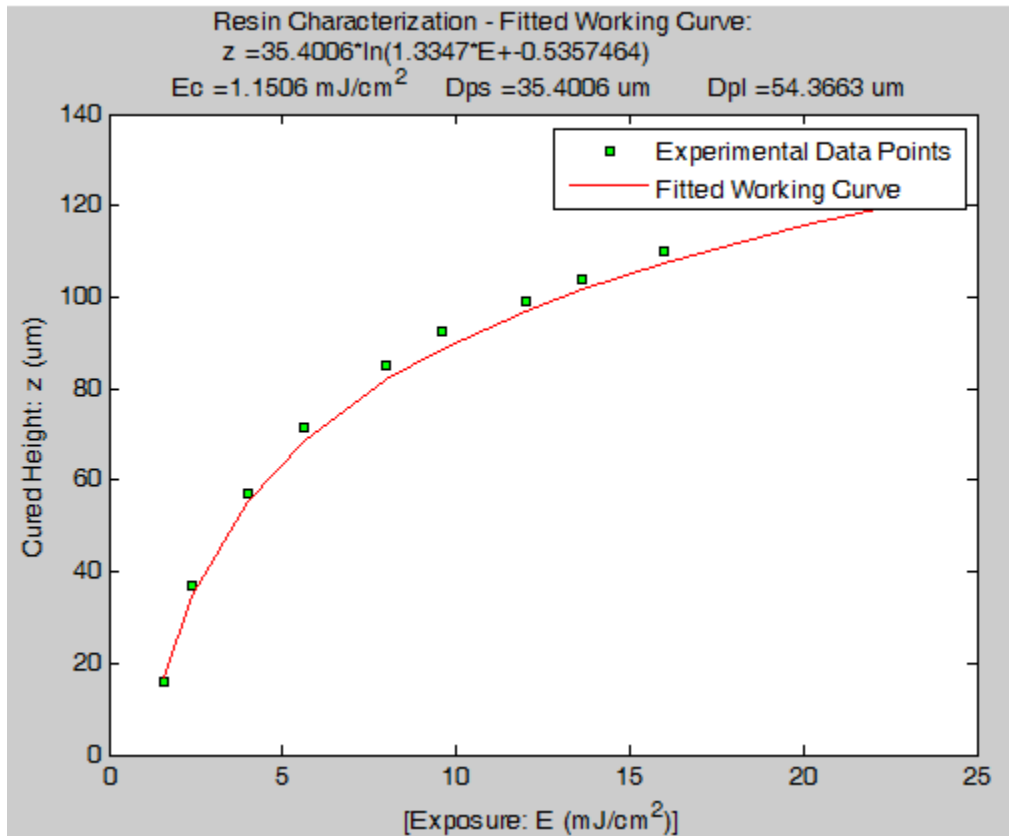
where  $D_{pL}$  is the depth of penetration for liquid resin and  $D_{pS}$  is the depth of penetration for a cured layer. The parameters  $E_c$ ,  $D_{pL}$  and  $D_{pS}$  are usually fit to experimental data at a specific resin composition and cure intensity, and were found to be  $1.23 \text{ mJ/cm}^2$ ,  $68.61 \text{ }\mu\text{m}$  and  $34.07 \text{ }\mu\text{m}$ , respectively. Figure 84 shows the plot of the working curve with the experimental data points superimposed and shown as green dots.



**Figure 84 Experimentally obtained working curve (in red) fitted with experimental data shown in green dots**

The COMSOL® finite element model was simulated assuming an irradiation generated by a bitmap of 90pixel width. The exposure profile obtained from the UV-CCD, as shown in Figure 62 was used to simulate the input irradiance condition to the FE model.

Figure 85 shows the working curve obtained from COMSOL® simulations. The experimental data points are shown in green dots. It can be seen that the simulations closely predict the experimental heights with the parameters,  $E_c$ ,  $D_{pL}$  and  $D_{pS}$  found to be 1.15 mJ/cm<sup>2</sup>, 54.37 μm and 35.40 μm, respectively.

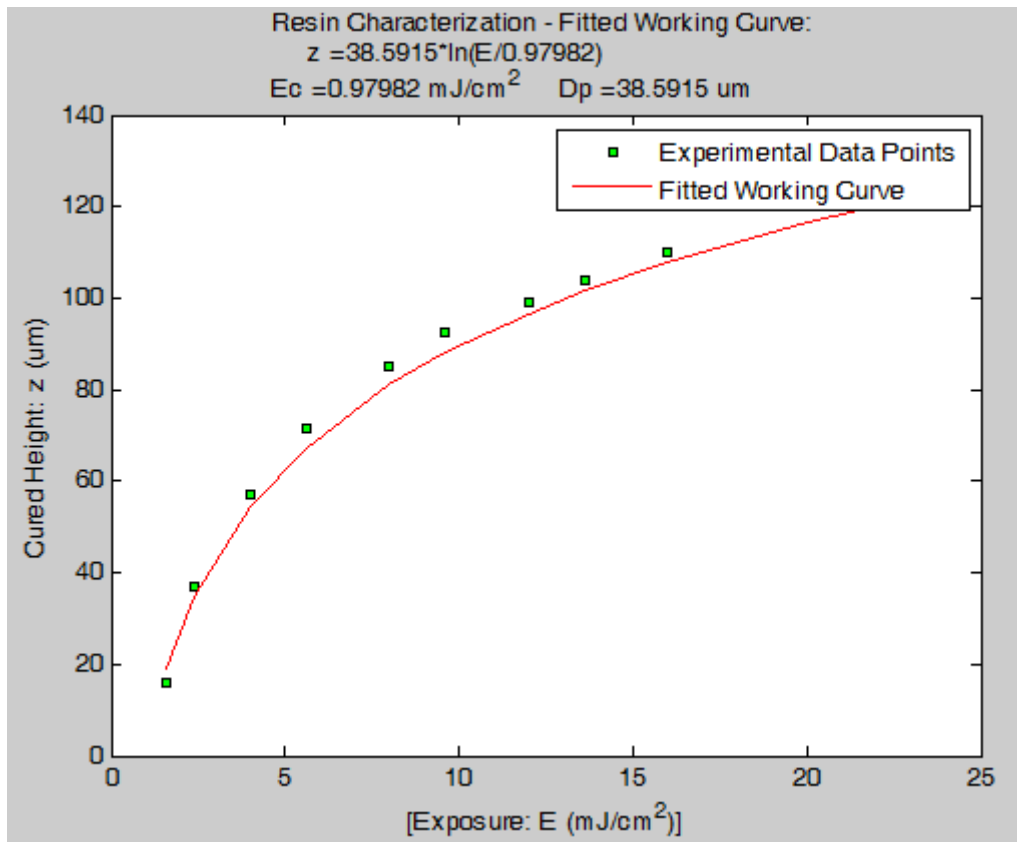


**Figure 85 Working curve (in red) obtained from COMSOL® simulations with experimental data shown in green dots**

Limaye [43] had introduced the idea of using  $D_{pS}$  and  $D_{pL}$ , instead of a single  $D_p$  to account for difference in attenuation rates between solid and liquid. The idea was that there is lesser attenuation when light passes through a cured solid compared to uncured liquid. Hence,  $D_{pS}$  is supposed to be significantly larger than  $D_{pL}$ . However, in this case, we find that  $D_{pS}$  is smaller than  $D_{pL}$ . This observation is plausible, since Limaye's

observations were based on a different resin material for much larger size domains. Hence, the well-known  $E_c - D_p$  model (as shown in Eq 6-14) was used to fit the simulation data, as shown in Figure 86. The  $E_c$  and  $D_p$  values after fitting to the equation were found to be  $0.98 \text{ mJ/cm}^2$  and  $38.59 \text{ }\mu\text{m}$ , respectively.

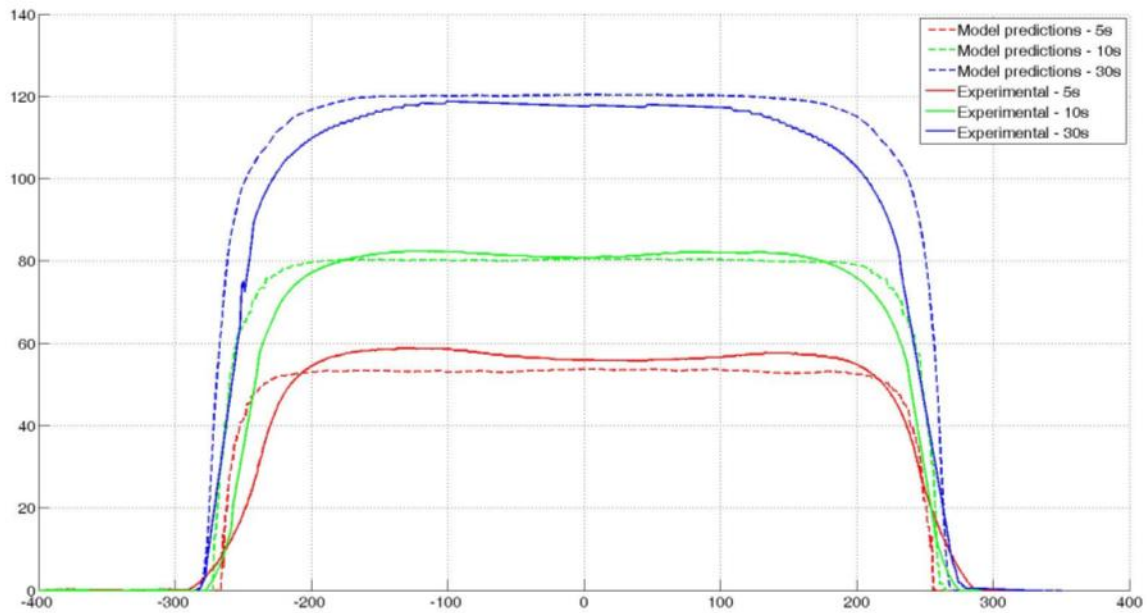
$$E(z) = E_{max} e^{\frac{-z}{D_p}} \quad (6-14)$$



**Figure 86 Working curve (red) obtained from COMSOL® simulations using simpler  $E_c$ - $D_p$  model to fit experimental data (green dots)**

The simulations seem to predict the height of the cured part fairly well. However, the primary utility of the two-dimensional model lies in its ability to estimate the part shape in two dimensions. To test this utility, the experimentally cured profiles were

superimposed on the simulated cured profile from COMSOL® simulations as shown in Figure 87. The dashed lines show the predicted profile of the cured part for different energy doses provided. The shape of the cured part was estimated by tracking the coordinates within the sample where the double bond conversion has reached the critical conversion limit of 20%.



**Figure 87 Comparison of experimental profiles (solid lines) with simulated profiles (dashed lines) Red: 5s exposure; Green: 10s exposure; Blue: 30s exposure. X & Y axes are in micrometers**

The simulations closely predict the height and width of the cured parts. Moreover, the edges also seem to show the curvatures resulting from greater oxygen inhibition effect at the edges than the center. A potential explanation for the mismatch in edge profile is that the rate constants and other coefficients are assumed independent of time and location in the reaction chamber in our study. This assumption needs further in-depth studies, which is beyond the scope of this thesis. A second potential explanation is

shrinkage. Shrinkage during resin cure causes reduction in feature dimensions, but it also causes residual stresses, which can lead to distortions in part shapes. Investigation of shrinkage can be a future scope of work, which may be conducted in order to improve the predictability of the model. Despite these limitations, the COMSOL® simulations successfully demonstrate the generation of curved edges for the cured parts. This effect of oxygen inhibition was not considered using the empirical  $E_c - D_p$  model. It can only predict that the final cured shape will be the same height and will fail to show the edge curvatures. Hence, the  $E_c - D_p$  model, in its original form, cannot be used to predict the shape of the cured part. This leads us to the third research question:

### **Research Question #3**

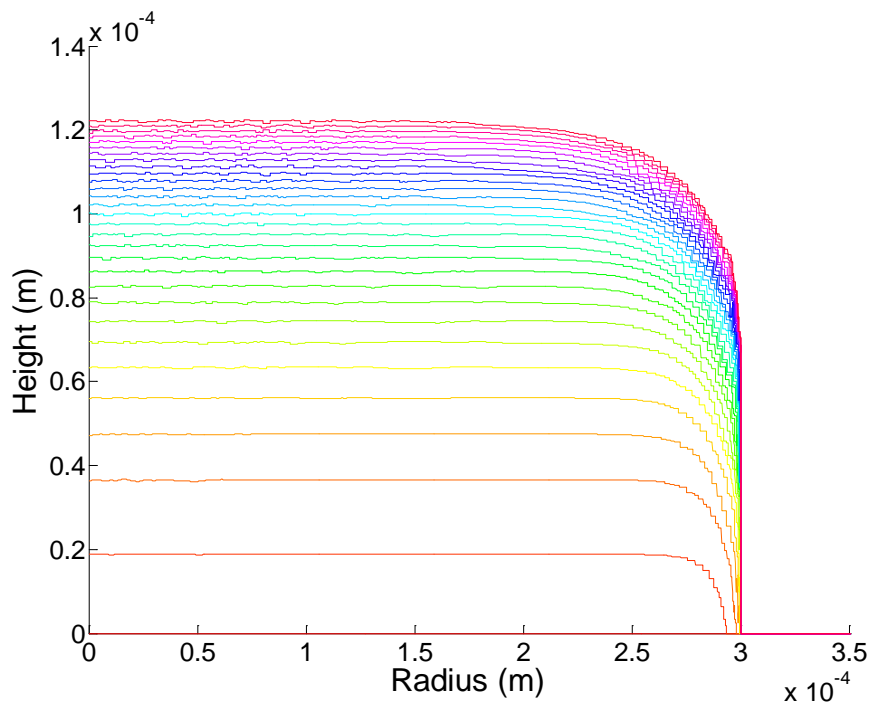
**How to model the photo-polymerization reaction to include the complex/coupled effects of Oxygen in the photopolymerization process for curing using ECPL process?**

### **6.3 Preliminary observations from axi-symmetric simulations**

For process planning purposes, an empirical material model is required, which could provide a relationship between the shape of the exposure projected at the substrate and the final cured part shape. This material meta-model will be implemented in the subsequent chapter for process planning purposes.

Since the COMSOL® simulations can predict the shape of the cured part, an empirical meta-model can be developed by systematically conducting numerous simulations. The final parts to be fabricated from the ECPL system are lens shaped and

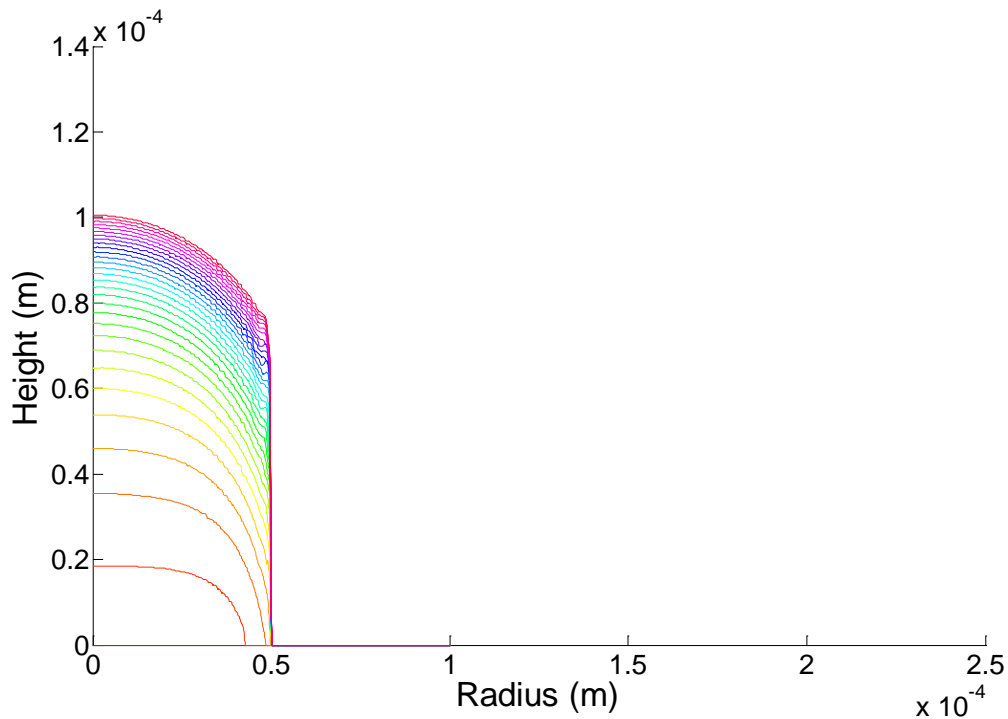
hence axi-symmetric in nature. In order to reduce the computational time and develop empirical models from COMSOL® simulations directly applicable for curing lens shaped structures, the rate equations with oxygen diffusion were simulated assuming an axi-symmetric geometry. Due to limitations with computational resources, three-dimensional simulations could not be performed. The following sections explain the simulation results and the approach in obtaining the material meta-model.



**Figure 88 Simulated cured part profiles obtained from COMSOL® simulations for radius of 300 microns for varying exposure doses**

Figure 88 shows the simulated cured part profiles obtained from COMSOL® simulations for exposed region of 300  $\mu\text{m}$ . Each line corresponds to a profile for a specified exposure time. The exposed times ranged from 1s (yielding no cure) to 30s (red curve) in 1s increments. The predicted profile of the cured part clearly shows a curvature

at the edges. Moreover, the radius of curvature increases for higher exposures. This is very well expected and can be explained as follows. The light attenuates as it goes deeper into the material. This leads to lesser and lesser generation of the live radicals. The dissolved oxygen molecules are already present and are continually diffusing into the curing region – simultaneously inhibiting the polymerization reaction. This dynamic (transient) process of oxygen inhibition and diffusion explains as to why the radii of curvature at the edges of the estimated cured part profiles increase with more exposure dose.

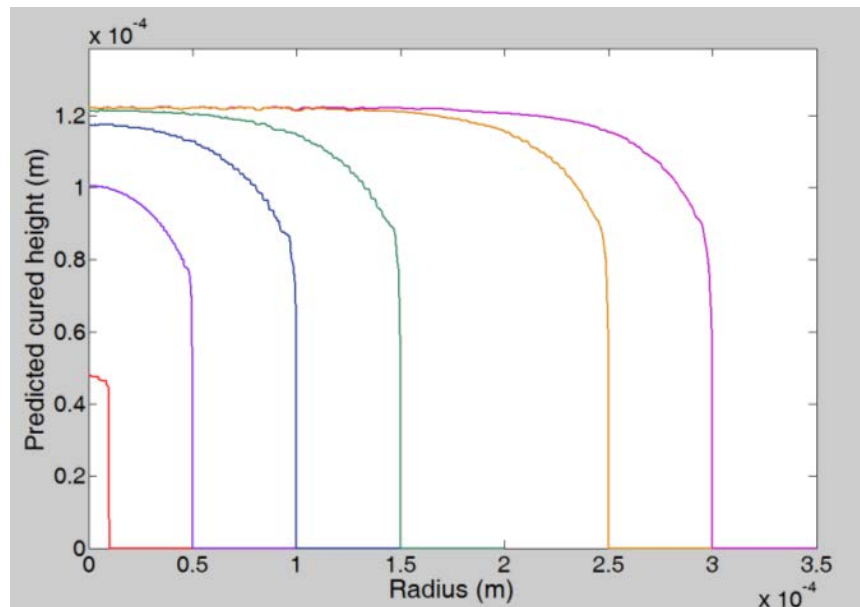


**Figure 89 Simulated cured part profiles obtained from COMSOL® simulations for radius of 50 microns for varying exposure doses**

Figure 89 shows the simulated cured part profiles obtained from COMSOL® simulations for exposed region of 50 $\mu$ m. Each line corresponds to a profile for a specified

exposure time. As shown for Figure 88, the exposed times ranged from 1s (yielding no cure) to 30s (red curve) in 1s increments. The maximum predicted cured height for an energy dose corresponding to 30s and the total exposed radius of 50 $\mu\text{m}$  is 100 $\mu\text{m}$ . Interestingly, this height is around 20 $\mu\text{m}$  lesser than the maximum predicted cured part height when the total exposed radius is 300 $\mu\text{m}$ .

Simulations were conducted by varying the total exposed region from 300 $\mu\text{m}$  to 10 $\mu\text{m}$ . The predicted part profiles for a total exposure of 30s are shown in Figure 90. The different colors represent the predicted part profiles obtained by varying the exposed radius. It is clearly seen that the oxygen inhibition and diffusion effects become prominent as the total exposed region is reduced.



**Figure 90 Predicted part profiles for a total exposure of 30s by varying exposed widths**

In order to develop a material meta-model, the simulation results obtained from COMSOL® can be used to formulate an empirical response surface, which can be used to



predict the height of the cured part at a given location for a given radius of exposure. This leads us to the following hypothesis:

### **Hypothesis to Research Question #3**

*Oxygen inhibition and diffusion are the primary factors, which result in a deviation of the material response from the known  $E_c - D_p$  model. This change in the resin behavior can be modeled by modifying the  $E_c - D_p$  model to incorporate the under curing observed at the edges due to oxygen inhibition and diffusion.*

### **6.4 Design of experiments for development of an empirical model**

The  $E_c - D_p$  model was developed for predicting the maximum cured part height for a given resin composition. This model seems to work perfectly well for predicting the maximum cured part heights (at the center) for large samples. From Figure 87 and Figure 88, it is evident that the cured parts show a curvature at the edges and this cannot be currently modeled by the  $E_c - D_p$  model. Moreover, Figure 90 shows that oxygen inhibition can substantially affect the applicability of the  $E_c - D_p$  model when applied for curing smaller samples.

The advantage of using an empirical closed form model like the  $E_c - D_p$  model, is that it can be used to estimate the required exposure,  $E$ , for a desired cured part height,  $Z$ , using the following equation.

$$Z = D_p * \ln\left(\frac{E}{E_c}\right) \quad (6-15)$$

The fundamental assumption in Eq. 6-15 is that the cured part height,  $Z$ , is only a function of the exposure,  $E$ , at a specific position in the resin vat. However, as seen from Figure 88 and Figure 90, the same exposure can yield different cured part heights. The height at any specific point in the resin depends on the total exposed region and its distance from the center. This effect can be modeled by modifying the  $E_c - D_p$  model such that the constants of the equation vary as a function of total radius of the exposed region and the distance of the pixel of interest from the center. There are two constants in the  $E_c - D_p$  model – the critical exposure to cure,  $E_c$  and the depth of penetration into the resin,  $D_p$ .

Slopek [45] showed that oxygen diffusion increases the gel time or the time required to start enough curing so as to form a cured part, i.e. to reach the level of double-bond conversion required to form a cured part. Hence, it is safe to assume that the critical exposure to cure the part  $E_c$  should vary as a function of distance from the center. Based on the above facts, the value of  $E_c$  should increase from the center to the radius of the exposed region. Although there is no substantial phenomenal explanation for varying the depth of penetration,  $D_p$ , it will be treated as a variable for fitting purposes. This is a rational approach, since the effect of oxygen inhibition and diffusion is dynamic in nature. It is insufficient to assume that oxygen inhibition will only affect the critical energy to start curing. Due to the dynamic nature of curing, the effect of oxygen inhibition will continue to affect the growth of the cured part.

Table 9 shows the input variables and the response variables for the design of experiments strategy used in the following sections. It is to be noted that the total exposure time has to be varied for obtaining a single set of values for  $E_c$  and  $D_p$ .

**Table 9 Input variables and response factors for Design of Experiments**

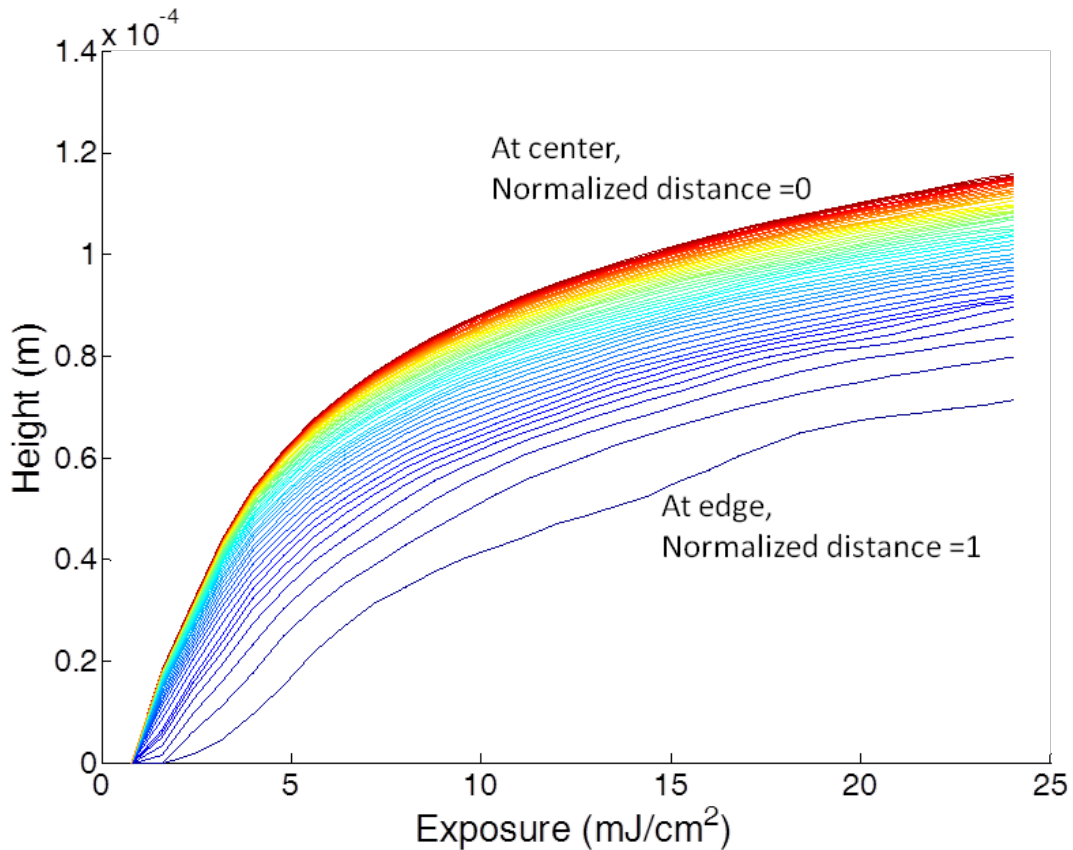
Input Variables →	Total exposure time at constant intensity (s)	Normalized distance ( <i>ratio of distance from the center to the maximum radius of exposure</i> )	Total exposed radius (μm)
Range →	1 – 30	0 – 1	10 – 300
Increments →	1	0.0016	10
Output Variables →	Critical Exposure to cure, $E_c$ (mJ/cm <sup>2</sup> ) (as a function of radial distance from the center)	Depth of penetration, $D_p$ (μm) (as a function of radial distance from the center)	

Using the COMSOL® simulations, a series of data points can be obtained, which can be used to estimate the relation between the amount of exposure and the cured height. By fitting the data points into the  $E_c - D_p$  model (Eq. 6-14), the resin parameters,  $E_c$  and  $D_p$  can be determined by minimizing the residual norm. The ‘*lscurvefit*’ function in MATLAB® was used to fit the simulated cured part heights to the  $E_c - D_p$  model. The objective function was to minimize the squared sum of errors, defined as *resnorm*, in Eq. 6-15.

$$\text{resnorm} = \sum (f(x) - y)^2 \quad (6-16)$$

### 6.4.1 Case study

Figure 91 shows the different working curves obtained for a total exposed radius of  $300\ \mu\text{m}$ . The different colors correspond to the working curves obtained by extracting the heights from the predicted cured profiles, at different distances from the center.

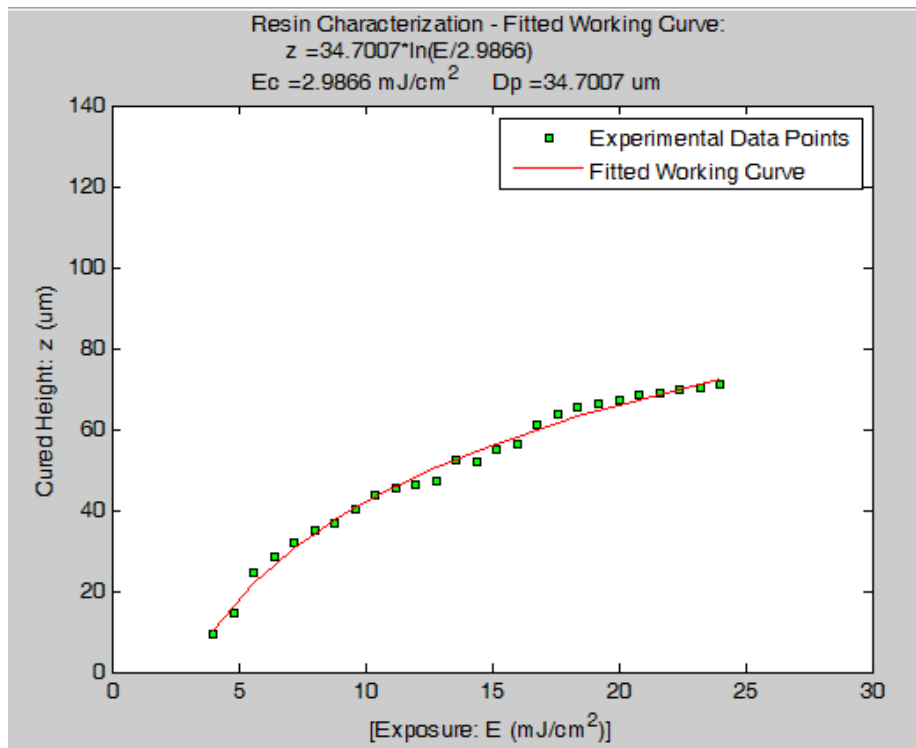


**Figure 91 Working curves obtained for total exposed radius of  $300\ \mu\text{m}$ . Different colors correspond to the working curves obtained at different distances from the center.**

The working curve obtained for the edge of the exposed region (i.e., at a normalized distance of 1) is shown in Figure 92. The value of  $\text{resnorm}$  in this case was found to be 21.105. The values of  $E_c$  and  $D_p$  for the center and the edge obtained by curve fitting for total exposed radius of  $300\ \mu\text{m}$ , are presented in Table 10.

**Table 10 Values of  $E_c$  &  $D_p$  obtained by curve fitting for total exposed radius of 300  $\mu\text{m}$**

	<b>Critical Energy to cure, <math>E_c</math> (mJ/cm<sup>2</sup>)</b>	<b>Depth of penetration, <math>D_p</math> (<math>\mu\text{m}</math>)</b>
At center, normalized distance = 0	0.97982	38.5915
At edge, normalized distance = 1	2.9866	34.7007



**Figure 92 Working curve obtained for edge of the exposed region for a total exposed region of 300  $\mu\text{m}$**

Using the above method, the critical energy to cure,  $E_c$  and the depth of penetration,  $D_p$  can be plotted as a function of distance from the center, as shown in Figure 93 & Figure 94, respectively.

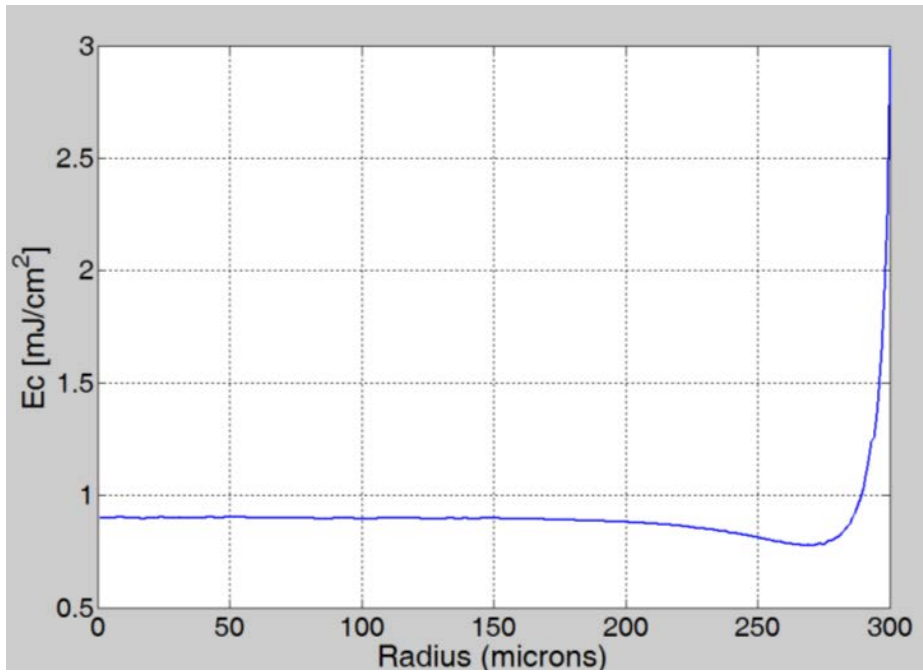


Figure 93 Variation of  $E_c$  as a function of distance from center for a total exposed region of 300  $\mu\text{m}$

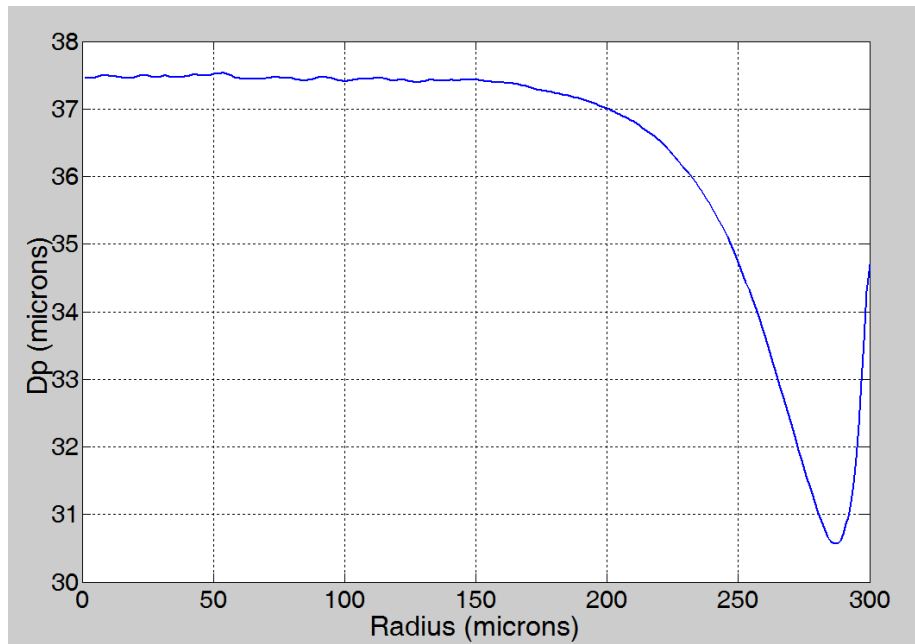
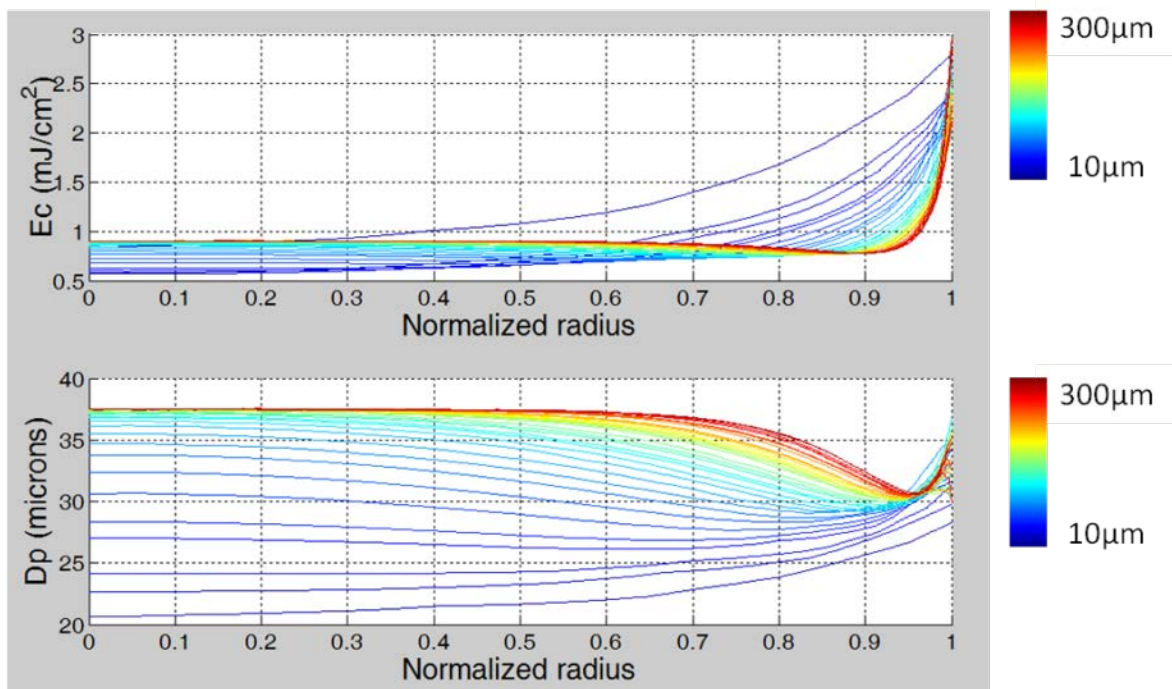


Figure 94 Variation of  $D_p$  as a function of distance from center for a total exposed region of 300  $\mu\text{m}$

Figure 95 shows the plots of  $E_c$  and  $D_p$  varying as a function of radius, when the total exposed regions are varied from  $10\mu\text{m}$  to  $300\mu\text{m}$ . As expected, the values of  $E_c$  are higher for a smaller exposed region, since there is greater oxygen inhibitory effect due to diffusion from all the radial direction and the top. Similarly, the value of  $D_p$  is lower for a smaller exposed region.



**Figure 95 Plot showing the variation of  $E_c$  and  $D_p$  as a function of radius for different exposed regions (red corresponds to  $300\mu\text{m}$  and blue corresponds to  $10\mu\text{m}$  of total exposed radius)**

The primary objective of this thesis is to formulate a process plan that can be used to fabricate individual or a combination of lens shaped (axi-symmetric) structures from the ECPL process. Hence, it is necessary to develop a material model that can estimate the necessary exposure conditions to cure a part with desired geometry specifications.

From the design of experiments conducted in section 6.4, a material parameter database was created, which can provide the radially varying values of  $E_c$  and  $D_p$  corresponding to the maximum radius of the part to be cured. The generic form of the empirical model developed is shown in Eq. 6-17.

$$Z(r, R) = \begin{cases} 0 & , \text{ for } E(r) < E_c(r, R) \\ D_p(r, R) * \ln\left(\frac{E(r)}{E_c(r, R)}\right) & , \text{ for } E(r) \geq E_c(r, R) \end{cases} \quad (6-17)$$

where  $R$  is the maximum radius ( $\mu\text{m}$ ) of the part to be cured,  $r$  is the distance ( $\mu\text{m}$ ) of the point of interest from the center and  $E(r)$  is the irradiance energy ( $\text{mJ}/\text{cm}^2$ ) incident at the point of interest.  $E_c(r, R)$  and  $D_p(r, R)$  are obtained from the material parameter database and  $Z(r, R)$  is the cured part height at the point of interest.

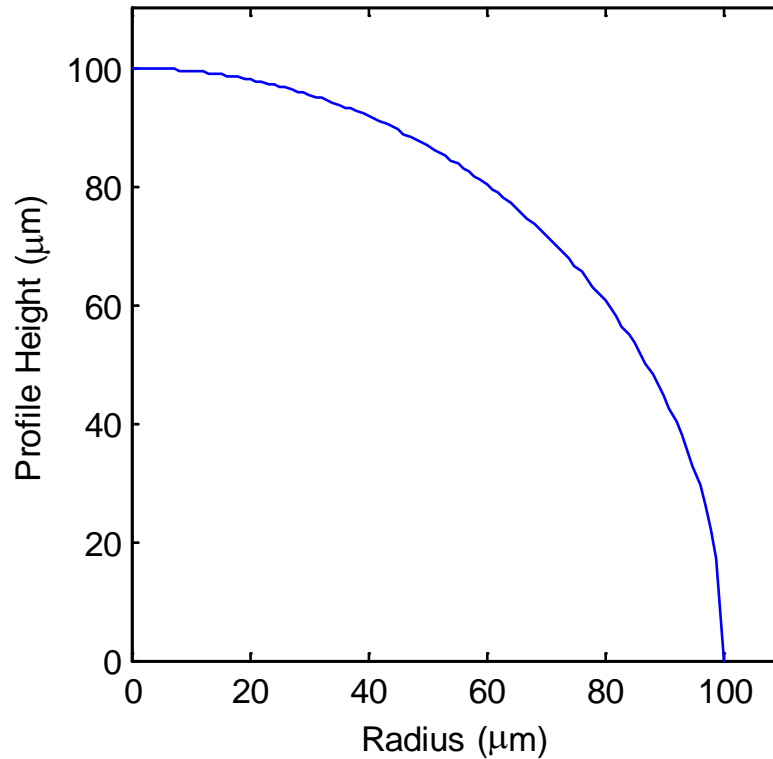
## 6.5 Validation of empirical material model

In the previous sections, the values of  $E_c(r, R)$  and  $D_p(r, R)$  were obtained by fitting the COMSOL® simulation data to the model based on Beer-Lambert's law for attenuation through a medium. The primary advantage of this model is that one need not run COMSOL® simulations to estimate the shape of the cured part. Moreover, the form of the model in Eq. 6-17 is closed form, which means that given the shape profile  $Z(r, R)$  of the part to be cured, the required exposure,  $E(r)$ , can be easily calculated using Eq. 6-18.



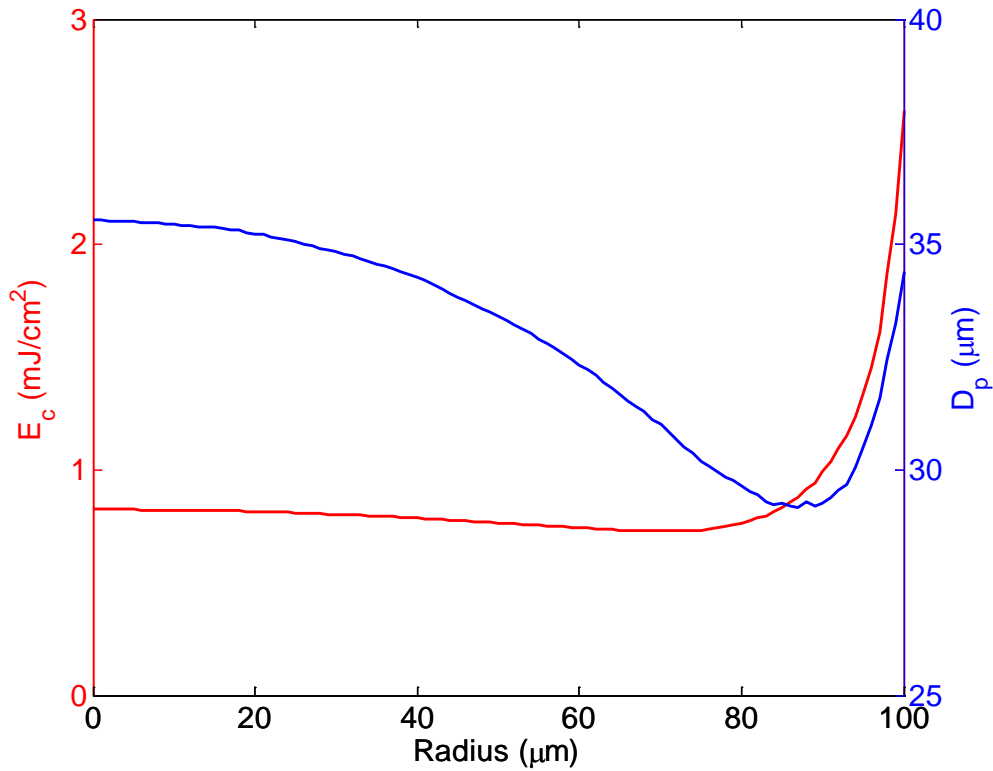
$$E(r) = \begin{cases} 0, & \text{for } Z(r, R) = 0 \\ E_c(r, R) * \exp\left(\frac{Z(r, R)}{D_p(r, R)}\right), & \text{for } Z(r, R) > 0 \end{cases} \quad (6-18)$$

In order to utilize the model in Eq. 6-18, it is necessary to ensure that this strategy of material modeling is indeed valid. To test the validity of the model, the following test case was considered. A spherical lens of radius 100 $\mu\text{m}$  with a height of 100 $\mu\text{m}$  was assumed as the desired cured part shape and so,  $R = 100\mu\text{m}$ . The half-sectional part profile is shown in Figure 96.



**Figure 96 Half-sectional view of the desired part geometry**

Using the material parameter database, the radially varying values of  $E_c$  and  $D_p$  are represented in Figure 97.



**Figure 97 Figure showing the radial variation of Ec and Dp for desired cured part of 100µm radius**

The half-sectional exposure profile required to cure the spherical structure was calculated using Eq. 6-18 and is shown in Figure 98. The red area plot shows the total energy required to cure the desired part geometry. The figure also shows the exposure profile as calculated without using the material database (plotted in black dashed lines). The dashed black curve shows the calculated exposure profile in absence of consideration of oxygen inhibition and diffusion. The square root of the squared sum of errors (Eq. 6-16) between the calculated exposures was  $10.7 \text{ mJ/cm}^2$ .

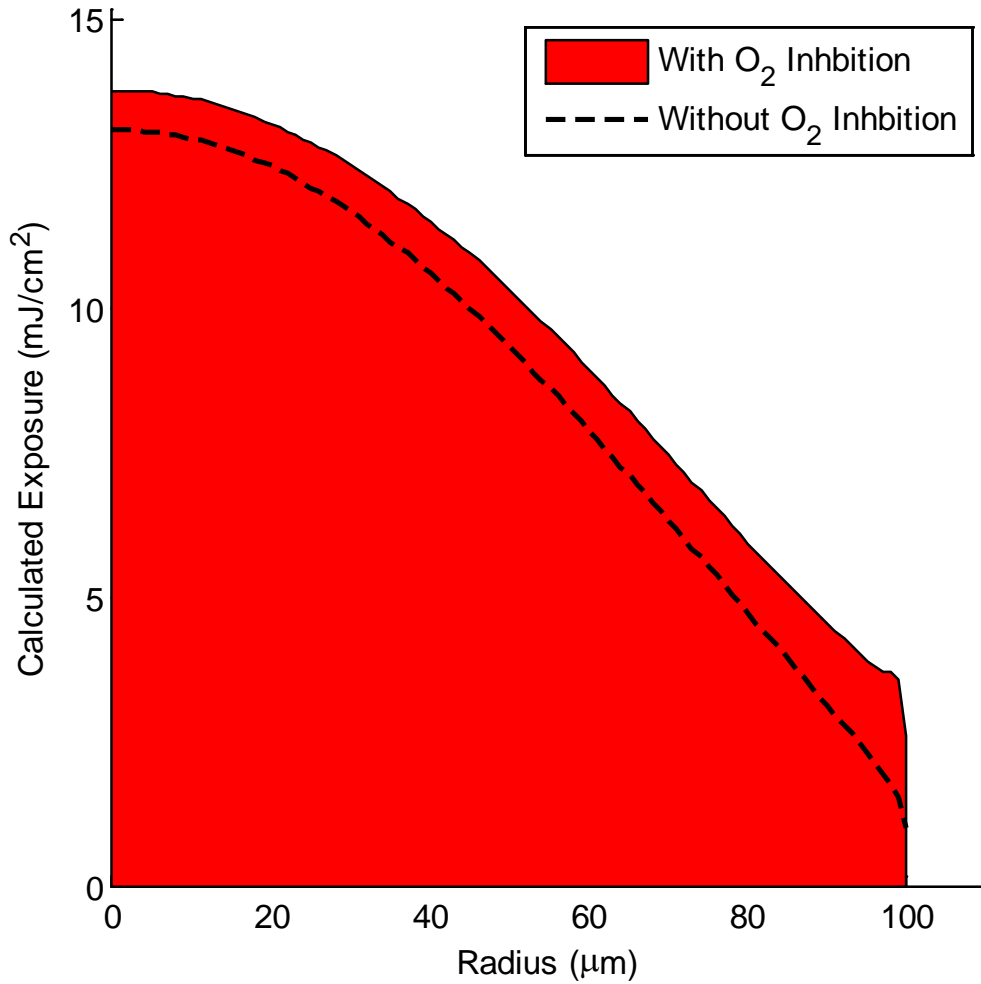


Figure 98 Calculated exposure profile for curing the spherical structure shown in Figure 96

The required exposure dose  $E$  ( $\text{mJ}/\text{cm}^2$ ) can be related with the irradiance,  $I$  ( $\text{mW}/\text{cm}^2$ ) and time,  $t$  (s) in the form of the following equation.

$$E = I * t \quad (6-19)$$

For a desired exposure profile  $E(r)$ , Eq. 6-19 can be expressed in two forms as follows.

$$E(r) = I(r) * t \quad (6-20)$$

$$E(r) = I * t(r) \quad (6-21)$$

Equations 6-20 and 6-21 show that there maybe two approaches to provide the same total exposure dose. Both these approaches were tried and the following sections present the results obtained from simulations.

### 6.5.1 Varying intensity at constant time

The exposure profile was converted into normalized intensity profile,  $I_n(r)$ , using the following equation

$$I_n(r) = E(r)/\max[E(r)] \quad (6-22)$$

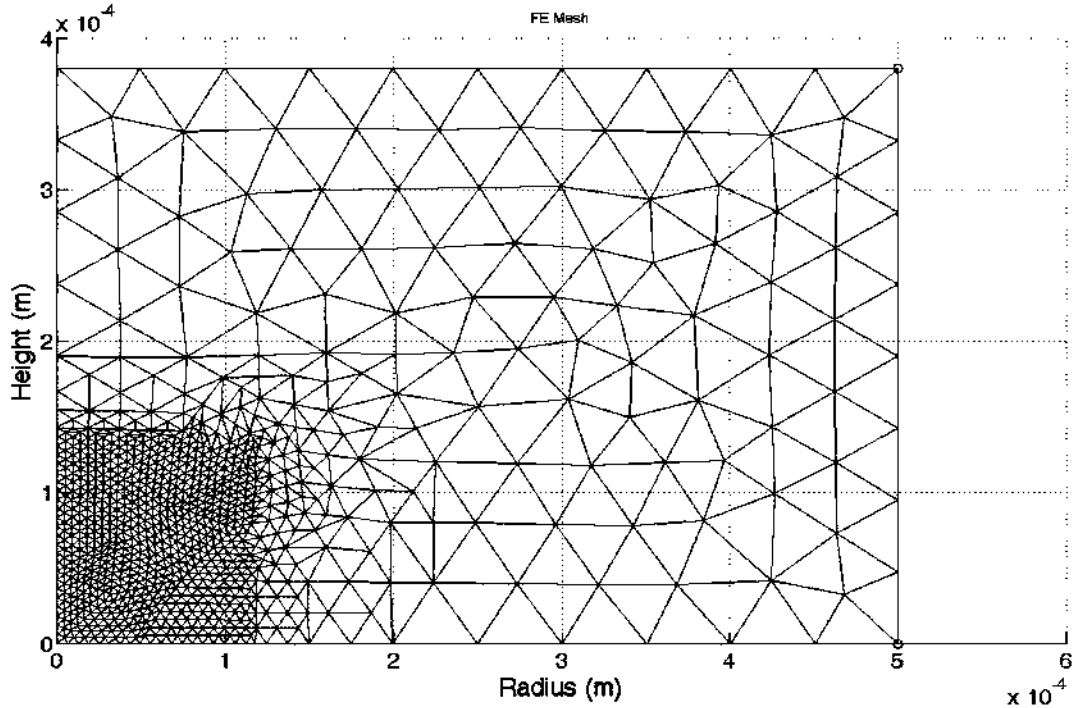
such that the resulting irradiance profile at the substrate,  $I(r) = I_n(r) * I_0$ , where  $I_0$  is the average irradiance at the substrate level. The value for this parameter was experimentally determined to be  $0.8\text{mW}/\text{cm}^2$ . Thus, the total time of exposure can be calculated using the following equation.

$$t = \max[E(r)] / I_0 \quad (6-23)$$

The exposure time calculated for this specific case was 17.2s. The calculated intensity profile and the exposure time were fed as inputs to the COMSOL® simulation software developed in section 6.3. Automatic mesh refinement was conducted to re-mesh the geometry with a finer mesh only in regions that receive exposure, while keeping the rest of regions under coarse mesh. This automatic mesh refining strategy helped in

reducing the overall simulation time, without affecting the accuracy of the final solution.

The final mesh plot used in the study is shown in Figure 99.



**Figure 99 Automatically generated finite element mesh used to simulate the exposure conditions**

Figure 100 shows the simulation results (solid red curve) with the desired part geometry (dashed black curve) superimposed to present the comparison between the desired part and the simulated part geometry. As seen from the figure, the simulated cured part shape does not precisely match the desired part shape. The root mean square error calculated for this case was  $6.6\mu\text{m}$ .

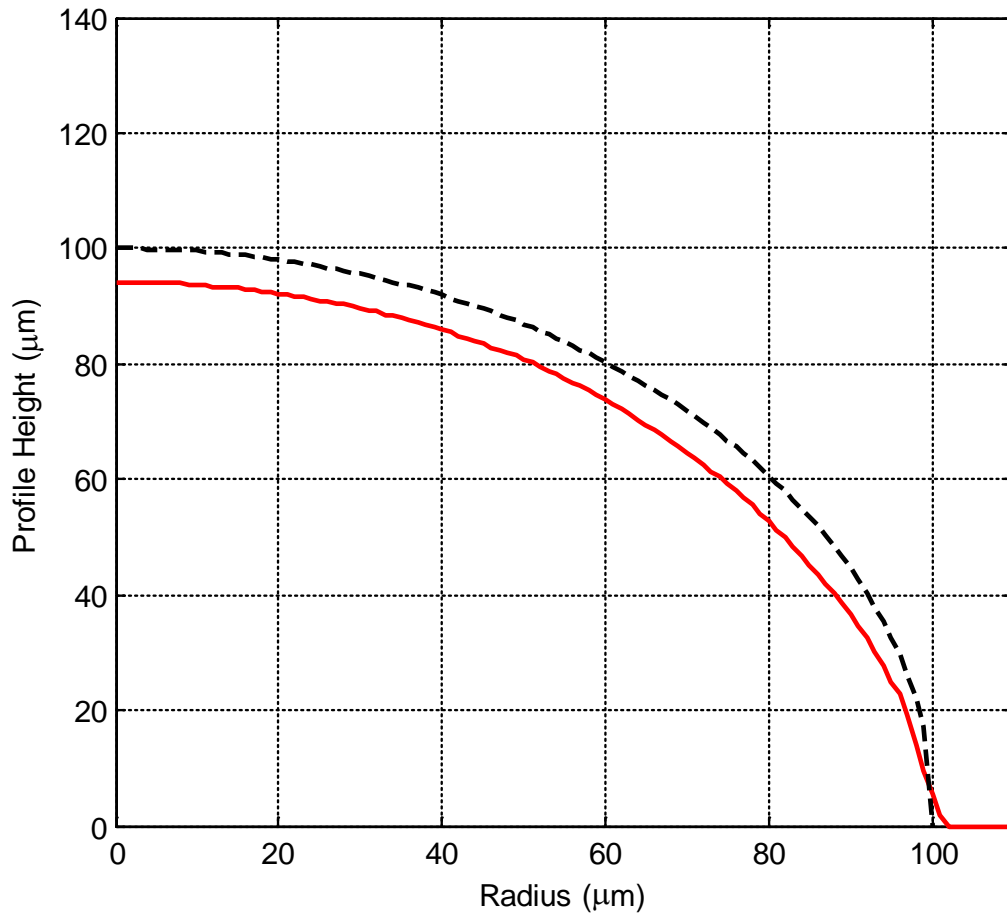


Figure 100 Simulation result showing the simulated cured part geometry (red) with the desired part geometry (dashed black)

### 6.5.2 Varying time at constant intensity

The  $E_c/D_p$  material database created in section 6.5 was developed using photopolymerization simulations conducted by assuming a constant irradiation of  $0.8\text{mW}/\text{cm}^2$ . Hence, it is reasonable to expect that the material database may be applicable for uniform irradiation conditions. To test the validity of this statement, simulations were conducted while keeping the irradiation constant and varying the

exposure time, i.e., applying the exposure profile by using Eq. 6-21. To do this, the exposure profile has to be segmented such that the regions receiving a similar amount of exposure are grouped together and exposed for the common time of exposure.

Researchers have proposed several approaches for segmentation [82]. Of all the available methods, clustering is widely used due to its simple application especially for segmentation of grey level images [83]. The k-means algorithm requires the number of clusters to be known beforehand, which must be supplied by the user. The following subsection briefly explains the algorithm of k-means algorithm as presented by Tou & Gonzales in their book [82].

### **k-Means algorithm**

The k-means method aims to minimize the sum of squared distances between all points and the cluster center. This procedure consists of the following steps:

Step #1: Choose  $K$  initial cluster centers  $z_1(1), z_2(1), \dots, z_K(1)$ .

Step #2: At the  $k^{th}$  iterative step, distribute the samples  $[x]$  among the  $K$  clusters using the relation,

$$x \in S_j(k) \text{ if } \|x - Z_j(k)\| < \|x - Z_i(k)\| \quad (6-24)$$

for all  $i = 1, 2, \dots, K; i \neq j$ , where  $S_j(k)$  denotes the set of samples whose cluster center is  $z_j(k)$ .

Step #3: Compute the new cluster centers  $Z_j(k+1), j = 1, 2, \dots, K$  such that the sum of the squared distances from all points in  $S_j(k)$  to the new cluster center is minimized. The

measure,  $Z_j(k+1)$ , which minimizes this performance index is simply the sample mean of  $S_j(k)$ . Therefore, the new cluster center is given by

$$Z_j(k+1) = \frac{1}{N_j} \sum_{x \in S_j(k)} x, j = 1, 2, \dots, K \quad (6-25)$$

where  $N_j$  is the number of samples in  $S_j(k)$ .

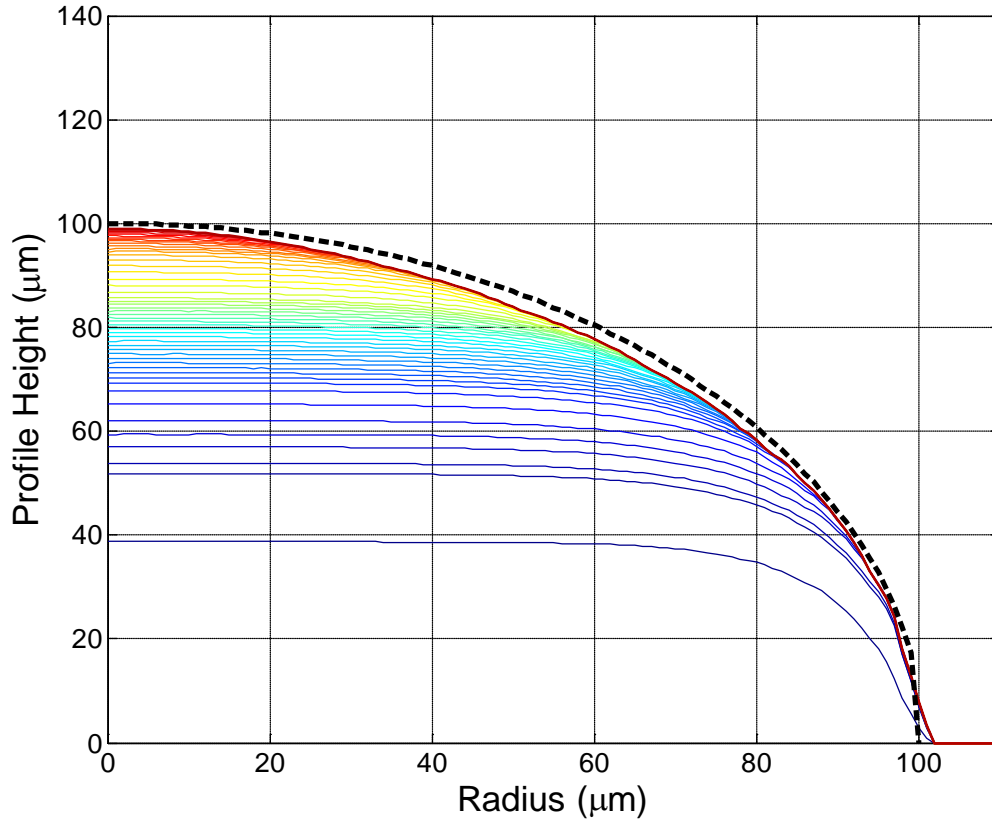
Step #4: If  $Z_j(k+1) = Z_j(k)$  for  $j = 1, 2, \dots, K$ , then the algorithm has converged and the procedure is terminated; otherwise go to Step# 2.

The final clustering completely depends on the initial cluster centers chosen and on the value of  $K$ . The latter is of the most concern since this requires some prior knowledge of the number of clusters present in the data. There will always be a trade-off between clustering errors and number of clusters.

Using the above k-means clustering algorithm, the total time of exposure was clustered into 50 clusters. Figure 101 shows the results from the simulations conducted in COMSOL® using constant irradiance of  $0.8\text{mW}/\text{cm}^2$ . Each colored solid curve represents the simulated cured part profile obtained by a single cluster of exposure dose. The root mean square error calculated for this case was  $2.2\mu\text{m}$ , which is almost 67% lesser than the error obtained by varying intensity at constant time. Moreover, the simulated sag height and the radius seem to match quite closely with the desired part profile. The exposure time for each cluster are presented in Appendix B. We can satisfactorily conclude that the material database created in section 6.5 is valid and can be used for explaining the material response in photopolymerization while considering oxygen inhibition and diffusion. Further, this example validates the hypothesis that *the*



resin behavior can be modeled by modifying the  $E_c - D_p$  model to incorporate the under curing observed at the edges due to oxygen inhibition and diffusion.



**Figure 101 Simulation results showing the simulated cured part geometry from sequentially clustered exposures and the desired part geometry (dashed black). The red curve closest to the black dashed curve is the final simulated cured part shape**

## 6.6 Chapter summary

This chapter presented the first ever semi-empirical material response model based on photopolymerization kinetics. An existing kinetic model with oxygen inhibition and diffusion (from literature) was used in this study. It was found that the rate constants available from literature failed to explain the impact of oxygen inhibition and diffusion during polymerization. Experimental values from literature were used to optimize the rate

constants. The new set of rate constants was used in COMSOL® to simulate the photopolymerization process and estimate the shape of the cured parts. Exhaustive photopolymerization simulations were conducted in COMSOL® to generate a semi-empirical material model based on the well-known Beer Lambert's law of attenuation ( $E_c - D_p$  model). The material model was formulated in the form of a database structure and used to test the case of curing spherical part geometry. It was found that the material database is relatively more accurate when used for uniform intensity conditions, rather than constant exposure time conditions. The impact of oxygen inhibition and diffusion on the required exposure profile was also demonstrated.

The chapter presented the third research question of this thesis on how to model the material behavior. The simulation results validated the hypothesis that a material model based on modification of the  $E_c - D_p$  model can be used to explain the material response in photopolymerization with oxygen inhibition and diffusion. There are two fundamental advantages of the simplified material response model created in this chapter – computationally expensive photopolymerization simulations need not be conducted to simulate the part shape during photopolymerization and the model is completely of the closed form, which allows for ease in estimation of the exposure profile required to cure a part shape of the desired dimensions.

## CHAPTER SEVEN

### PROCESS PLAN FORMULATION

This chapter will present a process-planning algorithm used to drive the ECPL system to generate parts of desired shapes. Process planning is a link between design and manufacturing. The design function provides the detailed design of the component for the finished product. The product and process requirements are then translated in form of instructions required to manufacture the product. This process of creating a set of instructions for manufacturing is called as process planning. Figure 102 [84] shows the block diagram of the process from design to inspection and highlights the interfacing role of process planning between design and manufacturing.

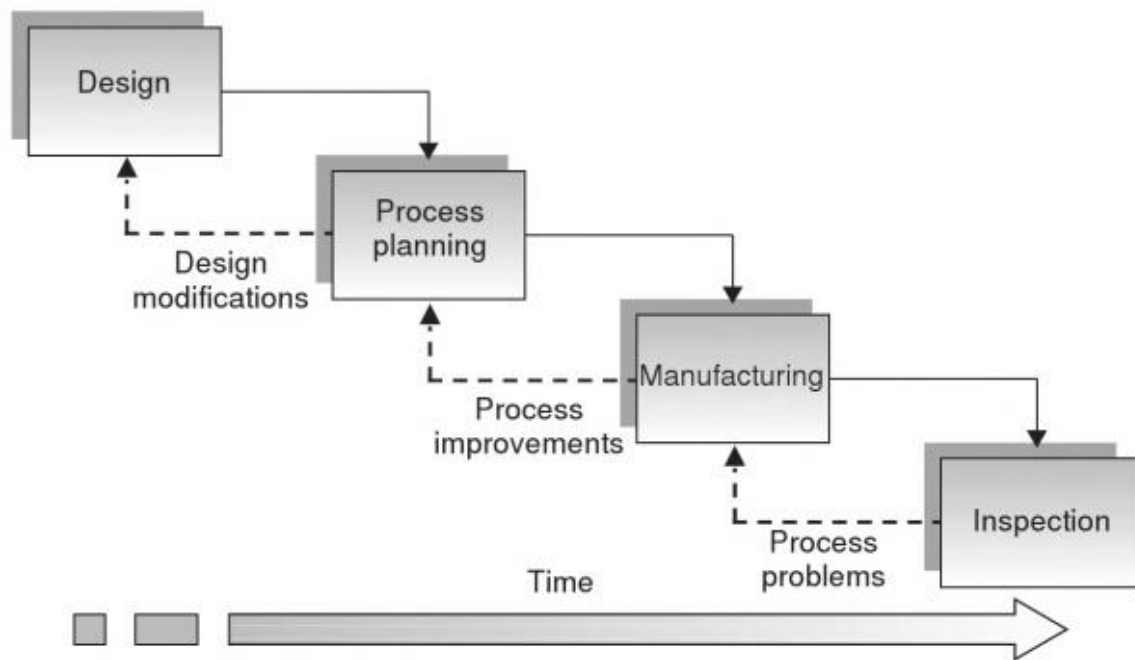


Figure 102 Process Planning - the design/manufacturing interface [84]

A process plan estimates the process parameters required to manufacture a product with the desired specifications. For any process plan, the primary input is the product specification. Apart from this, the process plan also requires specifications about the *raw materials* and the *system* that would eventually manufacture the final product. In the case of ECPL, the raw material is the photopolymer resin and the system corresponds to the ECPL optical system design.

The ECPL system, as the name implies, is controlled by controlling the exposure dose provided to the photopolymer resin. The exposure dose can be controlled spatially and temporally. The shape and size of the bitmaps control the pattern or spatial characteristics of the exposure. The temporal control is achieved by directly controlling the amount of time for which the bitmaps are turned on. In order to fabricate a part of desired dimensions from the ECPL system, we need to estimate the bitmaps and time of exposure for which the bitmaps must be turned on. This leads us to the following research question...

#### **Research Question #4**

**How to formulate a process plan to generate accurate process inputs in order to cure a part of desired shape and size in ECPL process?**

The process inputs are the micromirrors and the time duration during which each of them are switched ON. Since the research objective of this thesis is to fabricate lens shaped structures, the following discussion will be limited to fabricating axi-symmetrical shapes only. It is also to be noted that the current ECPL system is capable of fabricating

structures, which are monotonically decreasing in cross-section. In other words, the research question can be reformulated as:

$$\textit{How to convert } Z_{r,R} (\mu\text{m}) \rightarrow T_{i,j} (s)?$$

where  $R(\mu\text{m})$  is the maximum radius of the part to be cured and  $r(\mu\text{m})$  is the radial distance of the voxel from the center of the cured part on the substrate with corresponding desired height,  $Z_{r,R}$ . The index number of micromirrors which are to be switched ON are represented by  $i,j$  for a corresponding time,  $T_{i,j}(s)$  in order to cure the desired radial height field on the substrate. The micromirrors can be clustered together as bitmaps and projected on the DMD™ chip. Figure 103 adapted from Zhao, X. [14] presents the context of the overall problem. The desired geometry to be cured is at the substrate level. The curing is controlled by switching ON the individual micromirrors.

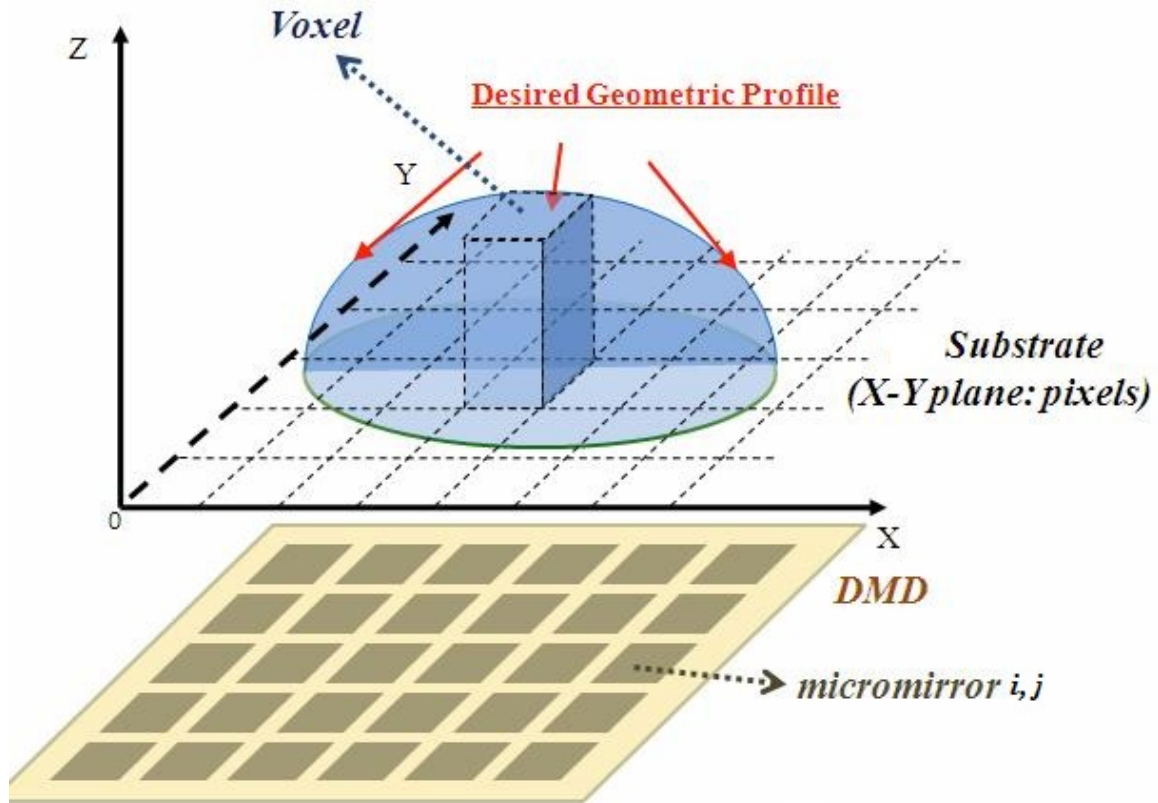
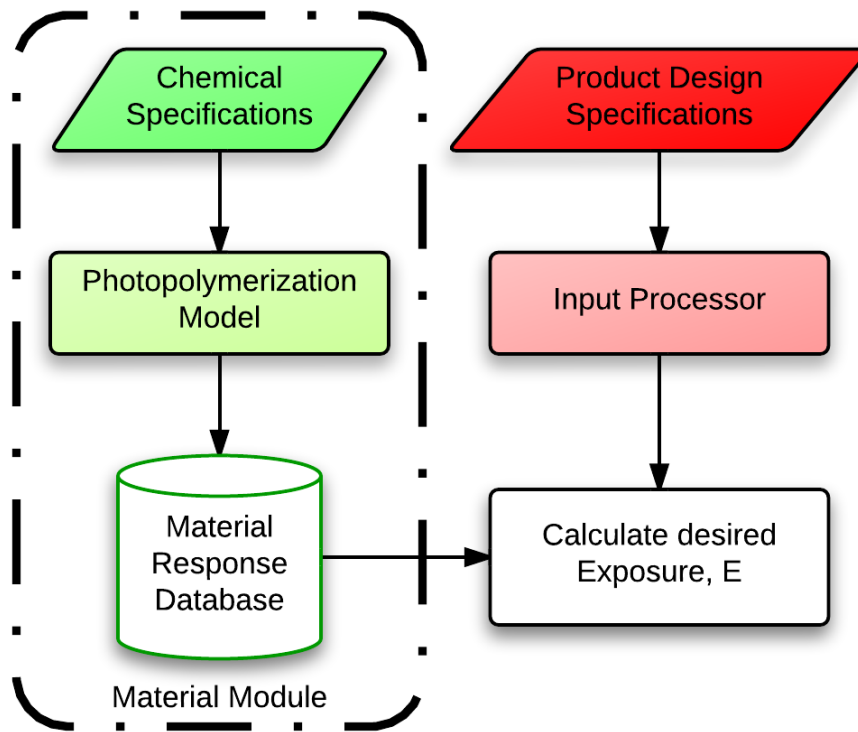


Figure 103 Figure showing the desired geometrical profile and the micromirrors

In order to translate from the design specifications (height field on substrate) to the bitmaps to be exposed, the desired exposure at the substrate level has to be calculated first. Figure 104 presents this sub-problem as partial formulation of the process plan.



**Figure 104** Flow-chart showing the partial formulation of the process-planning algorithm (derived from hypothesis to research question 4.1)

In other words, the desired radial height field,  $Z_{r,R}$  ( $\mu\text{m}$ ) has to be converted into desired exposure,  $E_{r,R}$  ( $\text{mJ}/\text{cm}^2$ ) at the substrate level. As was seen in Section 5.4.1, the rays of light entering the substrate continue to proceed through the photopolymer resin in a direction normal to the substrate. Hence, curing occurs along a direction normal to the substrate. Hence, the desired part specifications must be translated into height from the base of the substrate along a direction normal to the substrate. In Chapter 6, a photopolymerization material database was created which can be used to estimate the required exposure to cure the desired part shape. Specifically, eq. 6.18 presented the relation between exposure and desired height at the substrate level.

However, it is necessary to acknowledge that the product expected from the ECPL system is a lens shaped structure and hence the user may not specify the height field, but will specify the product dimensions in form of desired lens specifications. The following section explains the translation from the desired product specifications to desired radial height field on the substrate level.

## 7.1 Product Specifications

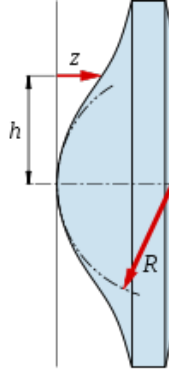
This module converts the product specifications provided in terms of radius,  $R$  and conic constants,  $K$  into the height field,  $Z = f(r)$ . Lens geometry can be spherical or aspheric shape. Figure 105 shows the geometry of a typical lens.

The aspheric surface profile can be expressed using the following equation [85].

$$z(r) = \frac{r^2}{R \left( 1 + \sqrt{1 - (1 + K) \frac{r^2}{R^2}} \right)} + \alpha_1 r^2 + \alpha_2 r^4 + \dots \quad (7-1)$$

where  $r$  is the radial distance from the center,  $R$  is the radius of curvature,  $K$  is the conic constant and  $\alpha_1, \alpha_2, \alpha_3 \dots$  are the coefficients that determine the deviation of the surface from the axially symmetric surface. The optic axis is presumed to lie in the  $z$  direction, and  $z(r)$  is the sag or the displacement of the surface from the vertex. When the conic constant and the  $\alpha_i$  coefficients are zero, the equation represents a perfectly spherical surface.





**Figure 105 Aspheric lens geometry, adapted from [85]**

For given specifications, the sag  $z(r)$  was calculated using the Eq. 7-1. This information was then converted in form of the height field,  $Z = f(r)$ , such that  $Z$  represents the height from the base of the substrate, using the following equation:

$$Z(r) = R - z(r) \quad (7-2)$$

A Matlab script was created to accept the user input in form of the radius  $R$ , and conic constant,  $K$  and translate it into the radial sag height from the substrate, also referred to as the radial height field,  $Z(r)$ .

## 7.2 Material Module

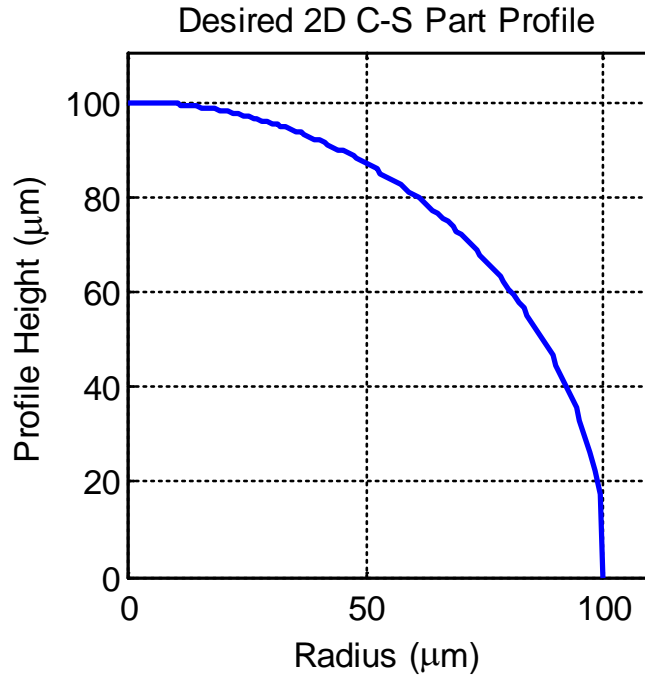
The material module primarily comprises of the material response models, which explain the behavior of the material to the specific processing conditions. In the case of ECPL process, this model is in form of a database, which was created in Chapter 6. The inputs to the database are the maximum part radius,  $R$  and the distance from the center,  $r$ . The resulting outputs are the critical exposure to cure at the given radial distance,

$E_c(r, R)$  and the depth of penetration,  $D_p(r, R)$ . Equation 6-18 can be used to estimate the exposure required,  $E(r)$  to the cure the part. It is presented again as follows:

$$E(r) = \begin{cases} 0, & \text{for } Z(r, R) = 0 \\ E_c(r, R) * \exp\left(\frac{Z(r, R)}{D_p(r, R)}\right), & \text{for } Z(r, R) > 0 \end{cases} \quad (7-3)$$

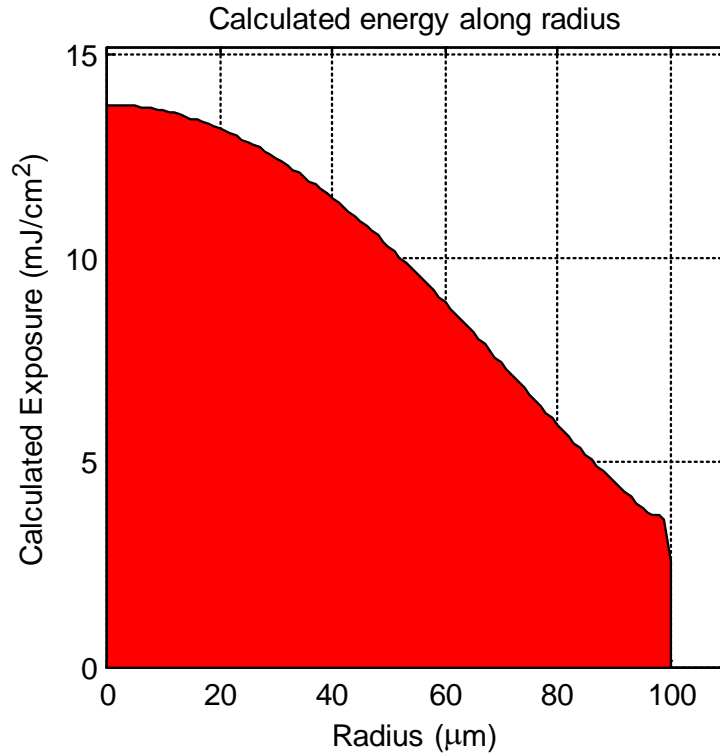
However, the calculated exposure is only for the half-sectional profile of the part. In order to cure the entire three dimensional geometry, the half-sectional exposure profile needs to be transformed into a full two dimensional circular profile. This can be achieved by rotating the profile, along 360 degrees similar to the ‘*revolve*’ feature used in 3D CAD software for generating axi-symmetric shapes. For process planning purposes, the substrate was divided into an array of square pixels of size  $1\mu\text{m} \times 1\mu\text{m}$ . This discretization method is similar to the approach used in Section 5.3 used to validate the irradiance model and hence ensures compatibility with the future additional modules to the process planning method. A Matlab script was created to transform the radial exposure at substrate level,  $E(r)$  to the exposure in terms of substrate coordinates,  $E_{p,q}$  where  $p$  and  $q$  are indices of the pixels on the substrate.

For the purposes of clarification, a similar case presented in Chapter 6 will be considered. The desired part geometry is a spherical lens with radius and sag of  $100\mu\text{m}$ . Figure 106 shows the height field of the desired lens geometry in form of half-cross sectional.



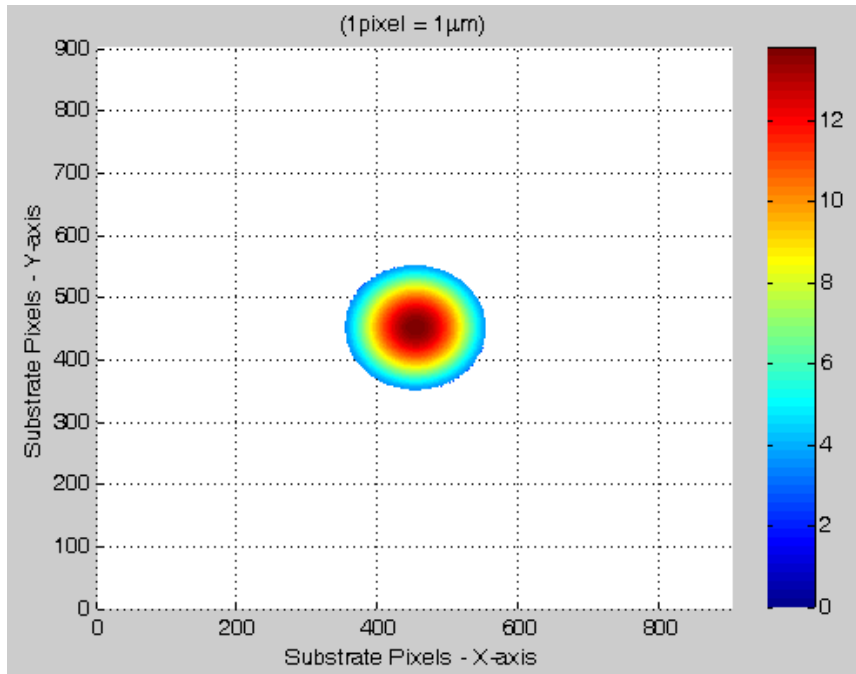
**Figure 106 Profile of desired spherical lens geometry**

This desired lens geometry,  $Z(r)$  was transformed into desired radial exposure profile at the substrate level,  $E(r)$  using equation 7-3 as shown in Figure 107.

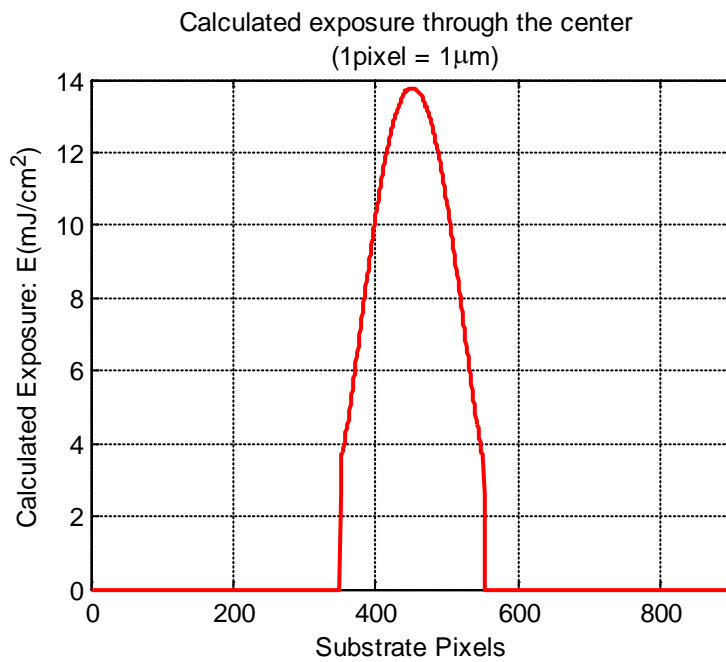


**Figure 107 Desired radial exposure profile**

The Matlab script allows the user to input the location of the lens and the lens specifications. For purposes of this study, the substrate was discretized into 900 x 900 pixels of 1μm x1μm size. The pixel (451, 451) corresponds to the center of the optical axis. Using the input location of the lens center on the substrate and the calculated exposure, the desired exposure field,  $E_{p,q}$  was calculated. Translation operation was used in a Matlab script (refer appendix) to translate the axis of the desired geometry to the center of the discretized substrate. Figure 108 shows the “top-view” of the desired exposure profile as calculated at the substrate level and Figure 109 shows the cross-sectional profile of the same desired exposure.



**Figure 108** Figure showing the gradient profile of the desired exposure at the substrate level in terms of substrate pixels



**Figure 109** Figure showing the cross-sectional profile of the desired exposure at the substrate level in terms of substrate pixels

Given that the exposure at the substrate level can now be estimated, the question arises as to how to calculate the time of duration during which each micromirror has to be switched ON. With reference to the R.Q. 4 presented earlier, the question was to transform  $Z_{r, R} (\mu m)$  to  $T_{i, j} (s)$ . So far, a solution method of estimating  $E_{p, q} (mJ/cm^2)$  from  $Z_{r, R} (\mu m)$  was presented. The overall research question can now be presented in form of the following sub-research question:

#### **Sub-Research Question #4.a**

**How to estimate the micromirrors and corresponding time duration during which they must be switched ON, in order to obtain the desired exposure profile at the substrate level? *How to convert  $E_{p, q} (mJ/cm^2) \rightarrow T_{i, j} (s)$***

### **7.3 System Module**

The beam conditioning system of the ECPL system provides the primary source of energy, UV light to start and sustain the fabrication process. This light is then ‘shaped’ using a Digital Micromirror Device – DMD™ that is controlled through the Powerpoint® Software. The projection system of the ECPL system images the bitmaps from the DMD™ to the resin substrate. This process was modeled as the irradiance model in section 5.3.1, which used optical ray tracing to relate the irradiance from the micromirror to the resin substrate. Given a micromirror on the DMD™, the irradiance model could estimate the resulting exposure at the substrate level. For purposes of creating the process plan, this model has to be inverted such that given a specific exposure at the substrate level; the micromirrors to be switched ON can be estimated. In order to create such an

inverse model, Limaye A. [43] presented an approach of creating a mapping database. This irradiance model can be run in iterative loops for each micromirror on the DMD™ to formulate the pixel-mapping database. This database is a set of all individual irradiance relationships between one micromirror to all pixels on the resin substrate. This database is then combined together into a large database with the actual irradiance readings from the experimental setup. This mapping database (which is a result of  $i \times j$  simulations of the Irradiance Model;  $i \times j$  is the total number of micromirrors on the DMD™ chip) is then transformed into an Irradiance Database. The Irradiance Database provides the mapping relationships between DMD micromirrors and resin substrate pixels. The typical element of the database is  $H_{pqij}$ , represents the irradiance at the  $p^{th}$  row and  $q^{th}$  column of the pixel matrix at the substrate resulting from the  $i^{th}$  row and  $j^{th}$  column of the micromirror. The Matlab code developed to create this database was simplified to reduce the dimensional complexity such that the number of rows of  $H$  equated with the total number of all the pixels on the resin substrate ( $p \times q$ ). Similarly, the total columns of  $H$  are equal to all the micromirrors of the DMD™ chip, ( $i \times j$ ). Given the Irradiance Database,  $H$  and the desired exposure  $E$ , the following hypothesis is proposed:

#### **Hypothesis for Research Question #4.a**

*The desired process inputs (micromirrors and time duration for switching 'ON') for curing a desired geometry can be estimated by optimizing the exposure, 'E' required at the substrate level.*

Figure 110 shows the complete form of the flow-chart of the process plan, which presents the relation between the material modules and the system module presented

earlier. It also shows how the proposed hypothesis relates the computational modules to estimate the necessary process inputs required to cure a desired geometry.

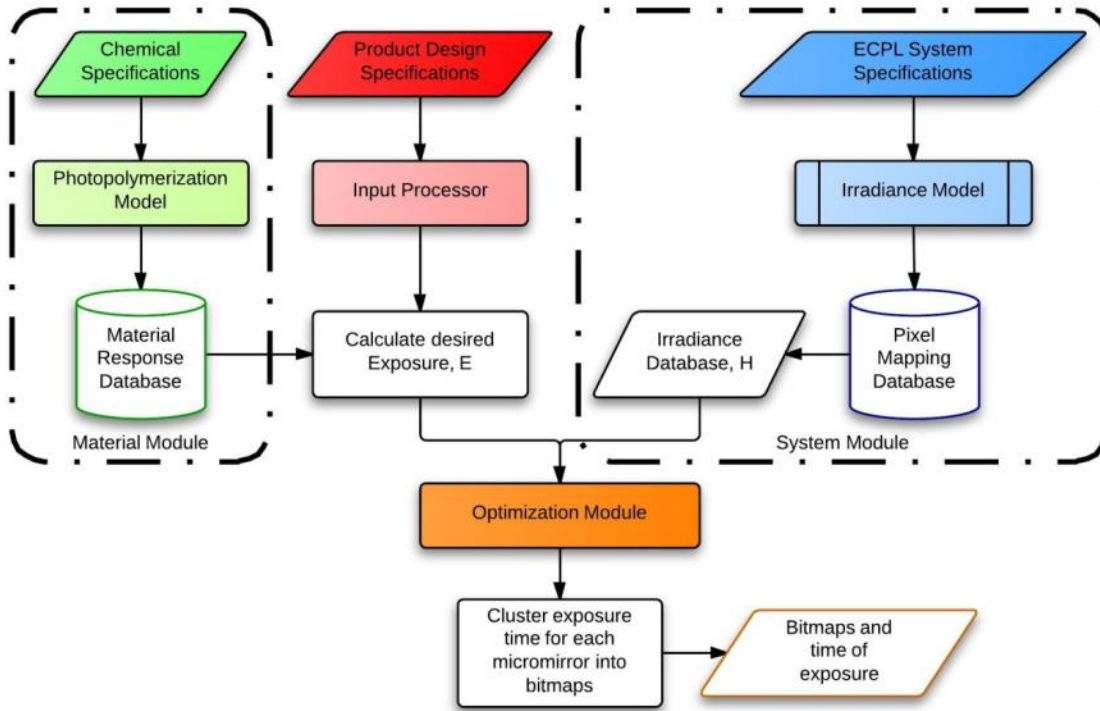


Figure 110 Flow-chart of the Process Plan for the ECPL system

## 7.4 Optimization Module

The exposure  $E$  on the substrate pixels is determined by the exposure time  $T$  of micromirrors on the DMD. Exposure energy is linearly accumulative both temporally and spatially. For a given pixel on the substrate, the exposure energy received by the specific pixel can be considered an addition of all exposure doses from any individual micromirror that has an irradiation effect on it. Thus, exposure for any specific pixel on the substrate is a weighted sum of the irradiance from all micromirrors on the DMD™ chip, where the “weights” are exposure time for each micromirror. Hence, using the



Irradiance Database, the exposure at a pixel,  $p, q$  on the substrate level can be estimated using the following equation.

$$E_{p,q} = H_{pqij} \times T_{ij} \quad (7-4)$$

To estimate which micromirrors at the DMD level need to be switched ‘ON’ and their duration, the following optimization problem can be solved:

Input: Desired Exposure profile:  $\bar{E}_{p,q}$  ( $mJ/cm^2$ ) (substrate is discretized into  $p \times q$  pixels)

Output: Switch ‘ON’ time for each micromirror,  $T_{ij}$  ( $s$ ) (Micromirrors are indexed in a matrix of  $i \times j$ )

Objective:  $\min\{(H_{pqij} \times T_{ij}) - \bar{E}_{p,q}\}$ , such that  $T_{ij} \geq 0$

The presented objective function effectively minimizes the difference between the exposure caused by the micromirrors and the desired exposure. For the current study, the substrate was meshed into  $900 \times 900$  pixels (of  $1\mu m \times 1\mu m$  size each), and  $90 \times 90$  micromirrors on the DMD™ chip were considered. Hence, the total size of the individual elements of the above problem are:

Micromirror Time:  $T: 91 \times 91 = 8281$

Desired Exposure Profile,  $\bar{E}: 901 \times 901 = 811801$

Irradiance Database,  $H: 811801 \times 8281$

The linear least squares optimization method was used to solve the optimization problem. Matlab has an in-built ‘lsqin’ solver, which can be used to solve bound constrained least-squares problem. The objective function can thus be written as:

$$\min_T \frac{1}{2} \|(H_{pqij} \times T_{ij}) - \bar{E}_{p,q}\|_2^2$$

such that,  $(H_{pqij} \times T_{ij}) \leq \bar{E}_{p,q}$  and  $T_{ij} \geq 0$

The problem was solved using Matlab such that the variable,  $T$  was bounded between zero to infinity. For a given geometry to be cured and the exposure profile, the solution to the above problem resulted in a matrix of exposure time for each individual micromirrors  $i, j$ . K-means clustering algorithm (previously introduced in section 6.5.2) was used to cluster the individual micromirrors with similar exposure times to create several bitmaps with corresponding exposure times. With reference to the spherical lens geometry, the above optimization module was used to generate the exposure time distribution for each micromirror on the DMD™ chip.

Figure 111 shows the estimated time distribution for the micromirrors required to cure the spherical lens geometry shown in Figure 106. The red line shows the time summation for all individual nine bitmaps. The bitmaps are shown in Figure 112.

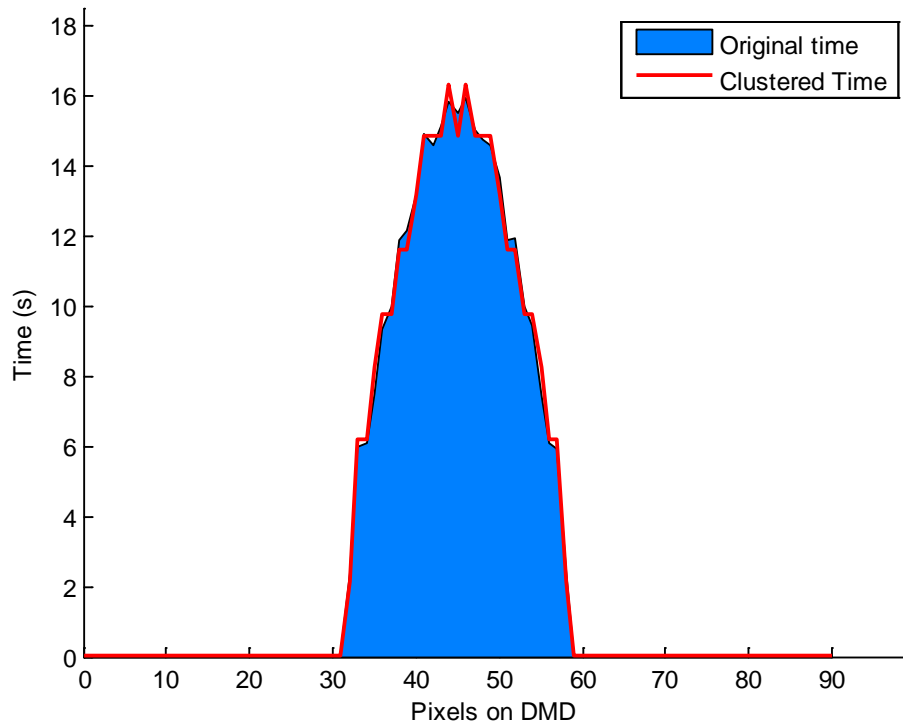








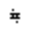


Figure 111 Estimated time for micromirrors on the DMD chip

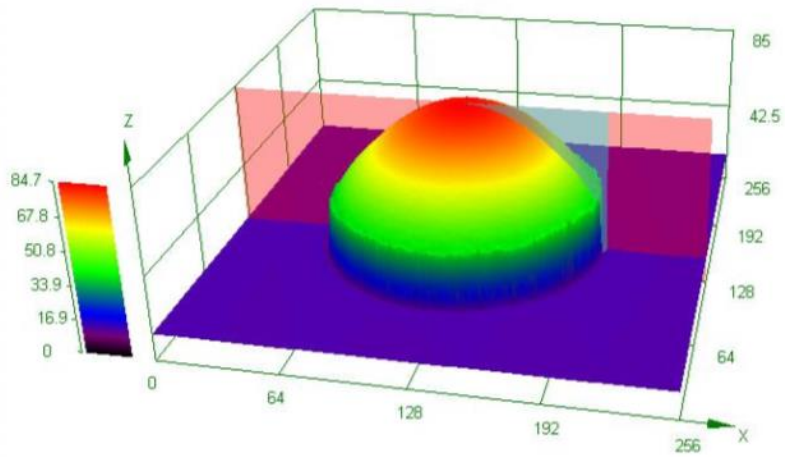
### 7.5 Validation of Hypothesis for Research Question 4

The least squares optimization method was used to estimate the bitmaps and exposure times in order to cure the desired geometry. The resulting bitmaps from the clustering algorithm are shown in Figure 112.

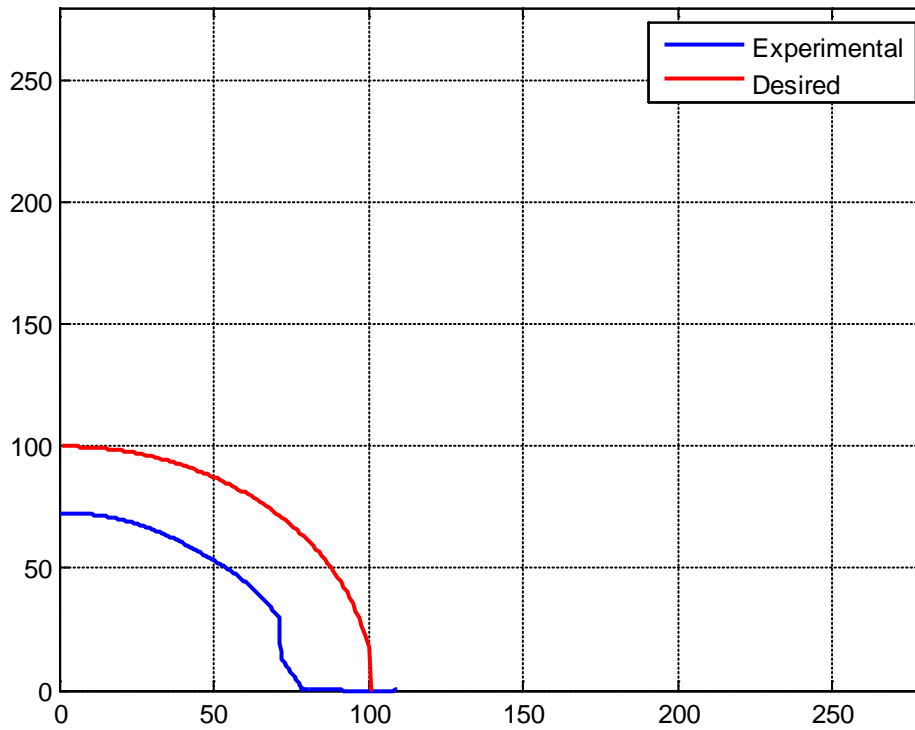
 2.1s	 2.2s	 1.9s
 2s	 1.5s	 1.8s
 1.6s	 1.7s	 1.5s

**Figure 112 Calculated bitmaps and corresponding exposure times**

Several test samples are used as examples to demonstrate the applicability of the process planning method. The resin chamber was loaded with the photopolymer and the generated bitmaps were projected on the DMD™ chip for the corresponding exposure times. The sample was then washed and post-cured. Figure 113 shows the snapshot of the cured part as observed from a 3D confocal microscope. Figure 114 presents the comparison between the desired part geometry and the experimentally cured part geometry in a half-sectional view. It can be clearly observed that the cured sample cures less than the desired part shape. The experiments were repeated and similar observations were noted.



**Figure 113 Snapshot of the image of the cured sample from LEXT 3D confocal microscope**



**Figure 114 Comparison of the half-sectional profiles of the cured part sample and the desired part geometry**

It was observed that the experimental samples had a uniform deviation of around  $25\mu\text{m}$  along the profile. The cause of such a deviation between the cured part sample and the desired part geometry cannot be identified and hence the input desired geometries were changed and several more experiments were conducted. The following section presents the experimental results of curing conical lens and aspherical lens.

### 7.5.1 Conical Lens Example

Figure 115 shows the desired half cross section of the geometry of a conical lens to be cured. The desired diameter was  $150\mu\text{m}$  and the height was  $80\mu\text{m}$ . The desired radial exposure profile was calculated from the material model (Ch. 6). Figure 117 shows the snapshot of the calculated exposure profile from Matlab at the substrate level.

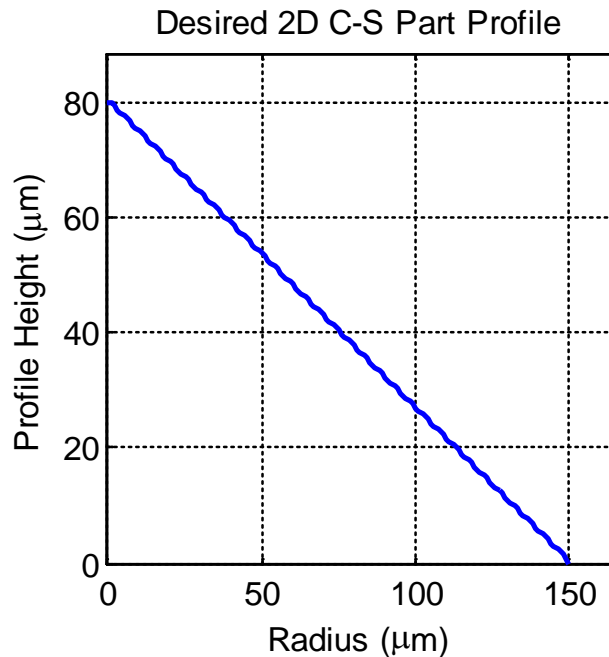


Figure 115 Half-sectional profile of desired cylindrical lens geometry

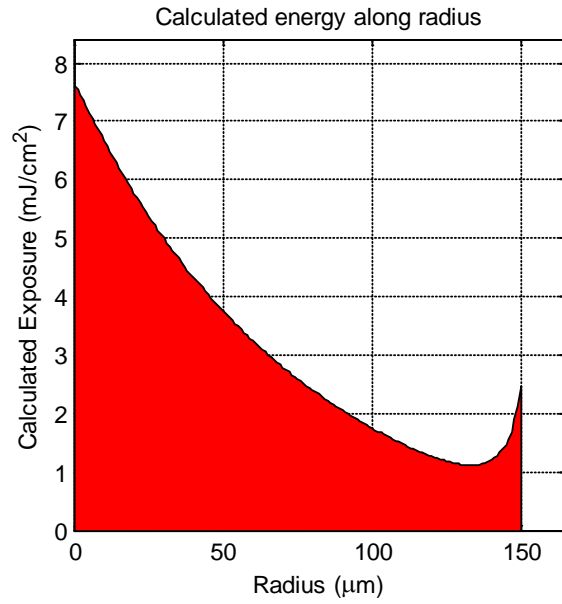


Figure 116 Desired radial exposure profile to cure conical lens

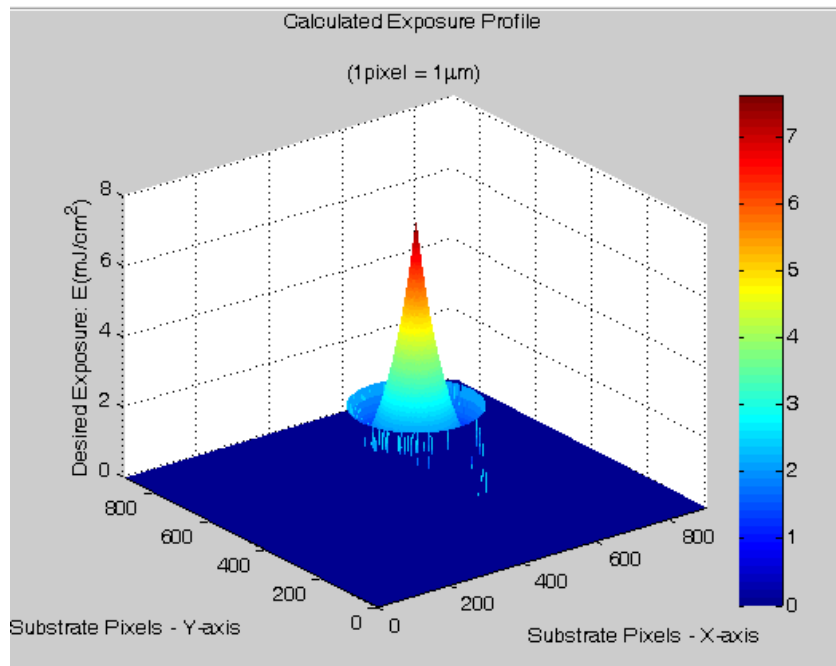











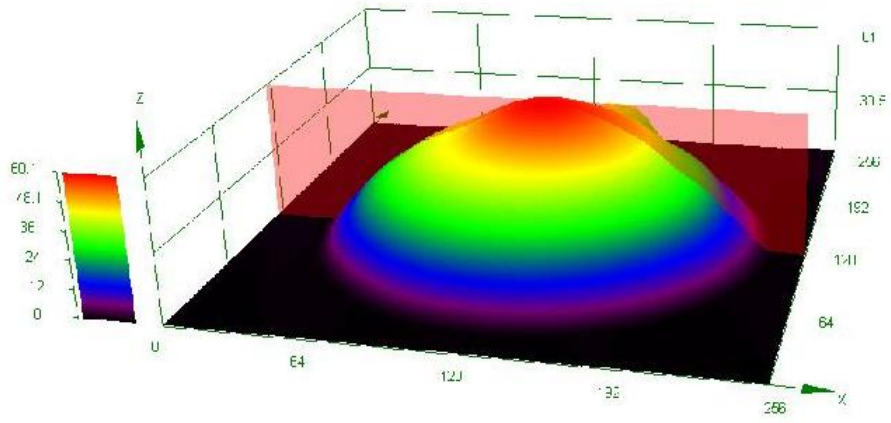
Figure 117 Snapshot of the calculated exposure profile in terms of substrate pixels

The exposures at the substrate were used to estimate the bitmaps and the time of exposure for each bitmap as shown in Figure 118. The experimental result is shown in Figure 119 and the comparison with desired part geometry is shown in Figure 120.

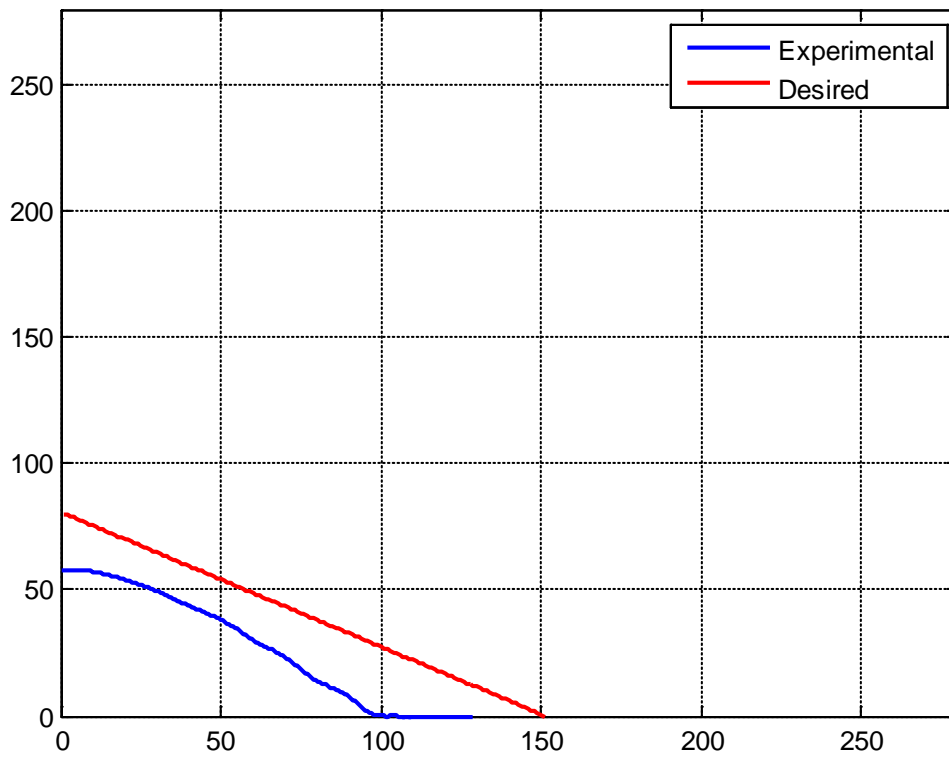
 0.9s	 0.7s	 0.7s
 0.9s	 1.0s	 1.0s
 1.1s	 1.4s	 1.3s

**Figure 118** Calculated bitmaps and corresponding exposure times





**Figure 119** Snapshot of the image of the cured sample from LEXT 3D confocal microscope



**Figure 120** Comparison of the half-sectional profiles of the cured part sample and the desired part geometry

From Figure 120, it can be observed that the process plan fails to adequately cure the heights and the overall diameter of the part. The height is under-cured by almost 20  $\mu\text{m}$  and the diameter mismatch is up to 50 $\mu\text{m}$ , which corresponds to around 30% deviation from desired part geometry.

### 7.5.2 Aspheric Lens Example

Figure 121 shows the desired half cross section of the geometry of a conical lens to be cured. The desired diameter was 200 $\mu\text{m}$ , conic constant was -1 and the sag height was 120 $\mu\text{m}$ . The desired radial exposure profile was calculated from the material model (Ch. 6) as shown in Figure 122.

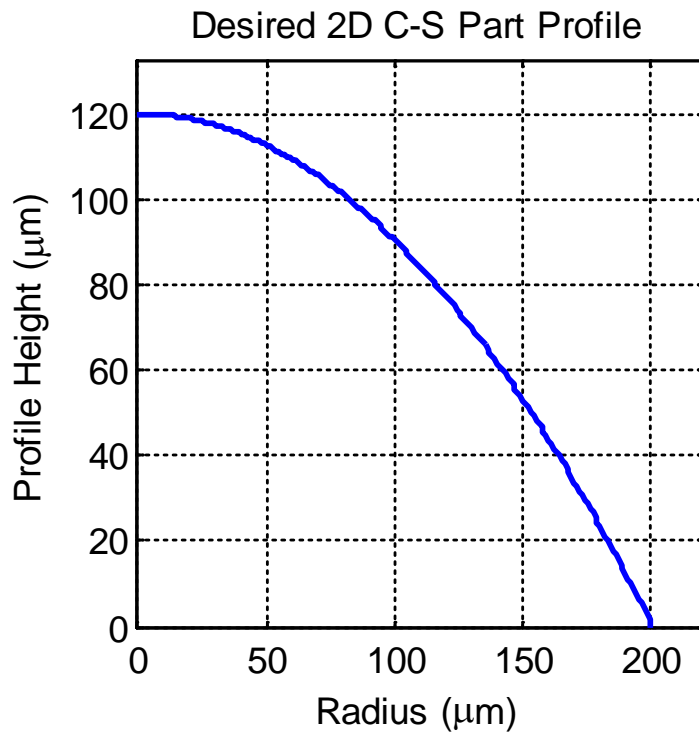
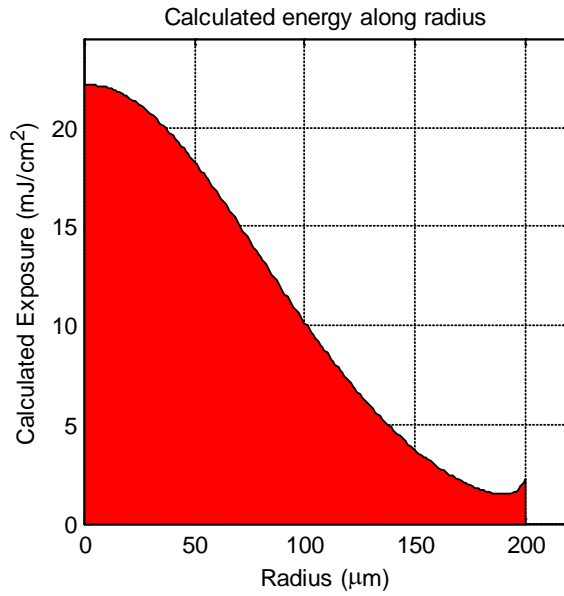
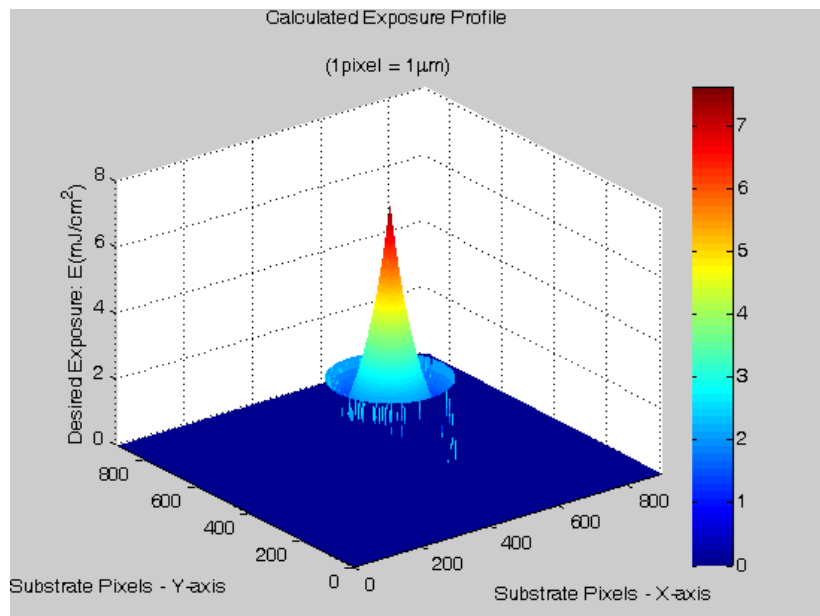


Figure 121 Half-sectional profile of desired aspherical lens geometry












**Figure 122 Desired radial exposure profile to cure aspheric lens**

Figure 123 shows the snapshot of the calculated exposure profile at the substrate.

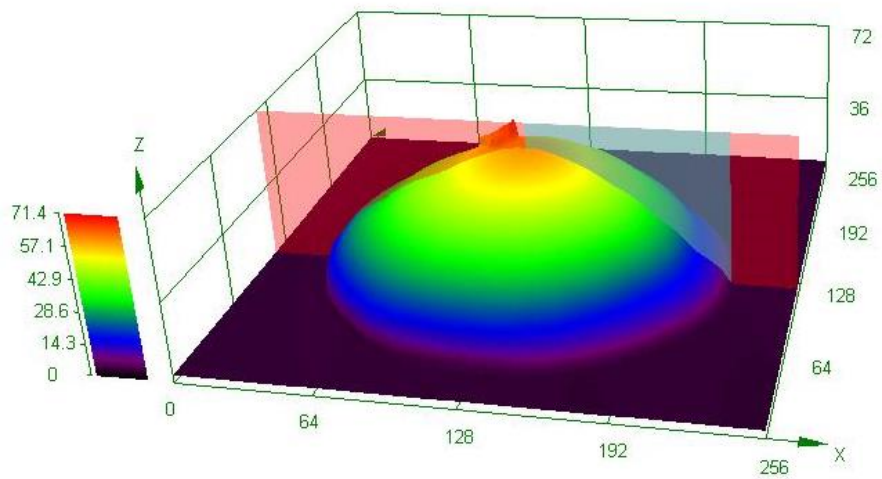


**Figure 123 Snapshot of the calculated exposure profile in terms of substrate pixels**

The resulting bitmaps with corresponding time of exposure for each bitmap is shown in Figure 124. The experimental result is shown in Figure 119.

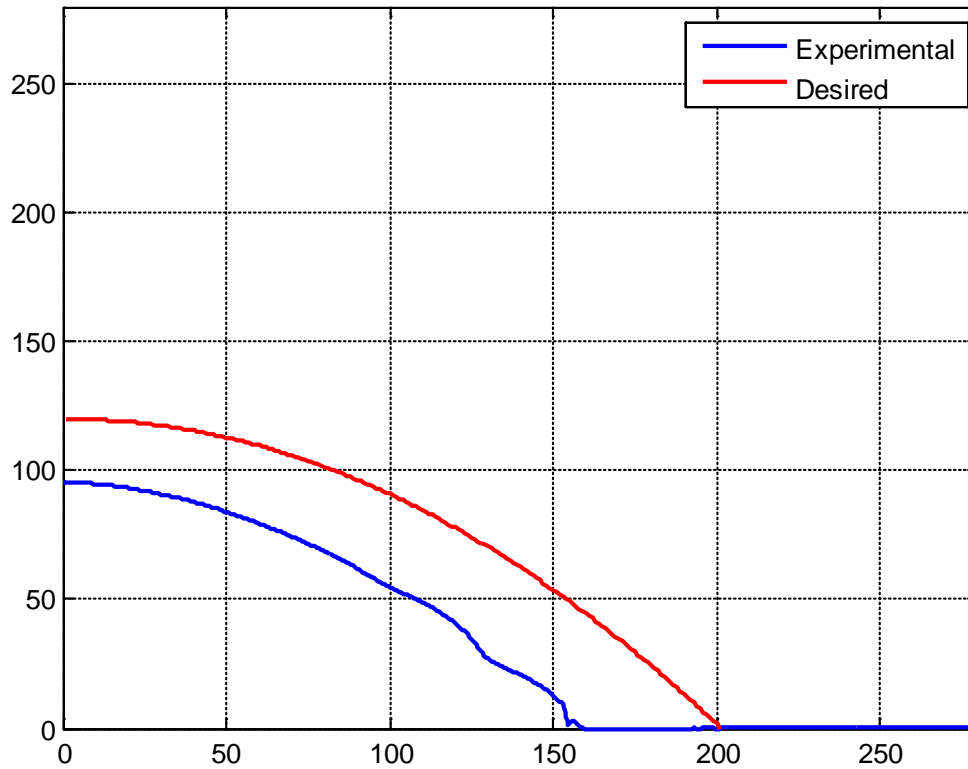
 2.3s	 2.6s	 2.9s
 2.8s	 2.9s	 3.1s
 2.6s	 2.9s	 2.8s

**Figure 124** Calculated bitmaps and corresponding exposure times



**Figure 125** Snapshot of the image of the cured sample from LEXT 3D confocal microscope

It is to be noted that the protrusion seen at the top edge of the sample is not a part of the cured sample, but an artifact of uncured region behind the sample. Figure 126 clarifies this observation and presents the comparison with desired part geometry.



**Figure 126 Comparison of the half-sectional profiles of the cured part sample and the desired part geometry**

From Figure 126, it can be observed that the process plan again fails to cure the part shape completely. The height deviation was measured to be around  $25\mu\text{m}$  and the diameter was undercured to the extent of  $45\mu\text{m}$ , which corresponds to around  $\sim 25\%$  deviation from desired part geometry.

## 7.6 Error Analysis

The experimental validation of the process planning method was not as successful as expected. The overall errors in the heights and diameters were found to be in the range of 20-30%. This represents a significant (unacceptable) deviation from the desired surface profile, considering that the intended application of the ECPL system is to fabricate lens shaped structures, where form accuracy is of high demand. Table 11 summarizes the experimentally observed errors for the four test cases considered in this chapter. Each experimental sample was repeated five times and the average dimensions were considered to calculate the errors presented in the table.

**Table 11 Summary of average errors observed from experiments**

<b>Sample Geometry</b>	<b>Error in height</b>	<b>Error in diameter</b>	<b>Comments</b>
Spherical	25% (undercure)	25% (undercure)	Uniform undercure along profile
Conical	25% (undercure)	30% (undercure)	More undercure at edges than center
Aspheric	25% (undercure)	20% (undercure)	More undercure at edges than center

It can be noted that the dimensional error cannot be directly attributed to shrinkage or post-processing. Most of the convex shaped samples exhibit undercuring. Hence, there is a need to validate the assumptions embedded in the material model and the process planning method. One of the underlying assumptions of the material model is that the irradiation resulting from the projected bitmaps will remain constant. With

reference to Figure 63, this assumption is valid only towards the center of the part to be cured, but it fails at the edges. Close examination of the figure shows that the irradiation profile (from both CCD response and simulation) shows that the maximum irradiation drops to zero with a taper edge of almost 20%. For instance, the irradiation produced by 60 micromirrors results in a total width of 400 $\mu\text{m}$  at the base being illuminated. However, the maximum irradiation width is only 320 $\mu\text{m}$ . This is caused due to spherical aberration in the optical system and although it can be reduced, it cannot be eliminated. In the validation of the material model in section 6.5, it was observed that the material model can be valid for constant intensities only. It fails to provide accurate results, if irradiation is assumed to vary (refer Figure 100). Although, the material model (developed in Ch. 6) is valid, it cannot be directly applied for the ECPL process, where intensity variation at the edges is almost unavoidable. Hence, the semi-empirical material model cannot be used independently to estimate the exposures required for curing desired part geometry for the ECPL system.

Yet another possible flaw in the process planning method maybe that the implicit assumption, that total cured part shape is the result of curing due to the sum of all exposures. It is reasonably accurate to assume that the following equations (Eq. 7-5 and 7-6) are valid:

$$E_T = \sum_{i=1}^n E_i \quad (7-5)$$

$$Z_T = \sum_{i=1}^m Z_i \quad (7-6)$$

Where  $E_T$  and  $Z_T$  represent total exposure and total cured part respectively. From the material model developed earlier, a relationship between exposures and cured part height was obtained, which can be presented simply as follows:

$$Z = f(E) \quad (7-7)$$

Hence, the total cured part,  $Z_T$  can be related to individual exposures as follows:

$$Z_T = \sum_{i=1}^n f(E_i) \quad (7-8)$$

However, when the individual micromirrors are clustered to generate the bitmaps, the implicit assumption made can be presented as shown in eq. 7-9.

$$Z_T = f(E_T) = f\left\{\sum_{i=1}^n E_i\right\} \quad (7-9)$$

Both eq. 7-8 and 7-9 could have been equivalent if the ECPL system had uniform flat-top intensity profile. This can be seen from section 6.5.2 Figure 101, where clustered exposures with constant irradiation were used to validate the material model. However, experimental samples suggest that the assumption of uniform irradiation cannot be applied to the ECPL system. This further complicated the problem. Since, if the irradiation is not constant, eq. 7-8 and 7-9 can no longer stay equivalent. It was already identified in section 6.5.1 that the material model is not applicable if the irradiation is not



constant. From the above discussion, the following drawbacks of the existing process planning method can be summarized (illustrated in Figure 127):

1. Independent use of the semi-empirical material model (developed in Ch. 6) is not directly applicable to the ECPL process, since the resulting irradiation from the system is not perfectly flat-top.
2. Due to variation inherent in the projected irradiation, the bitmap clustering method cannot be applied directly.

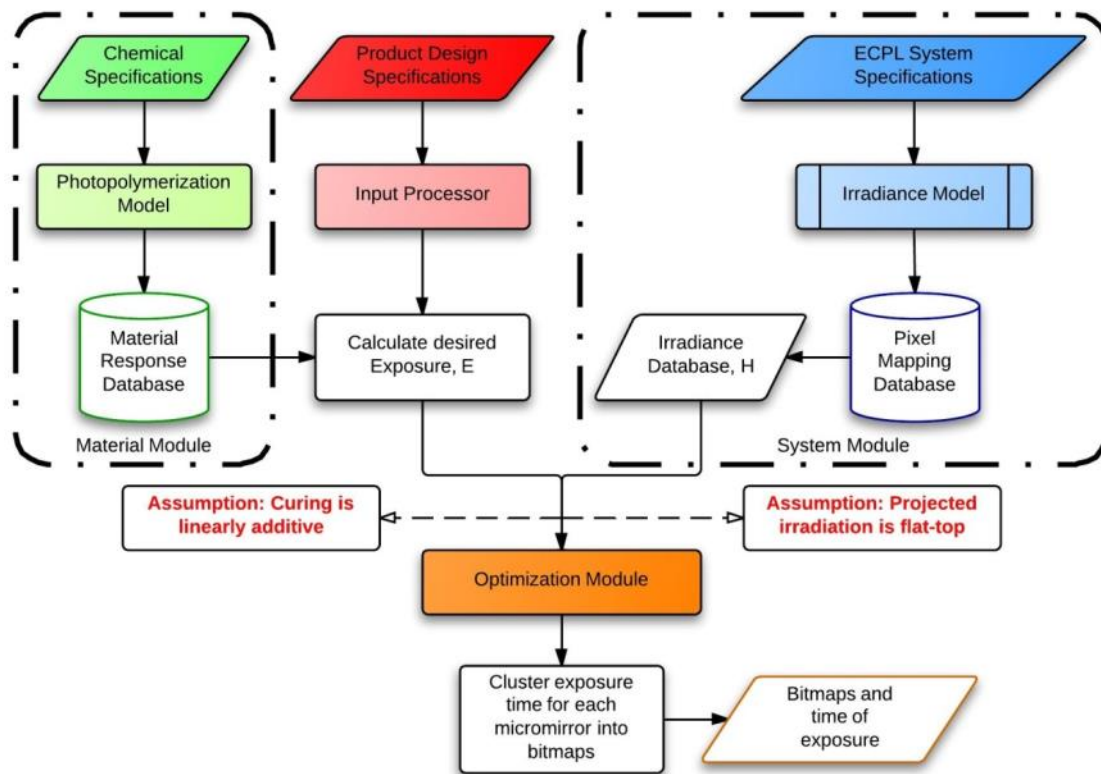


Figure 127 Invalid implicit assumptions in the process-planning algorithm

## 7.7 Effect of DMD operation on curing

Although the experiments and the discussion suggest that the process planning method has failed, it is worthwhile to identify if the failure was also caused (in part) by other factors. One of the potential causes can be the operation of the DMD micromirrors. The micromirrors on the DMD are not always set in one ON or OFF position. They are constantly switching on and off based on their intended gray scale values. If the diffusion length scales for oxygen are in range of several tens of  $\mu\text{m}$  for the time scales relative to the switching time for the micromirrors, then errors resulting from the DMD operation cannot be ruled out.

The diffusivity of oxygen is  $1 \times 10^{-10} \text{m}^2/\text{s}$ . According to the DMD manufacturer's (Texas Instruments) data sheet [86], the nominal micromirror switching time is  $140 \mu\text{s}$ . By first principles, the diffusion length is  $0.1183 \mu\text{m}$ . This is substantially smaller than the length scales of the fabrication errors observed experimentally, which were in the range of  $25 \mu\text{m}$ . Hence, the primary factor causing the process plan to fail should be the drawbacks in the algorithm as presented in Section 7.6 and they are not a result of the DMD operation in experiments.

## 7.8 Chapter Summary

The material model developed in Ch. 6 was implemented in a process plan similar to one from previous literature (Zhao X. [14]). Least squares optimization method was used to estimate the exposure time for each micromirror based for curing the desired part geometry. Four sample cases were fabricated and the cured profiles were compared with

desired part geometries. It was observed that the experiments did not accurately cure the samples.

A detailed error analysis was presented to identify the cause of errors. It was found that since the ECPL system is inadequate to project exposures with uniform irradiation, the semi-empirical material model could not be applied to the process planning method directly. Hence, an alternate strategy to process planning has to be incorporated in order to cure accurate samples. It was found necessary to refine the process planning method with a refined material model (suitable for the ECPL process) and to incorporate the effect of dynamic curing with bitmaps. The next chapter presents the refined process plan, which leverages from the material model developed earlier and few components of the process planning method developed in this chapter.

## CHAPTER EIGHT

### REVISED PROCESS PLANNING METHOD

This chapter presents a refined process planning method, which assumes a hybrid approach between using semi-empirical material models (developed in Ch. 6) and optimization of desired part shape using chemical kinetic simulations. Experimental validation is presented at the end of the chapter.

#### 8.1 Need for Revised Process Planning Method

The basic structure of the process planning method presented in Chapter 7 was derived from existing literature as presented in Jariwala [33, 56] & Zhao [14]. Through detailed experimentation and error analysis, it was shown that the process planning method had several drawbacks. The researchers did not have access to effective metrology tools and hence the experimental validation of their proposed planning methods was not adequate. Moreover, the process-planning algorithm assumed that the complex process of photopolymerization could be assumed as a simple exponential function of exposure (based on the Beer-Lambert law for attenuation). Although the incident exposure (required to cure the photopolymer) can be considered additive, the effect of curing is not necessarily additive in nature. As shown in Chapter 6, the polymerization process is highly coupled and the shape and dimensions of the final cured product depends on the entire exposure pattern and sequence of exposure.

The process-planning problem, as derived from existing literature was split into two parts

- i.) Conversion of desired product geometry/shape in to required exposure
- ii.) Estimation of required exposure in to process inputs
  - a. Estimation of time of exposure for each micromirror
  - b. Clustering of micromirrors into bitmaps with common times of exposure

From the error analysis (presented in Section 7.6), it was clear that splitting the original process planning problem into two separate problems ignored the coupling effect (between irradiation and curing) inherent in the photopolymerization process. The final cured geometry is not only a result of total exposure ( $\text{mJ}/\text{cm}^2$ ), but also the irradiance ( $\text{mW}/\text{cm}^2$ ) with which the resin was exposed. The lessons learned could be summarized as follows:

- i. The process inputs are not only the bitmaps and time of exposure, but also the sequence of exposure.
- ii. The material model cannot be used independently assuming a homogeneous flat-top irradiation profile, rather it should consider the optical aberration effects present in the ECPL system

It is clear that a more holistic approach towards process planning is necessary. Creating an independent material model without considering the optical system design is not suitable for process planning. The following section explains the revised holistic process planning method and presents a revised hypothesis to the originally posed research question #4.

## 8.2 Holistic process planning approach

Since the experimental validation suggested the need for a refined process planning method, the research question 4 (presented earlier in Ch. 7) was revisited. It is presented as follows:

### Research Question #4

**How to formulate a process plan to generate accurate process inputs in order to cure a part of desired shape and size in ECPL process?**

The newer holistic process planning approach leads to using both the material module and system module together to estimate the process inputs. Using the chemical kinetics based material model (developed in Chapter 6), given the bitmaps and the exposure time, the geometry of the cured part can be reliably estimated. This leads us to the revised hypothesis as follows:

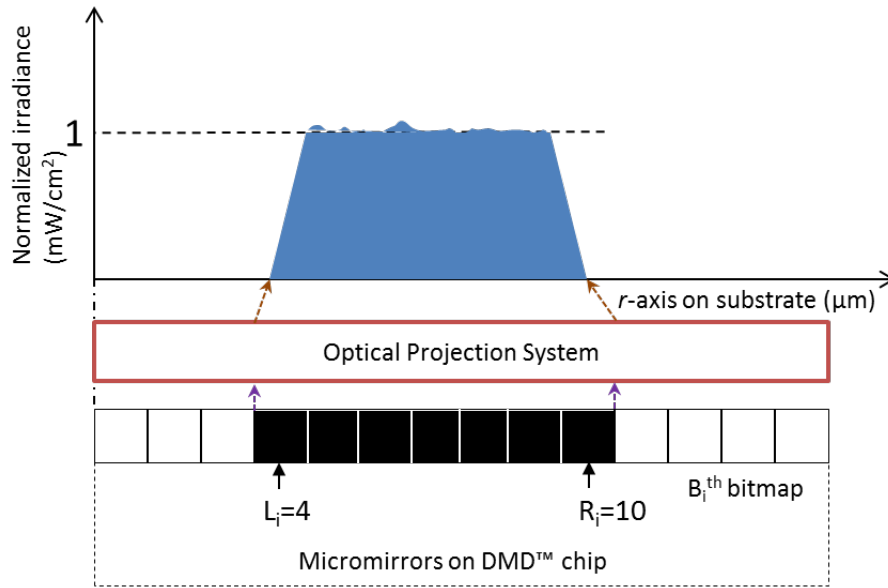
### Revised Hypothesis for Research Question #4

*The process inputs for the ECPL process (like bitmaps and corresponding exposure time) for a given desired part geometry can be estimated by optimizing the cured part geometry using the material model based on chemical kinetics (which was previously validated).*

A Matlab script (refer appendix) was written to simulate the shape of the cured part for given bitmaps and exposure time based on chemical kinetics modeled in Comsol. However, the problem for process planning is to estimate the accurate bitmaps and corresponding exposure time required to cure the desired part shape. This problem can be

simplified to a significant extent for the ECPL system studied in this research. The ECPL system can only fabricate structures with monotonically decreasing part geometries, i.e. it is reasonable to assume that the size of the total exposed region should gradually decrease (or remain constant) as more and more height of the cured part is formed. This helps in greatly constraining the optimization problem proposed in the revised hypothesis. Moreover, since the research objective was to fabricate lens like axi-symmetric shapes, the optimization problem can be kept limited to curing two-dimensional axi-symmetric profiles at the center of the substrate.

The overall problem presented by the research question can be simplified as generating the process inputs (a line of clustered micromirrors with corresponding times of exposure) necessary to cure the half-sectional profile of the desired part geometry. Once the line of clustered micromirrors is estimated, the bitmap can be generated by ‘rotating’ the micromirrors along  $360^\circ$  to generate the bitmap. Hence, the process inputs can be listed as follows and illustrated in Figure 128.



**Figure 128 Illustration of the parameters of the process inputs for the revised process planning method**

$B_i$  – Bitmap used to cure the  $i^{\text{th}}$  layer, such that  $L_i$  is the number of micromirrors offset from the center of the part to be cured and  $R_i$  is the total number of micromirrors from the center of the part to be cured.

$T_i$  – Calculated exposure time for  $i^{\text{th}}$  bitmap

From the discussion on material models and experimental observations, it was shown in Chapter 6 that each bitmap with a corresponding exposure time leads to curing of a single “layer”. From Figure 87, it can be seen that the overall dimensions of this “layer” increase as the exposure time is increased. However, it must be noted that the “layer” cured in ECPL is not similar to the one in conventional stereolithography (SLA) processes. In typical SLA processes, the layers are simply linearly additive, i.e. each layer is added to the previous layer in incremental format and the previous cured layer does not necessarily affect the dimensions of the next layer. Hence, it is reasonable to predict the



height of the layers in typical SLA processes. In ECPL, the “layers” refer to the cured part resulting from a specific bitmap for its corresponding time of exposure. The geometry of the subsequent “layer” formed on top of the previously cured layer depends not only on the size of the bitmap and exposure time, but also on the exposure history at a specific point of interest. This dependence of curing on the exposure history complicates the process planning method. However, this complication can be reduced by assuming that the overall size of the bitmap projected is always smaller than the previously exposed bitmap. Thus, the problem can be constrained such that if  $B_i$  is the bitmap to be projected on the DMD™ chip for curing the  $i^{\text{th}}$  layer (with reference to Figure 128),  $R_{i+1} \leq R_i$  and  $L_{i+1} \geq L_i$ .

It is to be noted that the first “layer” would be cured on the substrate and hence will not be affected by the previous history of exposure. Hence, estimation of the first group of process inputs (bitmaps and corresponding exposure time) can be made using a revised material model based on the strategy presented in Chapter 6 in section 6.4. The process inputs to cure the subsequent “layers” can be estimated using iterative simulations of the chemical kinetic model. Hence, the process planning method can be simplified in form of two-step process as follows:

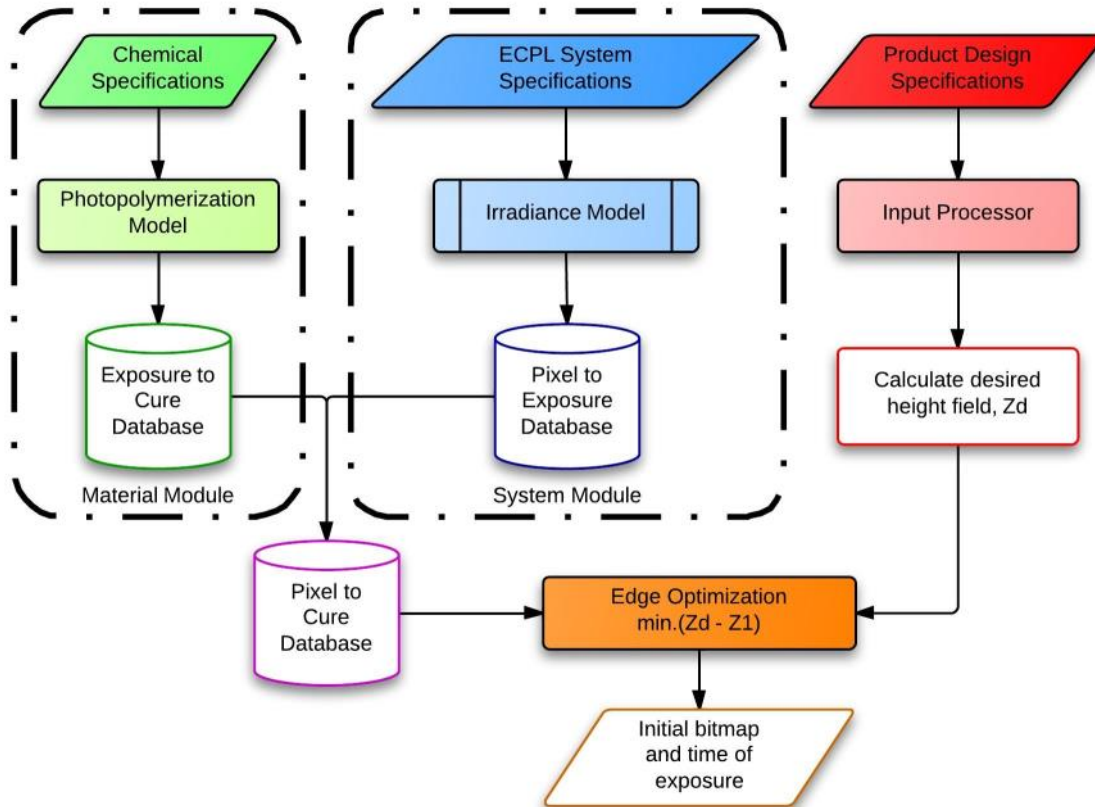
1. Estimate the first set of process input (bitmap#1 and exposure time) by optimizing the cured part shape using a revised material database.
2. Estimate the subsequent process inputs by optimizing the cured part shape using actual simulations of the chemical kinetic model.

### 8.2.1 Estimating first set of process inputs

In order to eliminate the primary drawback of the process plan discussed in Chapter 7, the revised material model has to be built such that it incorporates the varying irradiance produced at the edges because of the optical aberrations present in the ECPL system. An irradiation model for the ECPL system was presented in Chapter 5, which was validated using simulations and experiments. This model provided a relationship between the number of pixels exposed on the DMD™ chip and the irradiance produced on the resin substrate. This model was used to recreate the material model discussed in Chapter 6. Using the method presented in Section 6.4, an empirical material model (referred to as ‘Pixel to cure’ database) was created with the conditions as shown in Table 12. The process of estimating the first bitmap is illustrated in Figure 129.

**Table 12 Parameters used to create the revised material model (‘Pixel to Cure’ Database)**

Input Variables	→	Total exposure time (s)	Number of pixels exposed, $R_i$
Range	→	1 – 30	1 – 45
Increments	→	1	1
Output Variables	→	Cured Profile, $Z(r)$	Maximum cured part width at base, $R$



**Figure 129 Process Plan - STEP #1**

The revised material model database was created using Matlab (refer appendix). This model provided a relationship between the number of micromirrors projected on the DMD™ chip and the resulting cured profile, as estimated by the chemical kinetic model (which incorporating oxygen inhibition and diffusion).

With reference to Figure 129, the first bitmap and exposure time were estimated by optimizing the cured part edge. It is to be noted that the primary function of the first bitmap is not to cure the entire part geometry, but to cure the base and the corresponding edge of the desired part. Hence, the optimization problem is not to be assumed to optimize the entire cured part geometry. Rather, the objective function of the

optimization problem is changed based on the resulting cured part height. This explanation can be mathematically explained as follows.

Consider  $Z_d(r)$ , as the desired half-sectional cured part geometry, such that  $r$  is the radial distance from the center. The process of calculating from the product specifications was explained in Section 7.1. The variables are illustrated in Figure 130. The edge optimization problem can be written as

Input: Desired cured part geometry:  $Z_d(r)$  ( $\mu m$ ) (at the substrate level)

Output: Initial bitmap,  $B_1$  and corresponding exposure time,  $T_1$

Objective:  $\min\{f(B_i, T_i) - Z_{di}(r)\}$ , such that  $T_i > 0; R_i > L_i \geq 0$

where  $f(B_i, T_i)$  is the cured part geometry obtained from the chemical kinetics' based material model and  $Z_{di}(r)$  can be written as follows:

$$Z_{di} = \begin{cases} Z_k = \max[f(B_i, T_i)] & \text{if } r \leq k \\ Z_r & \text{if } r > k \end{cases} \quad (8-1)$$

such that  $k$  is the coordinate of the intersection between the curves  $Z_k$  and  $Z_r$  along the  $r$ -axis (as shown in Figure 128).

It is to be noted that the time increment for each bitmap was limited to 0.1s only, since this is the least possible time increment on the projection system used in the ECPL system studied in this research. Using the above method, the first set of bitmap and its corresponding exposure time was estimated.

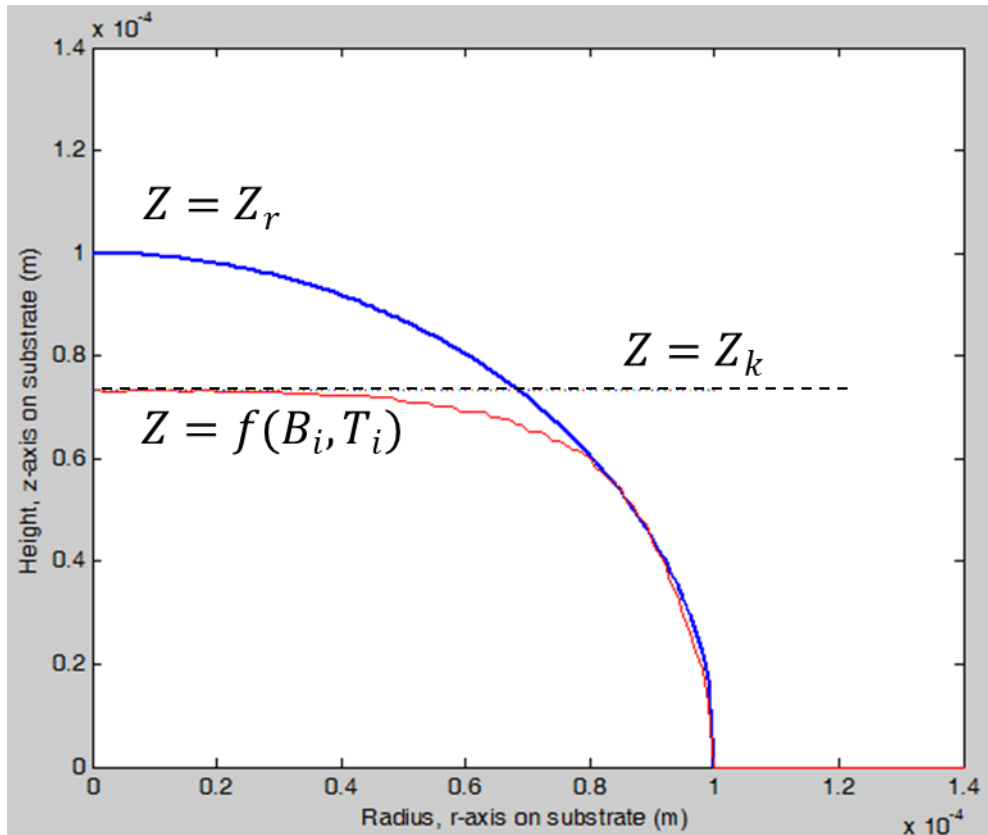
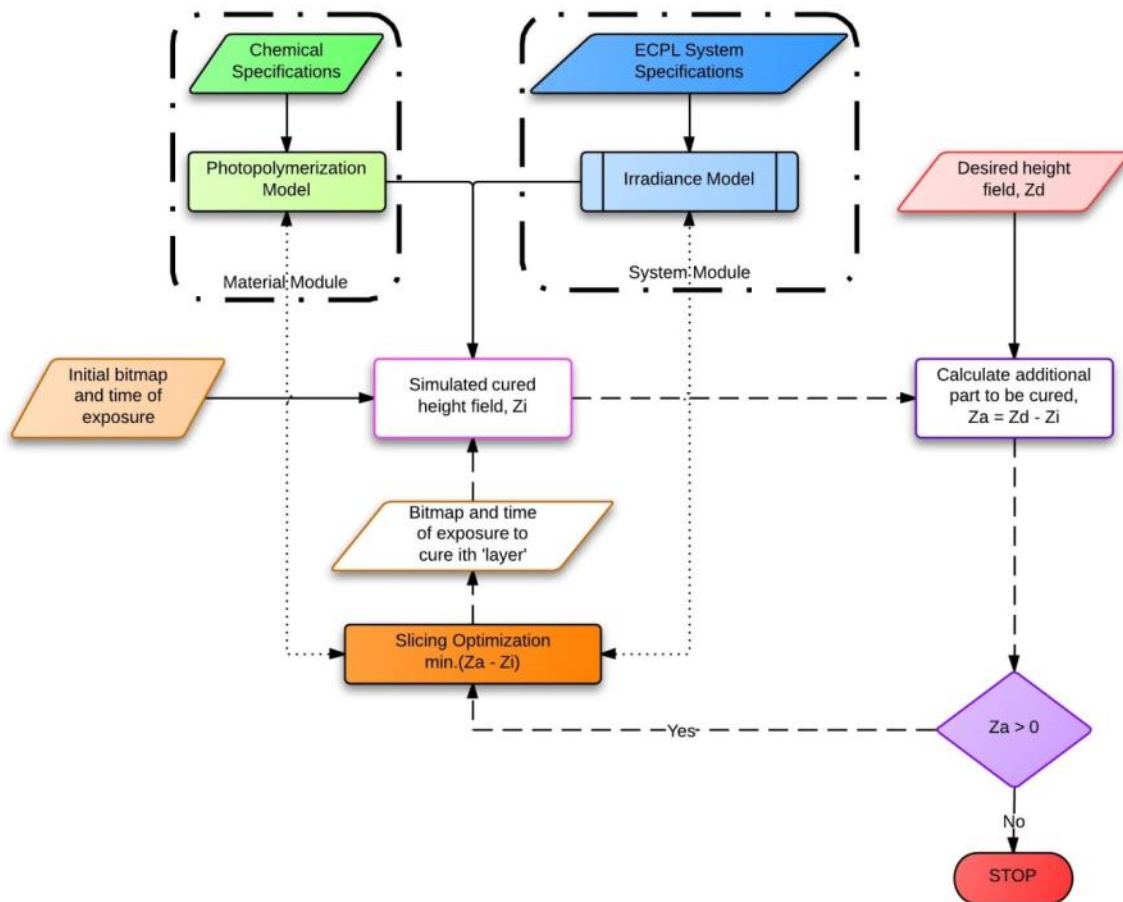


Figure 130 Variables used in the optimization problem

### 8.2.2 Estimating subsequent set of process inputs

Using the information of the first bitmap and its exposure time, the subsequent bitmaps cannot be estimated directly from the ‘pixel to cure’ material model. This is because the material model was generated for curing the part on the substrate level and cannot be used directly to estimate the cured part geometry on a previously cured surface. Hence, a revised optimization method is necessary that incorporates the history (and hence sequence) of curing. Figure 131 shows the flow chart for estimating the subsequent bitmaps and exposure times. The inputs to the flow chart are the first bitmap and exposure time (generated as discussed in section 8.2.1) and the desired cured part

geometry (similar to the explanation in section 7.1). The dotted lines show the simultaneous dependence of the optimization module on the system module and the material module. The dashed lines show the iterative nature of the loop and the process stops when the entire desired part geometry is cured completely (within a pre-set threshold).



**Figure 131 Process Plan - STEP #2 (Simulated cured height field,  $Z_i$  is obtained using COMSOL simulation)**

The objective function used in the optimization module for this process is similar to the one explained earlier (in Section 8.2.1), however the only change is that the simulated

cured part is a result of actual chemical kinetics simulations and not a pre-computed material model. The optimization module can be explained as follows.

Consider that the first step (section 8.2.1) of the process plan resulted in a bitmap,  $B_1$  with parameters,  $L_1$ ,  $R_1$  and exposure time as,  $T_1$ . Since the geometry to be cured is assumed to be monotonically decreasing in width as the height increases, the search space for the parameters of the next bitmap can be set as,  $L_2 \geq L_1$ ;  $R_2 \leq R_1$  and  $T_2 > 0$ . This can be generally denoted as:  $L_i \geq L_{i-1}$ ;  $R_i \leq R_{i-1}$  and  $T_i > 0$ ; where  $i$  is the specific “layer” for which optimization is being conducted. The optimization problem can be expressed as:

Input: Desired cured part geometry:  $Z_a(r)$  ( $\mu m$ ) (at the substrate level). Initial Bitmap  $B_1$ , and time of exposure,  $T_1$ .

Output: Bitmaps,  $B_i$  and corresponding exposure times,  $T_i$  to cure the entire desired part geometry

Objective:  $\min\{g(B_i, T_i) - Z_{ai}(r)\}$ , such that  $T_i > 0$ ;  $R_i > L_i \geq 0$

where  $g(B_i, T_i)$  is the cured part geometry obtained from the chemical kinetics’ based simulations and  $Z_{ai}(r)$  can be written as follows:

$$Z_{ai} = \begin{cases} Z_m & = \max[f(B_i, T_i)] - f(B_1, T_1) & \text{if } r \leq m \\ Z_r & & \text{if } r > m \end{cases} \quad (8-2)$$

such that  $m$  is the coordinate of the intersection between the curves  $Z_m$  and  $Z_a$  along the  $r$ -axis (similar to ‘k’, as shown in Figure 130).  $Z_a$  is the additional part to be cured and calculated as follows:

$$Z_a = Z_d - Z_i \quad (8-3)$$

Both the first and second stages of the process plan were coded using Matlab and several example cases were tested. The following sections present the validation to the revised hypothesis using the test cases, both through simulations and experiments.

### **8.3 Validation of Revised Hypothesis for Research Question 4**

In order to validate the revised hypothesis for research question 4, experiments were conducted using the revised process planning method. Matlab scripts were written to encode the revised process planning algorithm (refer appendix). Three test cases were built using the revised process planning software. The bitmaps resulting from the process planning method were projected on the DMD™ in the ECPL system for their corresponding times of exposure. The cured samples were then washed, post-cured and measured using the LEXT 3D confocal microscope. The following sub-sections present the results of each sample.

#### **8.3.1 Spherical Lens Example**

The desired part geometry is a spherical lens with radius and sag of 100µm. Figure 132 shows the height field of the desired lens geometry in form of half-cross sectional.



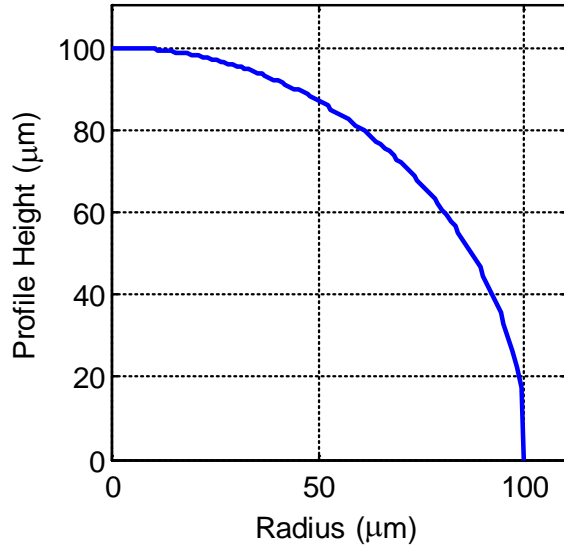


Figure 132 Profile of desired spherical lens geometry

The resulting 8 bitmaps are shown in Figure 133.









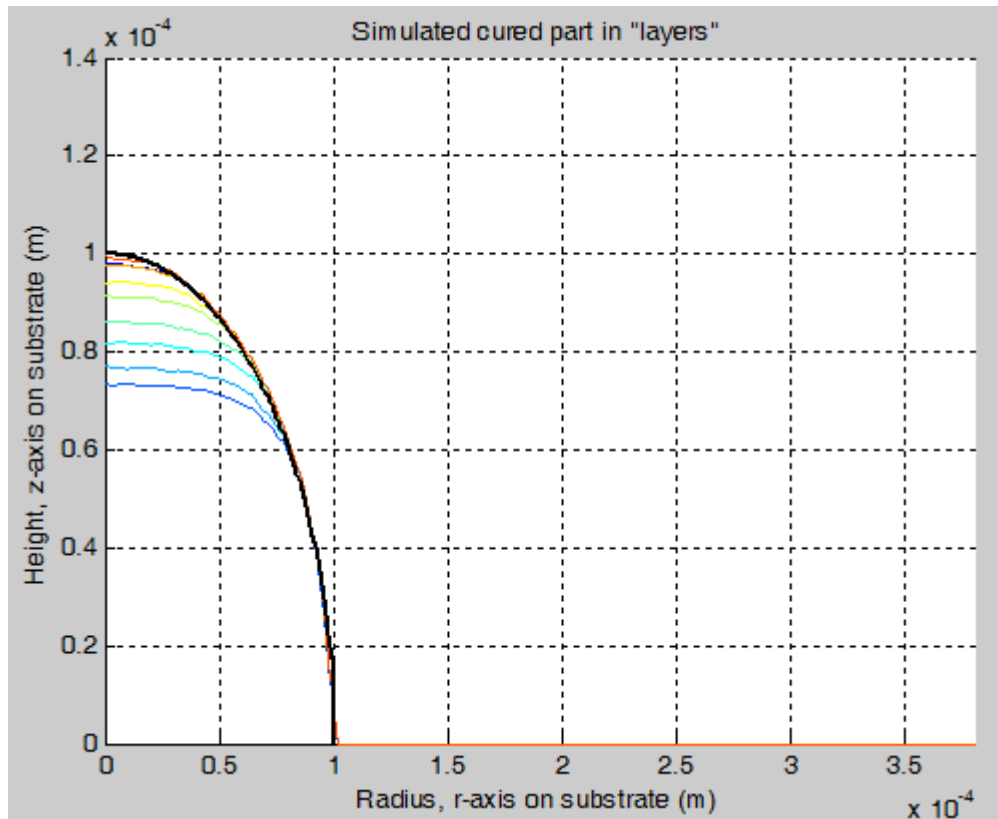
 $R_i=12, 7.9s$	 $R_i=11, 0.8s$	 $R_i=10, 1.3s$
 $R_i=9, 1.2s$	 $R_i=8, 1.8s$	 $R_i=7, 1.2s$
 $R_i=6, 1.7s$	 $R_i=5, 1.8s$	X

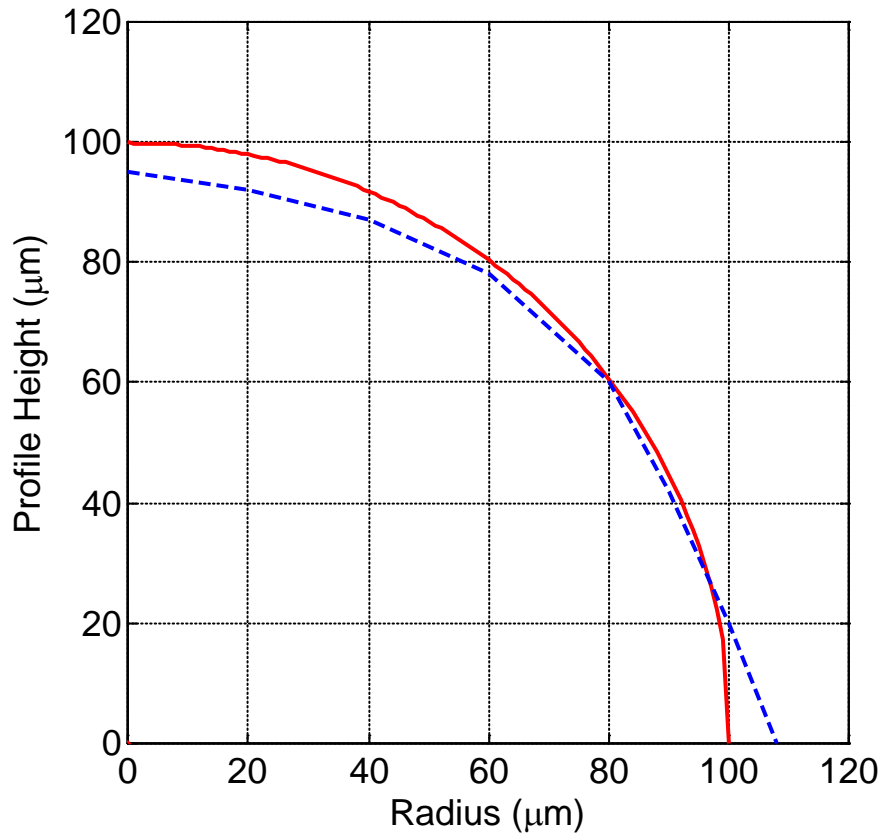
Figure 133 Calculated bitmaps and corresponding exposure times for spherical lens example

The simulation result showing the growth of curing process for every individual bitmap projected with the calculated exposure time is shown in Figure 134. Solid black line shows the superimposed desired part profile.



**Figure 134 Simulated cured part height from individual bitmaps resulting from the process plan**

The resin chamber was loaded with the photopolymer and the generated bitmaps were projected on the DMD™ chip for the corresponding exposure times. The sample was then washed and post-cured. Figure 135 presents the comparison between the desired part geometry and the experimentally cured part geometry in a half-sectional view. It must be noted that the experimental curves were obtained by interpolating the measurements of the part heights at approximate intervals of 10 $\mu$ m.

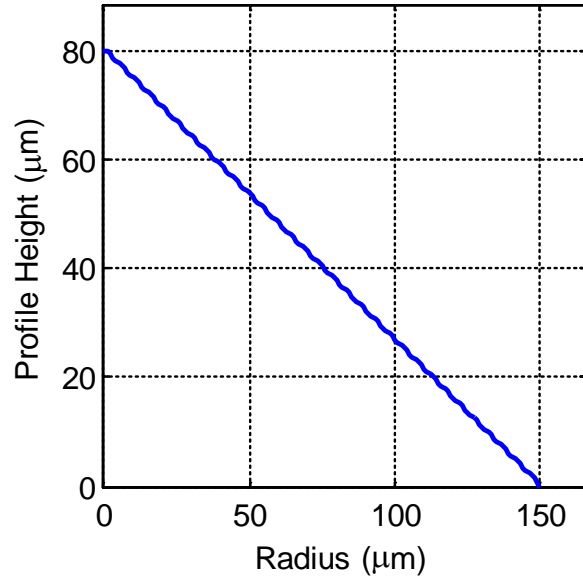


**Figure 135 Comparison of the half-sectional profiles of the cured part sample and the desired part geometry (Desired part profile is in red and experimentally cured profile is shown in blue)**

It was observed that the experimental samples matched the desired part profile more closely than from the earlier process planning method. The cured part radius (at the base) was larger than desired.
















### 8.3.2 Conical Lens Example

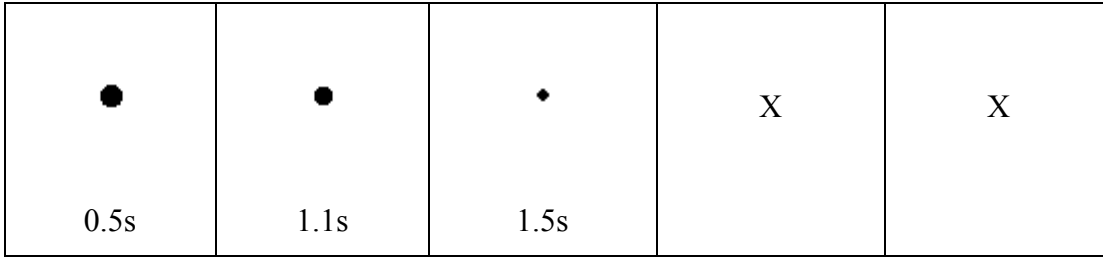
Figure 136 shows the desired half cross section of the geometry of a conical lens to be cured. The desired diameter was 150μm and the height was 80μm.



**Figure 136 Half-sectional profile of desired cylindrical lens geometry**

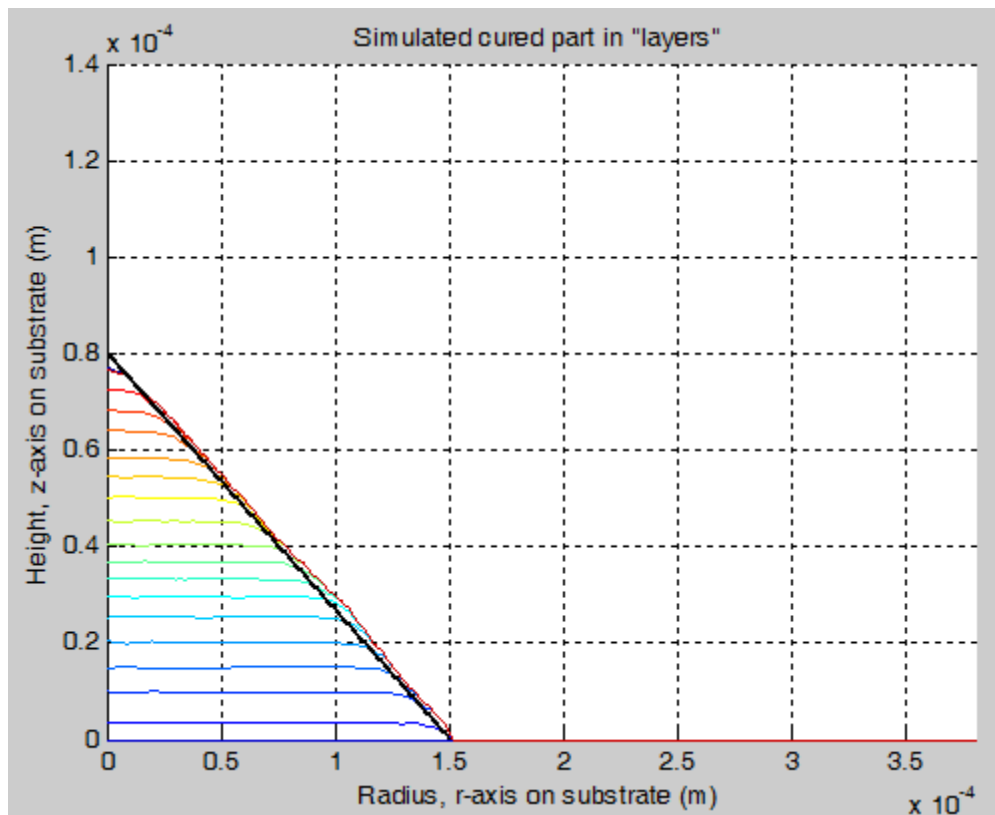
The calculated bitmaps (18) resulting from the process planning method are shown in Figure 137.

 1.2s	 0.1s	 0.1s	 0.1s	 0.2s
 0.1s	 0.2s	 0.1s	 0.2s	 0.2s
 0.4s	 0.3s	 0.4s	 0.4s	 0.8s



**Figure 137** Calculated bitmaps and corresponding exposure times for conical lens example

The simulation result showing the growth of curing process for every individual bitmap projected with the calculated exposure time is shown in Figure 138. Solid black line shows the superimposed desired part profile.



**Figure 138** Simulated cured part height from individual bitmaps resulting from the process plan for conical lens example

Figure 139 shows the comparison between the desired part geometry and the experimentally cured part geometry in a half-sectional view. The cured part shape is still under cured compared to the desired part shape. However, the error is smaller compared to the results obtained from the previous process plan.

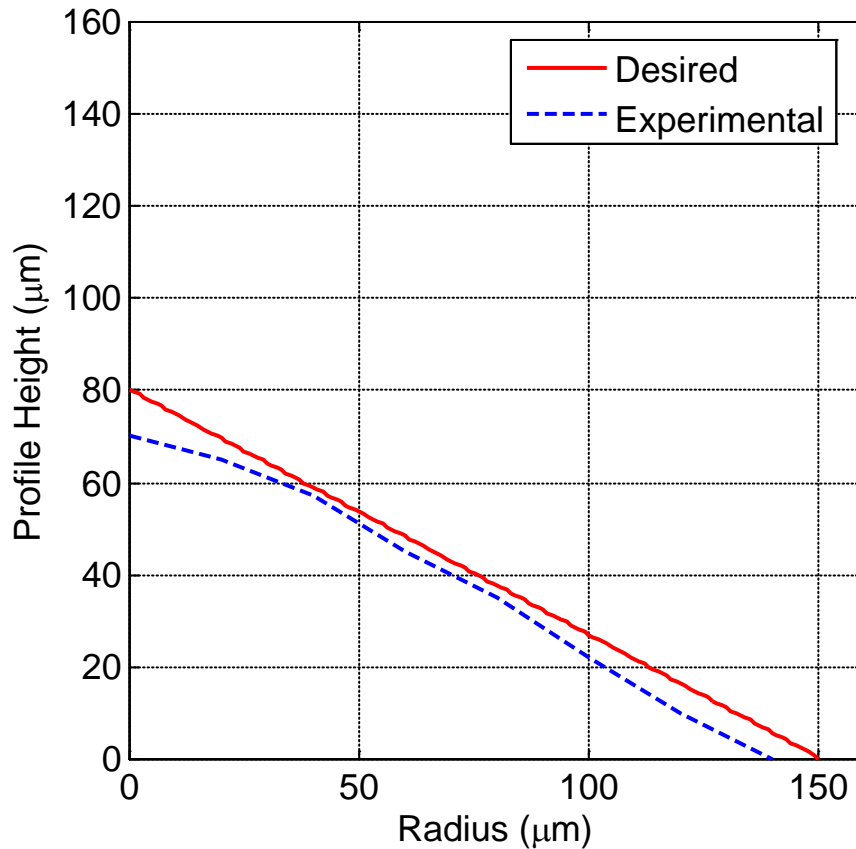
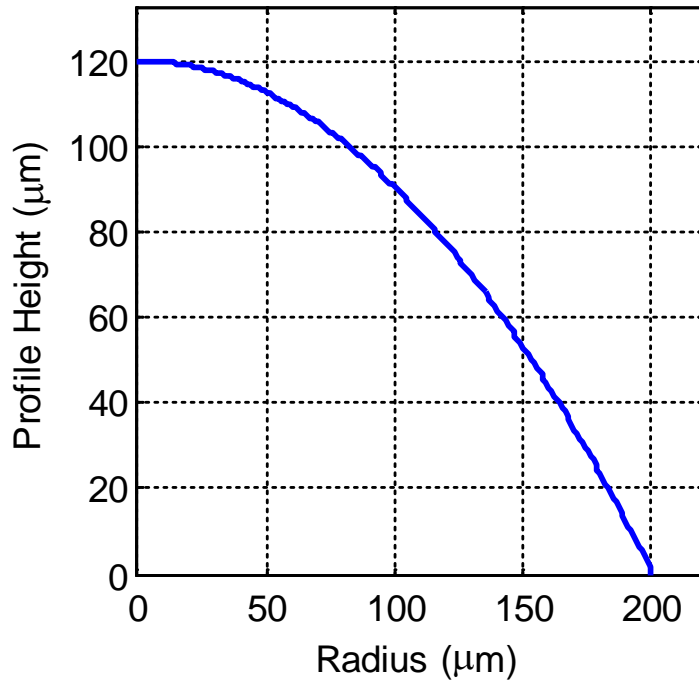


Figure 139 Comparison of the half-sectional profiles of the cured part sample and the desired part geometry






















### 8.3.3 Aspheric Lens Example

Figure 140 shows the desired half cross section of the geometry of a conical lens to be cured. The desired diameter was  $200\mu\text{m}$ , conic constant was  $-1$  and the sag height was  $120\mu\text{m}$ .



**Figure 140 Half-sectional profile of desired aspherical lens geometry**

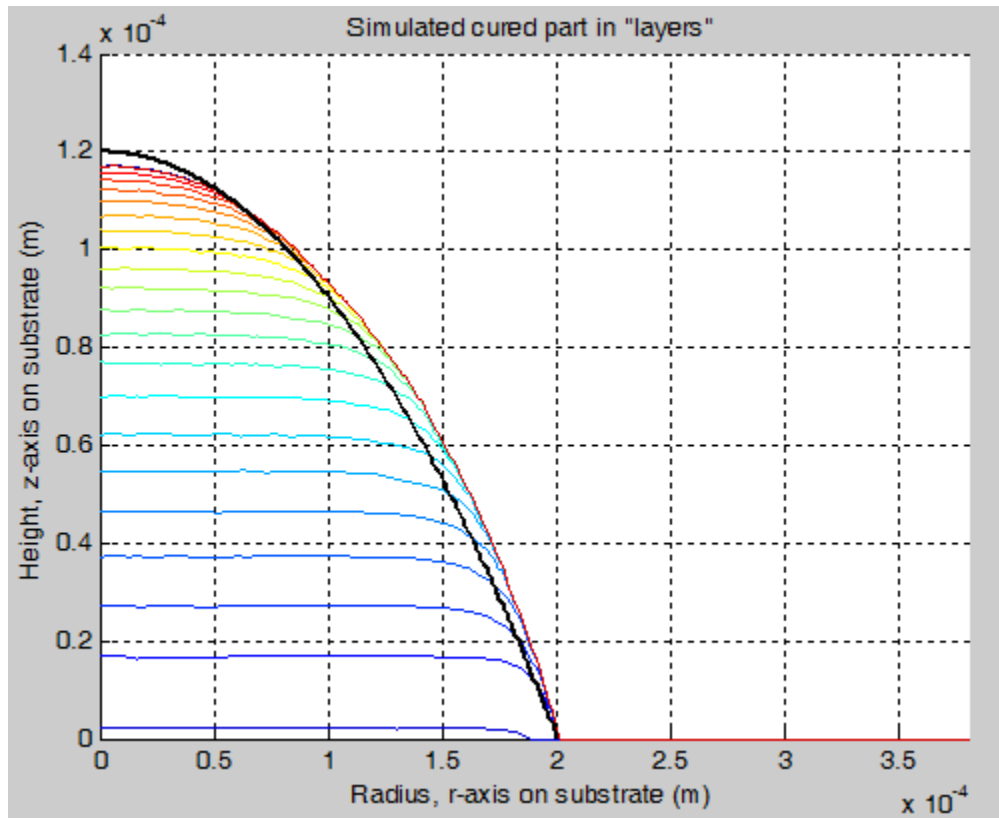
The process planning method resulted in 21 bitmaps and they are presented with corresponding time of exposure in Figure 141.

 1.5s	 0.4s	 0.5s	 0.6s	 0.7s
 0.8s	 0.9s	 1.2s	 1.2s	 1.4s
 1.3s	 1.5s	 1.5s	 1.8s	 1.7s
 1.9s	 2s	 2s	 2s	 2s
 2s	X	X	X	X

**Figure 141** Calculated bitmaps and corresponding exposure times

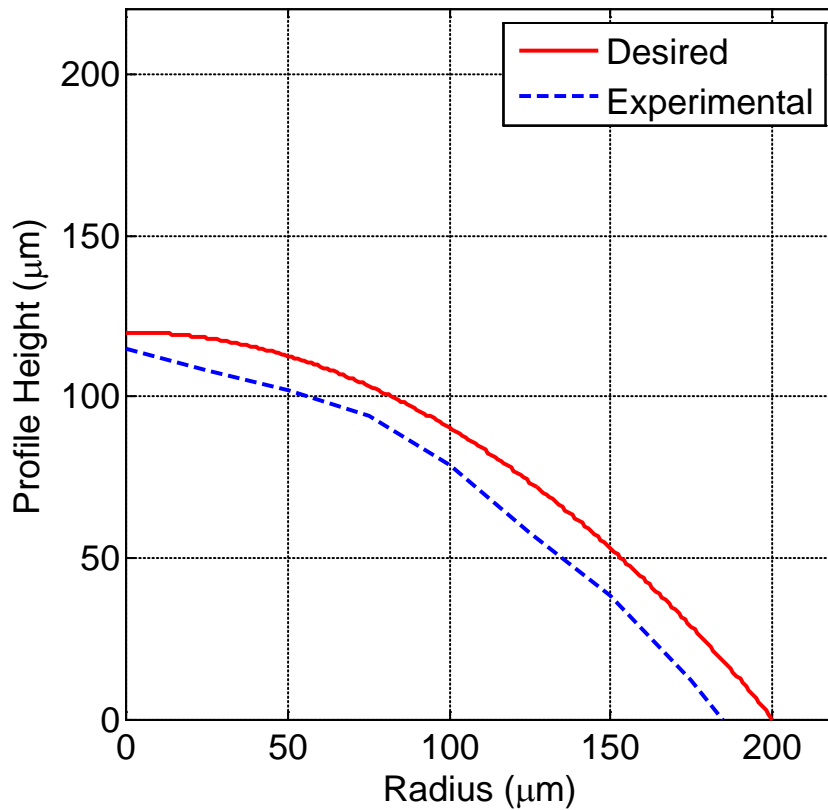
The simulation result showing the growth of curing process for every individual bitmap projected with the calculated exposure time is shown in Figure 138. Solid black line shows the superimposed desired part profile. Simulation results suggest that the cured part profile maybe slightly larger than the desired part shape.





**Figure 142 Simulated cured part height from individual bitmaps resulting from the process plan for aspheric lens example**

The experimental result is shown in Figure 143, which presents the comparison of the experimental part profile with desired part geometry. The experimental part profile was created by interpolating the measurements of the part heights at approximate intervals of 10 $\mu$ m along the radius of the cured par, and hence is shown in dotted lines.



**Figure 143 Comparison of the half-sectional profiles of the cured part sample and the desired part geometry**

From Figure 143, it can be observed that the resulting part profile matches the desired part shape. However, under curing is observed for both height and radius. The deviation in overall profile (both height and radius) was found to be less than 15% from the desired part geometry.

#### **8.4 Error Analysis & limitations**

Overall, the samples seem to match the desired part height fairly well. Table 11 shows the deviations between the measured samples and desired part geometry. It is to be

noted that three samples were fabricated for each test case and the results shown in the table are average of the total five samples.

**Table 13 Summary of average errors observed from experiments (revised process plan)**

<b>Sample Geometry</b>	<b>Error in height</b>	<b>Error in radius</b>	<b>Comments</b>
Spherical	-10%	+10%	Over-cured in radius and under-cured in height
Conical	-12.5%	-10%	Under-cured in both dimensions
Aspheric	-8%	-15%	Under-cured in both dimensions

When compared to Table 11, it is evident that the revised process planning method yields better results. Moreover, the deviation between the cured part geometry and the desired part geometry is less than 15%, both in sag height and diameter. The under-curing errors are higher for geometries cured with more number of “layers” or bitmaps. Hence, the observed under-curing can be attributed to the errors in accurately projecting the bitmaps using the projector. Post-processing might have been another cause for errors. Based on the experimental results and the simulation results, the revised hypothesis to research question 4 is validated.

It is to be noted that the revised process planning method is currently applicable only for axi-symmetric convex shaped structures. This is adequate for the ECPL system’s anticipated end application, which is to fabricate micro-optical components. However, this process planning method can be easily adapted to fabricating non-convex structures

(for example, concave lenses) by avoiding the first step and running only the second simulated slicing step. The drawback of avoiding the first step is that the software would take longer to estimate all the bitmaps to cure the desired part geometry, since the starting number of variables will be very large.

## **8.5 Chapter Summary**

This chapter was an extension of the earlier chapter, which presented the process planning method. It was seen earlier that a modular process planning approach had severe drawbacks and failed to yield accurate experimental results. A holistic approach to process planning method was presented in this chapter. The process-planning problem was split into two steps – estimating first bitmap and exposure time using material model database, and estimating subsequent bitmaps and exposure time based on simulated slicing techniques. A novel simulated slicing technique suitable for the ECPL process was presented in this chapter. This slicing technique was used to determine the total number of bitmaps to be projected and the size and exposure time for each bitmap.

The revised hypothesis to research question 4 was validated using both simulations and experiments. Experimental test cases (same as the ones in Chapter 7) were used for validating the hypothesis. The revised process planning method was found to yield more accurate results than the ones derived from existing literature. In summary, this chapter presented the successful implementation of new knowledge created in the earlier chapter by means of creating a novel process planning method.

## CHAPTER NINE

### CLOSURE AND CONTRIBUTIONS

This chapter summarizes the conclusions from the previous chapter and presents the knowledge created because of the research conducted for this dissertation. In Section 9.1, the entire work presented in this dissertation is summarized. The research questions and hypothesis evaluated in this thesis are revisited in Section 9.2. In Section 9.3, the intellectual and developmental/engineering contributions of this work are presented. The chapter ends with Section 9.4, which presents the scope of future work, which may be performed to mature the ECPL technology.

#### 9.1 Summary of the Dissertation

The overall objective of this research was to develop the Exposure Controlled Projection Lithography (ECPL) system in order to formulate a process planning method to enable fabrication of lens shaped structures. For reliable fabrication of accurate lens shaped structures from the ECPL system, the sources of variations were systematically analyzed. A real-time monitoring system was developed because of this study, which further helped in identifying the sources of variations. The process was improved to reduce the impact of variations. An in-depth research was conducted to understand the impact of various factors that govern the formation of the shape of the parts cured from the ECPL Process. The ECPL process model was created and presented in Chapter 5. A detailed study of the oxygen inhibition based photopolymerization model was presented in Chapter 6. Experiments were conducted to validate the photopolymerization model

based on chemical kinetics. A semi-empirical material model was developed. The process models were used in a refined version of an existing process planning method. Experiments were conducted to validate the process planning method, which did not match well with expectations. The experimental error analysis highlighted the errors caused due to implicit assumptions in the process planning method. The material models were refined and a new process planning method was presented in Chapter 8. The method was validated using experiments.

Using the work presented in this dissertation, a more accurate model prediction of the cured part shape resulting from photopolymerization process is possible. This dissertation also presents a feasible process planning method, which can be utilized to fabricate lens like structures from the ECPL process.

### **9.1.1 ECPL system design**

An Exposure Controlled Projection Lithography (ECPL) system was designed and built as part of this research. The system design evolved over four iterations. The primary challenge in system assembly was to obtain a homogenous irradiation profile at the substrate level. The finally assembled ECPL system was found to produce homogenous light intensity within  $\pm 5\%$ . The design and the bill of materials is documented in Chapter 3. A broadband UV lamp was used as the light source. A beam conditioning system was used to homogenize and collimate the light. A Digital Micromirror Device (DMD™) from a commercially available projector was used as the dynamic mask to control the patterned exposure into the resin chamber.

Preliminary experiments highlighted the need to identify the sources of variations in the ECPL process. An interferometric system was proposed and augmented to the existing ECPL system to provide a “window” into the actual curing process in real-time. This monitoring system helped improve the post-processing method and eventually increase the system’s repeatability. The post-process was experimentally improved, which reduced the overall variations in the ECPL system to less than 1%. The monitoring system was able to detect the height of the cured sample.

### **9.1.2 Process and material model**

Systematic investigations were conducted to identify the factors that affect the shape of the cured part. It was confirmed that optical self-focusing does not significantly affect the shape of the cured part in the ECPL system, as used in this research. Experimental studies concluded that the washing process developed in this study is well suited for parts fabricated from ECPL and does not cause a significant erosion effect on the height of the cured parts. It was found that oxygen inhibition affects the polymerization process and its effect was modeled in greater depth using models available in literature.

An existing kinetic model with oxygen inhibition and diffusion (from literature) was studied. It was found that the rate constants available from literature failed to explain the impact of oxygen inhibition and diffusion during polymerization. Experimental values from literature were used to optimize the rate constants suitable for the process conditions used in the ECPL system. Exhaustive photopolymerization simulations were conducted in COMSOL® to generate a semi-empirical material model based on the well-

known Beer Lambert's law of attenuation ( $E_c - D_p$  model). The semi-empirical material model presented a reversible relationship between the incident exposure and the cured part shape.

### **9.1.3 Process planning method**

The models created in earlier chapters were used in conjunction with an existing process plan to formulate a revised process planning method. The process planning method was coded in Matlab to accept lens specifications (in terms of radius, sag height, conic constants, etc.) and estimate the required process inputs to drive the ECPL system. The process inputs for the ECPL system are the bitmaps (clusters of micromirrors) and time of exposure for each bitmap. Experiments for four extreme test cases were conducted on the ECPL system using the process planning method. Experimental observations suggested that the process plan was inadequate to estimate the process inputs. Several samples were under cured. A detailed error analysis was conducted, which highlighted some implicit assumptions within the process planning method.

A refined material model and a new process planning method were developed to avoid the implicit assumptions. The improved process planning method was validated using simulations and experiments.

## **9.2 Revisiting Research Questions**

This section presents the research questions investigated and the hypothesis evaluated in this thesis. The objective of this research presented in Chapter 1, is restated here:



*“To formulate a process planning method to build sub-millimeter lens shaped structures from the ECPL process”*

In order to achieve this objective several research questions were identified and hypotheses were proposed for each of them. The validity of the hypotheses is tested in this section.

### **9.2.1 Research Question 1**

How to conduct an in-situ real time monitoring of the ECPL process without affecting the fabrication process?

**Hypothesis:** *A system that can track the change in speed of light through a medium can be used to visualize the extent of the polymerization process.*

**Validation of Hypothesis 1:** The basic working principle of a Mach-Zehnder interferometer was used to develop a monitoring system. During polymerization, the material cross-links and causes an increase in density. The speed of light slows down in a denser medium, as compared to a rarer medium. Experimental results validate that the interferometric system was capable of capturing the change in the speed of light through the medium as the polymer cured in the ECPL system. Experimental analysis and comparison with final cured part further provides validation that the interferometric system (which tracks the change in speed of light through the resin cell) can be used to visualize (and thus approximately quantify) the extent of the polymerization process.

### 9.2.2 Research Question 2

*What factors influence the generation of final shape/geometry of the cured part in the ECPL process?*

This research question was split into two sub-research questions as follows.

#### **Research Question 2.1**

**How does optical self-focusing affect the curing process in ECPL?**

**Hypothesis:** *Optical self-focusing is caused when light travels from the dense cured part into the relatively less dense uncured resin. Optical ray tracing simulations through the photopolymer resin can be used to verify if self-focusing leads to curing of parts with gradually reducing dimensions from near the substrate to the top free surface of the cured part.*

**Validation of Hypothesis 2.1:** Preliminary experimental results presented an impression that the cured parts resulting from the ECPL process may be subjected to edge rounding due to optical self-focusing. High fidelity optical simulations were conducted with simulating the presence of partially cured part over the substrate. The optical simulations conducted in LightTools® software demonstrated the negligible effects of self-focusing phenomena. Although this result was counter-intuitive, the observations make sense since the difference in refractive index between the cured geometry and the uncured resin is very small. Moreover, the rays of light enter the substrate at a shallow angle. In other words, the numerical aperture of the optical projection system of the ECPL system

studied in this research was less than 0.1, which reduces the possibility of optical self-focusing.

### **Research Question 2.2**

**How does post-processing affect the geometry of the final product resulting from the ECPL process?**

**Hypothesis:** *Post-processing steps like washing and post-curing affect the dimensions of the cured part resulting from the ECPL process. Confocal fluorescence microscopy can be used to determine the extent of swelling or erosion caused by post-processing on the final cured part.*

**Validation of Hypothesis 2.2:** The technique of confocal fluorescence microscopy was used to determine the part shape prior to washing and post-curing. A systematic experimental study was conducted to confirm that washing and post-curing does not significantly affect the final dimensions of the cured part resulting from the ECPL process. The overall study concluded that oxygen inhibition was a primary factor that affects the shape of the cured part, i.e. causes deviation of the final cured shape from the estimated part shape using empirical material models like the Beer-Lambert law.

### **9.2.3 Research Question 3**

**How to model the photo-polymerization reaction to include the complex/coupled effects of Oxygen in the photopolymerization process for curing using ECPL process?**

**Hypothesis:** *Oxygen inhibition and diffusion are the primary factors, which result in a deviation of the material response from the known  $E_c - D_p$  model. This change in the resin behavior can be modeled by modifying the  $E_c - D_p$  model to incorporate the under curing observed at the edges due to oxygen inhibition and diffusion.*

**Validation of Hypothesis 3:** An existing kinetic model with oxygen inhibition and diffusion (from literature) was used in this study with optimized rate constants for ECPL. The revised kinetic model was modeled using COMSOL® package to simulate the photopolymerization process and estimate the shape of the cured parts. The revised model was experimentally validated. Exhaustive photopolymerization simulations were conducted in COMSOL® to generate a semi-empirical material model based on the well-known Beer Lambert's law of attenuation ( $E_c - D_p$  model). Simulation results validated the hypothesis that a material model based on modification of the  $E_c - D_p$  model can be used to explain the material response in photopolymerization with oxygen inhibition and diffusion. One the primary contributions made during the course of validating the hypothesis was that a reliable model to estimate the shape of a cured part resulting from photopolymerization was created and experimentally validated. This model was further used in developing the process planning method.

#### **9.2.4 Research Question 4**

**How to formulate a process plan to generate accurate process inputs in order to cure a part of desired shape and size in ECPL process?**

This research question was reframed as follows.

**How to estimate the micromirrors and corresponding time duration during which they must be switched ON, in order to obtain the desired exposure profile at the substrate level? How to convert  $E_{p,q}$  ( $mJ/cm^2$ )  $\rightarrow$   $T_{i,j}$  (s)**

**Hypothesis:** *The desired process inputs (micromirrors and time duration for switching ‘ON’) for curing a desired geometry can be estimated by optimizing the exposure, ‘E’ required at the substrate level.*

**Validation of Hypothesis 4:** The experiments conducted with the process plan created based on the hypothesis did not match expected results and indicated that a revised hypothesis (and thus a revised process planning method) was necessary. A detailed error analysis conducted on the experiments presented in Chapter 7 highlighted the drawbacks of the process planning method derived from literature. The implicit assumption in this hypothesis was that curing depends only on the total exposure and not on irradiance. Moreover, the process planning method based on this hypothesis did not consider the transient effects of curing, or the history of exposure on the curing process.

It was concluded that a holistic approach to process planning was necessary and that utilizing independent material models was not appropriate. Hence, a revised hypothesis was proposed as follows:

**Revised Hypothesis:** *The process inputs for the ECPL process (like bitmaps and corresponding exposure time) for a given desired part geometry can be estimated by optimizing the cured part geometry using the material model based on chemical kinetics (which was previously validated).*

#### **Validation of Hypothesis 4:**

Experimental test cases were fabricated in the ECPL system using the revised process planning method. The simulation results and the final cured geometry closely matched the desired part geometry. The revised process planning method eliminates the assumptions made in creating the earlier version of the process plan. It incorporates the sequence of bitmaps projected, i.e. the history of exposure and effectively compensates for the effect of irradiance produced because of optical aberrations in the optical projection system of the ECPL apparatus.

### **9.3 Knowledge Contributions**

This section presents a summary of the new knowledge created during the course of research pursued in this thesis research.

The Exposure Controlled Projection Lithography System was studied as a fabrication process for the first time in this dissertation. This novelty was associated with very few existing literature about the behavior of material and light used to fabricate the desired part. Existing photopolymerization literature suggests using empirical models like the Beer-Lambert's model for estimating the shape of the cured part. Such models are well suited for estimating cured layer thickness or the minimum time required to cross-link/harden a layer of photopolymer resin with UV light. However, they fail to assist in the estimation of cured part shape. The experiments conducted in this research highlighted this severe drawback of using such a model. Past researchers tried to utilize the existing empirical model, but could not highlight the drawbacks of the model due to

lack of adequate experimentation. The existing literature could not be extended to the Exposure Controlled Projection Lithography process.

In Chapter 4, a real-time interferometric process monitoring system was created. This system provided new insights into the photopolymerization process in real-time. It confirmed the presence of incubation period, which is the period prior to start of cross-linking and the dark reaction. The Interferometric Cure Monitor provides a valuable addition to other analytical methods, both for improving the quality control of existing commercial processes and for aiding the development of improved photopolymer formulations. The results were published in Jariwala et. al [87] and Schwerzel et. al [88].

A reliable model to estimate the shape of a cured part resulting from photopolymerization was created and validated experimentally. The existing kinetic model from literature [44] was limited in its scope to determine the chemical composition recipe to obtain a desired Ec-Dp response from the material. This model was extended in to estimate the two-dimensional response of photopolymer to incident exposure in presence of oxygen inhibition and diffusion. This chemical kinetics' based model used to estimate the cured part height was published in Jariwala et. al [40]

Based on past literature study and optimization with experimental results, a revised range of appropriate rate constants (for the chemical kinetics' model) was identified. The kinetic model, with the optimized rate constants, was found to match the experimental observations with a higher degree of accuracy than the existing material models found in literature. This new material model better incorporates the material response expected during photopolymerization and is capable to predict the effect of

exposure conditions on polymerization. Existing stereolithography literature ignores the inhibition and diffusion phenomena and treats the curing due to exposure to be additive. The effect of oxygen inhibition and diffusion was experimentally quantified for the first time. This study provided a further understanding on extending the oxygen inhibition based photopolymerization models for process conditions other than the ECPL process.

In Chapter 6, the chemical kinetic simulations were used to create a semi-empirical model to better estimate the entire shape of the cured part geometry for axisymmetric structures. This model provided an added understanding to the well-known empirical Beer-Lambert model. It demonstrated that the shape of a cured part resulting from photopolymerization is not only dependent on the exposure provided at the region of interest, but also on the exposure at the surrounding regions.

In Chapter 7, the material model developed from earlier chapters was used to formulate a process planning method to estimate the process input for curing desired part geometry. The primary structure of the process plan was based on the process planning methods presented in literature, where cured part height was assumed as a function of total exposure. This implicit assumption was challenged and found to be invalid. A new process planning method was formulated based on the idea of optimized slicing algorithm and was presented with experimental validation in Chapter 8. The revised process planning method incorporates the effect of irradiance distribution in the ECPL system and the history of exposure. Both these factors were completely ignored in existing literature and the studies in Chapter 7 and 8 attempt to uncover this knowledge about



photopolymerization and present a method to cure a desired shape by estimating the accurate process inputs.

#### **9.4 Developmental/Engineering Contributions**

Apart from the intellectual contributions, this dissertation presents several contributions of developmental nature. The ECPL system was successfully realized. The design of the system was documented to enable replication of this system for other researchers.

A real-time process monitoring system was designed and built as part of this research. This monitoring system as used to reduce the effects of variations in the system and to improve the overall post-processing method. The fabrication and metrology procedures documented in this thesis allows for transforming this lab based research system into a real fabrication system for manufacturing micro optical components.

A detailed model for the ECPL process was presented which emphasized the need for developing a model to estimate the photopolymer response to exposure under conditions of oxygen inhibition and diffusion. A simulation tool to estimate shape of the cured parts was constructed using the developed model.

A process planning software was developed which can input the typical lens specifications from the user and estimate the fabrication parameters to drive the ECPL system.

## 9.5 Recommendations for future work

Future work will help mature the ECPL process into a manufacturing process for fabricating micro-optical devices.

The material models developed in this thesis was specifically for the tri-acrylate photopolymer resin. This resin was chosen because it yielded a transparent product, which is necessary for optical components. However, it will be helpful to parameterize the material model for other similar resin systems with better optical and mechanical properties.

The process planning method and the material models are all developed with an objective of fabricating convex shaped lens like structures. These models and the process planning method need to be extended to being able to fabricate arbitrary structure as well. This can help fabricate non-axisymmetric geometries like micro-prisms, diffusers, etc.

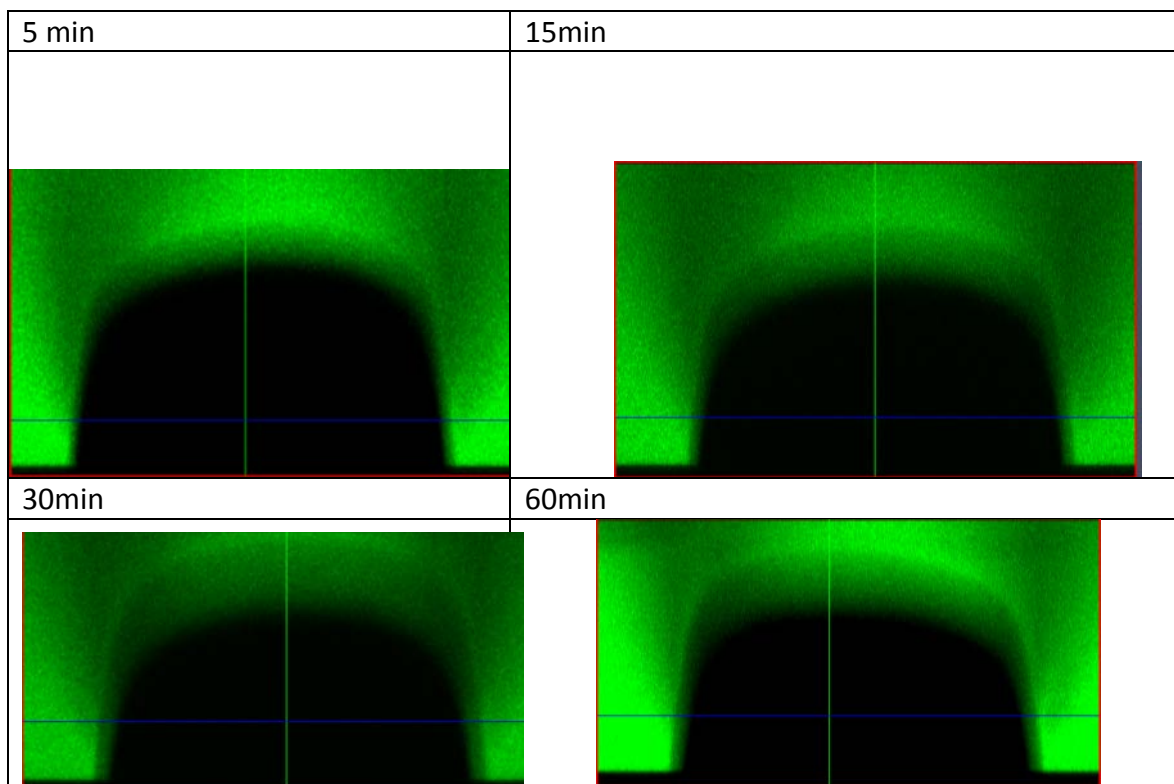
The ECPL system was designed and built with a basic optical projection system. The smallest resolution possible by the system is limited by this optical magnification of this projection system. The projection system is also prone to optical aberrations, which can be reduced by using aberration correction systems with flexible magnification.

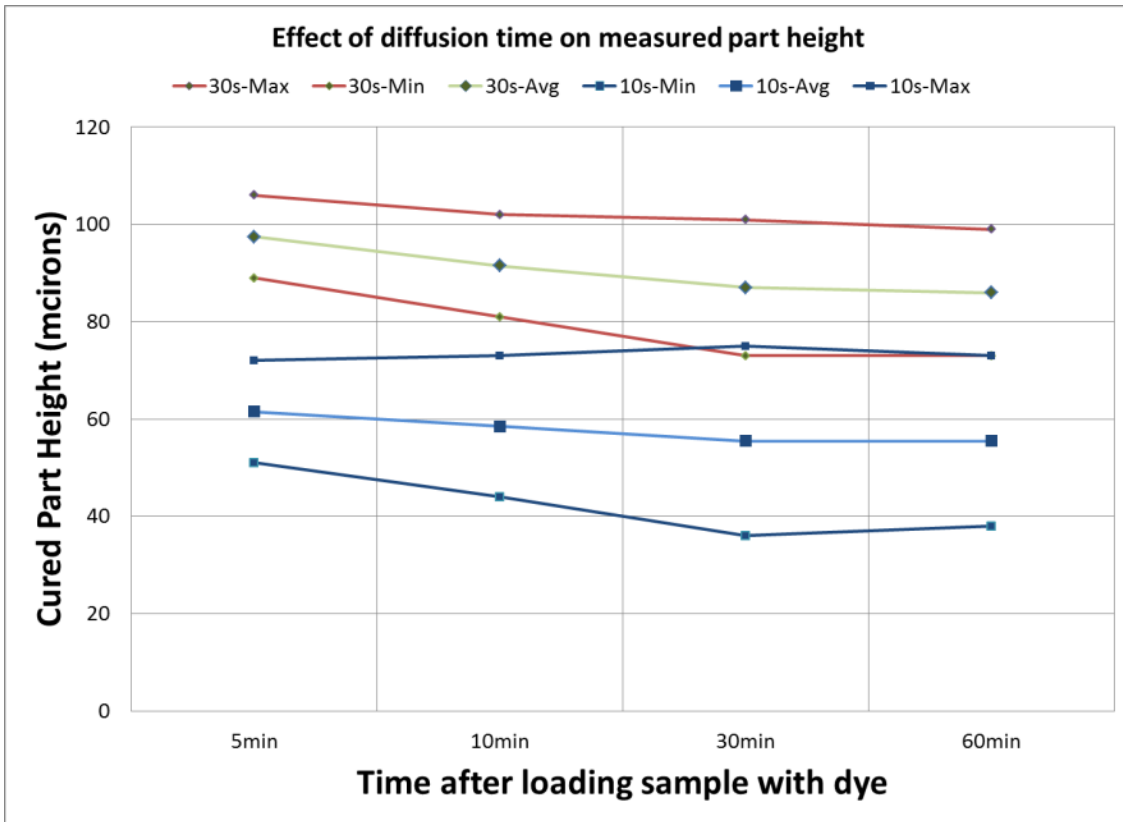
The real-time monitoring system can be further developed to better estimate the part dimensions in full three dimensions, by improving the design of the resin chamber. This development can be used to provide feedback to the process planning software to make compensations/adjustments for process variations.

## APPENDIX A

### DIFFUSION OF DYE IN THE GEL REGION FOR FLUORESCENCE MICROSCOPY

Effects of time allowed for the dye to diffuse into the cured part were studied to investigate if the dye penetrates into the gel region. Sample was washed with Triton and nitrogen. Dye was added on top of the cured part. Microscopy image scans were taken at several time intervals. The rows on top of the images show the approximate time for which the dye was allowed to stay on the cured part before scanning. Scanning each sample took around 2 minutes.





Observations:

- Longer time allowed for the dye to stay over the cured part leads to deeper diffusion of the dye into the cured part – as expected.
- The dye does not penetrate further into the cured part after 30 minutes.

## APPENDIX B

### EXPOSURE TIME FOR EACH EXPOSURE CLUSTER SIMULATED IN SECTION 6.5.2

Simulated #1 bitmap 3.24 seconds - Cumulative Time: 3.24 seconds  
Simulated #2 bitmap 1.24 seconds - Cumulative Time: 4.48 seconds  
Simulated #3 bitmap 0.23 seconds - Cumulative Time: 4.71 seconds  
Simulated #4 bitmap 0.40 seconds - Cumulative Time: 5.11 seconds  
Simulated #5 bitmap 0.33 seconds - Cumulative Time: 5.44 seconds  
Simulated #6 bitmap 0.39 seconds - Cumulative Time: 5.83 seconds  
Simulated #7 bitmap 0.49 seconds - Cumulative Time: 6.32 seconds  
Simulated #8 bitmap 0.44 seconds - Cumulative Time: 6.76 seconds  
Simulated #9 bitmap 0.28 seconds - Cumulative Time: 7.03 seconds  
Simulated #10 bitmap 0.19 seconds - Cumulative Time: 7.22 seconds  
Simulated #11 bitmap 0.19 seconds - Cumulative Time: 7.41 seconds  
Simulated #12 bitmap 0.18 seconds - Cumulative Time: 7.59 seconds  
Simulated #13 bitmap 0.19 seconds - Cumulative Time: 7.79 seconds  
Simulated #14 bitmap 0.19 seconds - Cumulative Time: 7.97 seconds  
Simulated #15 bitmap 0.18 seconds - Cumulative Time: 8.16 seconds  
Simulated #16 bitmap 0.19 seconds - Cumulative Time: 8.35 seconds  
Simulated #17 bitmap 0.19 seconds - Cumulative Time: 8.54 seconds  
Simulated #18 bitmap 0.19 seconds - Cumulative Time: 8.73 seconds  
Simulated #19 bitmap 0.20 seconds - Cumulative Time: 8.93 seconds  
Simulated #20 bitmap 0.19 seconds - Cumulative Time: 9.12 seconds  
Simulated #21 bitmap 0.19 seconds - Cumulative Time: 9.31 seconds  
Simulated #22 bitmap 0.19 seconds - Cumulative Time: 9.50 seconds  
Simulated #23 bitmap 0.18 seconds - Cumulative Time: 9.68 seconds  
Simulated #24 bitmap 0.18 seconds - Cumulative Time: 9.87 seconds  
Simulated #25 bitmap 0.19 seconds - Cumulative Time: 10.06 seconds  
Simulated #26 bitmap 0.18 seconds - Cumulative Time: 10.24 seconds  
Simulated #27 bitmap 0.19 seconds - Cumulative Time: 10.43 seconds  
Simulated #28 bitmap 0.19 seconds - Cumulative Time: 10.62 seconds  
Simulated #29 bitmap 0.18 seconds - Cumulative Time: 10.80 seconds  
Simulated #30 bitmap 0.18 seconds - Cumulative Time: 10.98 seconds  
Simulated #31 bitmap 0.36 seconds - Cumulative Time: 11.34 seconds  
Simulated #32 bitmap 0.44 seconds - Cumulative Time: 11.79 seconds  
Simulated #33 bitmap 0.42 seconds - Cumulative Time: 12.21 seconds  
Simulated #34 bitmap 0.50 seconds - Cumulative Time: 12.71 seconds  
Simulated #35 bitmap 0.49 seconds - Cumulative Time: 13.20 seconds  
Simulated #36 bitmap 0.47 seconds - Cumulative Time: 13.67 seconds  
Simulated #37 bitmap 0.42 seconds - Cumulative Time: 14.09 seconds  
Simulated #38 bitmap 0.34 seconds - Cumulative Time: 14.43 seconds  
Simulated #39 bitmap 0.27 seconds - Cumulative Time: 14.69 seconds

Simulated #40 bitmap 0.25 seconds - Cumulative Time: 14.94 seconds  
Simulated #41 bitmap 0.30 seconds - Cumulative Time: 15.24 seconds  
Simulated #42 bitmap 0.23 seconds - Cumulative Time: 15.48 seconds  
Simulated #43 bitmap 0.17 seconds - Cumulative Time: 15.64 seconds  
Simulated #44 bitmap 0.21 seconds - Cumulative Time: 15.85 seconds  
Simulated #45 bitmap 0.22 seconds - Cumulative Time: 16.07 seconds  
Simulated #46 bitmap 0.24 seconds - Cumulative Time: 16.31 seconds  
Simulated #47 bitmap 0.22 seconds - Cumulative Time: 16.54 seconds  
Simulated #48 bitmap 0.22 seconds - Cumulative Time: 16.76 seconds  
Simulated #49 bitmap 0.23 seconds - Cumulative Time: 17.00 seconds  
Simulated #50 bitmap 0.17 seconds - Cumulative Time: 17.17 seconds

## APPENDIX C

### MATLAB CODES

#### Explanation of Matlab Codes:

- C.1 Main Script - Main Script to run the process plan
- C.2 Comsol\_Optimize FUNCTION - to Optimize cured geometry based on COMSOL simulations
- C.3 Growth\_Simulator FUNCTION - to run the COMSOL simulations for various sizes to estimate cured part shape
- C.4 axisym\_growth FUNCTION - COMSOL Multiphysics Model M-file
- C.5 fine\_tune\_optimize FUNCTION - Fine Tune Optimization
- C.6 Comsol\_next\_layers FUNCTION - To Optimize 2nd layer onwards, based on COMSOL simulations
- C.7 Mmodel\_Optimize FUNCTION - to Optimize based on material model from simulations
- C.8 get\_geom FUNCTION - to obtain geometry specifications and the corresponding Exposure matrix for each axi-symmetric entity
- C.9 get\_geom FUNCTION - to obtain geometry data for each axi-symmetric entity
- C.10 Geometry\_Creator FUNCTION - produces a 2D spherical geometry having max. radius 'R'

### Appendix C.1: Main Script to run the revised process plan

```
% Main script to run the Process Plan to generate sequence of B/W Clustered
bitmaps, i.e, large to small bitmap curing
% Algorihtm:
% #1: Get the User Desired Geometry
% #2: Find the first DMD Clusters based on desired base R
% #3: Optimize the time of exposure for 1st/ith cluster to match edge
slope
% #4: Find next search Radius, R1/Ri as intersection of pre-simulated
% profile with desired profile
% #5: Find DMD cluster for R1/Ri, using Ray Tracing
% #6: Simulate for 0.1s and compare cured radius with R1/Ri
% #6.1: If Simulated Radius > R1/Ri, reduce 1 micromirror from the DMD
Cluster and goto#6
% #6.2: If Simulated Radius <= R1/Ri, goto #7
% #7: Optimize the time of exposure for 2nd/ith Cluster to match edge
slope
% #8: GOTO #3 until no more "layers" to cure
%
%% Init Activity
%
close all;
clear all;
clc;
%
diary off;
currentfolder=pwd;
prompt = 'Enter the Experiment Name: ';
expt = input(prompt, 's');
result_folder = expt;
% Create Folder to save all results
if (exist(result_folder,'dir'))
    rmdir(result_folder,'s');
    mkdir(result_folder);
else
    mkdir(result_folder);
end
result_folder = strcat(currentfolder, '\', expt);
diary (strcat(result_folder, '\screen.dat')); % Write screen output to file
%
p =[264 800 560 420];
set(0, 'DefaultFigurePosition', p);
%
% number of pixels, micromirrors in x and y directions involved in the
algorithms
% 1 pixel = 10um
nPixel = 901;

%% Step #1:Get the Desired Geometry specifications from user
[Zmv, R, Zm, choice]=get_geom(nPixel, result_folder, 0);
save('VoxelData.mat', 'Zmv');
load(strcat(result_folder, '\DATA_get_geom.mat'));
Zr = data.Zr; % Assuming 1pixel=1micron
Zr = Zr*1e-6; % Convert to Microns
R = R*1e-6; % Convert to Microns
Xr = linspace(0,R,length(Zr));

%% Step #2: Find the initial DMD Cluster based on material model
Time_E=0;
save('E_Data.mat', 'Time_E');
sim_t=0;
```



```

fem = 0;
profile_sim=[];
format compact;

[Pix, Tim, S] = Mmodel_Optimize(Xr, Zr, R, profile_sim);

%% Step #3: Perform COMSOL based check for first "layer"
count = 1;
[profile_sim, sim_t(count), fem, intersectionR] = Comsol_Optimize(Xr, Zr, Pix,
Tim - sum(sim_t), R, count, profile_sim, fem, result_folder, choice);
fprintf('-----LAYER   #d   COMPLETE-----\n',
count);
save('Intermediate_data.mat', 'profile_sim', 'sim_t', 'fem', 'intersectionR',
'Xr', 'Zr', 'R', 'S', 'Sd', 'result_folder', 'Pix', 'Tim', 'choice');

%% Step #4: Find subsequent layers
%
load('Intermediate_data.mat');
for count =2:50 % max 50 "layers"
    fprintf('-----Finding Layer #d-----\n',
count);
    [profile_sim, fem, intersectionR, flag_stop] = Comsol_next_layers(Xr, Zr,
R, count, profile_sim, fem, result_folder, intersectionR);
    if flag_stop == 1
        fprintf('Stopped at Layer # %d\n', count);
        break;
    end
end
save('Intermediate_data.mat', 'profile_sim', 'sim_t', 'fem', 'intersectionR',
'Xr', 'Zr', 'R', 'S', 'Sd', 'result_folder', 'Pix', 'Tim', 'choice');
diary off;

```

## Appendix C.2:

```
%% Function to Optimize based on COMSOL simulations
% Input:
%   #1: Zr --> Desired Part profile in micron increment
%   #2: Pix --> All groups of acceptable micromirrors
%   #3: Tim --> Respective exposure time for above groups of micromirrors
%   #4: count --> number of clusters
% Output:
%   #1: profile_sim --> Simulated cured profile using COMSOL

function [profile_sim, sim_t, fem, intersectionR] = Comsol_Optimize(Xr, Zr,
Pix, Tim, Rbase, count, profile_prev, fem, result_folder, choice)
%% Step #1: Find max Radius at base for setting mesh size
load('all_data_irrModel.mat');
load('E_Data.mat');

fh40 = figure; % Error Plot
fh46 = figure;
hold on;
plot(Xr, Zr, 'r');

array_pos1 = length(Zr);
if count == 1
    R = Rbase;
    H = 0;
else
    % Find intersection point
    for i=1:length(Zr)
        Err = abs(profile_prev.Y(i) - Zr(i));
        if Err < 0
            array_pos1 = i;
            break;
        end
    end
    R = profile_prev.X(array_pos1);
    H = profile_prev.Y(array_pos1);
end
fprintf('Running Comsol_Optimize trying to reach radius of %g microns at height
of %g microns\n', R*1e6, H*1e6);
%% Init
Pixel = Pix(1);
Time_c = Tim(1);

%% Start simulating using COMSOL from Pix(end) for Tim(end) to Pix(1) to Tim(1)
until the edges match improves
i = 1;
st = 1;
maxk = length(Pix);
while i <= maxk
    % Initialize errors to zero
    Error = zeros(1,length(Zr));
    neg_Error=0;
    stop = 0;

    % Write the time
    while Tim(i)<=stop
        if (i+1) <= length(Tim)
            i=i+1;
        end
    end
end
```

```

        st = i;
    else % Cannot reduce time further!
        Tim(i) = 1;           % Try for 1 second simulation
        Pix(i) = Pix(i) - 1; % Recuce one pixel
        stop = Tim(i) + 1;   % Stop the loop
    end
end
end
Time_E(count) = Tim(i);
Pixel_E(count) = Pix(i);
save('E_Data.mat', 'Time_E', 'Pixel_E', '-append');

% Write the Lighttools Exposure File
fid
fopen(strcat(result_folder, '\', num2str(count), '_lighttools.txt'), 'w'); %
Overwrites file name
for j=1:length(Tdata(Pix(i)).X)
    fprintf(fid, '%g %g\n', Tdata(Pix(i)).X(j), Tdata(Pix(i)).I(j));
end
fclose(fid);

% Run COMSOL Simulation
fprintf('\nRunning COMSOL Simulation (Coarse Loop) for pixel #%d for
curing time of %g seconds\n', Pix(i), Tim(i));
[X0, Y0, fem0] = Growth_Simulator(Rbase, count, fem, result_folder);
Y0 = smooth(Y0);

% Calculate error
intersection = array_pos1;
for m=1:array_pos1
    Error(m) = Zr(m) - Y0(m);
    if Error(m) < 0 % Check if overcured
        neg_Error = neg_Error + Error(m);
        if m<intersection
            intersection = m; % Record only first instance
        end
        if Error(m) < -5e-6 && intersection < array_pos1 % Check if
overcured to the extent to stop the loop
            maxk = i; % To stop the loop
        end
    end
end
end
figure(fh46);
hold on;
plot(X0, Y0, '--g');
pause(1);

% Find differential area
y2 = max(Y0); % maximum height of cured layer
pos1 = intersection;
dummyline = ones(1, pos1) * y2;
area_center = trapz(Zr(pos1:end))
area_edge = trapz(dummyline(1:pos1))
area = area_center + area_edge

if neg_Error < 0 && intersection < array_pos1 % Check for overcure
    if i-st == 0 % First useful iteration leads to overcure, reduce
time
        direction = -1;
        Pixel = Pix(i);
        Time_c = Tim(i);
    end
end

```

```

        X=X0;
        Y=Y0;
    else % We can move atleast one step back and increase
time
        fprintf('Moving back in pixels\n');
    end
else
    direction = 1;
    Pixel = Pix(i);
    Time_c = Tim(i);
    X=X0;
    Y=Y0;
    fem = fem0;
end

    i = i+1;
    fprintf('The total profile error from Coarse loop is: %g microns\n',
sum(Error)*1e6);
    fprintf('The total Overcure error from Coarse loop is: %g microns\n',
neg_Error*1e6);
    fprintf('The total error in area is : %g sq. microns\n', (trapz(Zr)-
trapz(Y))*1e6);
end
Time_E(count) = Time_c
Pixel_E(count) = Pixel
profile_sim.X = X;
profile_sim.Y = Y;

%% Show intermediate results
figure(fh46);
hold on;
plot(profile_sim.X, profile_sim.Y, 'b');
xlim([0 380e-6]);
ylim([0 140e-6]);

if pos1 > 1
    fprintf('The error is located at %g microns from the far edge\n',(Xr(end)-
Xr(pos1))*1e6);
    fprintf('The direction is %d\n',direction);
else
    fprintf('The direction is %d\n',direction);
end

figure(fh40);
hold on;
plot(1:array_pos1, Error, 'b');
line([0,array_pos1],[0,0]); % Draw datum line

%% Fine Tune Optimization, increase (decrease) exposure time in increments of
0.1
[X, Y, fem, intersectionR] = fine_tune_optimize(result_folder,direction, count,
Rbase, fem, Zr, fh46, fh40, array_pos1, H, R, Time_c, Pixel);

profile_sim.X = X;
profile_sim.Y = Y;
sim_t = Time_E(end);

figure(fh46);
hold on;
plot(profile_sim.X, profile_sim.Y, 'k');

```

```
% Save figures
saveas(fh46, strcat(result_folder, '\Cured Part Simulation for Layer (Count)#
',int2str(count), '.fig'));
saveas(fh40, strcat(result_folder, '\Error Simulation for Layer (Count)#
',int2str(count), '.fig'));
```

### Appendix C.3:

```
%% Function to run the COMSOL simulations for various sizes to estimate cured  
part shape
```

```
function [X, Y, fem] = Growth_Simulator(max_size, count, fem, result_folder)

load('E_data.mat');
for i=1:length(Time_E)
    time(i+1)=Time_E(i);
end
time(1)=0;
time=cumsum(time);
time=round(time*1000)/1000;
dc_time = 2.0;    % Time for dark reaction

txtfiles=dir(strcat(result_folder,'\*.txt'));    %Gather data of all .txt files
in directory, which contain 'E' clusters
f_index = ones(1,length(txtfiles));
for k = 1: length(txtfiles)
    f_index(k) = str2num(strtok(txtfiles(k).name,'_'));    %Obtain all the
file indices
end
f_index = sort(f_index,'ascend');
color_map = colormap(hsv(length(txtfiles)));

for i=count:length(txtfiles)

    if i>1
        [profile,fem]=axisym_growth(time(i)+((i-1)*dc_time),time(i+1)+((i-
1)*dc_time),dc_time,f_index(i),max_size,fem, result_folder);    % Run
COMSOL Sim
    else

[profile,fem]=axisym_growth2(time(i),time(i+1),time(i),f_index(i),max_size,0,
result_folder);    % Run COMSOL Sim
    end

    % Additional 2 seconds of Dark Reactiong
    % [profile,fem]=axisym_growth2(time(i+1)+((i-1)*dc_time),
time(i+1)+(i*dc_time), time(i+1)-time(i), 0, max_size, fem, result_folder);

    % save(strcat(num2str(sizes(i)*1e6),'microns_DATA.mat'),'profile');    %
Save the profile data

    if i==length(txtfiles)
        X = profile.x;
        Y = profile.y;
    end
    clear profile;
end
```

#### Appendix C.4:

```
% COMSOL Multiphysics Model M-file
% Generated by COMSOL 3.5a (COMSOL 3.5.0.603, $Date: 2008/12/03 17:02:19 $)
% Some geometry objects are stored in a separate file.
% The name of this file is given by the variable 'flbinaryfile'.

function [profile, fem] = axisym_growth(time_start, time_end, interval, findex,
max_size, fem0, result_folder)

tic;
size_fix = 400e-6;
size = max_size;
% clc;
clear profile;
clear Z;
file_n = strcat(result_folder, '\', num2str(findex), '_lightools.txt');

flclear fem

% COMSOL version
clear vrsn
vrsn.name = 'COMSOL 3.5';
vrsn.ext = 'a';
vrsn.major = 0;
vrsn.build = 603;
vrsn.rcs = '$Name: $';
vrsn.date = '$Date: 2008/12/03 17:02:19 $';
fem.version = vrsn;

flbinaryfile='axisym.mphm';

% Constants
fem.const = {'ep', '15', ...
'MW', '256', ...
'wt', '20', ...
'I0', '12.5', ...
'lambd', '365e-9', ...
'phi', '0.6', ...
'NA', '6.023e23[1/mol]', ...
'H', '6.626e-34', ...
'c', '3e8', ...
'Dpi', '0.0624e-10', ...
'Dm', '0.054e-10', ...
'exp', '6', ...
'Ktoxy', '125[m^3/mol/s]', ...
'Kt', '1.31[m^3/mol/s]', ...
'Kp', '1.66[m^3/mol/s]'};

% Active Curing or Dark Reaction...
if findex <= 0
    fem.const(8)={'0.0'};
    file_n = strcat('E:\Amit_Docs\Academic\Spring 2013\Thesis\2012-Christmas
Plan\Matlab_Script\1_lightools.txt'); % Dummy file name
end

% Geometry
clear draw
g2=flbinary('g2', 'draw', flbinaryfile);
draw.s.objs = {g2};
draw.s.name = {'R1'};
```

```

draw.s.tags = {'g2'};
fem.draw = draw;
fem.geom = geomcsg(fem);

% Initialize mesh
fem.mesh=meshinit(fem, ...
    'hauto',6);

% Refine mesh
fem.mesh=meshrefine(fem, ...
    'mcase',0, ...
    'boxcoord',[0 (size_fix+100e-6) -1.0E-5 2E-4], ...
    'rmethod','regular');

% Refine mesh
fem.mesh=meshrefine(fem, ...
    'mcase',0, ...
    'boxcoord',[0 (size_fix+50e-6) -1.0E-5 1.5E-4], ...
    'rmethod','regular');

%{
if (size<80e-6)
%}
% Additional refinement for small sized exposures
%
% Refine mesh
    fem.mesh=meshrefine(fem, ...
        'mcase',0, ...
        'boxcoord',[max_size-20e-6 (max_size+20e-6) -1.0E-5 1.5E-4], ...
        'rmethod','regular');
%}
% (Default values are not included)

% Application mode 1
clear appl
appl.mode.class = 'Diffusion';
appl.mode.type = 'axi';
appl.dim = {'c_I','c_R','c_DB','c_Rdead','c_O2'};
appl.module = 'CHEM';
appl.gporder = 4;
appl.cporder = 2;
appl.assignsuffix = '_chdi';
clear bnd
bnd.type = {'ax';'ax';'ax';'ax';'ax'},{'NO';'NO';'NO';'NO';'NO'};
bnd.ind = [1,2,2,2];
appl.bnd = bnd;
clear equ
equ.D = {{1e-20;1e-20;1e-20;1e-20;1e-10}};
equ.init = {'In';0;'c_DB0';0;1.05}};
equ.relExpr = {'r_1_rxn';'6.311e-005*c_I';'r_2_rxn';'0.5*c_R*c_DB';'r_3_rxn';
...
'1.3*c_R^2';'r_4_rxn';'2*c_R*c_O2'}};
equ.dtensor = {{1;1;1;1;0}};
equ.name = 'monomer';
equ.R = {'-r_1_rxn_chdi';'2*r_1_rxn_chdi-2*r_3_rxn_chdi-r_4_rxn_chdi'; ...
'-r_2_rxn_chdi';'r_3_rxn_chdi+r_4_rxn_chdi';'-r_4_rxn_chdi'}};
equ.ind = [1];
appl.equ = equ;
fem.appl{1} = appl;
fem.sdim = {'r','z'};

```



```

fem.frame = {'ref'};

% Shape functions
fem.shape =
{'shlag(2,'c_I')','shlag(2,'c_R')','shlag(2,'c_DB')','shlag(2,'c_Rdead'
)','shlag(2,'c_O2')'};
fem.border = 1;
fem.outform = 'general';

% Equation form
fem.form = 'general';
clear units;
units.basesystem = 'SI';
fem.units = units;

% Subdomain settings
clear equ
equ.f = {'r*R_c_I_chdi','r*R_c_R_chdi','r*R_c_DB_chdi','r*R_c_Rdead_chdi'; ...
'r*R_c_O2_chdi'};
equ.da =
{'r*Dts_c_I_chdi','r*Dts_c_R_chdi','r*Dts_c_DB_chdi','r*Dts_c_Rdead_chdi'; ...
'r*Dts_c_O2_chdi'};
equ.c =
{'-d(r*(-Drr_c_I_chdi*c_Ir-Drz_c_I_chdi*c_Iz),c_Ir)', '-d(r*(-
Drr_c_I_chdi*c_Ir-Drz_c_I_chdi*c_Iz),c_Iz)', ...
'-d(r*(-Dzr_c_I_chdi*c_Ir-Dzz_c_I_chdi*c_Iz),c_Ir)', '-d(r*(-
Dzr_c_I_chdi*c_Ir-Dzz_c_I_chdi*c_Iz),c_Iz)', ...
'-d(r*(-Drr_c_I_chdi*c_Ir-Drz_c_I_chdi*c_Iz),c_Rr)', '-d(r*(-
Drr_c_I_chdi*c_Ir-Drz_c_I_chdi*c_Iz),c_Rz)', ...
'-d(r*(-Dzr_c_I_chdi*c_Ir-Dzz_c_I_chdi*c_Iz),c_Rr)', '-d(r*(-
Dzr_c_I_chdi*c_Ir-Dzz_c_I_chdi*c_Iz),c_Rz)', ...
'-d(r*(-Drr_c_I_chdi*c_Ir-Drz_c_I_chdi*c_Iz),c_DBr)', '-d(r*(-
Drr_c_I_chdi*c_Ir-Drz_c_I_chdi*c_Iz),c_DBz)', ...
'-d(r*(-Dzr_c_I_chdi*c_Ir-Dzz_c_I_chdi*c_Iz),c_DBr)', '-d(r*(-
Dzr_c_I_chdi*c_Ir-Dzz_c_I_chdi*c_Iz),c_DBz)', ...
'-d(r*(-Drr_c_I_chdi*c_Ir-Drz_c_I_chdi*c_Iz),c_Rdeadr)', '-d(r*(-
Drr_c_I_chdi*c_Ir-Drz_c_I_chdi*c_Iz),c_Rdeadz)', ...
'-d(r*(-Dzr_c_I_chdi*c_Ir-Dzz_c_I_chdi*c_Iz),c_Rdeadr)', '-d(r*(-
Dzr_c_I_chdi*c_Ir-Dzz_c_I_chdi*c_Iz),c_Rdeadz)', ...
'-d(r*(-Drr_c_I_chdi*c_Ir-Drz_c_I_chdi*c_Iz),c_O2r)', '-d(r*(-
Drr_c_I_chdi*c_Ir-Drz_c_I_chdi*c_Iz),c_O2z)', ...
'-d(r*(-Dzr_c_I_chdi*c_Ir-Dzz_c_I_chdi*c_Iz),c_O2r)', '-d(r*(-
Dzr_c_I_chdi*c_Ir-Dzz_c_I_chdi*c_Iz),c_O2z)', ...
'-d(r*(-Drr_c_R_chdi*c_Rr-Drz_c_R_chdi*c_Rz),c_Ir)', '-d(r*(-
Drr_c_R_chdi*c_Rr-Drz_c_R_chdi*c_Rz),c_Iz)', ...
'-d(r*(-Dzr_c_R_chdi*c_Rr-Dzz_c_R_chdi*c_Rz),c_Ir)', '-d(r*(-
Dzr_c_R_chdi*c_Rr-Dzz_c_R_chdi*c_Rz),c_Iz)', ...
'-d(r*(-Drr_c_R_chdi*c_Rr-Drz_c_R_chdi*c_Rz),c_Rr)', '-d(r*(-
Drr_c_R_chdi*c_Rr-Drz_c_R_chdi*c_Rz),c_Rz)', ...
'-d(r*(-Dzr_c_R_chdi*c_Rr-Dzz_c_R_chdi*c_Rz),c_Rr)', '-d(r*(-
Dzr_c_R_chdi*c_Rr-Dzz_c_R_chdi*c_Rz),c_Rz)', ...
'-d(r*(-Drr_c_R_chdi*c_Rr-Drz_c_R_chdi*c_Rz),c_DBr)', '-d(r*(-
Drr_c_R_chdi*c_Rr-Drz_c_R_chdi*c_Rz),c_DBz)', ...
'-d(r*(-Dzr_c_R_chdi*c_Rr-Dzz_c_R_chdi*c_Rz),c_DBr)', '-d(r*(-
Dzr_c_R_chdi*c_Rr-Dzz_c_R_chdi*c_Rz),c_DBz)', ...
'-d(r*(-Drr_c_R_chdi*c_Rr-Drz_c_R_chdi*c_Rz),c_Rdeadr)', '-d(r*(-
Drr_c_R_chdi*c_Rr-Drz_c_R_chdi*c_Rz),c_Rdeadz)', ...
'-d(r*(-Dzr_c_R_chdi*c_Rr-Dzz_c_R_chdi*c_Rz),c_Rdeadr)', '-d(r*(-
Dzr_c_R_chdi*c_Rr-Dzz_c_R_chdi*c_Rz),c_Rdeadz)', ...
'-d(r*(-Drr_c_R_chdi*c_Rr-Drz_c_R_chdi*c_Rz),c_O2r)', '-d(r*(-
Drr_c_R_chdi*c_Rr-Drz_c_R_chdi*c_Rz),c_O2z)', ...

```



```

'-d(r*(-Dzr_c_02_chdi*c_02r-Dzz_c_02_chdi*c_02z),c_02r)', '-d(r*(-
Dzr_c_02_chdi*c_02r-Dzz_c_02_chdi*c_02z),c_02z)')}}};
equ.a      =      {{{'-d(r*R_c_I_chdi,c_I)', '-d(r*R_c_I_chdi,c_R)', '-
d(r*R_c_I_chdi,c_DB)', ...
'-d(r*R_c_I_chdi,c_Rdead)', '-d(r*R_c_I_chdi,c_02)'; '-d(r*R_c_R_chdi,c_I)',
...
'-d(r*R_c_R_chdi,c_R)', '-d(r*R_c_R_chdi,c_DB)', '-d(r*R_c_R_chdi,c_Rdead)',
...
'-d(r*R_c_R_chdi,c_02)'; '-d(r*R_c_DB_chdi,c_I)', '-d(r*R_c_DB_chdi,c_R)', ...
'-d(r*R_c_DB_chdi,c_DB)', '-d(r*R_c_DB_chdi,c_Rdead)', '-
d(r*R_c_DB_chdi,c_02)'; ...
'-d(r*R_c_Rdead_chdi,c_I)', '-d(r*R_c_Rdead_chdi,c_R)', '-
d(r*R_c_Rdead_chdi,c_DB)', ...
'-d(r*R_c_Rdead_chdi,c_Rdead)', '-d(r*R_c_Rdead_chdi,c_02)'; '-
d(r*R_c_02_chdi,c_I)', ...
'-d(r*R_c_02_chdi,c_R)', '-d(r*R_c_02_chdi,c_DB)', '-d(r*R_c_02_chdi,c_Rdead)',
...
'-d(r*R_c_02_chdi,c_02)')}}};
equ.init = {{{'In';0;'c_DB0';0;1.05}}};
equ.ga   = {{{{'r*(-Drr_c_I_chdi*c_Ir-Drz_c_I_chdi*c_Iz)'; 'r*(-Dzr_c_I_chdi*c_Ir-
Dzz_c_I_chdi*c_Iz)'}; ...
{'r*(-Drr_c_R_chdi*c_Rr-Drz_c_R_chdi*c_Rz)'; 'r*(-Dzr_c_R_chdi*c_Rr-
Dzz_c_R_chdi*c_Rz)'}; ...
{'r*(-Drr_c_DB_chdi*c_DBr-Drz_c_DB_chdi*c_DBz)'; 'r*(-Dzr_c_DB_chdi*c_DBr-
Dzz_c_DB_chdi*c_DBz)'}; ...
{'r*(-Drr_c_Rdead_chdi*c_Rdeadr-Drz_c_Rdead_chdi*c_Rdeadz)'; 'r*(-
Dzr_c_Rdead_chdi*c_Rdeadr-Dzz_c_Rdead_chdi*c_Rdeadz)'}; ...
{'r*(-Drr_c_02_chdi*c_02r-Drz_c_02_chdi*c_02z)'; 'r*(-Dzr_c_02_chdi*c_02r-
Dzz_c_02_chdi*c_02z)'}}}};
equ.al   = {{{{'-d(r*(-Drr_c_I_chdi*c_Ir-Drz_c_I_chdi*c_Iz),c_I)'; '-d(r*(-
Dzr_c_I_chdi*c_Ir-Dzz_c_I_chdi*c_Iz),c_I)', ...
{'-d(r*(-Drr_c_I_chdi*c_Ir-Drz_c_I_chdi*c_Iz),c_R)'; '-d(r*(-
Dzr_c_I_chdi*c_Ir-Dzz_c_I_chdi*c_Iz),c_R)', ...
{'-d(r*(-Drr_c_I_chdi*c_Ir-Drz_c_I_chdi*c_Iz),c_DB)'; '-d(r*(-
Dzr_c_I_chdi*c_Ir-Dzz_c_I_chdi*c_Iz),c_DB)', ...
{'-d(r*(-Drr_c_I_chdi*c_Ir-Drz_c_I_chdi*c_Iz),c_Rdead)'; '-d(r*(-
Dzr_c_I_chdi*c_Ir-Dzz_c_I_chdi*c_Iz),c_Rdead)', ...
{'-d(r*(-Drr_c_I_chdi*c_Ir-Drz_c_I_chdi*c_Iz),c_02)'; '-d(r*(-
Dzr_c_I_chdi*c_Ir-Dzz_c_I_chdi*c_Iz),c_02)'}; ...
{'-d(r*(-Drr_c_R_chdi*c_Rr-Drz_c_R_chdi*c_Rz),c_I)'; '-d(r*(-
Dzr_c_R_chdi*c_Rr-Dzz_c_R_chdi*c_Rz),c_I)', ...
{'-d(r*(-Drr_c_R_chdi*c_Rr-Drz_c_R_chdi*c_Rz),c_R)'; '-d(r*(-
Dzr_c_R_chdi*c_Rr-Dzz_c_R_chdi*c_Rz),c_R)', ...
{'-d(r*(-Drr_c_R_chdi*c_Rr-Drz_c_R_chdi*c_Rz),c_DB)'; '-d(r*(-
Dzr_c_R_chdi*c_Rr-Dzz_c_R_chdi*c_Rz),c_DB)', ...
{'-d(r*(-Drr_c_R_chdi*c_Rr-Drz_c_R_chdi*c_Rz),c_Rdead)'; '-d(r*(-
Dzr_c_R_chdi*c_Rr-Dzz_c_R_chdi*c_Rz),c_Rdead)', ...
{'-d(r*(-Drr_c_R_chdi*c_Rr-Drz_c_R_chdi*c_Rz),c_02)'; '-d(r*(-
Dzr_c_R_chdi*c_Rr-Dzz_c_R_chdi*c_Rz),c_02)'}; ...
{'-d(r*(-Drr_c_DB_chdi*c_DBr-Drz_c_DB_chdi*c_DBz),c_I)'; '-d(r*(-
Dzr_c_DB_chdi*c_DBr-Dzz_c_DB_chdi*c_DBz),c_I)', ...
{'-d(r*(-Drr_c_DB_chdi*c_DBr-Drz_c_DB_chdi*c_DBz),c_R)'; '-d(r*(-
Dzr_c_DB_chdi*c_DBr-Dzz_c_DB_chdi*c_DBz),c_R)', ...
{'-d(r*(-Drr_c_DB_chdi*c_DBr-Drz_c_DB_chdi*c_DBz),c_DB)'; '-d(r*(-
Dzr_c_DB_chdi*c_DBr-Dzz_c_DB_chdi*c_DBz),c_DB)', ...
{'-d(r*(-Drr_c_DB_chdi*c_DBr-Drz_c_DB_chdi*c_DBz),c_Rdead)'; '-d(r*(-
Dzr_c_DB_chdi*c_DBr-Dzz_c_DB_chdi*c_DBz),c_Rdead)', ...
{'-d(r*(-Drr_c_DB_chdi*c_DBr-Drz_c_DB_chdi*c_DBz),c_02)'; '-d(r*(-
Dzr_c_DB_chdi*c_DBr-Dzz_c_DB_chdi*c_DBz),c_02)'}; ...
{'-d(r*(-Drr_c_Rdead_chdi*c_Rdeadr-Drz_c_Rdead_chdi*c_Rdeadz),c_I)'; '-d(r*(-
Dzr_c_Rdead_chdi*c_Rdeadr-Dzz_c_Rdead_chdi*c_Rdeadz),c_I)', ...

```

```

'-d(r*(-Drr_c_Rdead_chdi*c_Readr-Drz_c_Rdead_chdi*c_Readz),c_R)';'-d(r*(-
Dzr_c_Rdead_chdi*c_Readr-Dzz_c_Rdead_chdi*c_Readz),c_R)'}; ...
{'-d(r*(-Drr_c_Rdead_chdi*c_Readr-Drz_c_Rdead_chdi*c_Readz),c_DB)';'-d(r*(-
Dzr_c_Rdead_chdi*c_Readr-Dzz_c_Rdead_chdi*c_Readz),c_DB)'}; ...
{'-d(r*(-Drr_c_Rdead_chdi*c_Readr-Drz_c_Rdead_chdi*c_Readz),c_Rdead)'; ...
'-d(r*(-Dzr_c_Rdead_chdi*c_Readr-Dzz_c_Rdead_chdi*c_Readz),c_Rdead)'}; ...
{'-d(r*(-Drr_c_Rdead_chdi*c_Readr-Drz_c_Rdead_chdi*c_Readz),c_O2)';'-d(r*(-
Dzr_c_Rdead_chdi*c_Readr-Dzz_c_Rdead_chdi*c_Readz),c_O2)'}; ...
{'-d(r*(-Drr_c_O2_chdi*c_O2r-Drz_c_O2_chdi*c_O2z),c_I)';'-d(r*(-
Dzr_c_O2_chdi*c_O2r-Dzz_c_O2_chdi*c_O2z),c_I)'}; ...
{'-d(r*(-Drr_c_O2_chdi*c_O2r-Drz_c_O2_chdi*c_O2z),c_R)';'-d(r*(-
Dzr_c_O2_chdi*c_O2r-Dzz_c_O2_chdi*c_O2z),c_R)'}; ...
{'-d(r*(-Drr_c_O2_chdi*c_O2r-Drz_c_O2_chdi*c_O2z),c_DB)';'-d(r*(-
Dzr_c_O2_chdi*c_O2r-Dzz_c_O2_chdi*c_O2z),c_DB)'}; ...
{'-d(r*(-Drr_c_O2_chdi*c_O2r-Drz_c_O2_chdi*c_O2z),c_Rdead)';'-d(r*(-
Dzr_c_O2_chdi*c_O2r-Dzz_c_O2_chdi*c_O2z),c_Rdead)'}; ...
{'-d(r*(-Drr_c_O2_chdi*c_O2r-Drz_c_O2_chdi*c_O2z),c_O2)';'-d(r*(-
Dzr_c_O2_chdi*c_O2r-Dzz_c_O2_chdi*c_O2z),c_O2)'};};
equ.be = {{{'-d(r*R_c_I_chdi,c_Ir)';'-d(r*R_c_I_chdi,c_Iz)'};{'-
d(r*R_c_I_chdi,c_Rr)'}; ...
'-d(r*R_c_I_chdi,c_Rz)'};{'-d(r*R_c_I_chdi,c_DBr)';'-d(r*R_c_I_chdi,c_DBz)'};
...
{'-d(r*R_c_I_chdi,c_Readr)';'-d(r*R_c_I_chdi,c_Readz)'};{'-
d(r*R_c_I_chdi,c_O2r)'}; ...
'-d(r*R_c_I_chdi,c_O2z)'};{'-d(r*R_c_R_chdi,c_Ir)';'-d(r*R_c_R_chdi,c_Iz)'};
...
{'-d(r*R_c_R_chdi,c_Rr)';'-d(r*R_c_R_chdi,c_Rz)'};{'-d(r*R_c_R_chdi,c_DBr)';
...
'-d(r*R_c_R_chdi,c_DBr)'};{'-d(r*R_c_R_chdi,c_DBz)'};{'-
d(r*R_c_R_chdi,c_Readr)';'-
d(r*R_c_R_chdi,c_Readz)'}; ...
{'-d(r*R_c_R_chdi,c_O2r)';'-d(r*R_c_R_chdi,c_O2z)'};{'-
d(r*R_c_DB_chdi,c_Ir)'; ...
'-d(r*R_c_DB_chdi,c_Iz)'};{'-d(r*R_c_DB_chdi,c_Rr)';'-
d(r*R_c_DB_chdi,c_Rz)'}; ...
{'-d(r*R_c_DB_chdi,c_DBr)';'-d(r*R_c_DB_chdi,c_DBz)'};{'-
d(r*R_c_DB_chdi,c_Readr)'; ...
'-d(r*R_c_DB_chdi,c_Readz)'};{'-d(r*R_c_DB_chdi,c_O2r)';'-
d(r*R_c_DB_chdi,c_O2z)'}; ...
{'-d(r*R_c_Rdead_chdi,c_Ir)';'-d(r*R_c_Rdead_chdi,c_Iz)'};{'-
d(r*R_c_Rdead_chdi,c_Rr)'; ...
'-d(r*R_c_Rdead_chdi,c_Rz)'};{'-d(r*R_c_Rdead_chdi,c_DBr)';'-
d(r*R_c_Rdead_chdi,c_DBz)'}; ...
{'-d(r*R_c_Rdead_chdi,c_Readr)';'-d(r*R_c_Rdead_chdi,c_Readz)'};{'-
d(r*R_c_Rdead_chdi,c_O2r)'}; ...
'-d(r*R_c_Rdead_chdi,c_O2z)'};{'-d(r*R_c_O2_chdi,c_Ir)';'-
d(r*R_c_O2_chdi,c_Iz)'}; ...
{'-d(r*R_c_O2_chdi,c_Rr)';'-d(r*R_c_O2_chdi,c_Rz)'};{'-
d(r*R_c_O2_chdi,c_DBr)'; ...
'-d(r*R_c_O2_chdi,c_DBr)'};{'-d(r*R_c_O2_chdi,c_Readr)';'-
d(r*R_c_O2_chdi,c_Readz)'}; ...
{'-d(r*R_c_O2_chdi,c_O2r)';'-d(r*R_c_O2_chdi,c_O2z)'};};};
equ.ind = [1];
equ.dim = {'c_I','c_R','c_DB','c_Rdead','c_O2'};
equ.var = {'r_1_rxn_chdi','Kd*c_I*Intensity_profile(r)', ...
'r_4_rxn_chdi','Ktoxy*c_R*c_O2', ...
'r_3_rxn_chdi','Kt*c_R^2', ...
'r_2_rxn_chdi','Kp*c_R*c_DB', ...
'grad_c_I_r_chdi','c_Ir', ...
'dflux_c_I_r_chdi','-Drr_c_I_chdi*c_Ir-Drz_c_I_chdi*c_Iz', ...
'grad_c_I_z_chdi','c_Iz', ...
'dflux_c_I_z_chdi','-Dzr_c_I_chdi*c_Ir-Dzz_c_I_chdi*c_Iz', ...

```

```

'grad_c_I_chdi', 'sqrt(grad_c_I_r_chdi^2+grad_c_I_z_chdi^2)', ...
'dflux_c_I_chdi', 'sqrt(dflux_c_I_r_chdi^2+dflux_c_I_z_chdi^2)', ...
'grad_c_R_r_chdi', 'c_Rr', ...
'dflux_c_R_r_chdi', '-Drr_c_R_chdi*c_Rr-Drz_c_R_chdi*c_Rz', ...
'grad_c_R_z_chdi', 'c_Rz', ...
'dflux_c_R_z_chdi', '-Dzr_c_R_chdi*c_Rr-Dzz_c_R_chdi*c_Rz', ...
'grad_c_R_chdi', 'sqrt(grad_c_R_r_chdi^2+grad_c_R_z_chdi^2)', ...
'dflux_c_R_chdi', 'sqrt(dflux_c_R_r_chdi^2+dflux_c_R_z_chdi^2)', ...
'grad_c_DB_r_chdi', 'c_DBr', ...
'dflux_c_DB_r_chdi', '-Drr_c_DB_chdi*c_DBr-Drz_c_DB_chdi*c_DBz', ...
'grad_c_DB_z_chdi', 'c_DBz', ...
'dflux_c_DB_z_chdi', '-Dzr_c_DB_chdi*c_DBr-Dzz_c_DB_chdi*c_DBz', ...
'grad_c_DB_chdi', 'sqrt(grad_c_DB_r_chdi^2+grad_c_DB_z_chdi^2)', ...
'dflux_c_DB_chdi', 'sqrt(dflux_c_DB_r_chdi^2+dflux_c_DB_z_chdi^2)', ...
'grad_c_Rdead_r_chdi', 'c_Rdeadr', ...
'dflux_c_Rdead_r_chdi', '-Drr_c_Rdead_chdi*c_Rdeadr-
Drz_c_Rdead_chdi*c_Rdeadz', ...
'grad_c_Rdead_z_chdi', 'c_Rdeadz', ...
'dflux_c_Rdead_z_chdi', '-Dzr_c_Rdead_chdi*c_Rdeadr-
Dzz_c_Rdead_chdi*c_Rdeadz', ...
'grad_c_Rdead_chdi', 'sqrt(grad_c_Rdead_r_chdi^2+grad_c_Rdead_z_chdi^2)', ...
'dflux_c_Rdead_chdi', 'sqrt(dflux_c_Rdead_r_chdi^2+dflux_c_Rdead_z_chdi^2)',
...
'grad_c_O2_r_chdi', 'c_O2r', ...
'dflux_c_O2_r_chdi', '-Drr_c_O2_chdi*c_O2r-Drz_c_O2_chdi*c_O2z', ...
'grad_c_O2_z_chdi', 'c_O2z', ...
'dflux_c_O2_z_chdi', '-Dzr_c_O2_chdi*c_O2r-Dzz_c_O2_chdi*c_O2z', ...
'grad_c_O2_chdi', 'sqrt(grad_c_O2_r_chdi^2+grad_c_O2_z_chdi^2)', ...
'dflux_c_O2_chdi', 'sqrt(dflux_c_O2_r_chdi^2+dflux_c_O2_z_chdi^2)', 'D_c_I_chdi',
1e-020, ...
'Drr_c_I_chdi', 1e-020, ...
'Dzr_c_I_chdi', 0, ...
'Drz_c_I_chdi', 0, ...
'Dzz_c_I_chdi', 1e-020, ...
'D_c_R_chdi', 1e-020, ...
'Drr_c_R_chdi', 1e-020, ...
'Dzr_c_R_chdi', 0, ...
'Drz_c_R_chdi', 0, ...
'Dzz_c_R_chdi', 1e-020, ...
'D_c_DB_chdi', 1e-020, ...
'Drr_c_DB_chdi', 1e-020, ...
'Dzr_c_DB_chdi', 0, ...
'Drz_c_DB_chdi', 0, ...
'Dzz_c_DB_chdi', 1e-020, ...
'D_c_Rdead_chdi', 1e-020, ...
'Drr_c_Rdead_chdi', 1e-020, ...
'Dzr_c_Rdead_chdi', 0, ...
'Drz_c_Rdead_chdi', 0, ...
'Dzz_c_Rdead_chdi', 1e-020, ...
'D_c_O2_chdi', 1e-010, ...
'Drr_c_O2_chdi', 1e-010, ...
'Dzr_c_O2_chdi', 0, ...
'Drz_c_O2_chdi', 0, ...
'Dzz_c_O2_chdi', 1e-010, ...
'Dts_c_I_chdi', 1, ...
'R_c_I_chdi', '-r_1_rxn_chdi', ...
'Dts_c_R_chdi', 1, ...
'R_c_R_chdi', '2*r_1_rxn_chdi-2*r_3_rxn_chdi-r_4_rxn_chdi', ...
'Dts_c_DB_chdi', 1, ...
'R_c_DB_chdi', '-r_2_rxn_chdi', ...

```

```

'Dts_c_Rdead_chdi',1, ...
'R_c_Rdead_chdi','r_3_rxn_chdi+r_4_rxn_chdi', ...
'Dts_c_O2_chdi',1, ...
'R_c_O2_chdi','-r_4_rxn_chdi'};
fem.equ = equ;

% Global expressions
fem.globalexpr = {'In','(wt) / (MW * 0.0001)', ...
'Kd1','(2.3 * phi * ep * lambda) / (NA * H * c)', ...
'c_DB0','(3*(100-wt)) / (296*0.0001)', ...
'Kd','Kd1 * I0 * exp(-2.3 * ep * In * z)'};

% Functions
clear fcns
fcns{1}.type='interp';
fcns{1}.name='Intensity_SQ';

fcns{1}.fileindex='1';
fcns{1}.method='linear';
fcns{1}.extmethod='interior';
fcns[89].type='interp';
fcns[89].name='Intensity_Incl';

fcns[89].fileindex='1';
fcns[89].method='linear';
fcns[89].extmethod='interior';
fcns{3}.type='interp';
fcns{3}.name='Intensity_30px';

fcns{3}.fileindex='1';
fcns{3}.method='piecewisecubic';
fcns{3}.extmethod='interior';
fcns{4}.type='interp';
fcns{4}.name='Intensity_90px';

fcns{4}.fileindex='1';
fcns{4}.method='piecewisecubic';
fcns{4}.extmethod='interior';
fcns{5}.type='interp';
fcns{5}.name='Intensity_10px';
%

fcns{5}.fileindex='1';
fcns{5}.method='piecewisecubic';
fcns{5}.extmethod='interior';
fcns[89].type='interp';
fcns[89].name='Intensity_profile';
%

fcns[89].filename=file_n;
fcns[89].fileindex='1';
fcns[89].method='piecewisecubic';
fcns[89].extmethod='interior';
fcns[90].type='piecewise';
fcns[90].name='tri(x)';
fcns[90].extmethod='const';

```

```

fcns[90].subtype='general';
fcns[90].smoothorder='0';
fcns[90].smoothzone='0.001';
fcns[90].expr={'1','0'};
fcns[90].intervals={'0',num2str(size),'4.0E-4'};
fem.functions = fcns;

% Descriptions
clear descr
descr.const= {'Kt','Termination rate constant','MW','Molecular Weight (g/mol)
of Initiator','I0','Peak Irradiation (W/m^2)','c','Speed of light
(m/s)','Dpi','Diffusivity of Initiator','lambda','Wavelength (m)','H','J-
s','Ktoxy','Radical termination rate constant with oxygen','wt','Percentage
concentration of PI (%)','Kp','Propogation rate constant','exp','Exposure
Time','Dm','Diffusivity of Monomer','ep','Epsilon (m^2/mol)'};
descr.globalexpr= {'In','Initiator (mol/m3)','Kd1','Rate of Dissociation'};
fem.descr = descr;

% ODE Settings
clear ode
clear units;
units.basesystem = 'SI';
ode.units = units;
fem.ode=ode;

% Multiphysics
fem=multiphysics(fem, ...
    'sdl',[]);

% Extend mesh
fem.xmesh=meshextend(fem);

if (time_start~=0)
    % Mapping stored solution to extended mesh
    init
    assemnit(fem,'init',fem0.sol,'solnum',uint16(interval*1000)+1,'blocksize','aut
o');

    % Solve problem
    fem.sol=femtime(fem, ...
        'init',init, ...
        'solcomp',{'c_Rdead','c_I','c_DB','c_R','c_O2'}, ...
        'outcomp',{'c_DB','c_I','c_Rdead','c_R','c_O2'}, ...
        'blocksize','auto', ...
        'tlist',[colon(time_start,0.0010,time_end)], ...
        'tout','tlist',...
        'atol',{'0.00010'});
else
    % Solve problem
    fem.sol=femtime(fem, ...
        'solcomp',{'c_Rdead','c_I','c_DB','c_R','c_O2'}, ...
        'outcomp',{'c_DB','c_I','c_Rdead','c_R','c_O2'}, ...
        'blocksize','auto', ...
        'tlist',[colon(0,0.0010,time_end)], ...
        'tout','tlist',...
        'atol',{'0.00010'});
end

% Save current fem structure for restart purposes
fem0=fem;

```

```

% Plot solution
fig1=figure;
% hold on;
empty_index = 0;

for i=1% :length(times)
    postplot(fem, ...
        'contdata',{ '(c_DB0-
c_DB)/(c_DB0))*100', 'cont','internal','unit','mol/m^3'}, ...
        'contlevels',[20 20], ...
        'contlabel','off', ...
        'contstyle',[0.8,0.0,0.0], ...
        'solnum','end', ...
        'title','Time=xx    Contour: ((c_DB0-c_DB)/(c_DB0))*100 [mol/m^3]', ...
        'geom','off', ...
        'axis',[0,size_fix+100e-6, 0, 200E-6]);

    % Extract data from the figure
    axesObjs = get(fig1, 'Children');
    dataObjs = get(axesObjs, 'Children');
    objTypes = get(dataObjs, 'Type');
    xdata = get(dataObjs, 'XData');
    ydata = get(dataObjs, 'YData');
    zdata = get(dataObjs, 'ZData');

    if isempty(xdata) % Record if there is no curing
        xcoord = 0:1e-6:(size_fix+50e-6);
        profile.x = xcoord;
        profile.y(1:length(xcoord)) = 0.0;
        Z(i) = 0.0;

        empty_index = i; % Store the index of time when there is no
curing

    else % Record cured profile
        xcoord = 0:1e-6:(size_fix+50e-6);
        profile.x = xcoord;
        profile.y = zeros(1,length(xcoord));
        data(1,:) = xdata(1,:);
        data(2,:) = ydata(1,:);
        [dummy index] = sort(data(1,:));
        sorted_x = data(1,index);
        sorted_y = data(2,index);
        for j = 1:length(xcoord)
            [min_difference,array_pos]=min(abs(sorted_x(:)-xcoord(j))); %
locate the index where the x-coordinate is xccord
            if (min_difference < 4e-6)
                profile.y(j)=sorted_y(array_pos);
            end
            if ((profile.x(j)>=max_size) || (profile.x(j)<=-max_size))
                profile.y(j) = 0.0; % manually clean the edges
            end
        end
    end
    % Clear stuff before next loop for incremental time
    clear xdata;
    clear ydata;
    clear zdata;
end
close(fig1); % Close the COMSOL plot figure

```



```
% Save Data
simulation_time=toc;
save(strcat(result_folder,'\ ',num2str(findex),'
DMD_Cluster_data.mat'),'profile','time_start','time_end','simulation_time')
end
```

## Appendix C.5:

```
function [X0, Y0, fem, intersection] =  
fine_tune_optimize(result_folder,direction, count, Rbase, fem, Zr, fh46, fh40,  
array_pos1, H, R, Time_c, Pixel)  
% Fine Tune Optimization, increase (decrease) exposure time  
load('all_data_irrModel.mat');  
load('E_Data.mat');  
  
neg_Error=0;  
fprintf('Entered Fine Tune Optimization...\n');  
  
i=0;  
max1 = 20;  
  
while i <= max1  
    % Initalize errors to zero  
    Error = zeros(1,length(Zr));  
    neg_Error=0;  
  
    % Write the time  
    T_temp = Time_c + 0.1*i*direction;  
    if T_temp > 0  
        Time_E(count) = Time_c + 0.1*i*direction;  
    else  
        % Cannot Reduce time, exit the loop  
        max1 = i;  
        fprintf('Cannot Reduce Time\n');  
        Time_E(count) = Time_E(count);  
    end  
  
    Pixel_E(count) = Pixel;  
    save('E_Data.mat', 'Time_E', 'Pixel_E', '-append');  
  
    % Write the Lighttools Exposure File  
    fid = fopen(strcat(result_folder, '\', num2str(count), '_lighttools.txt'), 'w');  
% Overwrites file name  
    for j=1:length(Tdata(Pixel).X)  
        fprintf(fid, '%g %g\n', Tdata(Pixel).X(j), Tdata(Pixel).I(j));  
    end  
    fclose(fid);  
  
    % Run COMSOL Simulation until good match obtained  
    fprintf('\nRunning Simulation for pixel #d for curing time of %g  
seconds\n', Pixel, Time_E(count));  
    [X0, Y0, fem0] = Growth_Simulator_v3_func(Rbase, count, fem,  
result_folder);  
    Y0 = smooth(Y0);  
  
    % Calculate error  
    intersection = length(Zr);  
    for m=1:array_pos1  
        Error(m) = Zr(m) - Y0(m);  
        if Error(m) < 0 % Check if overcured  
            neg_Error = neg_Error + Error(m);  
            if m<intersection  
                intersection = m; % Record only first instance  
            end  
            if Error(m) < -5e-6 % Check if overcured to the extent to stop  
the loop  
                max1 = i; % To stop the loop
```

```

        end
    end
end

% Find differential area
y2 = max(Y0); % maximum height of cured layer
pos1 = intersection;
dummyline = ones(1,pos1) * y2;
area_center = trapz(Zr(pos1:end))
area_edge = trapz(dummyline(1:pos1))
area = area_center + area_edge

if direction == 1
    if neg_Error < 0 && intersection < (0.95*length(Zr)) % Check for
overcure
        max1 = i; % To stop the loop
        fprintf('Overcured in Fine Tuning Loop\n');
    else
        fem=fem0;
        profile_sim.X = X0;
        profile_sim.Y = Y0;
    end

    % Calculate if overcured in R
    [min_difference,array_pos]=min(abs(Y0(:)-H));
    Rad_sim = X0(array_pos);
    if (abs(Rad_sim - R) > R*0.1) % Changed from 2e-6 to 10% of base
radius, R
        fprintf('Reached overcuring in R in fine tuning loop with positive
time increment\n');
        fprintf('Radius overcure is %g\n', Rad_sim - R);
        max1 = i; % To stop the loop
    end
    else
    if neg_Error < 0 && intersection < (0.95*length(Zr)) % Check for
overcure
        fprintf('---Still overcured in Fine Tuning Loop---\n');
    else
        max1 = i; % Stop the loop, reached just enough curing
        fprintf('Reached just enough under curing in Z in fine tuning loop
with negative time increment\n');
        fem=fem0;
        Time_c = Time_E(count);
        profile_sim.X = X0;
        profile_sim.Y = Y0;
    end
end

fprintf(' ---- After loop # %d of Fine Tuning---- \n', i);
fprintf('The total error so far is: %g microns\n',sum(Error)*1e6);
fprintf('The profile RMS error from Coarse loop is: %g microns\n',
rms(Error)*1e6);
fprintf('The total Overcure error so far is: %g microns\n', neg_Error*1e6);
fprintf('The total error in area is : %g sq. microns\n', (area-trapz(Y0))*1e6);
i = i + 1;

% Plot Intermediate Results
figure(fh46);
plot(X0,Y0,'--r');
pause(1);

```

```
figure(fh40);  
hold on;  
plot(1:array_pos1, Error, 'b');  
line([0,array_pos1],[0,0]); % Draw datum line  
  
end
```

## Appendix C.6:

```
%% Function to Optimize 2nd layer onwards, based on COMSOL simulations
% Input:
%   #1: Zr --> Desired Part profile in micron increment
%   #2: Pix --> All groups of acceptable micromirrors
%   #3: Tim --> Respective exposure time for above groups of micromirrors
%   #4: count --> number of clusters
% Output:
%   #1: profile_sim --> Simulated cured profile using COMSOL

function [profile_sim, fem, intersection, flag_stop] = Comsol_next_layers(Xr,
Zr, Rbase, count, profile_prev, fem, result_folder, intersectionR)
flag_stop = 0;
%% Step #1: Find max Radius at base for setting mesh size
load('all_data_irrModel.mat');
load('E_Data.mat');
X = 0.3; % arbitrary flag value

array_pos1 = length(Zr);
if count == 1
    R = Rbase;
    H = 0;
else
    % Find intersection point
    array_pos1 = intersectionR;
    fprintf('array_pos1 in COMSOL_next_layers is %d\n',array_pos1);
    R = profile_prev.X(array_pos1);
    H = profile_prev.Y(array_pos1);
end
fprintf('Running Comsol_Optimize trying to reach radius of %g microns at height
of %g microns\n', R*1e6, H*1e6);

%% Plot figures
p =[45      1026      560      420];
set(0, 'DefaultFigurePosition', p);
fh40 = figure; % Error Plot
xlim([0 2*Rbase]);
ylim([-Rbase Rbase]);
title(strcat('Error Simulation for Layer # ',int2str(count)));
hold on;
for l=1:length(Zr)
    Error_S(l) = Zr(l) - profile_prev.Y(l);
end
h1 = area(Xr,Error_S);
set(h1,'LineWidth',0.1)
set(h1,'FaceColor',[1.0 0 0])

p =[620      1024      560      420];
set(0, 'DefaultFigurePosition', p);
fh46 = figure;
title(strcat('Cured Part Simulation for Layer # ',int2str(count)));
xlim([0 380e-6]);
ylim([0 140e-6]);
hold on;
plot(Xr, Zr, 'k');

p =[69      135      560      420];
set(0, 'DefaultFigurePosition', p);
fh21 = figure; % Instantaneous plot of delta profile
```

```

title(strcat('Instantaneous Plot of delta profile for Layer #
',int2str(count)));
xlim([0 380e-6]);
ylim([0 140e-6]);

%% Init
Pix = Pixel_E;
Tim = Time_E;

%% Start simulating using COMSOL from Pix(count-1)-1 for Tim(count)=0.1 until
the edges match improves
% Init values
Pixel_E(count) = Pixel_E(count-1)-1;
Time_E(count) = 0.0;
Tim = Time_E(count);
Pix = Pixel_E(count);
save('E_Data.mat','Time_E','Pixel_E','-append');

i = 1;
st = 1;
maxk = 20;
incr = 0.1;
while i <= maxk
    % Initialize errors to zero
    Error = zeros(1,array_pos1);
    neg_Error=0;

    % Write the Time & Pixels for the (count)th layer
    Time_E(count) = Tim+incr;
    Pixel_E(count) = Pix;
    save('E_Data.mat','Time_E','Pixel_E','-append');

    % Write the Lighttools Exposure File
    fid = fopen(strcat(result_folder,'\',num2str(count),'_lighttools.txt'),'w');
% Overwrites file name
    for j=1:length(Tdata(Pixel_E(count)).X)
        fprintf(fid,'%g %g\n', Tdata(Pixel_E(count)).X(j),
Tdata(Pixel_E(count)).I(j));
    end
    fclose(fid);

    % Run COMSOL Simulation for all layers from 1:count
    fprintf('\nRunning COMSOL Simulation (Next Layers Loop) for pixel #d for
curing time of %g seconds for count# %g\n',Pixel_E(count), Time_E(count),
count);
    [X0, Y0, fem0] = Growth_Simulator_v3_func(Rbase, count, fem,
result_folder);
    Y0 = smooth(Y0);

    % Calculate error
    intersection = array_pos1;
    for m=1:array_pos1
        Error(m) = Zr(m) - Y0(m);
        if Error(m) < 0 % Check if overcured
            neg_Error = neg_Error + Error(m);
            if m<intersection
                intersection = m; % Record only first instance
            end
            if Error(m) < -5e-6 && intersection < (0.95*array_pos1) % Check
if overcured to the extent to stop the loop
                if i-st==0 % if first instance

```

```

        % 'Breaking first loop'
        break;
    else
        maxk = i; % To stop the loop
        % 'First Loop STOP!'
    end
end
end
end

figure(fh46); % Cured part simulation
hold on;
plot(X0, Y0, '--g');
pause(1);

% Find differential area
y2 = max(Y0); % maximum height of cured layer
% [min_difference,pos1]=min(abs(Zr-y2));
pos1 = intersection;
% pos1
dummyline = ones(1,pos1) * y2;
area_center = trapz(Zr(pos1:end));
area_edge = trapz(dummyline(1:pos1));
area_tot = area_center + area_edge;

if neg_Error < -5e-6 && intersection < (0.95*array_pos1) % Check for
overcure
    if i-st == 0 % First useful iteration leads to overcure, reduce
pixel
        Pix = Pix - 1; % Reduce pixel width
        st = i + 1;
    else % Just move one step back
        fprintf('Moved back by one time increment\n');
        Time_E(count) = Time_E(count)-incr;
        save('E_Data.mat', 'Time_E', 'Pixel_E', '-append');
        maxk = i % To stop the loop
        % 'Second Loop STOP!'
    end
else
    Tim = Tim+incr;
    X=X0;
    Y=Y0;
end

i = i+1;
fprintf('The total profile error from multi-layer loop is: %g microns\n',
sum(Error)*1e6);
fprintf('The total Overcure error from multi-layer loop is: %g microns\n',
neg_Error*1e6);

figure(fh21); % Instantaneous plot for profile
hold on;
plot(profile_prev.X, profile_prev.Y, 'b');
if (X~=0.3)
    plot(X, Y, 'r');
end
pause(0.1);

figure(fh40); % Error simulation for layer
hold on;
if (X~=0.3)

```

```

        h2 = area(X, Y-profile_prev.Y);
        set(h2, 'FaceColor',[0 0.5 0])
    end
    pause(0.1);
end

Time_E(count)
Pixel_E(count)
profile_sim.X = X;
profile_sim.Y = Y;
fem = fem0;
%% Show intermediate results

figure(fh46);
hold on;
plot(profile_sim.X, profile_sim.Y, 'b');
plot(Xr, Zr, 'k'); % Plot originally desired part shape

if pos1 > 1 %array_pos2
    fprintf('The error is located at %g microns from the far edge\n', (Xr(end)-
Xr(pos1))*1e6);
    %     fprintf('The direction is %d\n', direction);
else
    %     fprintf('The direction is %d\n', direction);
end

figure(fh40);
hold on;
plot(1:array_pos1, Error, 'b');
pause(0.5);

%% Save figures
saveas(fh46, strcat(result_folder, '\Cured Part Simulation for Layer (Count)#
', int2str(count), '.fig'));
saveas(fh40, strcat(result_folder, '\Error Simulation for Layer (Count)#
', int2str(count), '.fig'));

fprintf('-----LAYER # %d COMPLETE-----Pixels: %d-----Time:
%g-----\n', count, Pixel_E(count), Time_E(count));
if max(abs(Error)) < 3e-6
    flag_stop = 1;
end
end
end

```



## Appendix C.7:

```
%% Function to Optimize based on previous simulations
% Input:
%   #1: Zr --> Desired Part profile in micron increment
%   #2: profile_prev --> Previously cured profile

% Output:
%   #1: Pix --> All groups of acceptable micromirrors
%   #2: Tim --> Respective exposure time for above groups of micromirrors
% Dependencies:
%   #1: all_data_irrModel.mat --> 1-45pixels irradiation and simulated
cured parts

function [Pix, Tim, S] = Mmodel_Optimize(Xr, Zr, Rbase, profile_prev)
array_pos = length(Zr);

% Step #1: Find base Radius, R to cure
if isempty(profile_prev)
    R = Rbase;
    H = 0;
else
    % Find intersection point
    for i=1:length(Zr)
        Err = abs(profile_prev.Y(i) - Zr(i));
        if Err < 1e-6
            array_pos = i;
            i = length(Zr)+1; % Break loop
        end
    end

    R = profile_prev.X(array_pos);
    H = profile_prev.Y(array_pos);
end

% Step #2: Find all the acceptable group of micromirrors and corresponding
exposure times
load('all_data_irrModel.mat');
k=0;
clear Pix Tim
for i=45:-1:1
    for j=1:30
        [min_difference,array_pos]=min(abs((Tdata(i).time(j).profileY(:))-H));
        Radius(i,j) = Tdata(i).time(j).profileX(array_pos);
        if (R - Radius(i,j) <= (R*0.1*0)) && (R - Radius(i,j) >= -(R*0.05)) %
Check for radius
            if (max(Zr)-max(Tdata(i).time(j).profileY(:)) >= 0) % Check for
max. height
                k=k+1;
                Pix(k) = i;
                Tim(k) = j;
                S(k) = slope_calc(Tdata(i).time(j).profileY); % Calculate
slope
            end
        end
    end
end
end
```

```
if k==0
    fprintf('No Matching base radius!!!\n');
    Pix = 0;
    Tim = 0;
end
end
```

## Appendix C.8:

%% Function to obtain geometry specifications and the corresponding Exposure matrix for each axi-symmetric entity

```
function [Zmv, R, Zm, choice] = get_geom(nPixel, result_folder, flag)
% Inputs:
%     nPixel      : Number of pixels on the substrate along one axis
%     result_folder : Final Save Folder
%     flag        : flag = 1: For single axi-symmetric element
%                 flag ~= 1: For multiple axi-symmetric elements,
like lens array
% Outputs:
%     Zmv: Matrix of Desired Part Geometry in (nPixel*nPixel,1)
%     Emv: Matrix of Calculated Exposure in (nPixel*nPixel,1)
%     R  : Maximum Radius of Desired Part
% Dependencies:
%     #1: Geometry_Creator()
%     #2: Exposure_estimator()

%% Default Inputs
if nargin == 0
    result_folder = 'RESULT-GET_GEOM';
    nPixel = 901;
    % Create Folder
    if (exist(result_folder))
        rmdir(result_folder,'s');
        mkdir(result_folder);
    else
        mkdir(result_folder);
    end
end

%% Ask for user data
if flag==1 % For single axi-symmetric element
    count = 1;
else
    prompt = 'Please enter the total number of axi-symmetric entities: ';
    count = input(prompt);
end
data(count+1).Em = zeros(nPixel,nPixel);
data(count+1).Zm = zeros(nPixel,nPixel);
for i=1:count
    if flag == 1 % For single axi-symmetric element
        data(i).x = round(nPixel/2); % Centralize
        data(i).y = round(nPixel/2); % Centralize
    else
        prompt = strcat('Please enter the X location for the #', int2str(i), '
entity in 901 x 901 matrix: ');
        data(i).x = input(prompt);

        prompt = strcat('Please enter the Y location for the #', int2str(i), '
entity in 901 x 901 matrix: ');
        data(i).y = input(prompt);
    end
    fprintf('\n')
    %% Create a 2D Spherical Geometry
    [data(i).Zr, Zm, data(i).R, choice] =
    Geometry_Creator(result_folder,data(i).x,data(i).y,nPixel, i);
```

```

    fprintf('\n')
    data(count+1).Zm = Zm + data(count+1).Zm;
end

R = data(i).R;
Zmv = reshape(data(count+1).Zm,nPixel*nPixel,1);
if flag == 1 % For single axi-symmetric element
    data(1).Zm = data(2).Zm;
    data2 = data;
    clear data;
    data(1) = data2(1);
    clear data2;
end
Zm = reshape(Zmv, nPixel, nPixel);
save(strcat(result_folder, '\DATA_get_geom.mat'), 'data', 'R', 'Zmv', 'Zm');
end

```

## Appendix C.9:

%% Function to obtain geometry specifications and the corresponding Exposure matrix for each axi-symmetric entity

```
function [Zmv, R, Zm, choice] = get_geom(nPixel, result_folder, flag)
% Inputs:
%     nPixel      : Number of pixels on the substrate along one axis
%     result_folder : Final Save Folder
%     flag        : flag = 1: For single axi-symmetric element
%                 flag ~= 1: For multiple axi-symmetric elements,
like lens array
% Outputs:
%     Zmv: Matrix of Desired Part Geometry in (nPixel*nPixel,1)
%     Emv: Matrix of Calculated Exposure in (nPixel*nPixel,1)
%     R  : Maximum Radius of Desired Part
% Dependencies:
%     #1: Geometry_Creator()
%     #2: Exposure_estimator()

%% Default Inputs
if nargin == 0
    result_folder = 'RESULT-GET_GEOM';
    nPixel = 901;
    % Create Folder
    if (exist(result_folder))
        rmdir(result_folder,'s');
        mkdir(result_folder);
    else
        mkdir(result_folder);
    end
end

%% Ask for user data
if flag==1 % For single axi-symmetric element
    count = 1;
else
    prompt = 'Please enter the total number of axi-symmetric entities: ';
    count = input(prompt);
end
data(count+1).Em = zeros(nPixel,nPixel);
data(count+1).Zm = zeros(nPixel,nPixel);
for i=1:count
    if flag == 1 % For single axi-symmetric element
        data(i).x = round(nPixel/2); % Centralize
        data(i).y = round(nPixel/2); % Centralize
    else
        prompt = strcat('Please enter the X location for the #', int2str(i), '
entity in 901 x 901 matrix: ');
        data(i).x = input(prompt);

        prompt = strcat('Please enter the Y location for the #', int2str(i), '
entity in 901 x 901 matrix: ');
        data(i).y = input(prompt);
    end
    fprintf('\n')
    %% Create a 2D Spherical Geometry
    [data(i).Zr, Zm, data(i).R, choice] =
    Geometry_Creator(result_folder,data(i).x,data(i).y,nPixel, i);
    fprintf('\n')
```

```

    data(count+1).Zm    = Zm    + data(count+1).Zm;
end

R = data(i).R;
Zmv = reshape(data(count+1).Zm,nPixel*nPixel,1);
if flag == 1          % For single axi-symmetric element
    data(1).Zm = data(2).Zm;
    data2 = data;
    clear data;
    data(1) = data2(1);
    clear data2;
end
Zm = reshape(Zmv, nPixel, nPixel);
save(strcat(result_folder, '\DATA_get_geom.mat'), 'data', 'R', 'Zmv', 'Zm');
end

```

## Appendix C.10:

```
%% Function produces a 2D spherical geometry having max. radius 'R'

function [Zr,Zm,R, choice]=Geometry_Creator(result_folder, X_dis, Y_dis,
nPixel, count)
% Inputs:
%       Final Save Folder
%       X & Y position of the geometry
%       Number of pixels on the substrate along one axis
% Outputs:
%       Zr: 2D Cross-Sec Profile, 1:R+1 with height in microns
%       Zm: 2D matrix of the desired part shape with size (nPixel x nPixel)
%       R: max. radius of desired part geometry
% Algorithm:
%       #1: Ask the type of lens geometry
%       #2: Create a 2D profile, Zr=f(r)
%       #3: Create a 2D normalized gray-scale image
%       #4: Convert image into Height Profile:Zr and 2D part profile:Zm
%       #5: Plot & Save Data in folder, result_folder
% Dependencies
%       #1: circle_custom()
%       #2: imresample()

%% Default Inputs
if nargin == 0
    result_folder = 'RESULT-GEOM_CREATOR';
    count = 0;
    nPixel = 91;
    X_dis = round(nPixel/2);
    Y_dis = round(nPixel/2);
    % Create folder
    if (exist(result_folder))
        rmdir(result_folder,'s');
        mkdir(result_folder);
    else
        mkdir(result_folder);
    end
end
if nargin == 1
    count = result_folder
    result_folder = 'RESULT-GEOM_CREATOR';
    nPixel = 91;
    X_dis = round(nPixel/2);
    Y_dis = round(nPixel/2);
    % Create folder
    if (exist(result_folder))
        rmdir(result_folder,'s');
        mkdir(result_folder);
    else
        mkdir(result_folder);
    end
end
if nargin == 4
    count = 1;
end

%% Ask type of lens geometry
prompt = 'What lens profile do you wish? 1: Spherical/Aspheric; 2: Conical; 3:
Flat Cylinder ';
```

```

choice = input(prompt);

delta = 1;      % Convex if delta=1, concave if delta =0;

%% Ask Radius, Conic Constants and coefficients for spherical lens
if choice == 1
    prompt = 'Please enter Radius, R: ';
    R = input(prompt);
    prompt = 'Please enter Conic Constant, K: ';
    K = input(prompt);
    prompt = 'Please enter alpha coefficients: ';
    alpha = input(prompt);
    NOP = 20*R;    % Resolution circle data points
    gap = 2*R/NOP;
    h = [-R:gap:R];
    % [prof,h] = aspheric_profile(R,K,alpha,NOP,delta,fname);
    for i=1:length(h)
        for j=1:length(alpha)
            Z_sag = ((h(i)^2)/(R * (1 + sqrt(1-(1+K)*((h(i)^2)/(R^2))))) +
alpha(j)*power(h(i),(2*j)));
            if delta == 1      % Convex Lens
                prof(i) = R-Z_sag;
            else
                prof(i) = Z_sag;    % Concave Lens
            end
        end
    end
    end
    fname = 'Spherical';
end
%% For Triangular Profile
if choice == 2
    prompt = 'Please enter Radius, R: ';
    R = input(prompt);
    NOP = 20*R;    % Resolution circle data points
    gap = 2*R/NOP;
    h = [-R:gap:R];
    for i=1:NOP
        prof(i+1)=1 - (abs(NOP/2-i)/(NOP/2));
    end
    prof(1)=0;
    fname = 'Conical';
    %}
end
%% For flat cylinder
if choice == 3
    prompt = 'Please enter Radius, R: ';
    R = input(prompt);
    NOP = 20*R;    % Resolution circle data points
    gap = 2*R/NOP;
    h = [-R:gap:R];
    for i=1:NOP
        prof(i+1)=1;
    end
    % prof(1)=0;
    fname = 'Flat';
    %}
end
if (choice~=1) * (choice~=2) * (choice~=3)
    'ERROR!'
end
end

```



```

%% Shifts the profile to zero and normalizes it to 1
pro=(prof-min(prof))/(max(prof-min(prof)));
% Split the profile in half
pro2 = pro(1:round(length(pro)/2));
% Resample in 1:R+1 vector
pro3=imresample([1 1],pro2,[double(round(length(pro2)/R)) 1],'nearest');
% Corrections
pro3(1) = round(pro3(1));
pro3(end) = 1;
pry=pro3;

col=pry(end:-1:1); % reverse the vector from center to radius
if choice == 3 % For Flat cylinder, the edge must be sharp
    col(end) = 1;
end

%% Create 2D gray-scale image
blank=zeros(nPixel,nPixel); % prepare an all black image file
% Locate the center of the image
centerx=round(nPixel/2);
centery=round(nPixel/2);
% Create a circle at center of the image
for r=1:R+1
    % Generate X-Y coords for each circle
    circ = circle_custom([centerx,centery],r,NOP);

    % Apply each circle to the image with appropriate color
    for i=1:length(circ)
        blank(round(circ(i,1)),round(circ(i,2)))=col(r);
    end
end
% Correction for central pixel
blank(centerx,centery) = blank(centerx,centery+1);
% invert generated image
blank(:, :) = 1 - blank(:, :);
% Plot the gray scale image
figure
imshow(blank);
axis off
% Save the image file as a .BMP file
if choice == 1
    imwrite(blank,strcat(result_folder,'\ ',fname,'-R', int2str(R), '_Conic',
int2str(K), 'count# ', int2str(count),'.bmp'),'BMP')
else
    imwrite(blank,strcat(result_folder,'\ ',fname,'-R', int2str(R),
'count# ', int2str(count),'.bmp'),'BMP')
end
close;

%% Convert image into Height Profile:Zr and 2D part profile:Zm
Zm = 1-blank;
prompt = 'Please enter Sag height, H: ';
ht = input(prompt);
% Apply scaling to the geometry
Zm = double(Zm * ht);
Zr = ht*col;
% Shift geometry to user entered X & Y locations
Z2 = zeros(nPixel,nPixel);
for p=1:nPixel
    for q=1:nPixel

```

```

        if ((p-centerx+X_dis > 0) && (q-centery+Y_dis >0) && (p-
centerx+X_dis <=nPixel) && (q-centery+Y_dis <=nPixel))
            Z2(q - centery + Y_dis, p - centerx + X_dis) = Zm(q,p);
        end
    end
end
clear Zm;
Zm=Z2;
clear Z2;

%% Plot and save the profile
fig1=figure;
x_dis=linspace(0,R,length(Zr));
plot(x_dis,Zr);
xlabel('Radius (\mum)');
ylabel('Profile Height (\mum)');
title({'Desired 2D C-S Part Profile'});
xlim([0 R*1.1])
ylim([min(min(Zr),0) max(Zr)*1.1])
axis square;
saveas(fig1, strcat(result_folder,'\Desired Part Profile in 2D Count#
',int2str(count),'.fig'));

%% Plot and save Part Profile Data in Matrix
fig2 = figure;
surf(Zm,'EdgeColor','none','Marker','none');
colorbar('location','eastoutside');
xlim([0 nPixel]);
ylim([0 nPixel]);
xlabel('Substrate Pixels - X-axis'),ylabel('Substrate Pixels - Y-
axis'),zlabel('Desired Part Geometry: Z(\mum)'),
title({'Desired Part Geometry';'';'(1pixel = 1\mum)'})
saveas(fig2, strcat(result_folder,'\Desired C-S Part Profile Count#
',int2str(count),'.fig'));

end

```

**Trademarks Used:**

PowerPoint® is a registered trademark of Microsoft Corporation.

COMSOL® is a registered trademark of COMSOL AB.

SolidWorks® is a registered trademark of Dassault Systèmes SolidWorks Corporation

MATLAB® is a registered trademark of The MathWorks, Inc.

DMD™ is a registered trademark of Texas Instruments

## Works Cited

- [1] P. Jacobs, *Rapid Prototyping & Manufacturing: Fundamentals of Stereolithography*: Society of Manufacturing Engineers, Dearborn, MI, 1992.
- [2] K. Ikuta and K. Hirowatari, "Real three dimensional micro fabrication using stereo lithography and metal molding," in *Micro Electro Mechanical Systems, 1993, MEMS '93, Proceedings An Investigation of Micro Structures, Sensors, Actuators, Machines and Systems. IEEE.*, 1993, pp. 42-47.
- [3] I. H. Lee and D. W. Cho, "An investigation on photopolymer solidification considering laser irradiation energy in micro-stereolithography," *Microsystem Technologies-Micro-and Nanosystems-Information Storage and Processing Systems*, vol. 10, pp. 592-598, Nov 2004.
- [4] S. Maruo and S. Kawata, "Two-photon-absorbed near-infrared photopolymerization for three-dimensional microfabrication," *Journal of Microelectromechanical Systems*, vol. 7, pp. 411-415, Dec 1998.
- [5] Z. S. Bertsch A., Jezequel J., Corbel S. and Andre J., "Microstereolithography Using Liquid Crystal Display as Dynamic Mask-Generator," *Microsystems Technologies*, vol. 3, pp. 42-47, 1997.
- [6] C. Chatwin, M. Farsari, S. P. Huang, M. Heywood, P. Birch, R. Young, and J. Richardson, "UV microstereolithography system that uses spatial light modulator technology," *Applied Optics*, vol. 37, pp. 7514-7522, Nov 10 1998.
- [7] S. Monneret, V. Loubere, and S. Corbel, "Microstereolithography using a dynamic mask generator and a non-coherent visible Light source," *Design, Test, and Microfabrication of Memes and Moems, Pts 1 and 2*, vol. 3680, pp. 553-561, 1999.
- [8] C. Sun, N. Fang, D. M. Wu, and X. Zhang, "Projection Micro-Stereolithography Using Digital Micro-Mirror Dynamic Mask," *Sensors and Actuators A-Physical*, vol. 121, pp. 113-120, 2005.
- [9] Y. Pan, Y. Chen, and C. Zhou, "Fabrication of Smooth Surfaces based on Mask Projection Stereolithography," in *Proceedings of the 22nd Solid Freeform Fabrication Symposium*, Austin, TX, 2011, pp. 263-278.
- [10] B. Sager and D. Rosen, "Use of parameter estimation for stereolithography surface finish improvement," *Rapid Prototyping Journal*, vol. 14, pp. 213-220, 2008.
- [11] (08/15/2012). <http://www.envisiontec.de/index.php?page=news&p=2>.
- [12] L. Erdmann, A. Deparnay, G. Maschke, M. L. Langle, and R. Brunner, "MOEMS-based lithography for the fabrication of micro-optical components," *Journal of Microlithography Microfabrication and Microsystems*, vol. 4, Oct-Dec 2005.
- [13] (2013, 03/15/2013). *ProJet 5000 Product Brochure*. Available: [http://www.printin3d.com/sites/printin3d.com/files/downloads/Projet\\_5000\\_brochure\\_USEN.pdf](http://www.printin3d.com/sites/printin3d.com/files/downloads/Projet_5000_brochure_USEN.pdf)
- [14] X. Zhao, "Process Planning for thick-film mask projection micro stereolithography," MS, Mechanical Engineering, Georgia Institute of Technology, Atlanta 2009.

- [15] Y. J. Juang, L. J. Lee, and K. W. Koelling, "Hot embossing in microfabrication. Part I: Experimental," *Polymer Engineering and Science*, vol. 42, pp. 539-550, Mar 2002.
- [16] H. Becker and C. Gartner, "Polymer microfabrication methods for microfluidic analytical applications," *Electrophoresis*, vol. 21, pp. 12-26, Jan 2000.
- [17] Y. C. Su, J. Shah, and L. W. Lin, "Implementation and analysis of polymeric microstructure replication by micro injection molding," *Journal of Micromechanics and Microengineering*, vol. 14, pp. 415-422, Mar 2004.
- [18] R. Zauner, "Micro powder injection moulding," *Microelectronic Engineering*, vol. 83, pp. 1442-1444, Apr-Sep 2006.
- [19] J. S. Rossier, C. Vollet, A. Carnal, G. Lager, V. Gobry, H. H. Girault, P. Michel, and F. Reymond, "Plasma etched polymer microelectrochemical systems," *Lab on a Chip*, vol. 2, pp. 145-150, 2002.
- [20] J. C. McDonald and G. M. Whitesides, "Poly(dimethylsiloxane) as a material for fabricating microfluidic devices," *Accounts of Chemical Research*, vol. 35, pp. 491-499, Jul 2002.
- [21] R. Gaughan, "Femtosecond laser brings 3-D to microfluidics," *Photonics Spectra*, vol. 39, pp. 34+, Aug 2005.
- [22] R. Voelkel and K. J. Weible, "Laser Beam Homogenizing: Limitations and Constraints," *Optical Fabrication, Testing, and Metrology Iii*, vol. 7102, 2008.
- [23] P. Ruther, B. Gerlach, J. Göttert, M. Ilie, J. Mohr, A. Müller, and C. Obmann, "Fabrication and characterization of microlenses realized by a modified LIGA process," *Pure and Applied Optics: Journal of the European Optical Society Part A*, vol. 6, p. 643, 1997.
- [24] M. Hecke, W. Bacher, and K. D. Müller, "Hot embossing - The molding technique for plastic microstructures," *Microsystem Technologies*, vol. 4, pp. 122-124, 1998.
- [25] M. C. Hutley, *Micro-optics: Elements, Systems and Applications* Philadelphia, PA, USA: Taylor & Francis Inc., 1997.
- [26] D. Daly, R. F. Stevens, M. C. Hutley, and N. Davies, "The Manufacture of Microlenses by Melting Photoresist," *Measurement Science & Technology*, vol. 1, pp. 759-766, Aug 1990.
- [27] M. B. Stern and T. R. Jay, "Dry-Etching for Coherent Refractive Microlens Arrays," *Optical Engineering*, vol. 33, pp. 3547-3551, Nov 1994.
- [28] M. T. Gale, *Micro-optics: Elements, Systems and Applications*. Philadelphia, PA, USA: Taylor & Francis Inc., 1997.
- [29] B. Volckaerts, Ottevaere, H., Vynck, P., Debaes, C., Tuteleers, P., Hermanne, A., "Deep lithography with protons: a generic fabrication technology for refractive micro-optical components and modules," *Asian Journal of Physics*, vol. 10, pp. 195-214, 2001.
- [30] S. Mihailov and S. Lazare, "Fabrication of Refractive Microlens Arrays by Excimer-Laser Ablation of Amorphous Teflon," *Applied Optics*, vol. 32, pp. 6211-6218, Nov 1 1993.

- [31] D. L. Macfarlane, V. Narayan, J. A. Tatum, W. R. Cox, T. Chen, and D. J. Hayes, "Microjet Fabrication of Microlens Arrays," *Ieee Photonics Technology Letters*, vol. 6, pp. 1112-1114, Sep 1994.
- [32] R. Voelkel, "Micro-Optics: From High-End to Mass-Market," *Optik & Photonik*, vol. 4, pp. 36-40, 2009.
- [33] A. Jariwala, F. Ding, X. Zhao, and D. W. Rosen, "A Process Planning method for Thin Film Mask Projection Micro-Stereolithography," in *Proceedings of the ASME 2009 International Design Engineering Technical Conferences & Computers and Information in Engineering Conference*, San Diego, California, 2009.
- [34] A. S. Jariwala, F. Ding, X. Y. Zhao, and D. W. Rosen, "A Process Planning Method for Thin Film Mask Projection Micro-Stereolithography," *Asme International Design Engineering Technical Conferences and Computers and Information in Engineering Conference, Proceedings, Vol 2, Pts a and B*, pp. 685-694, 2010.
- [35] C. Decker, "Photoinitiated Curing of Multifunctional Monomers," *Acta Polymerica*, vol. 45, pp. 333-347, Oct 1994.
- [36] L. Flach and R. P. Chartoff, "A process model for nonisothermal photopolymerization with a laser light source. I: Basic model development," *Polymer Engineering & Science*, vol. 35, pp. 483-492, 1995.
- [37] L. Flach and R. P. Chartoff, "A process model for nonisothermal photopolymerization with a laser light source. II: Behavior in the vicinity of a moving exposed region," *Polymer Engineering & Science*, vol. 35, pp. 493-498, 1995.
- [38] Y. Tang, "Stereolithography Cure Process Modeling," PhD, School of Chemical & Biomolecular Engineering, Georgia Institute of Technology, Atlanta, 2005.
- [39] A. Boddapati, "Modeling Cure Depth during Photopolymerization of Multifunctional Acrylates," Masters of Science, School of Chemical & Biomolecular Engineering, Georgia Institute of Technology, Atlanta, 2010.
- [40] A. S. Jariwala, F. Ding, A. Boddapati, V. Breedveld, M. A. Grover, C. L. Henderson, and D. W. Rosen, "Modeling effects of oxygen inhibition in mask-based stereolithography," *Rapid Prototyping Journal*, vol. 17, pp. 168-175, 2011.
- [41] S. Nagamori and T. Yoshizawa, "Research on solidification of resin in stereolithography," *Optical Engineering*, vol. 42, pp. 2096-2103, Jul 2003.
- [42] A. S. Limaye and D. W. Rosen, "Process planning method for mask projection micro-stereolithography," *Rapid Prototyping Journal*, vol. 13, pp. 76-84, 2007.
- [43] A. S. Limaye, "MULTI-OBJECTIVE PROCESS PLANNING METHOD FOR MASK PROJECTION STEREOLITHOGRAPHY," PhD, Mechanical Engineering, Georgia Institute of Technology, Atlanta, 2007.
- [44] A. Boddapati, S. B. Rahane, R. P. Slopek, V. Breedveld, C. L. Henderson, and M. A. Grover, "Gel time prediction of multifunctional acrylates using a kinetics model," *Polymer*, vol. 52, pp. 866-873, 2011.

- [45] R. P. Slopek. (2008). *In-situ monitoring of the mechanical properties during the photopolymerization of acrylate resins using particle tracking microrheology*. Available: <http://hdl.handle.net/1853/22657>
- [46] E. Andrzejewska, M. B. Bogacki, and M. Andrzejewski, "Variations of Rate Coefficients and Termination Mechanism During the After-Effects of a Light- Induced Polymerization of a Dimethacrylate Monomer," *Macromolecular Theory and Simulations*, vol. 10, pp. 842-849, 2001.
- [47] C. Decker and A. D. Jenkins, "Kinetic Approach of O-2 Inhibition in Ultraviolet-Induced and Laser-Induced Polymerizations," *Macromolecules*, vol. 18, pp. 1241-1244, 1985.
- [48] T. M. Lovestead, A. K. O'Brien, and C. N. Bowman, "Models of multivinyl free radical photopolymerization kinetics," *Journal of Photochemistry and Photobiology a-Chemistry*, vol. 159, pp. 135-143, Jul 14 2003.
- [49] G. Odian, *Principles of Polymerization*, 4 ed. New York: John Wiley & Sons, 2004.
- [50] L. J. Gou, C. N. Coretsopoulos, and A. B. Scranton, "Measurement of the dissolved oxygen concentration in acrylate monomers with a novel photochemical method," *Journal of Polymer Science Part a-Polymer Chemistry*, vol. 42, pp. 1285-1292, Mar 1 2004.
- [51] W. H. Carothers, "Polymerization," *Chemical Reviews*, vol. 8, pp. 353-426, Jun 1931.
- [52] W. H. Carothers, "Polymers and polyfunctionality.," *Transactions of the Faraday Society*, vol. 32, pp. 0039-0053, 1936.
- [53] P. J. Flory, "Molecular size distribution in three dimensional polymers. I. Gelation," *Journal of the American Chemical Society*, vol. 63, pp. 3083-3090, Jul-Dec 1941.
- [54] R. P. Slopek. (2005). *In-situ monitoring of photopolymerization using microrheology*. Available: <http://smartech.gatech.edu/handle/1853/7194>
- [55] A. S. Limaye, "Design and Analysis of a Mask Projection Micro-Stereolithography System," M.S., Mechanical Engineering, Georgia Institute of Technology, Atlanta, GA, 2004.
- [56] A. Jariwala, F. Ding, X. Zhao, and D. Rosen, "A Film Fabrication Process on Transparent Substrate Using Mask Projection Stereolithography," in *Proceedings of the 19th Solid Freeform Fabrication Symposium*, Austin, TX, 2008, pp. 216-229.
- [57] B. K. Mann, R. H. Schmedlen, and J. L. West, "Tethered-TGF-beta increases extracellular matrix production of vascular smooth muscle cells," *Biomaterials*, vol. 22, pp. 439-444, Mar 2001.
- [58] (2010, 12/08/2010). *DLP System Optics*. Available: <http://www.ti.com/lit/an/dlpa022/dlpa022.pdf>
- [59] E. Optics. (08/01/2011). Available: <http://www.eisoptics.com/images/up/UpFile/LightTunnel.pdf>
- [60] J. H. Lee, R. K. Prud'homme, and I. A. Aksay, "Cure depth in photopolymerization: Experiments and theory," *Journal of Materials Research*, vol. 16, pp. 3536-3544, Dec 2001.

- [61] (2001, 09/10/2012). *CIBA Irgacure 651*. Available: [http://people.rit.edu/deeemc/courses/0305-676/reference/Imprint/irgacure\\_651.pdf](http://people.rit.edu/deeemc/courses/0305-676/reference/Imprint/irgacure_651.pdf)
- [62] M. Kaur and A. K. Srivastava, "Photopolymerization: A review," *Journal of Macromolecular Science-Polymer Reviews*, vol. C42, pp. 481-512, 2002.
- [63] J. Puskas, *In-situ Spectroscopy of Monomer and Polymer Synthesis*. New York: Kluwer Academic/Plenum Publishers, 2003.
- [64] Z. B. Alfassi, *General Aspects of the Chemistry of Radicals*. New York: Wiley, 1999.
- [65] O. Dudi and W. T. Grubbs, "Laser interferometric technique for measuring polymer cure kinetics," *Journal of Applied Polymer Science*, vol. 74, pp. 2133-2142, Nov 28 1999.
- [66] E. A. Fogleman, M. T. Kelly, and W. T. Grubbs, "Laser interferometric method for measuring linear polymerization shrinkage in light cured dental restoratives," *Dental Materials*, vol. 18, pp. 324-330, Jun 2002.
- [67] K. Inoue, S. Komatsu, X.-A. Trinh, T. Norisuye, and Q. Tran-Cong-Miyata, "Local deformation in photo-crosslinked polymer blends monitored by Mach-Zehnder interferometry," *Journal of Polymer Science Part B: Polymer Physics*, vol. 43, pp. 2898-2913, 2005.
- [68] Q. Tran-Cong-Miyata, D. T. Van-Pham, K. Noma, T. Norisuye, and H. Nakanishi, "The Roles of Reaction Inhomogeneity in Phase Separation Kinetics and Morphology of Reactive Polymer Blends," *Chinese Journal of Polymer Science*, vol. 27, pp. 23-36, Jan 2009.
- [69] D. Karalekas, D. Rapti, E. E. Gdoutos, and A. Aggelopoulos, "Investigation of shrinkage-induced stresses in stereolithography photo-curable resins," *Experimental Mechanics*, vol. 42, pp. 439-444, Dec 2002.
- [70] L. Flach and R. P. Chartoff, "Simple Polymer Shrinkage Model Applied to Stereolithography," in *Proc. Solid Freeform Fabrication Symposium*, Austin, TX, 1994, pp. 225-232.
- [71] J. Y. H. Fuh, L. Lu, C. C. Tan, Z. X. Shen, and S. Chew, "Curing characteristics of acrylic photopolymer used in stereolithography process," *Rapid Prototyping Journal*, vol. 5, pp. 27-34, 1999.
- [72] B. Wiedemann, K. H. Dusel, and J. Esch, "Investigation into the influence of material and process on part distortion," *Rapid Prototyping Journal*, vol. 1, pp. 17-22, 1995.
- [73] S. S. Hur and J. R. Youn, "Prediction of the deformation in stereolithography products based on elastic thermal shrinkage," *Polymer-Plastics Technology and Engineering*, vol. 37, pp. 539-563, 1998.
- [74] "Sartomer Application Bulletin - Shrinkage of UV Monomers," 2011.
- [75] S. W. Paddock, "Principles and practices of laser scanning confocal microscopy," *Molecular Biotechnology*, vol. 16, pp. 127-149, Oct 2000.
- [76] S. G. Li, Z. G. Xu, I. Reading, S. F. Yoon, Z. P. Fang, and J. H. Zhao, "Three dimensional sidewall measurements by laser fluorescent confocal microscopy," *Optics Express*, vol. 16, pp. 4001-4014, Mar 17 2008.



- [77] *Fluorol* 555. Available: <http://www.photonicsolutions.co.uk/datasheets/exci/Fluorol%20555.pdf>
- [78] H. Becker and H. Vogel, "Stabilization of acrylic esters," *Chemical Engineering & Technology*, vol. 27, pp. 1122-1126, Oct 2004.
- [79] H. Becker and H. Vogel, "The role of hydroquinone monomethyl ether in the stabilization of acrylic acid," *Chemical Engineering & Technology*, vol. 29, pp. 1227-1231, Oct 2006.
- [80] R. J. Li and F. J. Schork, "Modeling of the inhibition mechanism of acrylic acid polymerization," *Industrial & Engineering Chemistry Research*, vol. 45, pp. 3001-3008, Apr 26 2006.
- [81] A. K. O'Brien and C. N. Bowman, "Modeling the effect of oxygen on photopolymerization kinetics," *Macromolecular Theory and Simulations*, vol. 15, pp. 176-182, Feb 17 2006.
- [82] J. T. Tou, *Pattern recognition principles [by] Julius T. Tou [and] Rafael C. Gonzalez*. Reading, Mass.: Addison-Wesley Pub. Co, 1974.
- [83] *Handbook of pattern recognition and image processing*. Orlando :: Academic Press, Harcourt Brace Jovanovich, 1986.
- [84] P. Scallan, *Process Planning*: Butterworth-Heinemann, 2003.
- [85] (2012). *Aspheric Lens*. Available: [http://en.wikipedia.org/wiki/Aspheric\\_lens](http://en.wikipedia.org/wiki/Aspheric_lens)
- [86] T. Instruments. (03/26/2013). *DLP7000*. Available: <http://www.ti.com/lit/ds/dlps026a/dlps026a.pdf>
- [87] A. Jariwala, R. Schwerzel, and D. Rosen, "REAL-TIME INTERFEROMETRIC MONITORING SYSTEM FOR EXPOSURE CONTROLLED PROJECTION LITHOGRAPHY," in *Proceedings of the Twenty Second Annual International Solid Freeform Fabrication Symposium Austin, Texas, 2011*, pp. 99-110.
- [88] R. E. Schwerzel, A. S. Jariwala, and D. W. Rosen, "A simple, inexpensive, real-time interferometric cure monitoring system for optically cured polymers," *Journal of Applied Polymer Science*, vol. 128, 2013.
- [89] American Chemical Society. Meeting (211th : 1996 : New Orleans La.), A. B. Scranton, C. N. Bowman, R. W. Peiffer, and American Chemical Society. Division of Polymeric Materials: Science and Engineering., *Photopolymerization : fundamentals and applications*. Washington, DC: American Chemical Society, 1997.
- [90] D. G. Jenkins, B. R. Fulton, J. Pearson, C. J. Lister, M. P. Carpenter, S. J. Freeman, N. J. Hammond, R. V. F. Janssens, T. L. Khoo, T. Lauritsen, A. H. Wuosmaa, P. Fallon, A. Gorgen, A. O. Macchiavelli, M. McMahan, F. Haas, and D. E. Collaboration, "Doorway states as principal decay pathway in C-12(C-12,gamma) radiative capture," *Nuclei at the Limits*, vol. 764, pp. 367-372, 2005.